AIR FLOW CHARACTERISTICS OF MODEL INTERNAL-COMBUSTION ENGINES

ALI FEHMI BICEN

B.Sc.(Eng), M.Sc.(Eng), D.I.C.

Thesis submitted for the Degree of
Doctor of Philosophy
in the University of London

Imperial College of Science and Technology
Department of Mechanical Engineering

April 1983

To my loved ones

ABSTRACT

Experimental investigations of turbulent air motion in axisymmetric models of a reciprocating internal-combustion engine are reported. Laser Doppler anemometry was used to quantify both the mean motion and turbulence inside the cylinders of two reciprocating model engines motored at 200 rpm and in a steady flow simulation of an inlet port and valve arrangement. One engine was operated in the absence of compression, therefore in a two-stroke cycle, and simulated the intake and exhaust strokes only. The other, having similar geometric characteristics, was motored with compression ratios of 3.5 and 6.7 in a conventional four-stroke cycle.

In the two-stroke cycle engine, the emphasis was on the intake-related flow processes and the effects of flow and geometry boundary conditions, including piston crown, clearance volume and piston stroke, on the intake-generated flow patterns were examined. In all configurations a system of toroidal and ring type vortices was induced in the axial plane during intake by the jet-like flow which stems from the valve opening. The vortices progressively decayed in the second half of the intake stroke and were destroyed early in the return stroke. In the cases of longer stroke and smaller clearance volume, the vortices were stronger and elongated or contracted to accommodate the changes in geometry. The effect of piston crown geometry was found to be insignificant during intake, and in the return stroke in the absence of compression.

With the four-stroke model engine, the emphasis was more on the compression phase and the interaction between squish, induced by virtue of piston crown geometry, and intake-induced swirl was investigated for various shapes of combustion chamber including open and re-entrant type

piston bowls. In disc shape chambers, the mean motions in the axial plane decayed, independently of compression ratio, to insignificant levels at the end of compression contrary to intake swirl which prolonged conforming to near solid body rotation at TDC. The compression turbulence in disc shape chambers was near homogeneous and isotropic and remained almost constant during the stroke at levels of around 0.5 times the mean piston speed. The squish, generated in the open and re-entrant piston bowls, induced new mean motions near TDC, and its interaction with swirl caused profound changes in the TDC flow structure. When strong squish effect was present, for example as in the case of the re-entrant bowl, higher levels of compression turbulence than in disc shape chambers were observed.

An investigation of the flow near and at the exit plane of an intake valve was conducted under both steady and unsteady flow conditions for various fixed valve lifts. The quantitative description of the velocity field at the exit plane showed large deviations from a plug type flow in the intermediate-to-high lift range and explains the observed variations in discharge coefficient with valve lift. A close correspondence between the steady and unsteady flows, in particular with respect to the mean flow, suggests that the intake valve flow can be assumed to be quasi-steady.

ACKNOWLEDGEMENTS

I would like to take this opportunity to thank a number of people who helped with the realisation of this thesis in one way or another.

My most sincere gratitude goes to Professor J.H. Whitelaw who has provided me with his excellent guidance, continuous encouragement and precious advice and criticism, without which this thesis would not have materialised.

I have greatly benefited from the assistance of, and numerous discussion with, Mr. B. Ahmadi-Befrui, Mr. C. Arcoumanis, Dr. A.D. Gosman, Mr. A. Jahanbakhsh, Mr. C. Vafidis, Dr. N.S. Vlachos and Dr. M. Yianneskis. My thanks go to all.

My thanks also go to Ms. M. Founti, Dr. A.M.K.P. Taylor, Mr. B.E. Thompson and Mr. B. Younis for their valuable advice and discussions.

I am grateful to Messrs. N. Frost, J. Laker and O. Vis for their help with the design and contribution in the construction of the experimental apparatus.

I am indebted to the Atomic Energy Research Establishment for providing the financial support for this work.

Last but not least, I would like to thank my wife, Mrs. Rosalind Bicen, for her excellent and speedy typing of this thesis as well as for her constant encouragement along the course of this work.

TABLE OF CONTENTS

		Page
ABSTRACT		iii
ACKNOWLEDGEMENTS		v
TABLE OF CONTENTS		vi
LIST OF TABLES		x
LIST OF FIGURES		xi
NOMENCLATURE		xxii
CHAPTER 1	INTRODUCTION	1
1.1	Introductory Remarks	2
1.2	Previous Work	5
	1.2.1 Experiments	5
	1.2.2 Calculations	10
1.3	Present Contribution	13
1.4	Thesis Outline	15
TABLES		16
CHAPTER 2	IN-CYLINDER FLOW IN A TWO-STROKE CYCLE MODEL ENGINE	26
2.1	Introduction	27
2.2	Experimental System	28
	2.2.1 Flow Configurations	28
	2.2.2 Laser Doppler Anemometer:	32
	Optical Arrangement	33
	Seeding	37
	Signal Processing System	37

			Page
		2.2.3 Data Reduction Equations	40
		2.2.4 Data Processing System	41
		2.2.5 Measurement Procedure & System Performance	42
		2.2.6 Measurement Uncertainties:	44
		Positional Uncertainties	44
		Asymmetry	45
		Statistical Error	45
		Engine Speed	46
		Frequency Shift	46
		Velocity Gradient Broadening	47
		Crank Angle Broadening	48
		Biasing Effects	50
		Mass Continuity	52
	2.3 Results		53
		2.3.1 Introduction	53
		2.3.2 60 mm Stroke; Swept-to-Clearance Volume Ratio of 2	55
		2.3.3 90 mm Stroke; Swept-to-Clearance Volume Ratio of 3	58
		2.3.4 90 mm Stroke; Swept-to-Clearance Volume Ratio of 9	61
		2.3.5 Flat & Re-entrant Type Bowl Pistons	64
	2.4 Discussion		65
		2.4.1 Creation & Destruction of Vortices	65
		2.4.2 Influence of Stroke	68
		2.4.3 Influence of Clearance Volume	69
		2.4.4 Influence of Piston Crown Geometry	70
	2.5 Conclusions		71
FIGURES			73

			Page
CHAPTER	3	IN-CYLINDER FLOW IN A FOUR-STROKE MODEL ENGINE	97
	3.1	Introduction	98
	3.2	Experimental System	99
		3.2.1 Flow Configurations	99
		3.2.2 Pressure Measurements	103
		3.2.3 Laser Doppler Anemometer	103
		3.2.4 Measurement Procedure & System Performance	104
		3.2.5 Measurement Uncertainties	106
	3.3	Results	108
		3.3.1 Introduction	108
		3.3.2 Compression Ratio of 3.5:	108
		Flat Piston	108
		Cylindrical & Re-Entrant Bowls	112
		3.3.3 Compression Ratio of 6.7:	115
		Flat Piston	115
		Cylindrical Bowl with & without Swirl	116
		Re-entrant Bowl with & without Swirl	118
	3.4	Discussion	119
		3.4.1 Mean Motion & Turbulence in Disc Chamber	119
		3.4.2 Influence of Compression Ratio	125
		3.4.3 Squish & Swirl-Squish Interaction	127
		3.4.4 Assessment of Relevant Flow Calculations	131
	3.5	Conclusions	134
APPENDIX	3.1	CALCULATION OF SWIRL RATIO & ANGULAR MOMENTUM	137

			Page
APPENDIX	3.2	REFRACTION CORRECTION FOR LDA MEASUREMENTS IN FLOWS WITH CURVED OPTICAL BOUNDARIES	141
APPENDIX	3.3	COMPARISON BETWEEN MEASUREMENTS & RELEVANT FLOW CALCULATIONS	153
FIGURES			159
CHAPTER	4	STEADY & UNSTEADY FLOW THROUGH AN INTAKE VALVE	187
	4.1	Introduction	188
	4.2	Experimental System	189
		4.2.1 Flow Configurations	189
		4.2.2 Flow Metering & Pressure Drop Measurements	190
		4.2.3 Velocity Measurements	191
		4.2.4 Measurement Uncertainties	192
	4.3	Results	193
		4.3.1 Introduction	193
		4.3.2 Steady Flow	194
		4.3.3 Unsteady Flow	197
	4.4	Discussion	199
	4.5	Conclusions	203
APPENDIX	4.1	DEFINITION OF DISCHARGE COEFFICIENT & CALCULATIONS OF EFFECTIVE & GEOMETRIC VALVE AREAS	205
FIGURES			211
CHAPTER	5	CONCLUDING REMARKS	222
REFERENCES			227

LIST OF TABLES

Table		Page
1.1	Experimental investigations	17
1.2	Multi-dimensional calculations	24
2.1	Main characteristics of two-stroke cycle model engine	30
2.2	Parameters varied in two-stroke cycle model engine	32
2.3	Principal characteristics of optical system	36
3.1	Main characteristics of four-stroke model engine	101
3.2	Geometric details of piston crown configurations	102
3.3	Principal characteristics of laser Doppler anemometer	104

LIST OF FIGURES

Figure		Page
2.1	Schematic diagram of two-stroke model engine.	74
2.2	Piston crown configurations. (a) Flat piston (b) Re-entrant type bowl	74
2.3	Optical arrangement of laser Doppler anemometer.	75
2.4	Block diagram of signal and data processing systems	75
2.5	In-cylinder flow symmetry; axial velocity profiles at Θ = 90 degrees, z = 15 mm with S = 90 mm, c = 30 mm. (a) Mean velocity (b) Rms velocity	76
2.6	Streamline pattern and axial velocity profiles at Θ = 170 degrees; S = 60 mm, c = 30 mm. (a) Streamline pattern (b) Mean velocity (c) Rms velocity	77
2.7	Streamline pattern and axial velocity profiles at Θ = 190 degrees; S = 60 mm, c = 30 mm. (a) Streamline pattern (b) Mean velocity (c) Rms velocity	78
2.8	Streamline pattern and axial velocity profiles at Θ = 200 degrees; S = 60 mm, c = 30 mm. (a) Streamline pattern (b) Mean velocity (c) Rms velocity	79

Figure		Page
2.9	Streamline pattern and axial velocity profiles at Θ = 216 degrees; S = 60 mm, c = 30 mm. (a) Streamline pattern (b) Mean velocity (c) Rms velocity	80
2.10	Streamline patterns; S = 60 mm, c = 30 mm. (a) Θ = 36 degrees (b) Θ = 90 degrees (c) Θ = 144 degrees (d) Θ = 170 degrees (e) Θ = 190 degrees (f) Θ = 200 degrees (g) Θ = 216 degrees	81
2.11	Streamline pattern and axial velocity profiles at Θ = 36 degrees; S = 90 mm, c = 30 mm. (a) Streamline pattern (b) Mean velocity (c) Rms velocity	83
2.12	Streamline pattern and axial velocity profiles at Θ = 90 degrees; S = 90 mm, c = 30 mm. (a) Streamline pattern (b) Mean velocity (c) Rms velocity	84
2.13	Streamline patterns and axial velocity profiles at Θ = 144 degrees; S = 90 mm, c = 30 mm. (a) Streamline pattern (b) Mean velocity (c) Rms velocity	85

Figure		Page
2.14	Streamline pattern and axial velocity profiles at Θ = 170 degrees; S = 90 mm, c = 30 mm. (a) Streamline pattern (b) Mean velocity (c) Rms velocity	86
2.15	Streamline pattern and axial velocity profiles at Θ = 190 degrees; S = 90 mm, c = 30 mm. (a) Streamline pattern (b) Mean velocity (c) Rms velocity	87
2.16	Streamline pattern and axial velocity profiles at Θ = 200 degrees; S = 90 mm, c = 30 mm. (a) Streamline pattern (b) Mean velocity (c) Rms velocity	88
2.17	Streamline pattern and axial velocity profiles at Θ = 36 degrees; S = 90 mm, c = 10 mm. (a) Streamline pattern (b) Mean velocity (c) Rms velocity	89
2.18	Streamline pattern and axial velocity profiles at Θ = 90 degrees; S = 90 mm, c = 10 mm. (a) Streamline pattern (b) Mean velocity (c) Rms velocity	90

Figure		Page
2.19	Streamline pattern and axial velocity profiles at θ = 144 degrees; S = 90 mm, c = 10 mm. (a) Streamline pattern (b) Mean velocity (c) Rms velocity	91
2.20	Streamline pattern and axial velocity profiles at θ = 170 degrees; S = 90 mm, c = 10 mm. (a) Streamline pattern (b) Mean velocity (c) Rms velocity	92
2.21	Streamline pattern and axial velocity profiles at θ = 190 degrees; S = 90 mm, c = 10 mm. (a) Streamline pattern (b) Mean velocity (c) Rms velocity	93
2.22	Streamline pattern and axial velocity profiles at θ = 200 degrees; S = 90 mm, c = 10 mm. (a) Streamline pattern (b) Mean velocity (c) Rms velocity	94
2.23	Axial velocity profiles at θ = 36 degrees; re-entrant type bowl and flat piston. (a) Mean velocity (b) Rms velocity	95
2.24	Axial velocity profiles at θ = 90 degrees; re-entrant type bowl and flat piston. (a) Mean velocity (b) Rms velocity	95

Figure		Page
2.25	Axial velocity profiles at θ = 144 degrees; re-entrant type bowl and flat piston. (a) Mean velocity (b) Rms velocity	96
2.26	Axial velocity profiles at θ = 190 degrees; re-entrant type bowl and flat piston. (a) Mean velocity (b) Rms velocity	96
3.1	Schematic of four-stroke model engine and pressure measurement system.	160
3.2	Variation of cylinder pressure, valve lift and piston speed with crank angle.	160
3.3	Piston bowl configurations used with CR = 3.5. (a) Cylindrical bowls (b) Re-entrant type bowl	161
3.4	Piston bowl configurations used with CR = 6.7. (a) Cylindrical bowl (b) Re-entrant type bowl	161
3.5	Variation of axial rms velocity with crank angle for various crank angle windows at z = 15 mm, r = 25 mm; flat piston, CR = 3.5.	162
3.6	Variation of sample rate with crank angle for various crank angle windows at z = 15 mm, r = 25 mm; flat piston, CR = 3.5.	162

Figure		Page
3.7	Temporal profiles of axial and swirl mean velocity components at z = 15 mm, r = 25 mm; flat piston, CR = 3.5.	163
3.8	Temporal profiles of axial and swirl rms velocity components at z = 15 mm, r = 25 mm; flat piston, CR = 3.5.	163
3.9	Axial mean velocity profiles; flat piston, CR = 3.5. (a) θ = 90 degrees (b) θ = 216 degrees (c) θ = 270 degrees (d) θ = 324 degrees (e) θ = 380 degrees (f) θ = 450 degrees (g) θ = 630 degrees	164
3.10	Axial rms velocity profiles; flat piston, CR = 3.5. (a) θ = 90 degrees (b) θ = 216 degrees (c) θ = 270 degrees (d) θ = 324 degrees (e) θ = 380 degrees (f) θ = 450 degrees (g) θ = 630 degrees	166
3.11	Swirl mean and rms velocity profiles at z = 15 mm; flat piston, CR = 3.5. (a) θ = 36 degrees (b) θ = 90 degrees (c) θ = 270 degrees (d) θ = 324 degrees (e) θ = 360 degrees (f) θ = 396 degrees (g) θ = 450 degrees (h) θ = 684 degrees	168

Figure		Page
3.12	Axial mean velocity profiles; deep cylindrical bowl, CR = 3.5. (a) θ = 270 degrees (b) θ = 324 degrees (c) θ = 380 degrees (d) θ = 450 degrees	169
3.13	Axial rms velocity profiles; deep cylindrical bowl, CR = 3.5. (a) θ = 270 degrees (b) θ = 324 degrees (c) θ = 380 degrees (d) θ = 450 degrees	170
3.14	Axial mean velocity profiles; shallow cylindrical bowl, CR = 3.5. (a) θ = 270 degrees (b) θ = 324 degrees (c) θ = 380 degrees (d) θ = 450 degrees	171
3.15	Axial rms velocity profiles; shallow cylindrical bowl, CR = 3.5. (a) θ = 270 degrees (b) θ = 324 degrees (c) θ = 380 degrees (d) θ = 450 degrees	172
3.16	Axial mean velocity profiles; re-entrant type bowl, CR = 3.5. (a) θ = 270 degrees (b) θ = 324 degrees (c) θ = 380 degrees (d) θ = 450 degrees	173
3.17	Axial rms velocity profiles; re-entrant type bowl, CR = 3.5. (a) θ = 270 degrees (b) θ = 324 degrees (c) θ = 380 degrees (d) θ = 450 degrees	174

Figure		Page
3.18	Temporal profiles of axial, radial and swirl mean velocity components at z = 10 mm, r = 25 mm; flat piston, CR = 6.7.	175
3.19	Temporal profiles of axial, radial and swirl rms velocity components at z = 10 mm, r = 25 mm; flat piston, CR = 6.7.	175
3.20	Axial mean and rms velocity profiles at z = 10 mm; flat piston, CR = 6.7. (a) θ = 36 degrees (b) θ = 324 degrees	176
3.21	Swirl mean and rms velocity profiles; flat piston, CR = 6.7. (a) Radial profiles at θ = 360 degrees, z = 10 mm (b) Axial profiles at θ = 360 degrees, r = 25 mm	176
3.22	Axial mean and rms velocity profiles; cylindrical bowl, no swirl, CR = 6.7. (a) θ = 36 degrees (b) θ = 324 degrees	177
3.23	Mean and rms velocity profiles at θ = 360 degrees; cylindrical bowl, no swirl, CR = 6.7. (a) Axial velocity (b) Radial velocity	178
3.24	Mean and rms velocity profiles at θ = 360 degrees; cylindrical bowl, with swirl, CR = 6.7. (a) Axial velocity (b) Radial velocity	179

Figure		Page
3.25	Swirl mean and rms velocity profiles; cylindrical bowl, CR = 6.7. (a) θ = 324 degrees (b) θ = 360 degrees	180
3.26	Axial mean and rms velocity profiles; re-entrant bowl, no swirl, CR = 6.7. (a) θ = 36 degrees (b) θ = 324 degrees	181
3.27	Mean and rms velocity profiles at θ = 360 degrees; re-entrant bowl, no swirl, CR = 6.7. (a) Axial velocity (b) Radial velocity	182
3.28	Mean and rms velocity profiles at θ = 360 degrees; re-entrant bowl, with swirl, CR = 6.7. (a) Axial velocity (b) Radial velocity	183
3.29	Swirl mean and rms velocity profiles; re-entrant bowl, CR = 6.7. (a) θ = 324 degrees (b) θ = 360 degrees	184
3.30	Swirl mean and rms velocity profiles at z = 30 mm; re-entrant bowl, CR = 6.7. (a) θ = 36 degrees (b) θ = 324 degrees (c) θ = 396 degrees (d) θ = 684 degrees	185
3.31	Schematic diagrams of air motion in piston bowls at TDC; CR = 6.7. (a) & (b) No swirl (c) & (d) With swirl	186

Figures		Page
4.1	Schematic of steady flow test rig.	212
4.2	Geometric details of port and valve arrangement	212
4.3	Variations of discharge coefficient C_m with (a) Pressure drop (b) Mass flow rate	213
4.4	Variations of discharge coefficient C_l with (a) Pressure drop (b) Mass flow rate	214
4.5	Variations of discharge coefficients with valve lift. (a) C_m, based on minimum geometric area (b) C_l, based on peripheral lift area	215
4.6	Axial mean and rms velocity profiles at z = 15 mm and radial mean and rms velocity profiles at valve exit plane; steady flow, (•) mean, (o) rms. (a) L = 3 mm (b) L = 6 mm (c) L = 9 mm (d) L = 12 mm	216
4.7	Axial mean and rms velocity profiles; steady flow, L = 6 mm.	218
4.8	Axial mean and rms velocity profiles at z = 15 mm and radial mean and rms velocity profiles at valve exit plane; unsteady flow, Θ = 36 degrees, L = 6 mm, (•) mean, (o) rms.	218

Figure		Page
4.9	Radial mean and rms velocity profiles at valve exit plane; unsteady flow, L = 9 mm, (•) mean, (o) rms. (a) θ = 36 degrees (b) θ = 90 degrees (c) θ = 144 degrees (d) θ = 216 degrees	219
4.10	Radial mean and rms velocity profiles at valve exit plane; unsteady flow, L = 12 mm, (•) mean, (o) rms. (a) θ = 36 degrees (b) θ = 90 degrees (c) θ = 216 degrees	220
4.11	Axial mean and rms velocity profiles; unsteady flow, θ = 90 degrees, L = 6 mm.	221

NOMENCLATURE

Latin Characters

A_e	Effective flow area
A_l	Peripheral valve lift area
A_m	Minimum geometric area
C	Velocity-to-frequency conversion factor
C_l	Discharge coefficient based on A_l
C_m	Discharge coefficient based on A_m
CR	Compression ratio
c	Clearance distance between piston & cylinder head at TDC
D	Cylinder bore diameter
D_m	Mean valve diameter
D_p	Port diameter
D_s	Valve stem diameter
D_v	Valve head diameter
d	Beam waist diameter at e^{-2} intensity level
d_o	Beam diameter at e^{-2} intensity level
d_p	Probe volume diameter at e^{-2} intensity level
d_{ph}	Photomultiplier pinhole diameter
f_D	Doppler frequencey
$\bar{f}_D$	Ensemble-averaged mean Doppler frequency
$\tilde{f}_D$	Ensemble-averaged rms Doppler frequency
f_s	Frequency shift
f_1	Focal length of focussing lens L_1
f_2	Focal length of collimating lens L_2

f_3	Focal length of focussing lens L_3
f_4	Focal length of collecting lens L_4
H_o	Angular momentum
h_o	Angular momentum per unit mass
k	Turbulent kinetic energy
L	Valve lift
l_c	Connecting rod length
l_p	Probe volume length at e^{-2} intensity level
M	Optical magnification
m	Fluid mass
$\dot{m}$	Mass flow rate
$\bar{m}_p$	Mean mass flow rate ($\pi R^2 \rho \bar{V}_p$)
N	Total number of fringes, engine cycles, samples & profiles
$\dot{N}$	Count rate (number of samples per unit time)
N_{ph}	Number of fringes at photomultiplier pinhole
n	Number of engine cycle
P_d	Downstream static pressure
P_{uo}	Upstream stagnation pressure
R	Cylinder radius
R_v	Valve head radius
S	Piston stroke
S_n	Swirl number
S_r	Swirl ratio
SA	Valve seat angle
t_v	Valve thickness

U, V, W	Instantaneous velocity components
$\bar{U}, \bar{V}, \bar{W}$	Ensemble-averaged mean velocity components
u, v, w	Turbulent velocity fluctuations
$\tilde{u}, \tilde{v}, \tilde{w}$	Ensemble-averaged rms velocity components or turbulent velocity components
$\tilde{u}_c$	Rms of crank angle broadening
$\tilde{u}_v$	Rms of velocity gradient broadening
$\tilde{u}/\vec{U}$, $\tilde{v}/\bar{V}$, $\tilde{w}/\bar{W}$	Turbulence intensities
V_c	Cylinder bulk velocity
V_p	Instantaneous piston speed
$\bar{V}_p$	Mean piston speed
V_{pmax}	Maximum piston speed
Z_c	Constant of confidence limit
z, r, ϕ	Cylindrical polar coordinates
z_p	Instantaneous piston position

Greek Characters

α	Half angle of beam intersection
ψ	Stream function
ψ_W	Wall stream function
ε	Dissipation rate of turbulent kinetic energy
λ	Laser wavelength
ω	Angular speed of crankshaft
$\tilde{\omega}$	Rms of angular speed fluctuations of crankshaft

ω_f	Angular velocity of fluid
$\bar{\omega}_f$	Average angular velocity of fluid at TDC
μ	Viscosity of fluid
ρ	Density of fluid
ρ_{uo}	Upstream stagnation density
γ	Ratio of specific heats
θ	Crank angle
τ_p	Average time between particles
τ_s	Sampling time interval
τ_t	Integral time scale of turbulence
ΔP	Pressure drop
ΔR_v	Annular valve opening
Δx	Fringe spacing
$\Delta\theta$	Crank angle window

Abbreviations

ABDC	After bottom-dead-centre
ATDC	After top-dead-centre
BBDC	Before bottom-dead-centre
BDC	Bottom-dead-centre
BTDC	Before top-dead-centre
EVC	Exhaust valve closure
EVO	Exhaust valve opening
IVC	Intake valve closure
IVO	Intake valve opening
TDC	Top-dead-centre

CHAPTER 1

INTRODUCTION

1.1 Introductory Remarks

In the past few years the pressure of emission-control legislation, and increasing cost of oil, have spurred the motorcar industry to produce cleaner and more fuel-efficient engines. The requirements for developing such engines have, in turn, brought about the need for more complete understanding of the fundamental processes. It is known that the turbulent flow field in an engine cylinder is of great importance in determining the combustion characteristics and thermal efficiency of an engine. Engineers have made use of this concept in their cut-and-try approach by changing the combustion chamber and inlet port geometries to control exhaust emissions and improve fuel economy. No general rules, however, existed as the knowledge was empirical and deduced from global measurements in specific engines.

In recent years advances in measurement techniques and computer modelling have helped to reveal causes of inadequate combustion and subsequently led to improvements in engine performance. The problems associated with in-cylinder measurements, however, are still with us today. Access is limited and most experimental techniques are unable to cope with the hostile environment of an engine flow. As a result, few measurements have been obtained in engines under firing conditions and only a small number, usually qualitative, in motored engines. Computer models, on the other hand, show promise for describing the in-cylinder processes with considerable detail at small cost. Nevertheless, they are not totally predictive as they require inputs and embody approximations which can give rise to appreciable errors unless they are improved by testing against quantitative data from experiments. The use of

transparent model engines in conjunction with laser Doppler anemometry as in the present study, is a possible means of overcoming some of the problems and adding to the knowledge with quantitative measurements of velocity characteristics. Optical access is readily available and can provide, with relatively cheap laser Doppler anemometry systems, insight into internal dynamics of reciprocating internal-combustion engines. With conceptually simple geometries, model engines can also allow detailed measurements of quantitative velocity characteristics to serve as a testing ground for calculation methods, most of which are presently limited to simpler-than-practice geometries, as well as to provide input data for inlet, outlet and initial boundary conditions.

Swirl plays an important role in diesel engine combustion as it distributes fuel and prepares a mixture, through enhanced mixing, for ignition. Radial movement of gas during compression, known as squish and induced by virtue of combustion chamber geometry, generates additional bulk movement and turbulence, and redistributes such properties as swirl momentum. The merits of swirl-squish interaction have been long recognised in diesel combustion and in more recent years the concept of squish and swirl as turbulence promoters has taken a prime place in spark ignition engine research to improve the performance characteristics with lean combustible mixtures.

Inlet port and valve arrangements determine the breathing capacity (volumetric efficiency) of an engine and are expected to influence its performance characteristics. Understanding of the valve flow is, therefore, equally important as those inside the engine cylinder which are described above. In the past various port and valve

designs have been tested exclusively under steady state conditions, and the results extrapolated to engine situations with marked differences in performance; however, little was understood about the fluid dynamic detail of the valve flow. Although testing of a port and valve arrangement in an engine environment is desirable and realistic, it is an expensive and arduous task as opposed to steady state testing. Provided that the valve flow can be considered quasi-steady, probing of the flow under steady state can provide insight and correct boundary conditions for calculation methods with considerable economy and convenience.

From the above paragraphs, the significance of in-cylinder fluid dynamics prior to ignition is apparent. This thesis is, therefore, mainly concerned with velocity characteristics and involves the in-cylinder measurement of mean and turbulent velocity fields in axisymmetric model engines motored with and without compression. Some of the important flow processes such as intake-generated structures, compression-induced squish and its interaction with swirl are addressed and the effects of some influential parameters on these processes are examined and quantified. The extent to which steady state results can be used to characterise valve performance and to provide correct boundary conditions for calculation methods is also demonstrated by obtaining data under both steady and unsteady state conditions.

The rest of this Chapter is divided into three Sections. In the following Section previous experimental and theoretical work is reviewed. The present contribution is outlined in the light of previous work in Section 1.3 followed by the final Section in which the content of the remaining Chapters is briefly described.

1.2 Previous Work

The review of literature focusses on intake flow structure, squish and swirl, and is presented to provide the background for formulating the aims and purposes of the present contribution. It begins with experimental investigations first and calculations of in-cylinder flow processes follow.

1.2.1 Experiments

A comprehensive listing of the previous experimental work is given in Table 1.1 and is referred to in the following paragraphs.

Until the recent development and application of laser Doppler anemometry for engine research (eg. Melling and Whitelaw, 1976; Witze, 1978; and Rask, 1978), no absolute method existed for the measurement of fluid velocity in manifolds, ports and cylinders of internal-combustion engines. In the early studies, the problems of internal aerodynamics and assessing port performance were tackled by using pressure probes and vane anemometers in steady flow experiments. However, the description of in-cylinder motion was inadequate and a number of flow visualisation experiments (eg. Lee, 1939; Dicksee, 1940; and Willis et al, 1966) were conducted to qualitatively describe the flow in the cylinders of steady rigs and/or motored engines. Hot wire anemometry has also been used as a diagnostic technique to obtain knowledge of the turbulent flow field in the cylinder of motored internal-combustion engines (see, for example, Semenov, 1958; James, 1972; Lancaster, 1976; and Williams and Tindal, 1980).

The continuous output signal of a hot wire anemometer and the high frequency response of the hot wire allow the measurement of turbulence characteristics. This technique, however, has no directional sensitivity, cannot be readily used in combusting environments and has limitations in compressing motored engines where its response is influenced by varying temperature and pressure fields. Laser Doppler anemometry, on the other hand, has greater potential with its non-intrusive nature and its ability to identify flow direction and measure individual components of mean and turbulent velocities in both motored and firing engines. But it too has some disadvantages. These stem mainly from the need of gaining optical access and the greater expense of laser anemometry systems. The difficulty of obtaining high data rates is also a limitation to determine turbulence parameters, such as length and time scales, and power spectra.

The early flow studies were of cut-and-try nature and were conducted in steady test rigs to determine breathing (Tanaka, 1929) and swirl producing (Fitzegeorge and Allison, 1962) capabilities of different inlet port and valve arrangements. Various flow metering devices, pressure probes and rotating vane anemometers were used as diagnostic tools. Tanaka (1929) postulated four modes of the valve flow which were later verified, for example, by Kastner et al (1963) and Annand (1969). During the initial stages of valve lift the flow remained attached to the wall of the valve passage. In the second stage a vena contracta was formed stemming from the underside curvature of the valve head. In the third stage the flow separated from both the valve head and seat. And finally, at large lifts any breakaway occurring was insignificant

and consequently discharge coefficient recovered as lift was increased. Improvements on discharge coefficient with 30 and 45 degree seat angles were reported, for example, by Annand (1969) and Wallace (1967) as well as with rounding off the sharp edges in the valve passage (see Kastner et al, 1963).

The presence of swirl during compression and expansion phases is desirable and, as mentioned earlier, important particularly to diesel engine combustion. Swirl can be promoted either in the compression stroke as in the case of indirect-injection diesel engines or during induction as in direct-injection engines (Alcock, 1934). Swirl may be induced during intake by designing the inlet port to deflect the air round the cylinder converting the linear momentum to angular momentum. A port designed to produce high inlet velocities and swirl can result in large pressure drops and consequent reduction in volumetric efficiency unless its discharge coefficient is improved. This indicates the importance of port and valve design in achieving high swirl and volumetric efficiency. Induction swirl can also be obtained by means of helical ports which are designed to produce swirl as the air flows out of the valve. In this case angular momentum is imparted directly at the port contrary to its conversion from linear momentum inside the cylinder as in the case of directed port.

Steady flow tests of various swirl-producing ports by rotating vane anemometry generally show lower swirl levels than expected and observed in motored engines, as reported for example by Tanabe et al (1978), Brandl et al (1979) and Monaghan and Pettifer (1981). This is attributed mainly to the residual in-cylinder swirl carried over to the following cycle in motored engines,

as will be shown later in this thesis, and partly to the limitation of rotating vane anemometers in determining the correct swirl level with flows more complex than simple solid body rotation.

The intake flow in diesel engine cylinders is characterised by spiralling swirl motion approximating solid body rotation near the swirl centre with deviations to potential type flow in regions away from the core (Willis et al, 1966). The flow structure in the axial plane is complex and dominated by a jet-like flow (Semenov, 1958) stemming from the valve opening. A detailed description of the flow structure in an axi-symmetric non-compresing engine was reported, for example, by Gosman et al (1978b) and Morse et al (1979a and b, and 1980a and b). The axial flow consisted of toroidal vortices which are strongly dependent on inlet boundary conditions. The same non-compressing engine was adapted for most of the work reported in the second Chapter of this thesis, and a four-stroke version of it in the third Chapter and in the relevant work reported in the literature (see, for example, Bicen, 1980; Bicen et al, 1980 ; Bicen and Whitelaw, 1983; and Arcoumanis et al, 1982a, b c and d, and 1983). The jet-like velocity gradients induced during intake are a main source for turbulence generation (Semenov, 1958) and consequent turbulence is anisotropic (Dent and Salama 1975a and b) and non-homogeneous (Witze, 1977).

In the absence of bulk movements, such as swirl and squish, the intake-generated mean motion decays during compression as widely reported, for example, by Dent and Salama (1975a and b), James and Lucas (1975) and Lancaster (1976). When swirl is present and induced during intake, it relaxes into near solid body rotation

during compression (Johnston et al, 1979; and Morse and Whitelaw, 1981) and persists through expansion and exhaust stages (Williams and Tindal, 1980). Turbulence tends towards isotropy (Lancaster, 1976) with turbulent energy shifted towards lower frequencies during the compression stroke (see also Semenov, 1958; James, 1972; and Dent and Salama 1975a and b). The compression turbulence in disc shape combustion chambers remains virtually constant during most of the compression stroke as reported, for example, by Rask (1979). The increased levels observed near TDC in almost all hot wire data, apart from those of Lancaster (1976), are considered to be due to the difficulties associated in the interpretation of hot wire data during compression and expansion phases (Witze, 1980a).

Interaction of swirl with squish generated during later stages of compression by virtue of combustion chamber geometry, such as open and re-entrant piston bowls, changes the flow structure near TDC. The early flow visualisation experiments of Dicksee (1940) indicated a double toroidal vortex structure in the piston bowl due to the swirl-squish interaction and a simple toroidal movement when squish alone was the source for air movement. Hot wire measurements of Brandl et al (1979) and Williams and Tindal (1980) also indicated a complex flow structure inside the combustion bowl near TDC. A double toroidal motion was observed in re-entrant type piston bowls and swirl velocities were non-uniformly distributed inside the bowl. Higher angular momentum losses were observed with piston bowls than in disc shape chambers mainly attributed to increased wall friction. There were, however, no significant effects of squish on compression turbulence apart from some local regions close to the bowl entry.

Most parametric studies indicate a linear dependence of both the mean motion and turbulence on engine speed (eg. Horvatin and Hussmann, 1969; James, 1972; Lancaster, 1976; and Witze, 1977) and an insensitivity to compression ratio and volumetric efficiency during the compression stroke (see Lancaster, 1976). The motored and firing runs of Ohigashi et al (1972), Tanabe et al (1978), Rask (1979) and Wigley et al (1981) gave almost identical results up to the point of ignition in the cycle and indicate that the data obtained under motoring conditions can be expected to be equally valid for the flow in production engines and prior to combustion.

1.2.2 Calculations

A wide range of engine simulation models are comprehensively discussed in the literature, for example by Reynolds (1978), Blumberg et al (1979), Heywood (1980) and Witze (1981). They may be classified into two groups commonly referred to as zero-dimensional and multi-dimensional. The zero-dimensional or "phenomenological" models are usually thermodynamic in nature (Blumberg et al, 1979) and formulated in integral form over space so that the spatial variations within the cylinder are ignored and only temporal variations are considered. On the other hand, multi-dimensional models employ partial differential equations and resolve the spatial variations of mass, momentum and energy in one, two or three space dimensions and time, and thus account better for the flow processes (Reynolds, 1978). A comprehensive survey of work related to zero-dimensional models is given by Watkins (1977) and that of multi-dimensional calculations by Johns(1980) and Yianneskis

(1982). The present review concentrates on multi-dimensional calculations and refers to more recent studies and/or those omitted by Johns and Yianneskis; the calculation papers reviewed and referred to in the following paragraphs are listed in Table 1.2.

In recent years, the advances made in numerical methods and digital computers have resulted in increased use and development of multi-dimensional models for complex flow situations similar to those encountered in engine cylinders. One of the early attempts to devise such a computer prediction scheme in an axisymmetric model of reciprocating engine was made by Watkins (1973) who solved numerically the laminar form of the governing differential equations for the conservation of mass, momentum and energy using a novel grid system which expanded and contracted axially with piston motion.

There are two main approaches to the modelling of turbulent flow in piston engines. The first is known as "Full Field Modelling" (Reynolds, 1978) and treats the turbulence as the deviation of the flow at any point in space and time from the corresponding mean. In this approach the basic conservation equations governing the instantaneous flow are ensemble-averaged to yield a new set with additional unknown turbulent fluxes, such as the Reynolds stresses in the case of the momentum equations. The unknowns are then further modelled by either algebraic or differential equations which make the approach inexact. The second approach is a three-dimensional, time-dependent calculation of large scale turbulence field and is known as "Large Eddy Simulation". The averaging process and, therefore, the modelling of consequent unknowns are limited to eddies below the mesh

size of computational grids and, unlike the first approach, the large scale turbulence does not need modelling. Although this approach is potentially more exact than the former, the limitations on the capabilities of present computers prohibits its use for engine applications.

Gosman and Watkins (1976) and Watkins (1977) were of the early modellers who incorporated the k-ε turbulence model into the procedure of the first approach mentioned above for compressing axisymmetric flows in reciprocating engines; the model was originally developed for two-dimensional, incompressible thin-shear-layer flows (see eg. Jones and Launder, 1972). Because of the relative economy and simplicity of the k-ε model, it has been used extensively by others, for example, Ramos et al (1979), Grasso and Bracco (1981), Morel and Mansour (1982) and El-Tahry (1982).

Gosman and Johns (1978) and Johns (1980) incorporated a curvilinear orthogonal grid system into the method of Gosman and Watkins (1976) to account for more realistic diesel engine combustion chambers, such as prechamber and piston bowl geometries. The predictions of the velocity field during the repeated compression and expansion strokes, starting with different solid body swirl levels at BDC, showed the strong influence of swirl level on the TDC flow structure of piston bowls. These works were later extended to incorporate fuel-air mixing and subsequent combustion processes (see, for example, Gosman and Johns, 1980; and Gosman and Harvey, 1982). Johns (1980) has also made calculations for a non-compressing engine with an open axisymmetric annular port and induction swirl. The results were compared with the experimental data of Morse et al

(1980a) and showed reasonable quantitative agreement with discrepancies attributed mainly to the uncertainties in inlet and initial boundary conditions.

An assessment of a class of turbulent combustion models with the employment of the k-ε model was given by Ahmadi-Befrui et al (1981). The suitability of a representative combustion model based on the dissipation-rate-control hypothesis was demonstrated for a homogeneous-charge engine. The more recent calculations of Ahmadi-Befrui et al (1982) in an axisymmetric four-stroke engine were compared with the present experimental data and the results, as discussed later in sub-section 3.4.4, were generally in moderate agreement.

1.3 Present Contribution

The above review showed that there is a shortage of detailed experimental information on the velocity characteristics in piston bowls to provide a better understanding of the interaction between swirl and squish during late compression stages; that no quantitative velocity information on the intake valve flow exists under either steady or unsteady state conditions; that laser Doppler anemometry is an accurate technique to measure velocity characteristics in engine cylinders; and that experimental data obtained in simpler than-practice geometries are limited in number but provide a satisfactory testing ground for calculation methods which are presently constrained to simple geometries. The work presented in this thesis is intended to address these areas by obtaining laser Doppler anemometry measurements of mean and turbulent velocity fields in

transparent model engines, both with and without compression.

In the non-compressing arrangements the intake-generated flow structures are examined and their evolution in the cycle is demonstrated. The effects of influential parameters such as piston stroke, clearance volume and piston head geometry on these flow structures are quantified.

In the compressing four-stroke engine, attention is focussed more on the compression-related flow processes with particular interest in squish and its interaction with swirl. The effects of compression ratio and piston bowl geometry are also examined and quantified. The data can also assist the evaluation of relevant flow calculations.

In order to demonstrate the extent to which steady state testing can be used to characterise the valve performance of an internal-combustion engine, the flow in the near region of an intake valve is examined by obtaining the velocity characteristics under both steady and unsteady state conditions.

The measurements of mean and turbulent velocity fields were all conducted in axisymmetric configurations to simplify the task of interpreting the results and of understanding the consequent flow structures. As a result, the number of measurements is reduced and calculation requirements are better satisfied.

1.4 Thesis Outline

The remainder of this thesis comprises four Chapters. The next Chapter describes the work conducted on the flow in a non-compressing model engine. Following a brief introduction, the experimental method is described and includes an extensive analysis of the errors incurred in the measurements. The results are then presented and discussed with particular reference to the influence of piston stroke, clearance volume and piston crown geometry on intake-related flow structures.

Chapter 3 presents the measurements obtained in a compressing four-stroke model engine with flat and various open and re-entrant type bowl piston configurations. After a short introduction the Chapter proceeds with the description of the model engine. As the laser Doppler anemometry was virtually identical to that in Chapter 2, only the modifications are described and their subsequent effects on experimental errors discussed. Following the presentation of results, they are discussed with particular interest in squish and swirl-squish interaction. The significance of the results for the assessment of relevant calculations is highlighted. The Chapter concludes by summarising the main findings of the work.

In Chapter 4 the work conducted on steady and unsteady flows through an intake valve is presented. The descriptions of the steady flow simulation and the modifications made on the four-stroke model engine are followed by the presentation of the results. The results are discussed and this is followed by the summary of the main findings.

Finally, Chapter 5 presents the main conclusions of the thesis and concludes by suggesting the areas in which further work may be needed.

TABLES

Table 1.1 Experimental Investigations

Author(s) & Year	Flow Configuration(s)	Technique(s)	Synoptic Findings
Tanaka (1929)	Steady flow through valves with various valve & seat profiles.	Pressure Probes	Four different modes of the valve flow with increasing lift observed together with discontinuities in discharge coefficient.
Alcock (1934)	Motored engines	Rotating vane anemometry	Roughly constant swirl ratio over a wide range of speed; an optimum swirl ratio existed for each arrangement
Lee (1939)	Motored engine	Flow visualisation with feathers	Air motion persisted through compression but was suppressed in expansion contrary to that (swirl) induced by a shrouded valve
Dicksee (1940)	Motored engine with a toroidal piston bowl	Flow visualisation on cylinder & bowl surfaces using aluminium paint	A double toroidal vortex structure due to the interaction of swirl with squish; reverse squish effect in expansion
Wood et al (1942)	Steady flow through various valve & port combinations	Pressure probes	Improvements on discharge coefficients by eliminating sharp corners
Molchanov (1953)	Motored engine with a cylindrical disc chamber	Hot wire anemometry	Maximum fluid velocities observed near the maximum piston speed during intake remaining virtually constant thereafter; a little effect of CR was found
Semenov (1958)	Motored engine with a cylindrical disc chamber	Hot wire anemometry	Both the mean motion & turbulence decayed steadily but sustained almost constant levels during second half of compression; jet flow found to be major source of turbulence
Alcock & Scott (1962)	Motored engine with a toroidal piston bowl	Flow visualisation with cotton tufts	Strong reverse squish was observed after TDC
Fitzegeorge & Allison (1962)	Steady flow through various swirl-producing cylinder head assemblies	Flow visualisation & rotating vane anemometry	Effect of port configuration on swirl velocities was investigated; spiral solid body air motion was observed
Kastner et al (1963)	Steady & unsteady flows through valves with a 45° seat angle	Pressure probes	In steady flow tests similar findings to those of Tanaka (1929); unsteady experiments generally supported the results of steady state tests
Woods & Khan (1965)	Steady flow through intake & exhaust valves	Pressure probes	Effective area was found to be independent of pressure ratio in small lift cases but to increase with increasing pressure drop at higher lifts
Willis et al (1966)	3-D water model of a 4-stroke engine simulating intake stroke only	Flow visualisation with lucite beads	Hybrid vortex structure consisting of solid body rotation in the centre surrounded by a potential flow; cycle-to-cycle variation of swirl centre was observed

Table 1.1 cont'd...

Author(s) & Year	Flow Configuration(s)	Technique(s)	Synoptic Findings
Wallace (1967)	Steady flow through 2-stroke & 4-stroke diesel engine ports	Pressure probes	Air & exhaust flow losses were primarily determined by the geometric area with secondary effects of valve lift, seat angle, head profile & port shape
Annand (1969)	Steady flow through various valve & port assemblies with 30^{o}, 45^{o} & 60^{o} seat angles	Pressure probes	Similar findings to those of Tanaka (1929) & Kastner et al (1963); a bi-stable flow at low lifts was observed and 60^{o} seat angle was found to be inferior to 30^{o} & 45^{o}
Horvatin & Hussmann (1969)	Motored diesel engine	Hot wire anemometry	Fluid velocity increased linearly with engine speed; swirl velocities increased in the piston bowl & approximated solid body rotation
Shimamoto & Akiyama (1970)	Motored diesel engine with an open combustion chamber	Velocity detector of solenoid type	Peak squish velocities were observed at about 18^{o} BTDC
El-Khafaji et al (1971)	Motored diesel engine	Hot wire anemometry with probe mounted on a traversing mechanism	Development of hot wire anemometry for in-cylinder measurements
Arnold et al (1972)	Motored engine with hemispherical cylinder head	Hot wire anemometry with moving & fixed probes	Mean velocities decayed during compression & expansion with some increase in the exhaust stroke
Huebner & McDonald (1972)	Motored model diesel engine simulating intake process	Hot wire anemometry, rotating vane anemometry & flow visualisation with a grid of tufts	Non-solid body rotation was observed; no significant effect of engine speed; angular momentum decreased with decreasing CR
James (1972)	Spark ignition engine with disc chamber & piston bowl	Hot wire anemometry	No indication of squish at low CR but reverse squish was observed in the expansion phase; mean velocity varied linearly with engine speed
Ohigashi et al (1972)	Motoring & firing diesel engine	Electric spark discharge	Although the intake flow was different in motoring & firing runs, the swirl motion near TDC was the same in both
Derham (1972) & Dent & Derham (1974)	Motored diesel engine	Hot wire anemometry with moving & fixed probes	Solid body rotation was observed during most of the intake & compression strokes; swirl velocities increased linearly with engine speed; higher swirl ratio was found with masked valve
Tindal et al (1974)	Motored diesel engine with flat & bowled piston crowns	Hot wire anemometry with moving probes	Higher velocities were observed at TDC with the piston bowl arrangement
Dent & Salama (1975a & b)	Motored spark ignition engines with wedge & "Heron" combustion chambers	Hot wire anemometry	Mean motion & turbulence decayed until IVC but increased near TDC with the wedge chamber

Table 1.1 cont'd...

Author(s) & Year)	Flow Configuration(s)	Technique(s)	Synoptic Findings
James & Lucas (1975)	Motored spark ignition engines with squish & disc chambers	Hot wire anemometry	Most turbulence energy was contained in low frequencies (below 700 Hz) during compression; the mean velocity varied linearly with speed
Woods & Girlando (1975)	Motored engines with flat & bowled piston crowns	Hot wire anemometry	Negligible squish velocities with the flat piston; strong squish & reverse squish with the piston bowl
Lancaster (1976)	Motored engine with disc chamber & valves with & without shroud	Hot wire anemometry	Mean & turbulent velocities increased linearly with speed; turbulence decayed after IVC but sustained constant levels near TDC; some cycle-to-cycle variations were observe
Melling & Whitelaw (1976)	Motored diesel & model non-compressing engines	Laser Doppler anemometry	Development of LDA system for in-cylinder measurements; frequency counting technique was found suitable for signal processing together with back-scatter optics for diesel engine
Witze (1976a)	Motored L-head engine	Hot wire anemometry	Maximum mean velocities at 110^{o} ATDC in intake & 20^{o} BTDC in compression were observed; turbulence decayed during compression with some increase near TDC
Morse (1977)	Motored model non-compressing engine	Laser Doppler anemometry	Crank angle broadening effect was quantified; 10^{o} crank angle window was found to be an optimum window for accuracy & adequate data rate
Witze (1977)	Motored L-head engine	Hot wire anemometry	Linear dependence of mean motion & turbulence on speed; non-homogeneous turbulence near cylinder head
Cole & Swords (1978)	Motored engine	Laser Doppler anemometry	Linear dependence of fluid velocities on engine speed; local flow structure existed near spark plug; residual turbulence at high engine speeds
Gosman et al (1978b)	Axisymmetric motored non-compressing engine with orifice & pipe inlets	Laser Doppler anemometry	Vortical flow during intake was observed with both inlets; the jet trajectory determined the vortex structure
Ishikawa & Daily (1978)	Square cross-sectioned model engine	High speed Schlieren cinematography	Appreciable influence of the vortex roll-up on compression & expansion turbulence; size of the vortex was affected by the piston bevel
Rask (1978)	Motored L-head engine	Laser Doppler anemometry	Highly vortical nature of the flow during intake was observed; in-phase precession of swirl centre

Table 1.1 cont'd...

Author(s) & Year	Flow Configuration(s)	Technique(s)	Synoptic Findings
Tanabe et al (1978)	Motoring & firing diesel engine & steady flow through the cylinder head of the engine	Electric spark discharge, high speed photography & rotating vane anemometry	Solid body in-cylinder motion; lower swirl velocities under steady state; 55% loss of angular momentum during compression; close correspondence between motoring & firing runs
Wigley & Hawkins (1978)	Steady flow through helical & directed ports	Laser Doppler anemometry	A more ordered flow with helical port; higher peak velocities and velocity gradients with directed port; fluctuating component of velocity was constant in both cases & independent of shear
Witze (1978)	Motored L-head engine	Hot wire & laser Doppler anemometry	Hot wire results were unsatisfactory near & after TDC due to their gas temperature dependence
Asanuma & Obokata (1979)	Motoring & firing engine	Laser Doppler anemometry	Reverse squish velocities were different in motoring & firing runs during the expansion stroke
Brandl et al (1979)	Motored diesel engine with bowl-in-piston & flat piston, & with 3 different inlet port designs (2 helical & one tangential)	Hot wire anemometry	Higher velocities with helical ports & better overall performance over a wide speed range; small effect of squish on bowl turbulence; higher angular momentum loss with piston bowl
Davis & Kent (1979)	Motored PROCO engine & steady flow through axisymmetric ports	Spark discharge/ time of flight method & angular momentum flux swirl meter	Swirl was approximately proportional to speed; at high speeds swirl ratio decreased
Ekchian & Hoult (1979)	Water analogue model engine simulating intake process	Flow visualisation with polystyrene beads	Bi-stable jet flow was observed at small lifts; linear dependence of velocities on engine speed; unstable flow with increasing stroke
Johnston et al (1979)	Motoring & firing L-head engine	Flow visualisation, laser Doppler anemometry, & continuous-wave & pulsed laser Raman spectroscopy	Axisymmetric swirling flow was virtually independent of axial position & exponentially decayed in the cycle; a high degree of stratification during injection; flame propagation dominated by swirl-driven convection
Lucas & Anton (1979)	Motoring & firing spark ignition engine with variable squish	Hot wire anemometry & ionisation probes	Turbulence intensities were not significantly affected by squish; charge velocities decreased with squish
Morse et al (1979a)	Motored non-compressing model engine with pipe & annular port inlets & with flat & bowled pistons	Laser Doppler anemometry	Pipe entry gave rise to a strong vortex near the piston: annular port resulted in a large vortex occupying all of the flow space with smaller vortices in the corners; small effect of piston bowl

Table 1.1 cont'd...

Author(s) & Year	Flow Configuration(s)	Technique(s)	Synoptic Findings
Morse et al (1979b)	Motored non-compressing model engine	Laser Doppler anemometry	No significant effect of engine speed on flow patterns; velocities scaled linearly with speed
Rask (1979)	Motored & firing L-head engine	Laser Doppler anemometry	Highly vortical flow was observed; mean & rms velocities scaled with engine speed; turbulence had almost constant levels during compression
Coghe et al (1980)	Motored engine	Hot wire & laser Doppler anemometry	Solid body rotation observed in only a limited region at the end of compression; a good correspondence between HWA & LDA results; relative turbulence intensity of 0.5 during compression
Cole & Swords (1980)	Firing spark ignition engine	Laser Doppler Anemometry	Strong correlations were measured between the mean velocity near spark plug & the peak pressure, but a much weaker dependence on turbulence intensity variations was observed
Gany et al (1980)	Motored axisymmetric model engine with & without compression	Laser Doppler anemometry	Intake flow patterns were similar with moving & fixed valves; cycle-to-cycle variations were considered to be unimportant
Morse et al (1980a)	Motored non-compressing model engine with various induction swirl levels	Laser Doppler anemometry	Similar flow patterns were observed in all cases with some differences generally in the detail of the flow
Morse et al (1980b)	Motored non-compressing model engine with an asymmetric open port	Laser Doppler anemometry	Similar flow patterns to those of Morse et al (1980a), but the vortices were no longer symmetric about the cylinder axis and varied both in size & intensity with circumferential position
Namazian et al (1980)	Square cross-sectioned firing spark ignition engine	Flow visualisation by Schlieren photography & high speed cinematography	Cylinder head/wall corner vortex was found to be present in all four strokes
Williams & Tindal (1980)	Motored diesel engine with toroidal, re-entrant & simplified re-entrant bowl configurations	Hot wire anemometry with fixed & moving probes	Different flow structures were observed in the two bowl types; higher swirl rates were measured in the re-entrant bowl with more pronounced squish effects & longer persistence of swirl in the expansion stroke
Witze (1980a)	Motored L-head engine	Hot wire & laser Doppler anemometry	Comparison of HWA & LDA measurements; for known flow direction, low turbulence & CR, useful mean velocity results were obtained by HWA; however, no accurate measurements of turbulence intensity during compression & expansion

Table 1.1 cont'd...

Author(s) & Year	Flow Configuration(s)	Technique(s)	Synoptic Findings
Witze (1980b)	Motored & firing L-head engine with variable induction swirl	Laser Doppler anemometry & laser shadow-graph photo-graphy	With increasing induction swirl level higher swirl velocities but lower turbulence intensities were measured & swirling motion departed from solid body rotation; at high swirls flame propagation was convection dominated
Hirotomi et al (1981)	Steady & unsteady water flow through various swirl-producing inlet ports, simulating intake process	Flow visualis-ation with powdered vinyl traces	A good correspondence between steady & unsteady flow patterns was observed; two vortices with a standard port as opposed to one in the others; the two vortices, however, were damped easier than one
Monaghan & Pettifer (1981)	Steady flow through directed & helical ports; motored engine fitted with the same ports	Laser Doppler, hot wire & rotating vane anemometry & impulse swirl meter	Close correspondence between LDA & swirl meter results; lower than expected squish velocities; large cycle-to-cycle variations; difficulties with HWA in high turbulence regions
Morse & Whitelaw (1981)	Motored diesel engine with & without compression	Laser Doppler anemometry	Similarities in intake flow were found with & without compression; swirling motion relaxed into solid body rotation during compression; in-phase movement of swirl centre during the engine cycle
Rask (1981)	Motored L-head engine	Laser Doppler anemometry	Comparison of various data analysis; smoothed-ensemble & window methods were used to determine mean velocity but unable to distinguish cyclic variations; window size of 5^{o} was found to be a good compromise
Wigley et al (1981)	Motored & firing diesel engine	Laser Doppler anemometry	Similar swirl velocities in motored & firing runs prior to injection, but smaller velocities after ignition than motored runs
Catania (1982)	Motored diesel engine with different induction systems	Hot wire anemometry	3-D flow during induction showing features of solid body rotation at higher valve lifts; the swirl ratio was virtually the same for each duct but was less when both duct were operated simultaneously
Fukutani & Watanabe (1982)	Steady & unsteady flow through poppet inlet valves	Pressure probes	Static flow coefficient increased with increasing valve lift in the low lift range but decreased at higher lifts; dynamic flow coefficient was generally smaller than the static one
Liou & Santavicca (1982)	Motored engine	Laser Doppler anemometry	Large relative cyclic fluctu-ations of mean velocity were observed; velocity fluctuations w.r.t. ensemble-averaged mean velocity were from 50% to 100% greater than those w.r.t. cycle-resolved mean

Table 1.1 cont'd...

Author(s) & Year	Flow Configuration(s)	Technique(s)	Synoptic Findings
Namazian & Heywood (1982)	Square cross-sectioned firing spark ignition engine	Flow visualisation by Schlieren photography & high speed cinematography	A low-velocity expanding flow out of crevice entrance around the piston was observed shortly after peak cylinder pressure, followed by a jet-type flow through top piston-ring gap later in the expansion stroke
Tindal et al (1982)	Steady flow with different shapes of inlet port & motored diesel engine	Hot wire & vane anemometry	Helical ports produced more organised flow patterns & resulted in higher swirl than deflector wall port under both steady & motoring conditions; no significant effect of port design on compression turbulence
Wakisaka et al (1982)	Motored over-head & side valve engines	Hot wire anemometry	Turbulence of air swirl near TDC was found to be in unrelaxed state & intake turbulence contributed considerably to TDC turbulence
Witze (1982)	Firing L-head engine with variable swirl level & spark location	Laser Doppler anemometry & laser shadowgraph photography	Ignition at chamber centre was found to be preferable except at very high swirl for which side-wall ignition produced fastest burn; decreased swirl resulted in cyclic variations with increased burn durations

Table 1.2 Multi-dimensional calculations

Author(s) & Year	Flow Configuration(s)	Calculation Procedure	Synoptic Findings
Gosman & Johns (1978)	Compression & expansion strokes of a motored engine cycle with various shapes of axisymmetric piston bowl & initial swirl levels	Numerical solution of equations for conservation of mass, momentum, energy, turbulent energy (k) & its dissipation (ε) with curvilinear orthogonal grids	TDC flow structure strongly influenced by initial swirl level & piston bowl geometry resulting in rather complex vortical structure in the bowl
Ramos et al (1979)	Axisymmetric laminar & turbulent 4-stroke motored cycle with an instantaneously opening & closing valve	Numerical solution of the Navier Stokes equations with k-ε turbulence model for turbulent flow	In laminar flow case a large vortex during intake was calculated & decayed during compression & expansion phases; the turbulent case showed that the turbulence generated in the shear layers was convected and diffused through the cylinder
Gosman & Johns (1980)	Axisymmetric open-chamber direct-injection diesel engine without combustion	An extension of the method of Gosman & Johns (1978) to allow solution of the fully-coupled equations of motion, heat & mass transfer governing the dispersal of a spray	Spray created its own mixing environment in the close vicinity of the injector with mean & turbulent gas velocities which were comparable to those produced by swirl & squish
Johns (1980)	As in Gosman & Johns (1978), as well as 2-stroke non-compressing & 4-stroke motored engine cycles	As in Gosman & Johns (1978)	Non-compressing engine results are in good agreement with experimental data of Morse et al (1979a, b) & those of 4-stroke with the data of Witze (1976b)
Ramos & Sirignano (1980)	As in Ramos et al (1979) with additions of swirl & an annular orifice of varying area	As in Ramos et al (1979)	Two eddies calculated during intake both with & without swirl; eddies persisted to TDC of compression; swirl velocity profiles resembled solid body rotation
Ahmadi-Befrui et al (1981)	Idealised homogeneous-charge spark ignition engine with centrally located spark plug & valve	Numerical method of Gosman & Watkins (1976) with a dissipation-controlled combustion model	Flame front did not provoke significant turbulence production in unburnt gases
Borgnakke et al (1981)	Open chamber, cup-in-piston engine under motoring conditions	Swirl model based on an integral formulation of angular momentum equation, coupled with a global k-ε model to represent turbulence	Predictions of swirl velocity & turbulence showed good agreement with experimental data indicating superiority of the swirl model used over the solid-body model
Gosman & Jahanbakhsh (1981)	Same as in Johnston et al (1979)	Numerical method of Gosman & Watkins (1976)	Comparison of calculations with the experimental data of Johnston et al (1979) showed a moderate agreement at lower engine speed but better agreement was obtained at higher speed of 1200 rpm

Table 1.2 cont'd...

Author(s) & Year	Flow Configuration(s)	Calculation Procedure	Synoptic Findings
Grasso & Bracco (1981)	Axisymmetric motored engines with & without swirl	Numerical solution of Navier Stokes equations with k-ε turbulence model to represent turbulence	Predictions without swirl were compared with experimental data of Lancaster (1976) & with swirl with those of Witze(1977); in good agreement with experiments, proportionality of TDC turbulence to speed, insensitivity to CR & linear dependence on load (without swirl) were predicted
Ramos & Sirignano (1981)	Axisymmetric simulation of 4-stroke homogeneous-charge spark ignition engine with an infinitely thin valve	Numerical method of Ramos et al (1979) with modified version of k-ε model incorporating compressibility effects & one-step irreversible chemical reaction	Intake-generated turbulence rapidly diffused & became uniform during compression; turbulence was generated at the flame front due to strong axial acceleration of the flow
Ramos et al (1981)	Motored version of the engine employed by Ramos & Sirignano (1981)	As in Ramos et al (1979)	Comparison between calculations & measurements showed fair agreement; recirculation zone behind valve was overpredicted; increased levels of turbulence during exhaust were attributed to outgoing jet flow
El-Tahry (1982)	Motored axisymmetric engine with flat & re-entrant-bowl pistons	A version of the numerical method used by Grasso & Bracco (1981)	Larger angular momentum losses with higher swirl levels; TDC turbulence was almost independent of IVC turbulence; higher turbulence levels & stronger mean motion, but higher angular momentum loss were observed with re-entrant-bowl piston
Gosman & Harvey (1982)	High speed direct injection firing diesel engine with an open chamber	Numerical method of Gosman & Johns (1980) extended to include a combustion model of a kind which allows for both chemical-kinetic & turbulence effects on burning rate	An example calculation which demonstrated that the method produced qualitatively realistic predictions of the combustion process; usefullness of multi-dimensional methods in revealing the causes of inadequate performance was also illustrated
Harvey & Gosman (1982)	As in Gosman & Harvey (1982) with addition of various induction swirl levels	As in Gosman & Harvey (1982)	Combustion period was reduced with decreasing swirl; interaction of swirl field with the flow in the axial plane produced different patterns depending on initial swirl level; the peak pressure decreased with increased swirl ratio
Morel & Mansour (1982)	Compression phase of a motored engine with intially homogeneous turbulence	Numerical solution of Navier Stokes equation with modified k-ε turbulence model to account for rapid unidirectional & cylindrical-radial compression	The modified model gave much more plausible behaviour for length scale during compression

CHAPTER 2

IN-CYLINDER FLOW IN A TWO-STROKE CYCLE MODEL ENGINE

2.1 Introduction

This Chapter describes the experimental investigations of in-cylinder flows prevailing with various axisymmetric configurations in a motored model engine. The engine was operated in a two-stroke cycle and in the absence of compression due to a permanently open valve, thus simulating only the intake and exhaust strokes of a conventional engine cycle. Laser Dopper anemometry was used to quantify the turbulent flow field inside the engine cylinder. The work focusses mainly on the intake stroke and gives an extensive description of the flow and its development during the cycle up to a point where intake valves usually close in real engines.

The effects of some flow and geometry boundary conditions are also examined, which include piston stroke, clearance volume (compression ratio) and piston crown geometry. These parameters were selected because of their relative importance in engine design. The piston stroke influences, for example, both combustion rate and volumetric efficiency (Taylor, 1978), but has to be limited due to mechanical stresses. The compression ratio is an important aspect in engine thermodynamics since it determines the thermal efficiency of both diesel and petrol engines. The piston crown geometry plays an equally important role in engine design as it alters the flow structure prior to mixing and combustion processes. Thus a comparative study has been made to quantify the effects of these influential parameters on the in-cylinder flow and, in particular, on the intake-generated flow patterns.

The description of the model engine is given in the following section together with that of the laser Doppler anemometer and the analysis of the uncertainties incurred in the measurements. The results are presented in section 2.3. In all configurations, the measurements of the axial velocity,which is the predominant component,

were obtained in both temporal and spatial detail and were sufficient, due to symmetry, to provide a concise description of the flow in the axial plane. The induction swirl was introduced in most configurations because of its relevance to practice, except in the piston bowl configuration whereby the results were to be compared with other data in the literature obtained in the absence of swirl. The discussion of the results are presented in section 2.4 followed by the summary of the most important conclusions of this Chapter in section 2.5.

2.2 Experimental System

2.2.1 Flow Configuration

A schematic diagram of the model engine is shown in Figure 2.1. Both the cylinder and the piston were fabricated from plexiglass to provide optical access for velocity measurements by laser Doppler anemometry. The cylinder was 75 mm in bore diameter with a wall thickness of 3.5 mm and was mounted with its axis horizontal on a rigid table. The piston was driven inside the cylinder by an electric motor and crank arrangement which achieved simple harmonic motion by a cross-head moving on a pair of orthogonal slide bars as depicted in Figure 2.1. Friction between the piston and the cylinder was minimised by reducing the area of contact to eight PTFE studs fitted around the piston periphery, four at each end, hence eliminating the need for lubrication. The 0.2 mm clearance between the piston and the cylinder wall was sealed by polythene piston rings located far from the piston crown so that they did not wipe or smear the wall in the regions where optical access was required. The speed of the motor was controlled by a gear mechanism and kept constant at

200 rpm. Although this engine speed was much lower than those experienced in practice, it was sufficient to ensure a fully turbulent flow and to reflect, as fluid velocity scales with engine rpm, the in-cylinder flow phenomena corresponding to a wide range of engine speeds (see sub-section 1.2.1).

As the piston reciprocates in simple harmonic motion, the speed variation with crank angle θ is given by

$$V_p = \frac{S\omega}{2} \sin \theta \qquad (2.1)$$

where V_p is the instantaneous piston speed, S the piston Stroke and ω the angular speed of the crankshaft. Thus, the maximum piston speed V_{pmax} during a stroke (at θ = 90 and 270 degrees) is given by

$$V_{pmax} = \frac{S\omega}{2} \qquad (2.2)$$

and the mean piston speed $\bar{V}_p$ of the stroke by

$$\bar{V}_p = \frac{1}{\pi} \int_0^{\pi} V_p \, d\theta = \frac{S\omega}{\pi} \qquad (2.3)$$

The position of the piston with respect to the cylinder head, z_p, can be determined from

$$z_p = c + \frac{S}{2} (1 - \cos \theta) \qquad (2.4)$$

where c is the clearance distance between the piston crown and cylinder head at TDC.

The cylinder head was flat with an axisymmetric open-valve configuration, as shown in Figure 2.1. The centrally located valve which was fixed flush with the head, was 34 mm in diameter and chamfered at a 60 degree angle to the plane of the cylinder head; the angle is commonly referred to as "valve seat angle". Due to the permanent annular valve opening of 4 mm there was no compression. As a consequence, the model engine was operating in a two-stroke cycle simulating only the intake and exhaust strokes. The main characteristics

of the model engine which are common in all the configurations used in this Chapter are summarised in Table 2.1.

Table 2.1

Main characteristics of two-stroke cycle model engine

Engine speed, rpm	200
Cylinder bore, mm	75
Valve seat angle, degrees	60
Valve diameter, mm	34
Annular valve opening, mm	4

Figure 2.2 shows the two piston crown configurations used; one was flat representing a disc shape combustion chamber and the other had a cylindrical bowl with a rectangular-sectioned lip as an idealised representation of re-entrant type combustion bowls. The bowl was centrally located on the piston head, as shown in Figure 2.2b, and had a diameter of 43 mm. The bowl depth and entry diameter were both chosen to be equal to the bowl radius.

Piston strokes of 60 and 90 mm were employed and corresponded to bore-to-stroke ratios of 1.25 and 0.83, respectively. The crankshaft had a number of pinholes located at different radii which allowed the stroke to be changed and set at a required value by locking the cross-head in the corresponding pinhole location. The clearance distance between the piston crown and cylinder head at TDC was set at 10 or 30 mm by means of a set of interchangeable connecting rods. The 30 mm clearance was used in conjunction with both strokes and thus

resulted in swept-to-clearance volume ratios* of 2 and 3, respectively. The clearance distance of 10 mm, however, was used only with the 90 mm stroke, corresponding to a swept-to-clearance volume ratio of 9.

Most of the measurements were conducted in the presence of induction swirl, apart from those presented in sub-section 2.3.5. It was induced, when required, by means of vanes incorporated into the inlet port upstream of the valve, and inclined at 30 degrees to the cylinder axis. This inlet arrangement, according to Morse et al (1980a), resulted in an axisymmetric swirling flow with a swirl number of 1.2 ($\pm$10%). The swirl number S_n is defined as the ratio of the angular and axial momentum fluxes at the entry to the cylinder, normalised by the width of the jet. It is given for uniform density flow by

$$S_n = \frac{1}{\Delta R_v} \frac{\int_{R_v}^{R_v+\Delta R_v} r^2 \bar{U} \bar{W} \, dr}{\int_{R_v}^{R_v+\Delta R_v} r \bar{U}^2 \, dr} \qquad (2.5)$$

where R_v is the valve radius and ΔR_v the annular gap. Morse et al (1980a) evaluated S_n from the axial and swirl profiles measured nearest to the cylinder head and averaged over the intake stroke.

The additional operating and geometric characteristics of the model engine used in each set of measurements, presented in sub-sections 2.3.2 to 2.3.5, are tabulated in Table 2.2 together with the corresponding Reynolds numbers based on the maximum piston speed, cylinder bore and atmospheric density.

---

* Swept-to-clearance volume ratio is synonymous to compression ratio CR which is, however, more appropriate when compression is present.

Table 2.2

Parameters varied in two-stroke cycle model engine

sub-section / parameters	stroke S, mm	clearance distance c, mm	swept-to-clearance volume ratio	bore-to-stroke ratio	swirl number S_n	piston crown configuration	mean piston speed $\bar{V}_p$, ms^{-1}	max. piston speed V_{pmax}, ms^{-1}	Reynolds number* Re x 10^3
2.3.2	60	30	2.0	1.25	1.2	flat	0.40	0.63	3.18
2.3.3	90	30	3.0	0.83	1.2	flat	0.60	0.94	4.77
2.3.4	90	10	9.0	0.83	1.2	flat	0.60	0.94	4.77
2.3.5	60	30	1.6	1.25	0	re-entrant type bowl	0.40	0.63	3.18

* Reynolds number is based on maximum piston speed, cylinder bore diameter and atmospheric density $\frac{V_{pmax} D \rho}{\mu}$

2.2.2 Laser Doppler Anemometer

A single-channel laser Doppler anemometer was used to measure the velocity characteristics of the flow field. The anemometer operated in a "dual beam" or "fringe" mode and made use of forward-scattered light from moving particles introducted artificially in the working fluid. This technique is able to resolve the flow direction when operated with "frequency shifting" devices which are essential in flows with regions of recirculation and/or high turbulence intensity (> 30%). The principle and practice of laser Doppler anemometry are described extensively in a number of texts, see for example Drain (1980) and Durst et al (1981), and thus only the optical and signal processing system features of the present anemometer are given here.

Optical Arrangement

The optical arrangement of the anemometer is shown in Figure 2.3. The transmitting part of the system consisted of a low power laser source (5 mW He-Ne laser, Spectra Physics model 120), a plano-convex lens L_1, a rotating radial diffraction grating and a system of other plano-convex lenses L_2 (collimating lens) and L_3 (focussing lens). The position of the lens L_1 with respect to the diffraction grating was so chosen that the beam was incident with its waist at the grating surface. The radial grating diffracted the beam into a zero order and pairs of higher order beams. The two first order beams were used to form the dual beam anemometer and the rest was blocked by a mask, as shown in Figure 2.3.

The magnitude of reverse velocities as well as turbulence intensities encountered in the present measurements necessitated the use of frequency shifting. It was achieved from the frequency difference between the first order beams, induced by rotating the grating at a fixed steady speed - for various techniques of frequency shifting see, for example, Durst and Zare (1974). The desirability of shifting the Doppler frequency was first to ensure an unambiguous range of frequencies which could accommodate the spread of the velocity probability distribution at every point in the flow, and secondly to increase the frequency separation between Doppler and "pedestal"* frequencies which is essential in regions where the flow lies at large angles to the sensitivity vector of the anemometer (Durst and Zare, 1974). The grating, Technisch Physische Dienst type H, was driven by a Siemens 1AD-20 motor at a fixed speed of 3360 rpm resulting in a frequency shift f_s of 1.83 MHz; the

---

* The low frequency component of a Doppler signal, associated with the residence time of a scattering particle across the light beams.

motor speed was monitored by means of a counter (TSA model 6636/2) timing a preset number of motor shaft revolutions. Both the grating and the motor were housed in an optical unit, together with the lenses L_2 and L_3, as shown in Figure 2.3. The principal characteristics of the grating are given by Taylor (1981) and further information can be obtained from Oldengarm et al (1976).

The first order beams emerging from the grating were collimated by the lens L_2 and subsequently focussed, by the lens L_3, to intersect in a region inside the cylinder known as the "probe volume". This is a region of interference between two electromagnetic waves producing areas of high and low energy which produces a fluctuating scattered-light intensity in the presence of a moving particle; see, for example, Rudd (1969). Provided that the laser beams intersect at their waist, which was ensured to be the case by the exact positioning of the lens L_1, the interference fringes are plane and uniformly distributed, according to Kogelnik and Li (1966), in the smallest possible probe volume. Then, the "effective probe volume", using the value of the e^{-2} intensity level to define its boundaries, is ellipsoidal in shape, as shown in Figure 2.3, with length l_p (major axis) and diameter d_p (minor axis) given by

$$l_p = \frac{d}{\sin \alpha} \qquad (2.6)$$

$$d_p = \frac{d}{\cos \alpha} \qquad (2.7)$$

where α is the half angle of the beam intersection and d is the beam waist diameter, defined at the e^{-2} intensity level, at the probe volume which is given by

$$d = \frac{4\lambda f_1 f_3}{\pi d_o f_2} \qquad (2.8)$$

where λ is the laser wave length, f_1, f_2 and f_3 the focal lengths of the lenses L_1, L_2 and L_3 respectively and d_o the beam diameter at the e^{-2} intensity level. The fringe spacing Δx is

$$\Delta x = \frac{\lambda}{2 \sin \alpha} \qquad (2.9)$$

and the number of fringes N is, therefore, given by

$$N = \frac{d_p}{\Delta x} \qquad (2.10)$$

A particle passing through the probe volume produces a periodic variation in the scattered-light intensity with a frequency f_D (Doppler frequency) given by

$$f_d = \frac{U}{\Delta x} = \frac{2 \sin \alpha}{\lambda} U = CU \qquad (2.11)$$

where U is the component of instantaneous velocity in the direction of the sensitivity vector of the anemometer. The above relation shows that the particle velocity, assumed to be that of the associated fluid, is linearly related to the frequency of the scattered-light intensity and the constant of proportionality C is uniquely defined by parameters that are independent of the flow.

The collecting part of the optical system consisted of a bi-convex lens L_4, a pinhole and a photomultiplier tube (E.M.I. 9817B) which converted the optical signal (Doppler frequency information) into electrical signal.

The optical geometry of the collecting part was considered carefully to achieve optimum signal-to-noise ratio. The pinhole diameter d_{ph} was chosen, according to Durst et al (1981), from the following relation:

$$d_{ph} = \frac{N_{ph} M \lambda}{2 \sin \alpha} \qquad (2.12)$$

where N_{ph} is the number of fringes observed by the photomultiplier and M the magnification of the lens L_4. The recommended value of N_{ph} which is 80% of the total number of fringes N in the probe volume, was used and ensured that the outer region of the fringe pattern with its poor signal quality, did not contribute to the measurements. The principal characteristics of the optical system are summarised in Table 2.3.

Table 2.3

Principal characteristics of optical system

He-Ne laser power, mW	5
Laser wave length λ, nm	632.8
Beam diameter at e^{-2} intensity level d_o, mm	0.65
Half angle of beam intersection α, degrees	6.4
Fringe spacing Δx, μm	2.84
Velocity-to-frequency conversion factor C, MHz/ms^{-1}	0.35
Length of probe volume at e^{-2} intensity level l_p, mm	1.11
Diameter of probe volume at e^{-2} intensity level d_p, μm	125

(Table 2.3 cont'd...)

Number of fringes within e^{-2} intensity level N	44
Magnification of collecting lens M	5
Photomultiplier pinhole diameter d_{ph}, mm	0.5
Number of fringes seen by photomultiplier N_{ph}	35
Frequency shift f_s, MHz	1.83

Seeding

The use of a low power laser with air as the working fluid implied that artificial seeding was needed to increase the rate of Doppler signals. The silicone oil particles generated in a glass, blast type atomizer (see Melling and Whitelaw, 1973) were used in small concentrations and introduced to a plenum located upstream of the inlet port as a means of seeding the indrawn air. Although the resulting seeding was polydispersed, ranging from 1 to 3 μm, the size distribution was narrowed by natural deposition of large particles on the atomizer and plenum walls. The upper limit of the resulting range was small enough, according to Melling (1971), to follow the expected velocity fluctuations of the in-cylinder air motion.

Signal Processing System

A typical Doppler signal from the photomultiplier is shown in Figure 2.4 and comprises a discrete burst in the shape of an envelope with the following main characteristics:

(i) The signal has a low frequency component, pedestal, associated with the passage of particles through the laser beams.

(ii) The higher frequency component of the signal corresponds to the velocity of the particle passing through the probe volume and would include the frequency shift if applied.

(iii) The modulation depth of the envelope varies with the size of particle, the particle position within the probe volume and the relative intensities of the two light beams.

(iv) The signal is also randomly modulated by noise from several sources including optical and electronic noise.

This output signal of the photomultiplier can be processed by a number of electronic devices which includes frequency analysers, frequency trackers, filter banks, photon correlators, transient recorders and frequency counters. The principles of these signal processors and their application to various flow situations with the advantages and disadvantages are comprehensively described by Durst et al (1981).

The frequency counting (or period timing) technique was employed here by means of a fixed-gate frequency counter. This technique was chosen in preference to its counterparts mainly due to the intermittency of Doppler signal and short time available for processing, and partly due to the good signal-to-noise ratio achieved in the model engine with the anemometer operating in the forward scatter mode (see Melling and Whitelaw, 1976); for the principle of period timing with a fixed-gate frequency counter refer to, for example, Durao (1976).

The signal processing system is schematically shown in Figure 2.4, together with the data processing hardware. The Doppler signals from the photomultiplier were band-pass amplified (Harwell, 91-2151-2/6) to remove the low frequency pedestal and high frequency electronic noise and then passed to "Channel A" of an oscilloscope (Hewlett Packard, 1740A) to be displayed prior to their input to "Channel A" (0-10 MHz) of the fixed-gate frequency counter (Hewlett Packard, 5360A). The triggering mechanism of the oscilloscope was used to accept Doppler signals above a certain threshold level. For each accepted burst, an arming pulse was sent from the delayed output of the oscilloscope to a gating circuit which opened and closed, at a rate determined by the engine speed, after a preset number of pulses were received from an optical shaft encoder (Digitech DR 1034) coupled to the engine crankshaft. The encoder transmitted 1000 pulses per revolution and had its marker pulse synchronised with TDC; a Venner counter was used to time a preset number of marker pulses in order to determine and monitor the engine speed. The gated arming pulses from the circuit were then passed to the "measuring time" input of the counter activating it to determine the frequency of the input Doppler burst. For each frequency measurement, a d.c. logic signal was returned from the counter to "Channel B" of the oscilloscope to display the part of the burst whose frequency had just been measured and subsequently to verify that the measurement was carried out properly. The counter had a minimum cycle time of 3 ms (a sampling rate of 333 Hz) in which incorporated a variable measurement time. The measurement time was usually chosen between 2 - 6 μs to ensure that most of the time no less than 3 signal cycles contributed to the frequency measurement of the burst. Setting the trigger level of the oscilloscope to -6 dB, together with the characteristics of the

band-pass filter (see Durao, 1976) implied an effective bandwidth of 0.2 to 6.0 MHz corresponding to the range of expected Doppler frequencies. A combination of the trigger level and measurement time, together with the appropriate delay time, allowed the frequency measurements to be obtained from the central region of the Doppler burst which was least affected by noise.

2.2.3 Data Reduction Equations

The data reduction for reciprocating engine application requires special attention because of the periodic as well as turbulent nature of the flow (ie. statistically non-stationary). The instantaneous velocity varies not only due to turbulence, but with crank angle too, and consequently will not be the same from cycle to cycle at a given crank angle θ. Suitable averaging is needed to determine the mean velocity $\bar{U}(\theta)$ and the corresponding rms of the velocity fluctuations $\tilde{u}(\theta)$* at crank angle θ. The instantaneous velocity may be written as

$$U(\theta,n) = \bar{U}(\theta) + u(\theta,n) \qquad (2.13)$$

where $u(\theta,n)$ is the turbulent velocity fluctuation at engine cycle n and crank angle θ.

Ensemble-averaging of a set of values of $U(\theta,n)$, obtained at the same crank angle θ for N cycles, is used to obtain the mean velocity $\bar{U}(\theta)$ given by

$$\bar{U}(\theta) = \frac{1}{N} \sum_{n=1}^{N} U(\theta,n) \qquad (2.14)$$

---

* Hereinafter, it will be referred to as the rms velocity (or the turbulent velocity) and the ratio $\tilde{u}/\bar{U}$ as the turbulence intensity.

Similarly, the corresponding rms velocity is determined by

$$\tilde{u}(\theta) = \left[\left[\frac{1}{N} \sum_{n=1}^{N} U^2(\theta,n) \right] - \bar{U}^2(\theta) \right]^{\frac{1}{2}} \qquad (2.15)$$

Since the relationship between the instantaneous velocity U and the Doppler frequency f_D is linear (equation 2.11), the ensemble-averaged mean and rms values of a set of frequencies obtained at the same crank angle for many engine cycles were used to obtain $\bar{U}(\theta)$ and $\tilde{u}(\theta)$ from

$$\bar{U}(\theta) = C^{-1} \bar{f}_D(\theta) \qquad (2.16)$$

$$\tilde{u}(\theta) = C^{-1} \tilde{f}_D(\theta) \qquad (2.17)$$

2.2.4 Data Processing System

The frequency counter could be used as a data processor with a key board to programme the instrument to compute the mean and rms frequency values, as described for example by Vlachos (1977). This system had no signal or data validation criteria and as a consequence was susceptible to error with low signal-to-noise ratio signals due to the contribution from noise-induced counts.

To overcome the above deficiency, a software-controlled system was developed as reported in detail by Bicen et al (1981) and is briefly given here. The frequency counter was interfaced to a microprocessor (Apple II) as schematically shown in Figure 2.4. The frequency values were obtained from a large number of engine cycles during a preset crank angle window, $\theta - \Delta\theta/2$ and $\theta + \Delta\theta/2$, and were stored in the microprocessor memory for subsequent processing. The microprocessor controlled the

data acquisition by a combination of assembly (6502) and BASIC language and had an effective sampling rate of 5 Hz corresponding to a 200 ms time interval. The data reduction software was written in BASIC and performed wide-band filtering of the data, prior to the calculation of statistical moments, by accepting frequency values within three standard deviations in order to reject noise-induced counts; the validation of Doppler frequencies by this method was approximately 99%. Alternatively, the histogram of each set of measured frequency values was determined by the software and displayed on a visual display unit (VDU) in order to determine and set the limits of the wide-band data filtering. Following the data validation criteria, the ensemble-averaged mean and rms, as well as higher order moments if required, of each frequency set were calculated and converted into velocity by the software. They were then transferred to a mainframe computer (CDC 6500) where the profiles of velocity and streamline patterns were plotted as presented in Section 2.3.

2.2.5 Measurement Procedure and System Performance

The optical system was mounted horizontally on a traversing table with three degrees of freedom and aligned, using the symmetry of the light beam reflections, with its axis perpendicular to that of the engine cylinder which was also mounted horizontally on a rigid table free from any kind of vibrations.

Measurements of the axial component of velocity were obtained and are presented in this Chapter. For these measurements the optical orientation was such that the plane containing the beams passed through the cylinder

axis with the beam bisector at right angles to it. The probe volume was then moved along the diameter of the bisector; in this case, both the probe volume traverse and the velocity conversion factor C were unaffected by the beam refraction at the cylinder wall (see Appendix 3.2). The origin of the cylindrical coordinate system was chosen to be the centre of the axisymmetric cylinder head. The probe volume was set both radially and axially by visual observation of the coincidence of the beam intersection point with the inner wall of the cylinder and the head, respectively.

The maximum signal-to-noise ratio was achieved in the regions away from the cylinder wall, head and piston crown and was of the order of 50 (34 dB). Fouling of the optical surfaces due to the accumulation of oil seeding particles affected the signal-to-noise ratio, especially close to the wall region, and regular cleaning of the surfaces was required to attain signal-to-noise ratios better than 20 (26 dB).

Due to the minimum sensitivity (100 mV) of the counter, the signals were amplified, on the average to 2 - 3 V peak-to-peak, before input to the counter. An external trigger level of -6 dB (see sub-section 2.2.2) ensured that the counter operated safely away from its threshold level and that only well modulated signals with high signal-to-noise ratio passed to the counter.

The crank angle Θ and the crank angle window $\Delta\Theta$ were both selected on the gating circuit by setting the encoder pulse following the marker and the number of pulses for which the gate remained open; each encoder pulse corresponded to 0.36 crank angle degrees for the two-stroke cycle. The marker pulse was synchronized with TDC by using a dial gauge in conjunction with the gating circuit. The encoder, disengaged from the crankshaft,

was rotated until the gating circuit indicated that its marker pulse was on. Before the encoder was reconnected to the crankshaft, the piston was moved and set at the end of its travel (ie at TDC) by means of the dial gauge. The crank angle window of 10 degrees (28 pulses) was used throughout the measurements at selective crank angles. Within this window ensemble sets consisting of frequency values in the range of 700 - 2000 were stored and subsequently processed to yield the mean and rms values. The overall data acquisition was determined by the engine speed and the gating circuit which, at 200 rpm, opened every 300 ms and stayed open for about 8 ms corresponding to the crank angle window of 10 degrees. During this time no more than 3 samples were counted due to the 3 ms cycle time of the counter, but only one was processed with the slower sampling microprocessor. The overall data rate depended on the point in the cycle and the location inside the cylinder with a maximum value of 3 s^{-1} in the jet region at mid-intake and a minimum of about 1 s^{-1} in recirculation regions and/or at BDC.

2.2.6 Measurement Uncertainties

Major error sources may include positional uncertainties, flow asymmetry, statistical error, variations in engine speed and frequency shift, velocity gradient and crank angle broadenings, and biasing effects. Their consequences for the present measurements are discussed in turn and quantified where possible.

Positional Uncertainties

Positional uncertainties were associated with the probe volume traverse as well as with both the crank angle and probe volume settings. The traversing table was

adjustable within 0.05 mm which represents an uncertainty of about $\pm$ 2% between positions separated by 1.25 mm (minimum separation used in the measurements). The positional error in the probe volume setting was about $\pm$ 0.2 mm being of the order of the probe volume size. The synchronization of the marker pulse with TDC was achieved within $\pm$ 1 pulse, thus resulting in a crank angle uncertainty of $\pm$ 0.36 degrees.

Asymmetry

The symmetry of the flow in all configurations was checked by obtaining axial velocity profiles across a diameter close to the cylinder head. Figure 2.5 shows such a profile which typifies the flow symmetry established throughout the cylinder and the engine cycle. The maximum flow asymmetries observed were generally less than 5% when expressed in terms of the maximum velocity at the same crank angle and axial locations.

Statistical Error

The error in the value of mean velocity obtained from N samples can be estimated within a certain confidence limit, according to Yanta (1973), by

$$(\text{error})_{\bar{U}} = \frac{Z_c}{\sqrt{N}} \frac{\tilde{u}}{\bar{U}} \qquad (2.18)$$

where Z_c is equal to 2.0 and 2.6 for 95 and 99% confidence limits, respectively. The error is dependent on the local flow conditions. In the region of the flow with 30% turbulence intensity, for example, the minimum sample size (ie. 700) results in a mean velocity error of about 2% with the 95% confidence limit.

The corresponding error in the rms value is independent of the flow conditions and given by

$$(\text{error})_{\tilde{u}} = \frac{Z_c}{\sqrt{2N}} \qquad (2.19)$$

which indicates, with the 95% confidence limit, an error of about 5% for the minimum sample size used in the measurements.

Engine Speed

Unsteadiness in the engine speed mainly arises from the torque fluctuations over the cycle due to the varying sliding friction between the piston and the cylinder wall. These fluctuations were kept to a minimum by the smoothing action of the flywheel resulting in short term speed variations of less than $\pm$ 0.5%. Long term drifts were about $\pm$ 1% and any greater drifts were compensated by altering the motor speed control. The error in the mean velocity value is insignificant and that associated with the rms value can be estimated from

$$(\text{error})_{\tilde{u}} = \left[1 + \frac{(\tilde{\omega}/\omega)^2}{(\tilde{u}/\bar{U})^2}\right]^{\frac{1}{2}} - 1 \qquad (2.20)$$

where ω is the nominal angular speed of the crankshaft and $\tilde{\omega}$ the rms of the angular speed fluctuations. According to the above equation 1% rms fluctuation in engine speed (ie $\tilde{\omega}/\omega = 0.1$) results, with turbulence intensity level of 0.1, in an error of about 0.5% in the measured rms velocity values. Since the observed in-cylinder levels are usually higher than 0.1, the effect of engine speed fluctuations of such magnitude on measured rms velocity values can be neglected.

Frequency Shift

The diffraction grating was rotated by a dc motor with feedback control which resulted in a highly stable rotational speed of the motor and therefore the frequency shift. The short term variations which tend to be random fluctuations around the nominal shift of 1.83 MHz, were always less than $\pm$ 0.5% and are likely to influence the rms rather than the mean values.

According to Melling (1977) fluctuations of such magnitude have insignificant effect on the rms velocity value; it was shown that even in regions of low turbulence intensity the errors do not exceed 2%. Due to the drift in frequency shift of no more than 0.2%, the error in the mean velocity value is thought to be insignificant except in very low velocity regions.

Velocity Gradient Broadening

The probe volume is necessarily of finite size and when it lies across a mean velocity gradient in the flow, particles crossing the probe volume will have a range of velocities which is proportional both to the gradient and to the dimension of the volume parallel to the gradient. As a consequence, the velocity probability distribution is broadened and may be skewed. Since the probe volume diameter d_p is much less than l_p (see sub-section 2.2.2), only broadening from radial gradients need be considered. The measured mean velocity value will not be affected by the broadening if the volume lies across a constant gradient. It can, however, be biased at positions where the mean velocity profile is strongly curved. The associated mean velocity error can, as deduced from Gosman et al (1977) be estimated from

$$(\text{error})_{\bar{U}} = \frac{l_p^2}{32\bar{U}} \frac{\partial^2 \bar{U}}{\partial r^2} \qquad (2.21)$$

The velocity gradient broadening is of main concern in the measurements of turbulence intensity, where the total rms value contains contributions from both the turbulence and the spatial variation in the mean velocity. The rms value of the gradient broadening,

$\tilde{u}_v$, is given by (Durst et al, 1981):

$$\tilde{u}_v = \left| \frac{l_p}{4} \frac{\partial \bar{U}}{\partial r} \right| \qquad (2.22)$$

and the error in the measured rms value due to $\tilde{u}_v$ can be deduced from

$$(\text{error})_{\tilde{u}} = \left[1 + \left(\frac{\tilde{u}_v}{\tilde{u}} \right)^2 \right]^{\frac{1}{2}} - 1 \qquad (2.23)$$

The uncertainty in the mean value was calculated, from equation 2.21, to be less than 2% in most regions with a maximum of about 5% in regions of largely varying gradients. Similar magnitudes of the mean velocity error also resulted from the calculations made with the one-dimensional computer simulation procedure of Vlachos (1977). In brief, the probe volume was placed at a position on the measured profile with its length l_p parallel to the radial velocity gradient. The velocities of 1000 particles whose paths across the volume were simulated via a random number generator, were then computed from the profile. The mean and rms values of each set of 1000 velocities were subsequently calculated and compared with the measured values. Sample calculations of Bicen and Vlachos (1980) showed that the broadening effect on the rms value is negligible apart from those measured in regions of very steep velocity gradients, corresponding to the edges of the incoming jet, where the values were overestimated by about 10%.

Crank Angle Broadening

Sampling the velocity over a finite crank angle interval $\Delta\theta$ gives rise to a broadening if a temporal (crank angle) mean velocity gradient exists during this interval. In

analogy to the spatial velocity gradient broadening, the velocity variation will increase with the crank angle interval and in proportion to the acceleration of the flow and hence is expected to be largest in the jet region near TDC and BDC of the intake stroke. As in the case of the velocity gradient broadening, the rms value is affected more than the mean velocity. The rms variation due to the crank angle broadening, $\tilde{u}_c$, is given by Melling (1977) as

$$\tilde{u}_c = \left| \frac{\Delta\theta}{\sqrt{12}} \quad \frac{\partial \bar{U}}{\partial \theta} \right| \tag{2.24}$$

and an estimate of the error in the measured rms value can be deduced from equation 2.23 by replacing $\tilde{u}_v$ with $\tilde{u}_c$. The crank angle broadening effects on both the mean and rms velocity values for intervals up to 20 degrees are well described by Morse (1977). The estimates of the mean and rms velocity errors, based on the analysis of Morse, are given by Arcoumanis et al (1982b) as

$$(\text{error})_{\bar{U}} = \frac{\Delta\theta^2}{12} \left(\frac{1}{\bar{U}} \frac{\partial \bar{U}}{\partial \theta}\right) \left(\frac{1}{\dot{N}} \frac{\partial \dot{N}}{\partial \theta}\right) \tag{2.25}$$

and

$$(\text{error})_{\tilde{u}} = \frac{\Delta\theta^2}{24} \left(\frac{1}{\bar{U}} \frac{\partial \bar{U}}{\partial \theta}\right)^2 \tag{2.26}$$

where $\dot{N}$ is the count rate (ie. the number of Doppler signals measured per unit time) at a crank angle θ. For crank angle intervals of less than 10 degrees Morse showed, both theoretically and experimentally, that the effect on the mean values was negligible, while the rms values were overestimated up to 10% only in regions of steep temporal gradients. However, he suggested a window of 10 degrees as a compromise between loss of accuracy

and an adequate data rate. The experimental quantification of the crank angle broadening effects together with the testing of the validity of equations 2.25 and 2.26 are given and discussed in more detail in subsection 3.2.5 where observed variations of the rms velocity with crank angle are presented for various window sizes ranging from 1.5 to 20 degrees.

Biasing Effects

Possible bias effects include "velocity biasing" due to the averaging employed and associated with the observation of more fast moving particles, "amplitude bias" due to the integration characteristics of the photomultiplier, and "filter bias" related to the filtering characteristics of the instrument used. These effects are comprehensively discussed in the literature (for example, Durst et al, 1981) and are briefly mentioned here in relation to the present measurements.

For turbulent flow measurements where ensemble-averages of velocities are obtained by individual realisation laser anemometry, the results are biased towards higher velocity values due to the greater contribution from fast moving particles passing through the probe volume (McLaughlin and Tiederman, 1973). Various remedies for velocity bias have been proposed for example by Durao and Whitelaw (1975), Buchhave (1975), Dimotakis (1976), Hoesel and Rodi (1977), Wilson (1978), Durao et al (1980) and Edwards (1981). Durao and Whitelaw (1975), for example, suggested the storing of all frequency values contributing to a measurement and then randomly sampling them in a closed loop until the required number of signals has been considered. Dimotakis (1976) approached the problem mathematically and proposed the

calculation of the ensemble-average by weighting the frequency value with the particle residence time in the probe volume, which requires the simultaneous measurement of the Doppler burst duration in addition to its frequency. Durao et al (1980) considered the bias problem in relation to the time scales which include the average time between particles τ_p, the sampling time interval τ_s, and the integral time scale of turbulence τ_t. It was pointed out that when $\tau_p < \tau_t$, the velocity bias is reduced if τ_s is increased to be longer than either of the time scales and that only under this condition the weighted averages will yield the correct results. If, however, $\tau_s < \tau_p$ or $\tau_p > \tau_t$, the unweighted averages will be biased and the associated error can only be removed by weighting each frequency value with the duration of the Doppler burst.

Durao and Whitelaw (1978) indicated an opposite bias effect to that of the velocity bias, which can occur due to the integration characteristics of the photomultiplier and the use of finite discrimination levels. Although it is difficult to quantify this amplitude bias effect, Durao and Whitelaw suggest that it acts to mitigate the velocity bias and thus reduce the overall bias effect.

In the measurements presented in this thesis, the frequency range encountered was relatively small for a particular discrimination level and the amplitude bias is thought to be small. The relationship between the time scales varied with the measurement location but usually implied that $\tau_p < \tau_t$. On the other hand, the slow sampling rate imposed by the microprocessor software (sub-section 2.2.4) meant that τ_s was longer than the integral time scale τ_t and thus is expected to reduce the velocity bias effect according to Durao et al (1980). The collective bias effect cannot be quantified exactly. It is, however, thought to be insignificant in most

regions of the flow and certainly does not influence any of the fluid dynamic conclusions of this thesis.

A bias effect may stem from the use of a band-pass filter in highly turbulent flows if the measured frequency range lies partly outside the bandwidth of the filter. The mean velocity is then biased towards higher or lower values depending on the relative position, in frequency domain, of the velocity probability distribution with respect to the filter characteristic curve. In the present series of measurements the effective bandwidth of the filter (0.2 to 6.0 MHz at -6 dB) was chosen to cover the expected ranges of Doppler frequency in all parts of the flow, apart from a few locations very close to the head and at the edge of the jet where frequency values higher than 6.0 MHz were present in the corresponding frequency range. The total number of such frequencies did not contribute to the population more than 2% and the related error, therefore, is thought to be insignificant.

Mass Continuity

According to the preceding considerations and analyses, the measurement uncertainties arise mainly from broadening effects due to both spatial and temporal velocity gradients. The overall error in the measured mean velocity value is not likely to be more than 5%, except in the regions of low mean and high rms velocity values. The related uncertainty in the measured rms can be as high as 15% in the regions of very steep velocity gradients which prevail in the immediate vicinity of the cylinder head and at the beginning of the cycle. The overall rms velocity error, however, is likely to be less than 10% in most regions of the flow.

Some confirmation of the overall error in the mean velocity value can be obtained from the mass continuity equation:

$$\frac{\partial}{\partial z} \int_0^R \rho \bar{U}(\theta) r \, dr = 0 \qquad (2.27)$$

which implies that the net mass flow rate, $\dot{m}$, at a given crank angle location is constant across each normal plane along the length of the cylinder.

The present results indicate that the mass continuity is usually satisfied within 10% which is, of course, larger than the estimated overall error in the mean velocity value. The difference may be attributed mainly to the difficulties in integrating the measured profiles over the regions of steep velocity gradient and, to a small extent, to the constant density assumption used in equation 2.27; computations by Johns (1980) showed that the density variations, both in space and with crank angle, affect the validity of equation 2.27 by about 2%.

In short, the uncertainties incurred in the measurements are considered to be small and do not impair the implications of the results and the related conclusions in any way.

2.3 Results

2.3.1 Introduction

In all cases, the results are presented in the form of radial profile and are representative of a large sample of measurements. The axial mean ($\bar{U}$) and the corresponding

rms ($\tilde{u}$) velocity values are both normalised by the mean piston speed $\bar{V}_p$ ($\bar{V}_p$ = 0.4 ms^{-1} for S = 60 mm, and $\bar{V}_p$ = 0.6 ms^{-1} for S = 90 mm). In most cases the measurements are shown at crank angle locations of 36, 90, 144 and 170 degrees during intake and of 190 and 200 degrees in the return stroke, except in sub-section 2.3.2 where attention is focussed more around BDC, at crank angle locations of 170, 190, 200 and 216 degrees. These angles were selected to give a concise description of the flow development during intake and in the return stroke up to a point where the intake valve closure (IVC) usually takes place under operating conditions. In all figures, an outline of a symmetrical half plane of the cylinder and the head is shown together with that of the piston crown in a position corresponding to the crank angle under consideration. The direction and the magnitude of the instantaneous piston velocity normalised by the mean piston speed, are also shown by an arrow on the piston crown. The profiles of $\bar{U}/\bar{V}_p$ and $\tilde{u}/\bar{V}_p$ are both plotted relative to base lines drawn at the appropriate axial locations of measurement.

As a consequence of the uniform fluid density and the symmetry of the flow, the results are also presented for those configurations employing the flat piston, in the form of streamline contours obtained from the stream function ψ, defined by

$$\frac{\partial \psi}{\partial r} = \rho \bar{U} r \qquad (2.28)$$

The stream function values obtained by integrating the above equation are normalised by the mean mass flow rate $\bar{m}_p(\pi R^2 \rho \bar{V}_p)$ which is 2.10 x and 3.15 x 10^{-3} kgs^{-1} for 60 and 90 mm strokes, respectively. The streamlines were plotted with linear interpolation of the stream function values between the measured profiles. From continuity consideration, the integrations of velocity

profiles at a given crank angle Θ should result in the same wall stream function ψ_w $(V_p/2\pi\bar{V}_p)$ which is also normalised by the mean mass flow rate.

2.3.2 60 mm Stroke; Swept-to-Clearance Volume Ratio of 2

The flow development during the early part of the intake stroke is well described by Morse et al (1980a) up to the crank angle location of 144 degrees. In brief, the flow pattern consists of a system of vortices which includes a main toroidal vortex occupying most of the flow space, a ring type corner vortex between the head and the cylinder wall, and another small toroidal vortex just behind the valve. The size and strength of these vortices grow as the piston accelerates and reaches mid-stroke and then remain almost constant up to the crank angle location of 144 degrees.

The profiles of both the axial mean and rms velocities and the streamline patterns obtained from the mean velocity profiles are shown in Figures 2.6 to 2.9, pertaining to the crank angle locations of 170 degrees in the intake and 190, 200 and 216 degrees in the return stroke, respectively. The corresponding streamline patterns are reproduced in Figure 2.10 together with those obtained from the data of Morse et al (1980a) at 36, 90 and 144 degrees in order to provide a complete description of the in-cylinder flow development through the cycle and to assist the related discussion presented in sub-section 2.4.1.

The results obtained at Θ = 170 degrees, just before BDC, are shown in Figure 2.6. A similar flow pattern to that at Θ = 144 degrees is observed, apart from the formation of a new ring vortex in the corner between the piston and the cylinder wall as shown in Figure 2.6a. The main vortex is almost unaltered in position but is reduced significantly in strength, circulating less than

0.6 $\bar{m}_p$ as opposed to about 1.6 $\bar{m}_p$ at 144 degrees (Figure 2.10c). The counter-rotating corner vortex between the head and the wall is also reduced in mass rotation, from 0.6 $\bar{m}_p$ at θ = 144 degrees to about 0.15 $\bar{m}_p$. The ring vortex formed recently in the piston corner gains in size and mass circulation at the expense of the main vortex and rotates almost 20% of the mean mass flow rate $\bar{m}_p$. The mean velocity profiles close to the head and shown in Figure 2.6b, exhibit peaks associated with the incoming jet. The velocity peak, of about 3.5 $\bar{V}_p$ near the head, moves closer to the wall at mid-distance between the piston crown and the head with a value in excess of 4 $\bar{V}_p$ at z = 30 mm. The profiles further away from the head are less structured with peaks diminishing as the piston crown is approached. In accord with the mean velocity field, the rms velocity profiles, Figures 2.6c, show peaks close to the head, which are associated with the shear layers of the incoming jet.

At the beginning of the return stroke at θ = 190 degrees, the four vortices are still present as shown in Figure 2.7a, although the emphasis has shifted towards the corner vortex near the piston from the main one which has now become a ring type vortex with a reduced mass circulation of about 0.4 $\bar{m}_p$. The rotational direction of the four vortices remains the same, but the streamlines reaching the piston have clearly changed direction with consequent straightening of the flow along the axis and squeezing of the main vortex towards the wall. The corner vortex near the piston has gained in size and mass, and now circulates about 0.25 $\bar{m}_p$. The ring vortex in the corner between the head and the wall has further decayed rotating a mass of less than 0.1 $\bar{m}_p$. The small toroidal vortex behind the valve is least affected by the straightening action of the returning piston and continues to

survive there independent of its relatively low strength. It is of particular interest to note that the sudden reversal of the piston motion causes the flow to reverse equally rapidly at the open port. Although the piston is travelling with the same speed as that at θ = 170 degrees but in the opposite direction, the mean fluid velocities are reduced in comparison, as shown in Figure 2.7b. In parallel with the decay of mean flow, the turbulent velocity profiles have also reduced in magnitude tending to become uniform as indicated in Figure 2.7c.

Figure 2.8 shows the results obtained at θ = 200 degrees. The corner vortex close to the head is washed out as indicated by Figure 2.8a. The main vortex has squeezed closer to the wall with consequent reduction in size and now circulates a mass less than 0.2 $\bar{m}_p$. The ring vortex which was originally in the corner between the piston and the wall, has moved away from the corner towards the axis and also has been reduced in strength circulating about 0.05 $\bar{m}_p$. As the vortex structure breaks down, the mean velocity profiles, Figure 2.8b, tend to become uniform with reduced magnitudes in the recirculation regions. The rms velocity values are generally lower than those at θ = 190 degrees and the turbulence tends to become homogeneous inside the entire cylinder as shown in Figure 2.8c.

The process of vortex breakdown is complete by 216 degrees in the return stroke, as depicted in Figure 2.9a. The streamlines have become straight in most parts of the cylinder, except in the region close to the head where the fluid tends to move towards the open port. The fluid near the piston moves with the piston velocity resulting in flat mean velocity profiles, as shown in Figure 2.9b. The profiles close to the head, on the other hand, exhibit peaks associated with the fluid moving directly towards the port. The corresponding turbulent velocities have

been further reduced in magnitude to about 1.0 $\bar{V}_p$ almost everywhere inside the cylinder (Figure 2.9c).

2.3.3 90 mm Stroke; Swept-to-Clearance Volume Ratio of 3

The results which include the streamline patterns and the axial mean and rms velocity profiles are presented in Figures 2.11 to 2.16 for the crank angle locations of 36, 90, 144 and 170 degrees during intake and 190 and 200 degrees in the return stroke, respectively. These crank angles were chosen to be the same as those in the previous sub-section to enable comparison.

The in-cylinder flow pattern at θ = 36 degrees consists of two vortices, Figure 2.11a, formed by the interaction of the incoming jet with the more stagnant fluid inside the cylinder. The main vortex is toroidal and circulates about 0.4 $\bar{m}_p$ while the ring vortex formed in the corner between the wall and the head rotates a mass of only 0.2 $\bar{m}_p$. The fluid enters the cylinder at an angle of about 60 degrees to the vertical, in accord with the seat angle used. The peak jet velocity value of about 11 $\bar{V}_p$ is observed close to the head, as shown in Figure 2.11b, and gradually decays to about 2.3 $\bar{V}_p$ as the piston is reached. The corresponding rms velocity profiles, Figure 2.11c, exhibit two peaks associated with the inner and outer shear layers of the annular jet. As the turbulence diffuses downstream of the head, the rms velocity profiles tend to become uniform and reduce in peak values close to the piston crown.

The results obtained at mid-intake (θ = 90 degrees) are presented in Figure 2.12. The main vortex has grown appreciably in size and strength, Figure 2.12a, and circulates a mass of about 1.6 $\bar{m}_p$. The jet trajectory changes downstream of the head and moves towards the wall

with consequent shortening of the corner vortex which now circulates almost twice the mass at θ = 36 degrees (about 0.35 $\bar{m}_p$). A small vortex has formed behind the valve during the growth and translation of the main vortex, but circulates a small amount of mass of about 0.05 $\bar{m}_p$. The peak jet velocity increases to about 15 $\bar{V}_p$, Figure 2.12b, as the piston reaches its maximum velocity in the stroke. The change in the jet trajectory is also evident in the mean profiles with the peak rapidly moving towards the wall. The turbulent velocities, Figure 2.12c, are generally higher due to the increase in mean velocities, particularly in the jet region close to the head where steep velocity gradients were observed as indicated in Figure 2.12b. Turbulence is highly non-homogeneous near the head with a maximum rms value of about 5.3 $\bar{V}_p$ and results in more uniform rms profiles close to the piston crown.

With the piston moving away from its mid-stroke and towards BDC (θ = 144 degrees), the main vortex translates and stretches along the length of the cylinder, Figure 2.13a, circulating less than half of the mass at θ = 190 degrees (of about 0.75 $\bar{m}_p$). The corner vortex remains unchanged in size and position, and is slightly reduced in mass rotation to about 0.25 $\bar{m}_p$. The small toroidal vortex behind the valve also remains in the same position as in the previous crank angle, but now circulates only 1% of the mean flow rate $\bar{m}_p$. The mean velocity field, according to Figure 2.13b, has generally retarded in parallel with the decelaration of the piston past mid-stroke. The trends of the mean profiles, however, are very much the same as those at mid-intake. The turbulence has also decayed, but the rms profiles still exhibit peaks close to the head as shown in Figure 2.13c. The overall turbulence level is higher than that at θ = 36 degrees, although the incoming jet has the same

magnitude of the mean velocity at both crank angles. The increased mixing process since the beginning of the cycle is, no doubt, responsible for the observed difference between the two levels.

At Θ = 170 degrees, the piston has almost reached the end of its travel with fluid velocities much higher than that of the piston. As the fluid has higher momentum than that of the retarding piston, it deflects off the piston face forming a ring type vortex in the corner as indicated in Figure 2.14a. This corner vortex, like the other near the head, rotates in an opposite direction to that of the main one and circulates a mass of about 0.3 $\bar{m}_p$. It squeezes the main vortex axially at the expense of the small one behind the valve. The main vortex and the corner one near the head both almost maintain their strengths from the previous crank angle, now circulating about 0.7 $\bar{m}_p$ and 0.2 $\bar{m}_p$ respectively. The mean velocities, Figure 2.14b, have further decreased in magnitude together with the corresponding rms values as shown in Figure 2.14c. The rms profiles are uniform in most of the cylinder space, except in the region close to the cylinder head.

During the return stroke at Θ = 190 degrees, the process of vortex breakdown is underway immediately as the piston reverses direction at BDC (Figure 2.15a). The corner vortex near the piston has increased in size and moved towards the axis circulating a mass of only 0.15 $\bar{m}_p$. The main vortex which has been squeezed against the wall and consequently has become a ring type vortex, is confined in a small space and circulates no more than 0.1 $\bar{m}_p$. The corner vortex close to the head starts to move towards the port and has also reduced in mass rotation to about 0.05 $\bar{m}_p$. The mean velocity profiles, Figure 2.15b, have further decreased in magnitude and tend to become uniform. The turbulence follows the similar trend and becomes almost homogeneous as indicated in Figure 2.15c.

Figure 2.16 shows the results at Θ = 200 degrees. All the vortices have disappeared, apart from that which was in the piston corner at the previous crank angles. Nevertheless, it is very low in strength and circulates only 0.5% of the mean flow rate $\bar{m}_p$. It is anticipated that it will also disappear in the next few crank angle degrees. The mean fluid velocities have generally increased in accord with the piston speed, Figure 2.16b, especially in the near head region where the fluid moves directly towards the open port. The near homogeneous turbulence has an overall level of about 1.0 $\bar{V}_p$, as indicated in Figure 2.16c.

2.3.4 90 mm Stroke; Swept-to-Clearance Volume Ratio of 9

The corresponding profiles of both the axial mean and rms velocities together with the streamline patterns are presented in Figures 2.17 to 2.22 at the same crank angle locations as those selected with the previous configuration to provide a direct comparison.

During the early part of the intake stroke at Θ = 36 degrees, two vortices have been observed as shown in Figure 2.17a. The main toroidal vortex which occupies a larger portion of the space circulates a mass of about 0.35 $\bar{m}_p$. The incoming jet whose trajectory is very much in accord with the seat angle, impinges directly on the piston face. The ring type corner vortex is much stronger than the main one due to the enhancement associated with the fluid deflection off the piston face, and circulates about 0.55 $\bar{m}_p$. The mean velocity peak of about 11 $\bar{V}_p$ near the head, Figure 2.17b, gradually moves up as the piston is approached, in agreement with the flow entry angle of 30 degrees. The turbulent velocities are generally high everywhere due to the enhanced mixing as a result of the

jet impingement on the piston face. The turbulent velocity peaks assoicated with the inner and outer boundaries of the jet, however, still predominate the turbulence field as shown in Figure 2.17c.

Figure 2.18a shows the flow pattern prevailing at mid-intake (θ = 90 degrees). The main vortex has rapidly grown in size pushing the corner vortex closer to the head and consequently contracting the jet passage near the cylinder wall. It has gained also in mass circulation, rotating about 1.9 $\bar{m}_p$. The contracted ring vortex near the head, however, circulates almost the same mass as that in the previous crank angle. Another toroidal vortex rotating only 2% of the mean flow rate $\bar{m}_p$ has formed behind the valve as a consequence of the growth and translation of the main vortex. In parallel with the increase of piston velocity, the fluid velocities have generally increased with a peak mean velocity value of about 15.5 $\bar{V}_p$ near the entry as shown in Figure 2.18b. The turbulent velocity profiles reflect the steep velocity gradient regions of the flow, Figure 2.18c, exhibiting increased peaks close to the cylinder head. As the mean velocity gradients decrease at locations away from the head, the corresponding rms profiles conform more towards uniformity as the piston is approached.

The results obtained at θ = 144 degrees are shown in Figure 2.19. A small ring vortex has formed close to the piston as shown in Figure 2.19a and circulates less than 10% of the mean mass flow rate $\bar{m}_p$. All other vortices have reduced in strength. The main vortex circulates about 1.0 $\bar{m}_p$, almost half of the mass at θ = 90 degrees. The vortex in the cylinder head corner rotates a mass of about 0.4 $\bar{m}_p$ and the one behind the valve no more than 1% of the mean flow rate $\bar{m}_p$. The magnitude of the mean velocities has decreased in general as shown in Figure 2.19b, with a peak jet velocity value near the

head of no more than 9.5 $\bar{V}_p$. The rms velocities have also reduced in magnitude in parallel with the decay of the mean flow field.

Just before BDC at θ = 170 degrees, the main vortex splits forming a small vortex near the axis and the piston face as indicated in Figure 2.20a. Although the overall flow pattern is similar to that at 144 degrees, it has gradually decayed with the main vortex now circulating a mass of 0.45 $\bar{m}_p$ and the corner one close to the head about 0.2 $\bar{m}_p$. The other two vortices which are relatively low in strength have both stretched along the cylinder length and maintain their mass circulations from the previous crank angle. The mean velocities, Figure 2.20b, have further decreased in magnitude. As the mean flow field decays and the velocity gradients become smaller, the turbulence generation goes down and as a consequence the rms velocity values are reduced with the profiles tending to become uniform especially in regions close to the piston crown as indicated in Figure 2.20c.

During the early part of the return stroke at θ = 190 degrees and as shown in Figure 2.21a, the vortex structure, as in the previous configurations, undergoes a breakdown process. The corner vortex which was close to the piston face has moved towards the axis and away from the piston circulating less than 10% of the mean flow rate. The main vortex which is now of a ring type and squeezed against the wall rotates the same amount of mass as the one in the cylinder head corner, which is of about 0.1 $\bar{m}_p$. As the vortex structure collapses, the overall mean and rms velocity values further reduce as indicated in Figures 2.21b and 2.21c.

The vortices are almost destroyed at θ = 200 degrees as shown in Figure 2.22a, except the one which has recently moved towards the axis from the piston corner. It is,

however, very weak and circulates less than 5% of the mean flow rate $\bar{m}_p$. With the flow progressively becoming one-dimensional the mean velocity gradients disappear, Figure 2.22b, and the turbulence which has been undergoing a decay process becomes near-homogeneous with an overall level of about 1.0 $\bar{V}_p$ as shown in Figure 2.22c.

2.3.5 Flat and Re-Entrant Type Bowl Pistons

The profiles of both the axial mean and rms velocities for the two piston crown configurations are presented together in Figures 2.23 to 2.26, corresponding to the crank angle locations of 36, 90 and 144 degrees during intake and 190 degrees in the return stroke. The profiles for the flat piston are indicated with broken lines and those corresponding to the intake stroke are extracted from the results of Morse et al (1979a) to provide a more concise comparison.

During the intake stroke the two flow fields are very similar to each other. At θ = 36 degrees, Figure 2.23, the peak velocities near the head and associated with the incoming jet differ no more than 8% between the two cases. The mean profiles close to the piston are uniform with identical magnitudes which are almost equal to that of the piston at this crank angle. The corresponding turbulent velocities are also in good agreement, with the profiles near the head exhibiting peaks associated with the shear layers of the jet. As the turbulence is generated more in the jet region and does not have enough time to diffuse, the rms velocity profiles close to the piston crown are uniform and much smaller in magnitude as depicted in Figure 2.23b. The same is also true for the rest of the stroke. Although

the magnitudes which are generally higher in the bowl case may show differences up to 15% at mid-intake, the main features of the two flows are qualitatively in good agreement as shown in Figures 2.24 and 2.25 corresponding to 90 and 144 degrees, respectively. In general, both the mean flow and turbulence are enhanced as the piston reaches its maximum speed and then undergo a decay process during the second half of the stroke as shown in Figure 2.25.

Figure 2.26 shows the profiles during the early part of the return stroke, at θ = 190 degrees. The mean and turbulent velocities have further reduced to identical magnitudes in both cases. The turbulence which has been progressively decaying, tends to become homogeneous as shown in Figure 2.26b. These results suggest that the effect of the piston crown geometry on the flow structure is unlikely to be important during the rest of the return stroke.

2.4 Discussion

2.4.1 Creation and Destruction of Vortices

The flow patterns depicted in Figure 2.10 present a typical description of the in-cylinder flow development and its evolution through the engine cycle. The axial flow structure during intake is characterised by a system of vortices induced by an annular jet, which includes a major toroidal vortex, a ring vortex in the corner between the head and the wall, another toroidal vortex behind the valve, and a second ring vortex in the piston corner formed later on in the intake stroke.

This flow structure also prevails in the other configurations presented in this Chapter, and its characteristics are mainly determined by the inlet boundary conditions (Yianneskis, 1982). In the absence of induction swirl (Morse et al, 1980a), the number of vortices in the axial plane is reduced with the disappearance of the weak toroidal vortex behind the valve. A similar flow pattern is maintained in the case of an asymmetric valve (see Morse et al, 1980b; and Arcoumanis et al, 1981), but with the vortices inclined at an angle to the cylinder axis. The flow structure obtained by Arcoumanis et al (1982a) with a 30 degree seat angle, on the other hand, shows considerable differences. A single toroidal vortex occupies most of the flow space with suppression of the vortices in the cylinder head corner and behind the valve. The incoming jet adheres to both the head and the wall, contrary to the one resulting with the present 60 degree seat angle. Ekchian and Hoult (1979) showed that a bi-stable flow is also possible with a 30 degree seat angle whereby the jet either remains detached or adheres to the wall.

The flow patterns presented clearly show that the vortex structure progressively decays in the second half of the intake stroke and subsequently undergoes a breakdown process during the return stroke. The vortices are not swept out of the port, as suggested by Gosman et al (1978a), but rather are destroyed by the squeezing and shearing action of the fluid as it tends to move directly from the piston face towards the open port. The vortex breakdown is complete by 216 degrees in the cycle (36 degrees after BDC) which corresponds to about 10% of the piston travel during the return stroke. Although the flow patterns are obtained in the absence of compression due to the permanently open port, the results imply that in real engines with intake valves

usually closing after BDC in the return stroke, any system of vortices induced during intake is likely to disappear before IVC. A more direct implication of the results is that any vortex structure present in the cycle, whether as a result of the intake, compression or combustion processes, will most probably break down in the exhaust stroke before the next cycle begins. The calculations of Gosman et al (1978a) and Johns (1980), although they do not present the vortex structure in every detail, show the vortex breakdown in the early part of the return stroke, particularly soon after 216 degrees. A longer persistence of the intake vortices in the return stroke is also possible with different inlet boundary conditions. Arcoumanis et al (1982a) (see also Arcoumanis and Vlachos, 1980), show that with a 30 degree seat angle the main toroidal vortex is maintained further in the return stroke, although it has become of a ring type, than in the case of the 60 degree seat angle used with the present configurations.

There is some evidence in the literature that a spiral vortex motion, known as "vortex roll-up", is induced in the piston corner as a result of the scraping of the wall boundary layer by the piston during the compression and/or exhaust stroke (see for example Tabaczynski et al, 1970;and Ishikawa and Daily, 1978). In the flow visualisation tests of Tabaczynski et al, it was observed that the characteristic size of the vortex was small compared with the diameter of the cylinder. The present results do not confirm the existence of such a vortex and it is the intake-generated structure which dominates the flow during intake and at the early part of the return stroke. The results of Morse et al (1979a, b) and (1980a, b) at a later stage in the return stroke also show no such evidence of the vortex roll-up phenomenon which is unlikely to be important in engine practice.

The shear flow induced during intake is a major source for turbulence generation. The intake turbulence is non-homogeneous and probably anisotropic, too. During the second half of the intake stroke the turbulence, following the trend of the mean flow, undergoes a decay process as the mean velocity gradients disappear, and it tends to become homogeneous in the return stroke. Ramos et al (1981), however, report increased turbulence levels near the head during the exhaust stroke of a four-stroke model engine and attribute them to the mean velocity gradients induced by the fluid moving towards the open valve. However, it can be argued that such a local generation of turbulence near the head is more likely to be convected and washed out of the port. It is, therefore, most probable that the increase is due to the generation of turbulence associated with the fluid jetting into the cylinder at exhaust valve opening (EVO), as discussed in the next Chapter (sub-section 3.4.1).

2.4.2 Influence of Stroke

The influence of the piston stroke on the axial flow structure prevailing inside the cylinder and during the cycle may be quantified by comparing the results obtained with the 60 mm stroke and presented in sub-section 2.3.2 with those of the 90 mm one in sub-section 2.3.3.

Increasing the piston stroke, with constant engine speed, implies that the piston velocities increase linearly with the stroke throughout the engine cycle (see equation 2.1). As a result the jet velocities increase with the longer stroke and induce qualitatively similar but stronger vortices during the intake stroke. The

associated percentage increase in the strength of the vortices is not always in line with that of the piston speed at every point in the cycle. During the early part of the intake stroke this increase is generally higher and may be attributed to the increase of the piston acceleration, thus of the inertia forces exerted on the fluid, in the case of the longer stroke. The opposite is true during the second half of the intake stroke whereby a faster decay of the vortices is observed with the longer stroke as the piston decelerates towards BDC. The vortices elongate in the axial direction to accommodate the increase in geometry associated with the longer stroke of the piston. Ekchian and Hoult (1979) report, although only qualitatively, a similar behaviour of the vortex structure during intake; with increasing piston stroke the vortices become unstable and break up around BDC. The two flow patterns again show similar trends during the return stroke. The faster decay process associated with the longer stroke, however, persists and results in an earlier breakdwon of the vortices in the return stroke.

The turbulence follows the similar trends of the mean flow and is, therefore, generally higher in the case of the longer stroke. Although the associated increase in turbulent velocities scales well with that of the piston speed during the first half of the intake stroke, it becomes less pronounced as the turbulence decays later on in the intake and tends to become homogeneous during the return stroke.

2.4.3 Influence of Clearance Volume

Comparison of the results presented in sub-section 2.3.3 with those in sub-section 2.3.4 quantifies the influence of the clearance volume on the in-cylinder flow structure in the axial plane.

During the first half of the intake stroke the smaller clearance volume, which simulates a higher compression ratio case, causes the formation of stronger vortices as the fluid impinges on the piston crown and reflects back off it enhancing, in particular, the strength of the ring vortex in the cylinder head corner. The eyes of the vortices are situated much closer to the piston than those with the larger clearance volume. Later on in the stroke the vortices progressively decay in the smaller clearance case and break down almost at the same crank angle location in the return stroke as that in the other case.

At the early part of the intake stroke and with the smaller clearance volume, the turbulence levels are generally higher due to a stronger impingement of the inlet jet on the piston face. Later on in the intake and during the return stroke, however, both clearance volumes have similar magnitudes of turbulent velocities indicating an insignificant effect of the clearance volume (or compression ratio) on the turbulent velocity field of the return stroke.

2.4.4 Influence of Piston Crown Geometry

The effect of the piston head geometry on the flow structure is quantified by contrasting the results obtained with the idealised representation of a re-entrant type piston bowl to those with the flat piston. The comparison shows that similar velocity fields result in both cases during the engine cycle with some quantitative differences existing in the intake stroke. These differences are generally small and occur in regions of steep velocity gradients and may, therefore, be attributed to the measurement uncertainties incurred in

those regions. The results of Morse et al (1979a) obtained with a cylindrical piston bowl show similar trends of the in-cylinder flow. The fluid inside the bowl is least affected and moves together with the piston as a whole.

During the early part of the return stroke the two configurations have identical mean and turbulent velocity profiles indicating the insignificant effect of the piston crown geometry on the flow characteristics of the return stroke. In the presence of compression, the squish motion associated with the piston bowl geometry will, no doubt, influence the characteristics of the flow. This compression-induced motion and its effects are, however, discussed later in sub-section 3.4.4 in relation to the results obtained, with the presence of compression, in the four-stroke engine.

2.5 Conclusions

The most important conclusions of this Chapter can be summarised as follows:

(1) The in-cylinder flow field during intake is dominated by a jet-like flow which induces a system of vortices prevailing in the axial plane. The flow pattern comprises a toroidal vortex occupying most of the cylinder space and two ring vortices formed one in each of the two cylinder corners.

(2) The vortices progressively decay from mid-intake and are destroyed early in the return stroke by the squeezing action of the fluid as it moves

directly towards the open port. Later on and after the breakdown of the vortices the flow becomes one-dimensional almost everywhere, except in the region close to the head where a sink-type flow prevails.

(3) The shear flow associated with the inlet jet is the major source for turbulence production. Although the turbulence is non-homogeneous during intake, it tends towards homogeneity in the return stroke and decays steadily after mid-intake.

(4) The variation of piston stroke does not change the basic axial flow structure. The longer stroke causes the formation of stronger vortices, but the increase in vortex strength during the cycle is not monotonic with that of the piston speed.

(5) The influence of clearance volume is small and of secondary importance. The smaller clearance volume generates stronger vortices and higher turbulence during early intake due to the stronger impingement of the jet on the piston face. Later on in the intake and during the return stroke, however, the differences become less pronounced.

(6) Piston crown geometry has insignificant effect on the axial flow characteristics during intake, and in the return stroke in the absence of compression.

FIGURES

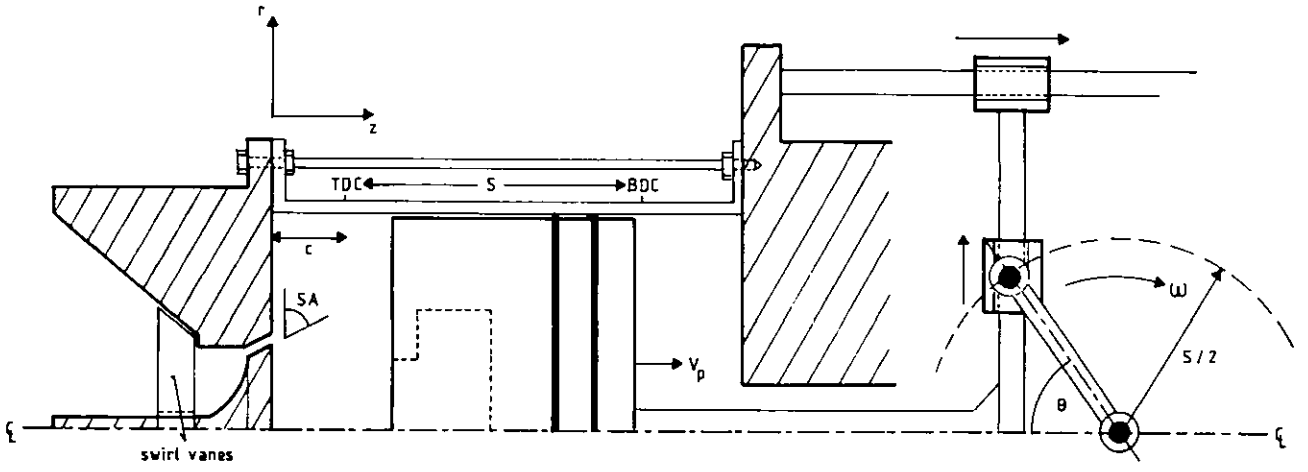

Figure 2.1 Schematic diagram of two-stroke cycle model engine.

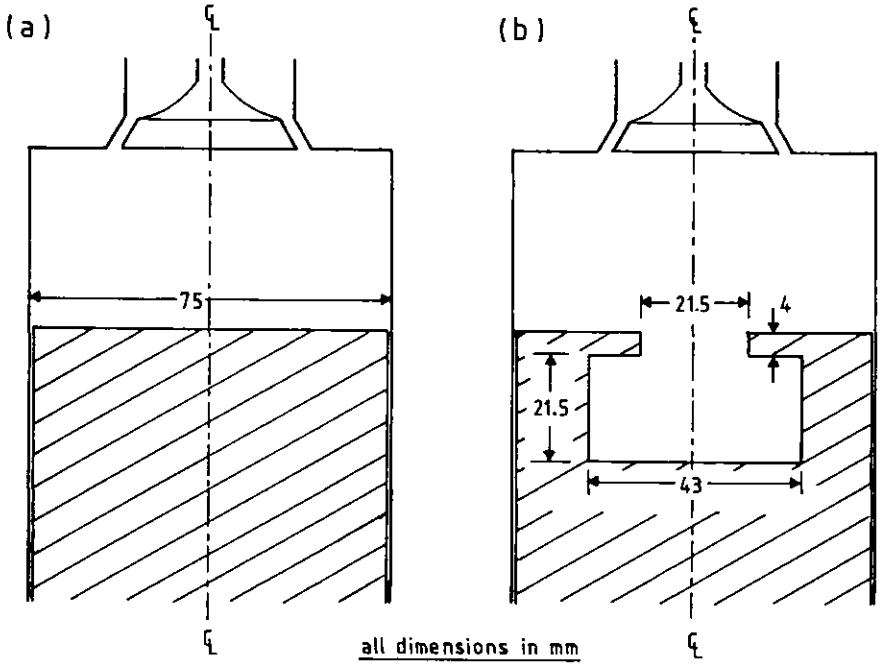

Figure 2.2 Piston crown configurations.
(a) Flat piston
(b) Re-entrant type bowl

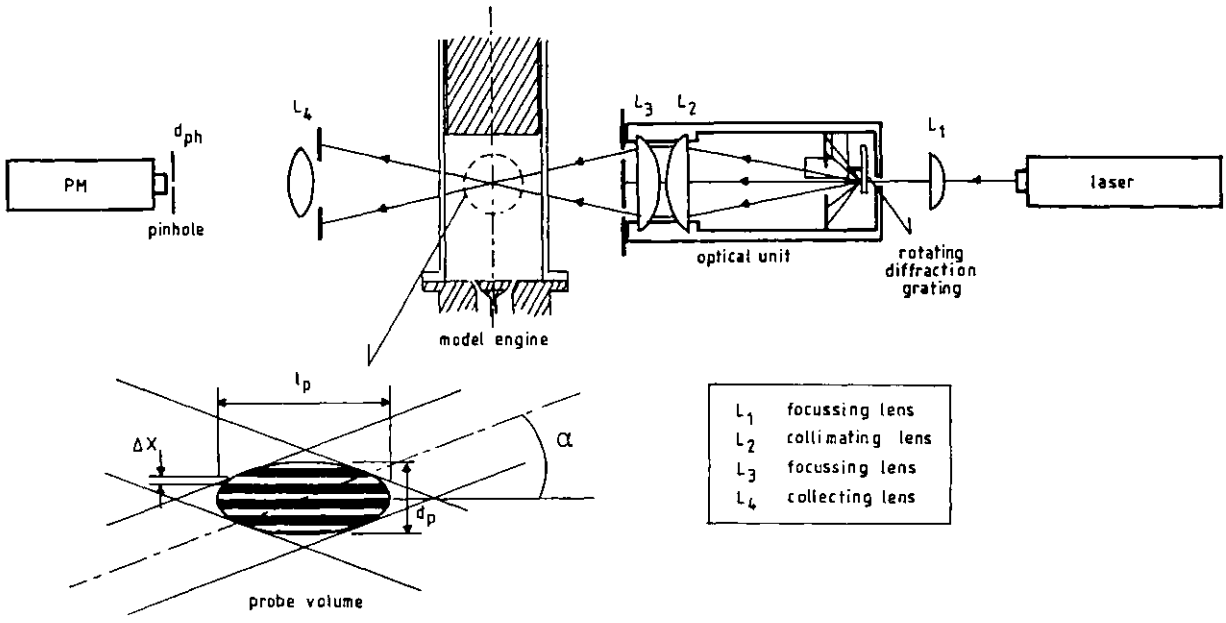

Figure 2.3 Optical arrangement of laser Doppler anemometer.

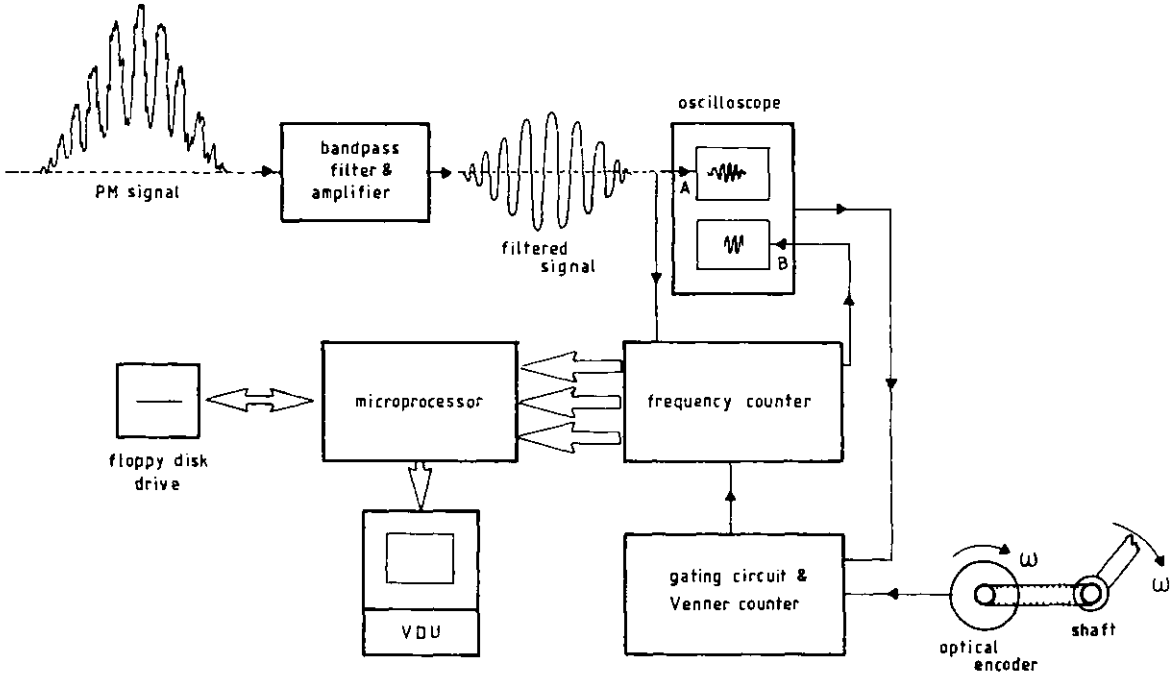

Figure 2.4 Block diagram of signal & data processing systems.

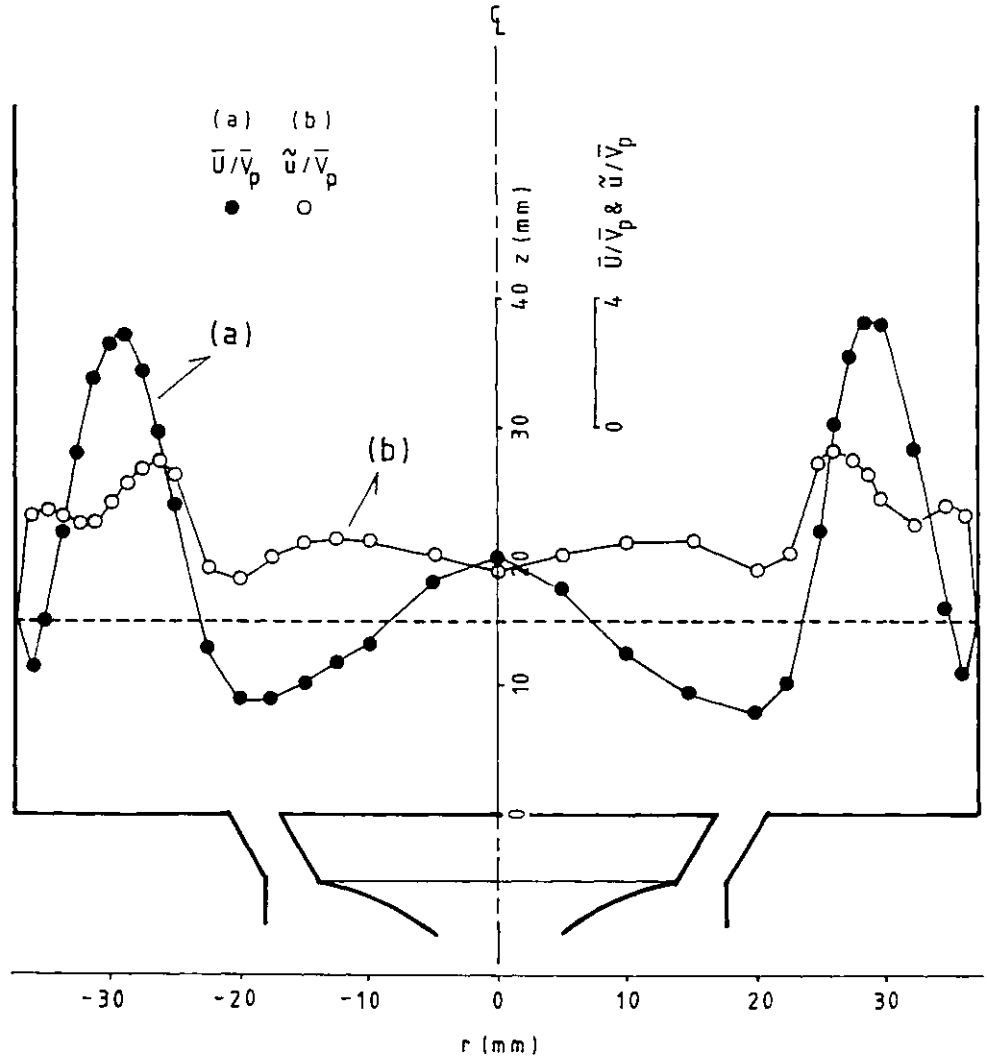

Figure 2.5 In-cylinder flow symmetry;axial velocity profiles at Θ = 90 degrees,z = 15 mm with S = 90 mm,c = 30 mm.

(a) Mean velocity

(b) Rms velocity

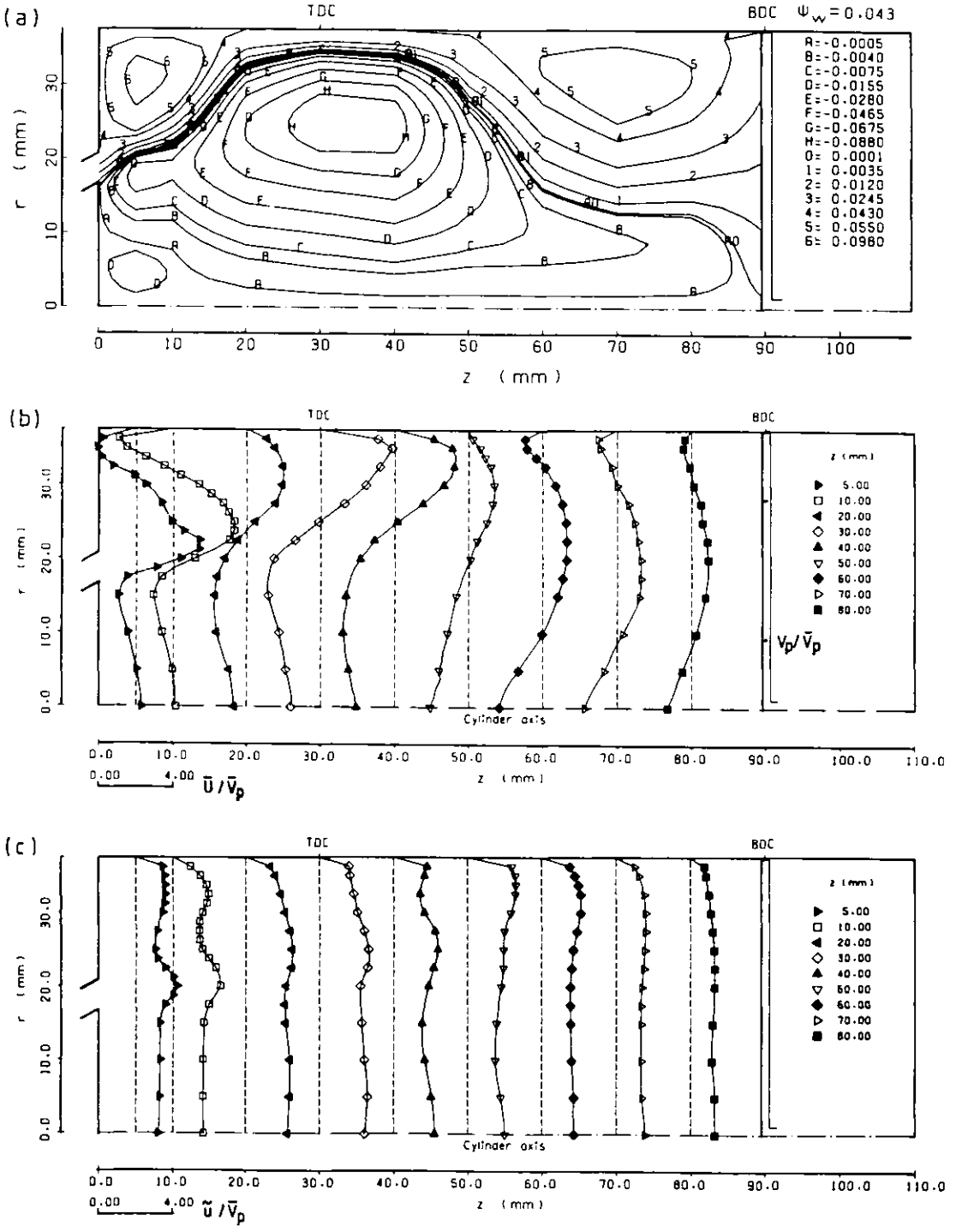

Figure 2.6 Streamline pattern and axial velocity profiles at θ = 170 degrees; S = 60 mm, c = 30 mm. (a) Streamline pattern (b) Mean velocity (c) Rms velocity

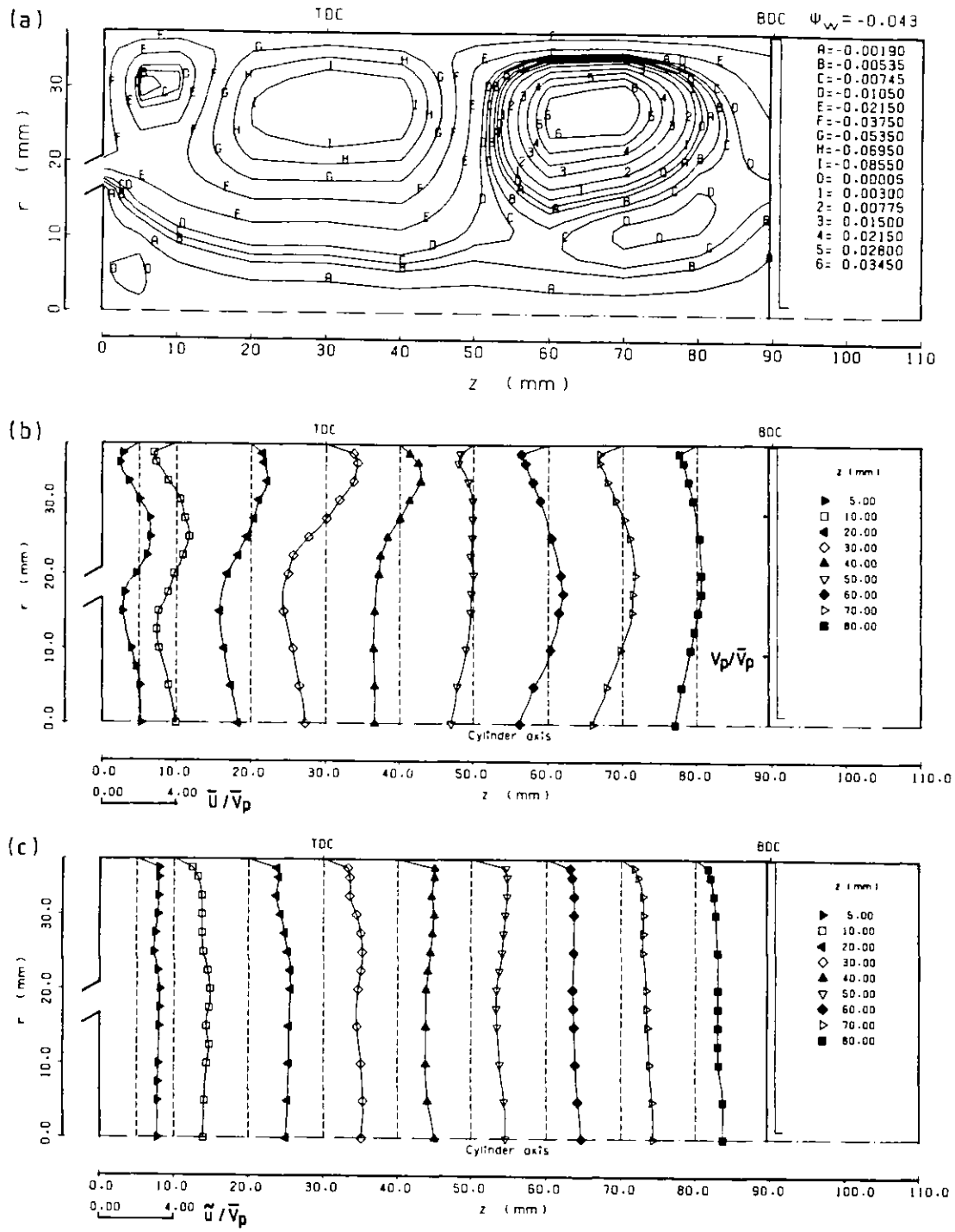

Figure 2.7 Streamline pattern and axial velocity profiles at Θ = 190 degrees; S = 60 mm, c = 30 mm. (a) Streamline pattern (b) Mean velocity (c) Rms velocity

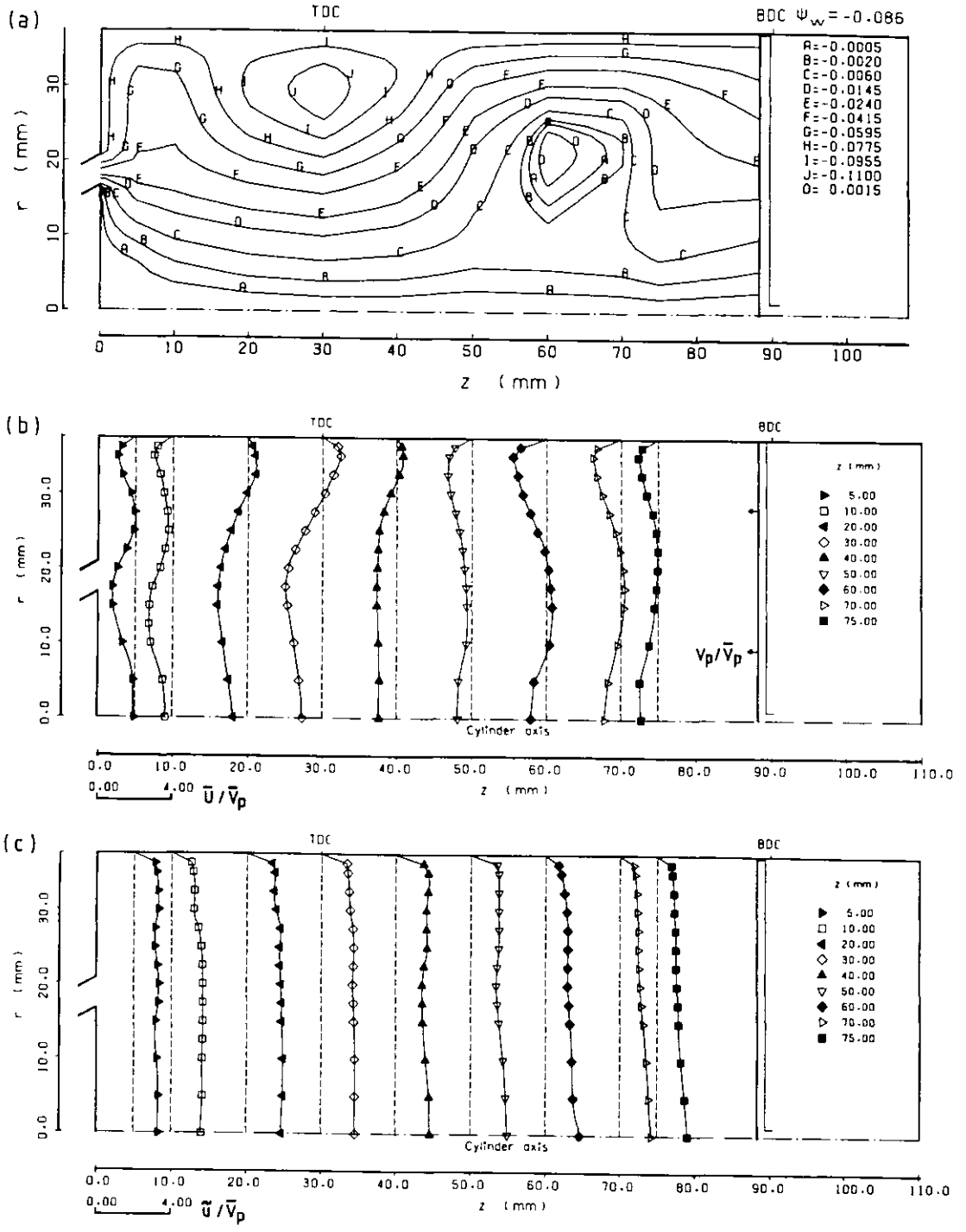

Figure 2.8 Streamline pattern and axial velocity profiles at θ = 200 degrees; S = 60 mm, c = 30 mm. (a) Streamline pattern (b) Mean velocity (c) Rms velocity

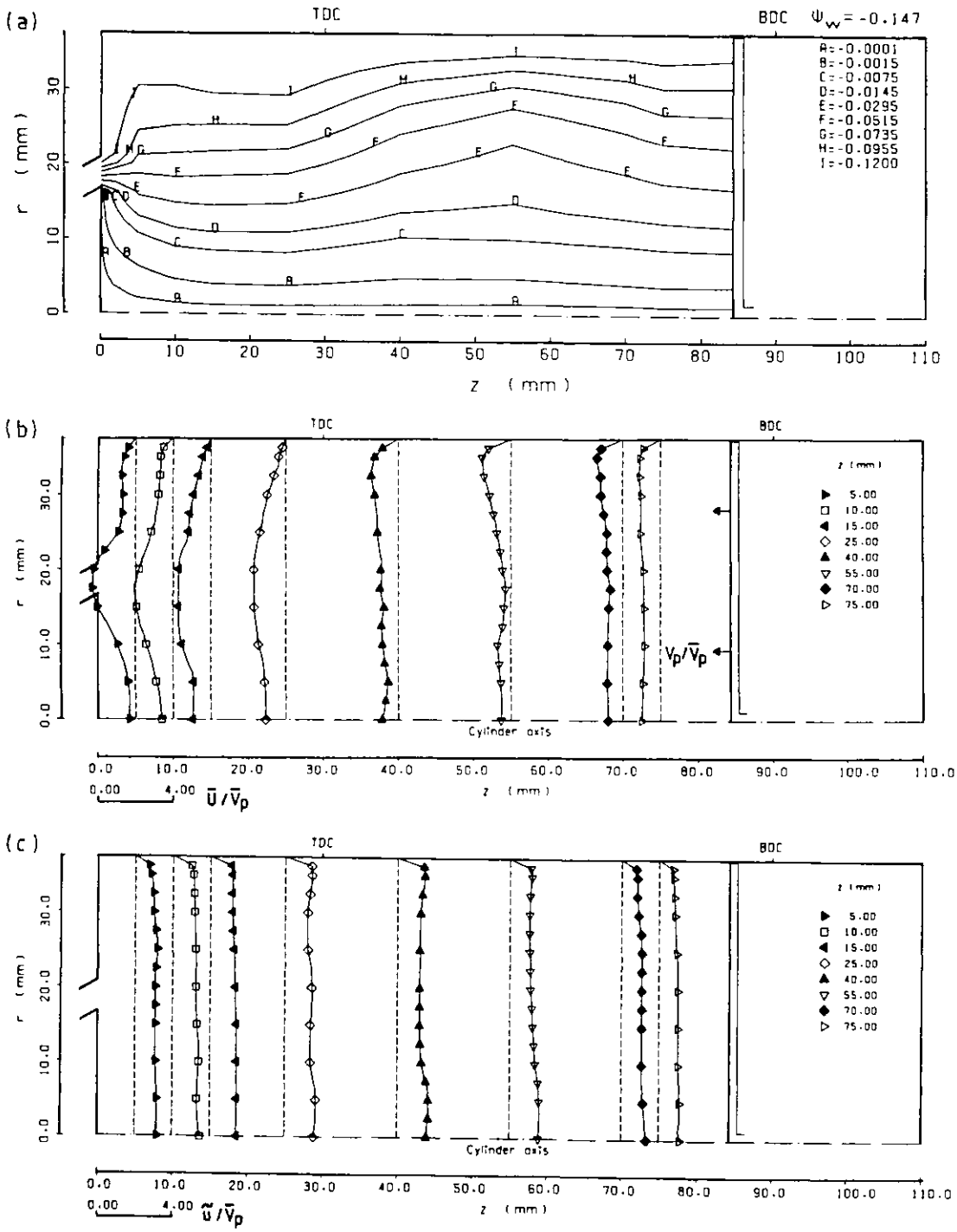

Figure 2.9 Streamline pattern and axial velocity profiles at Θ = 216 degrees; S = 60 mm, c = 30 mm. (a) Streamline pattern (b) Mean velocity (c) Rms velocity

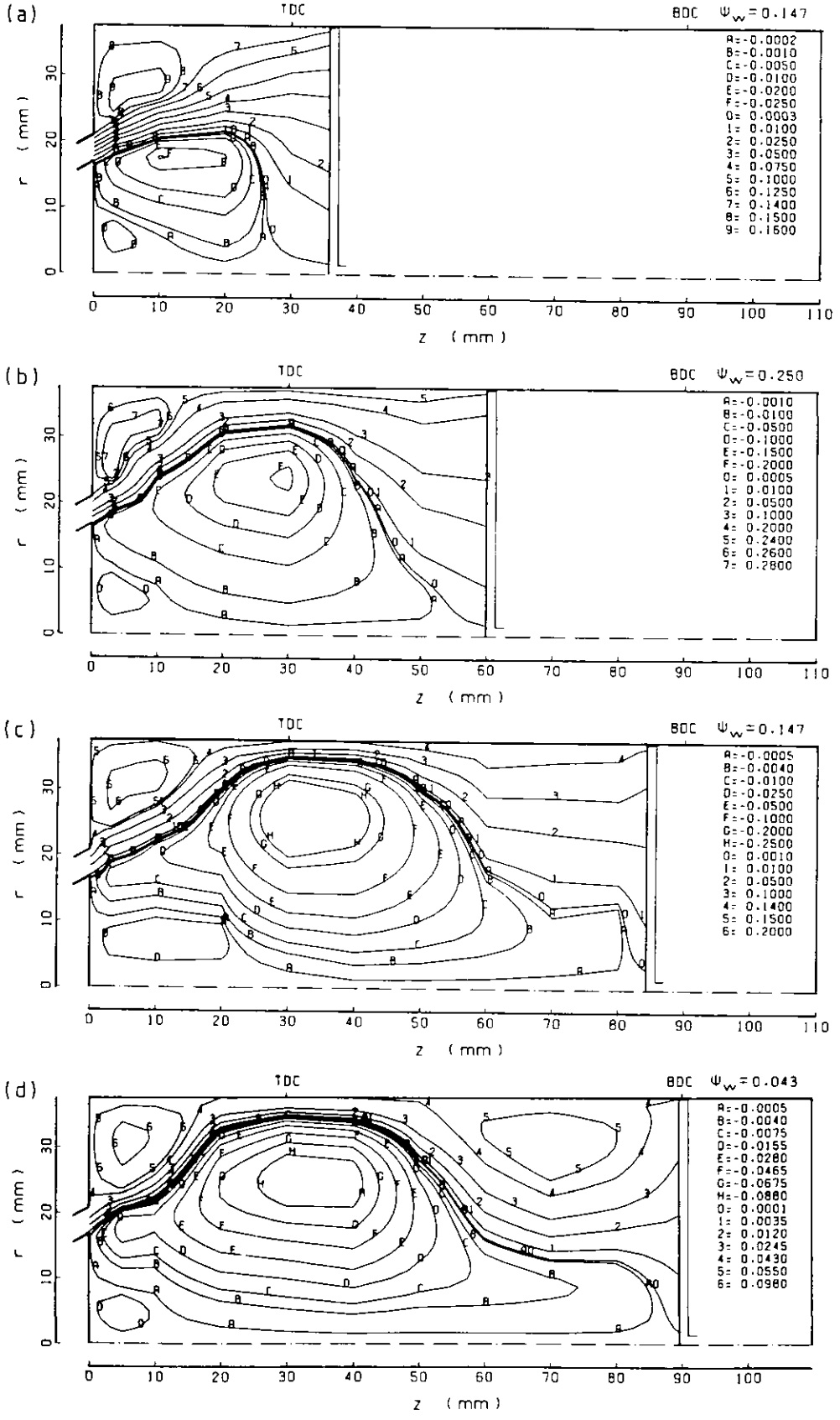

Figure 2.10 cont'd...

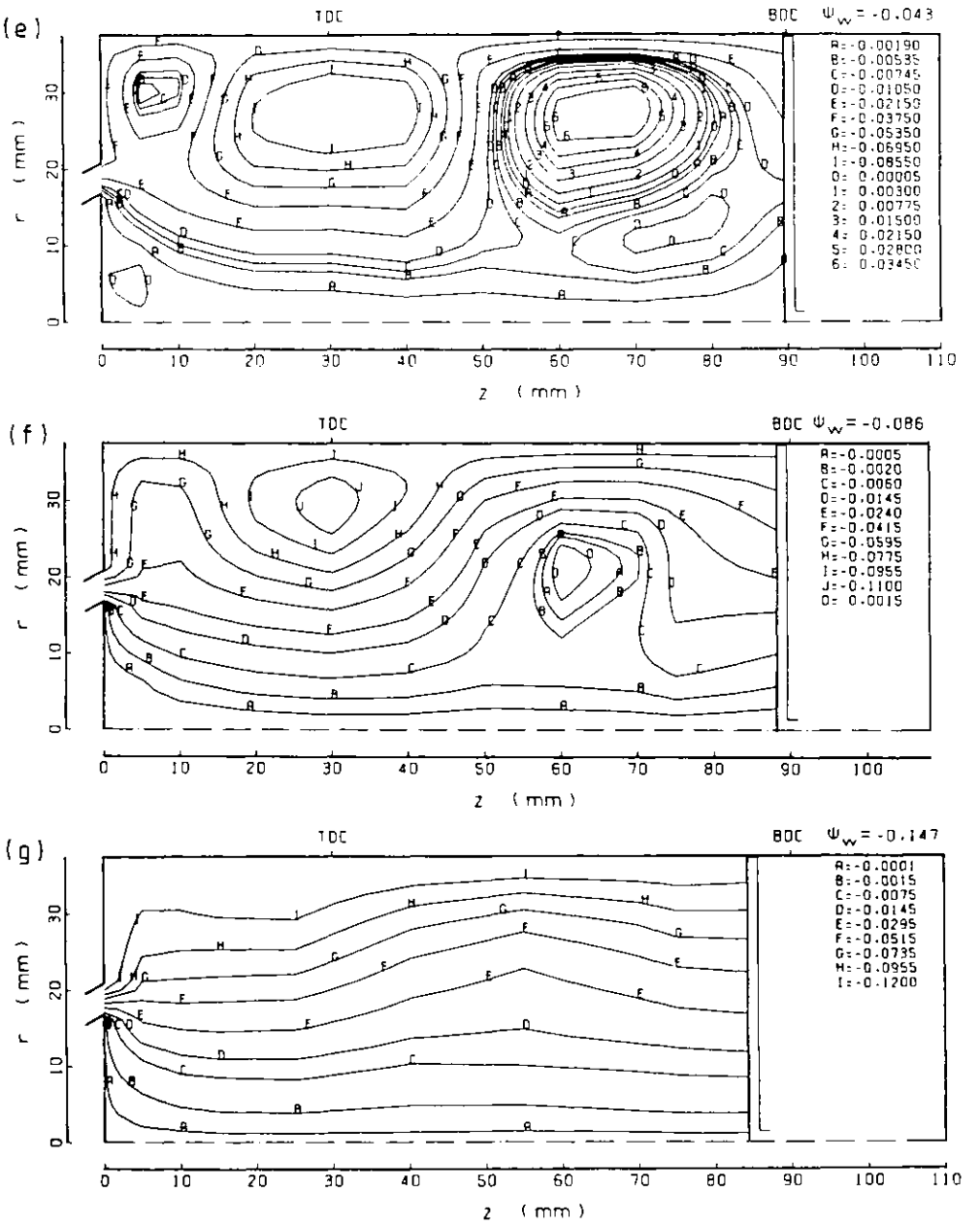

Figure 2.10 Streamline patterns;S = 60 mm, c = 30 mm.
(a) θ = 36 degrees (b) θ = 90 degrees
(c) θ = 144 degrees (d) θ = 170 degrees
(e) θ = 190 degrees (f) θ = 200 degrees
(g) θ = 216 degrees

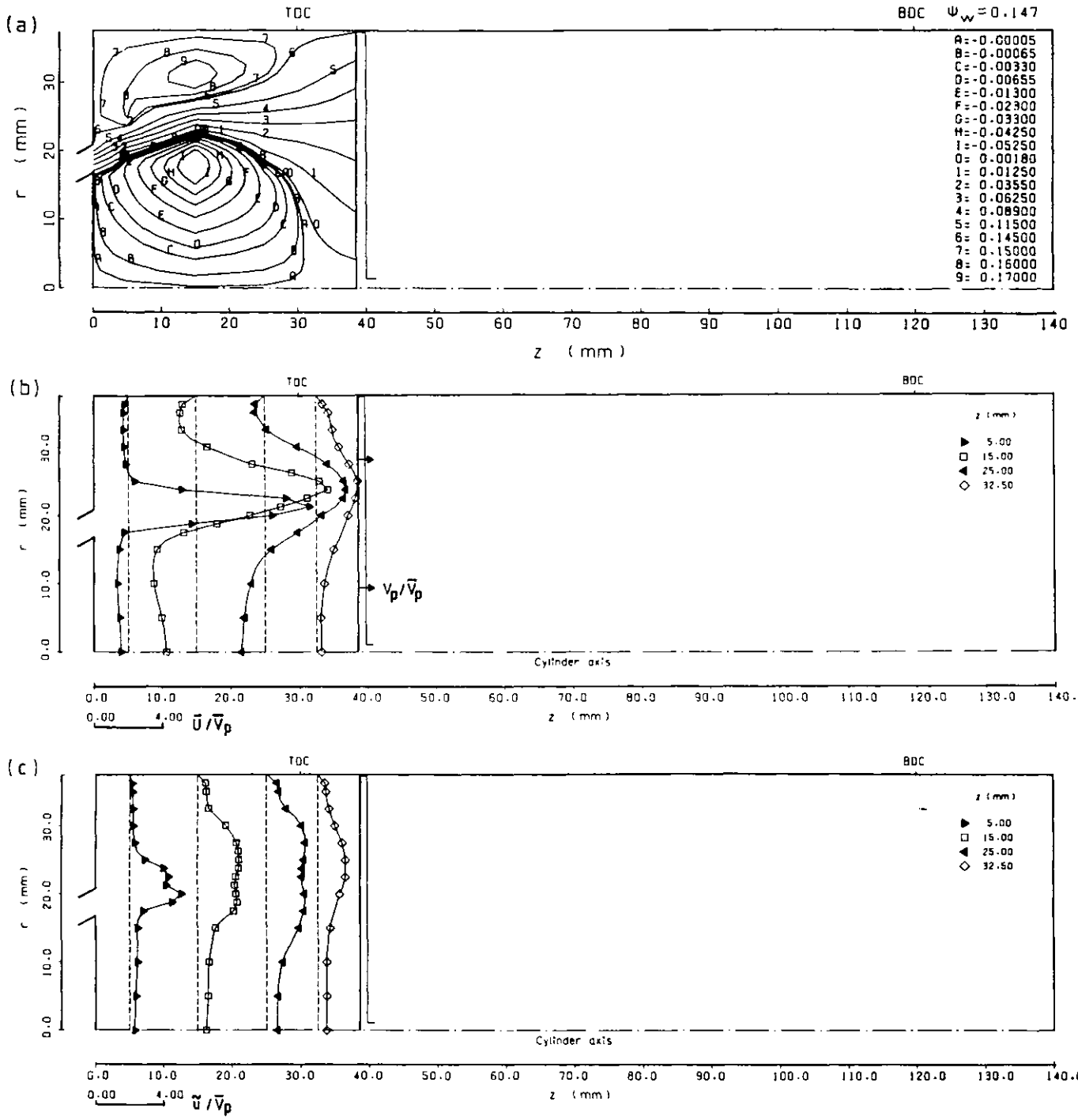

Figure 2.11 Streamline pattern and axial velocity profiles at θ = 36 degrees; S = 90 mm, c = 30 mm.
(a) Streamline pattern (b) Mean velocity
(c) Rms velocity

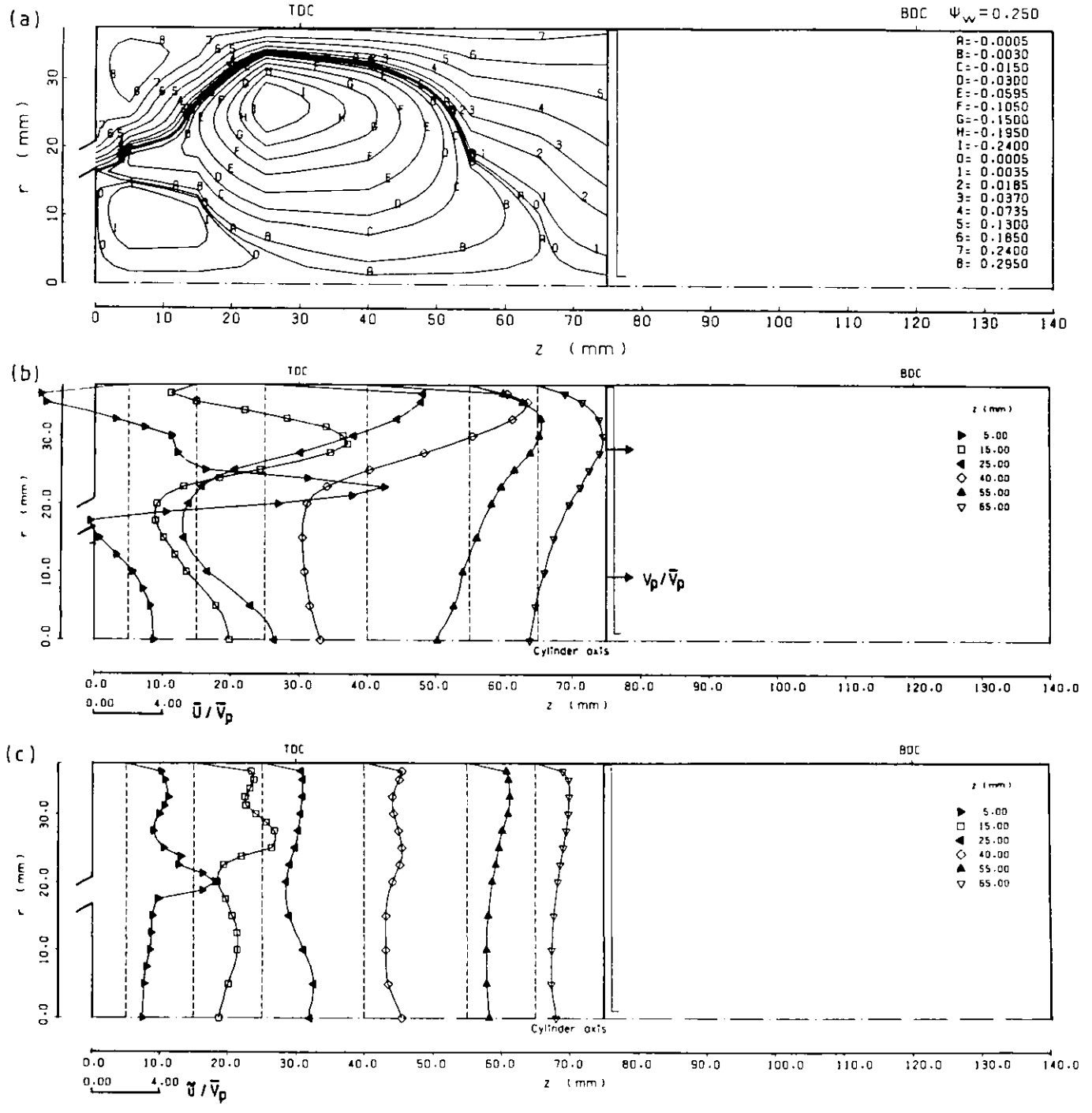

Figure 2.12 Streamline pattern and axial velocity profiles at θ = 90 degrees; S = 90 mm, c = 30 mm.
(a) Streamline pattern (b) Mean velocity
(c) Rms velocity

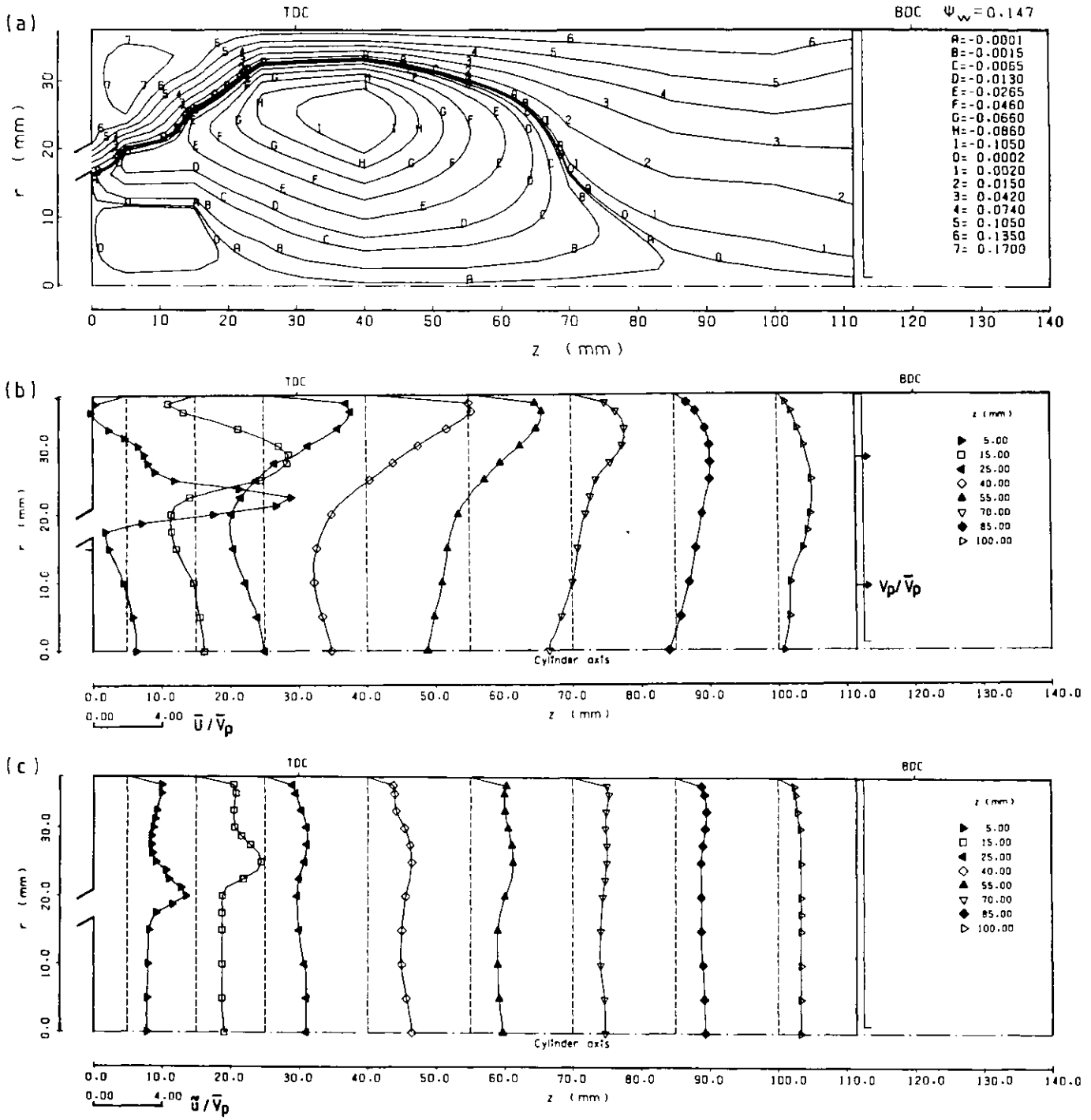

Figure 2.13 Streamline pattern and axial velocity profiles at Θ = 144 degrees;S = 90 mm,c = 30 mm.
(a) Streamline pattern (b) Mean velocity
(c) Rms velocity

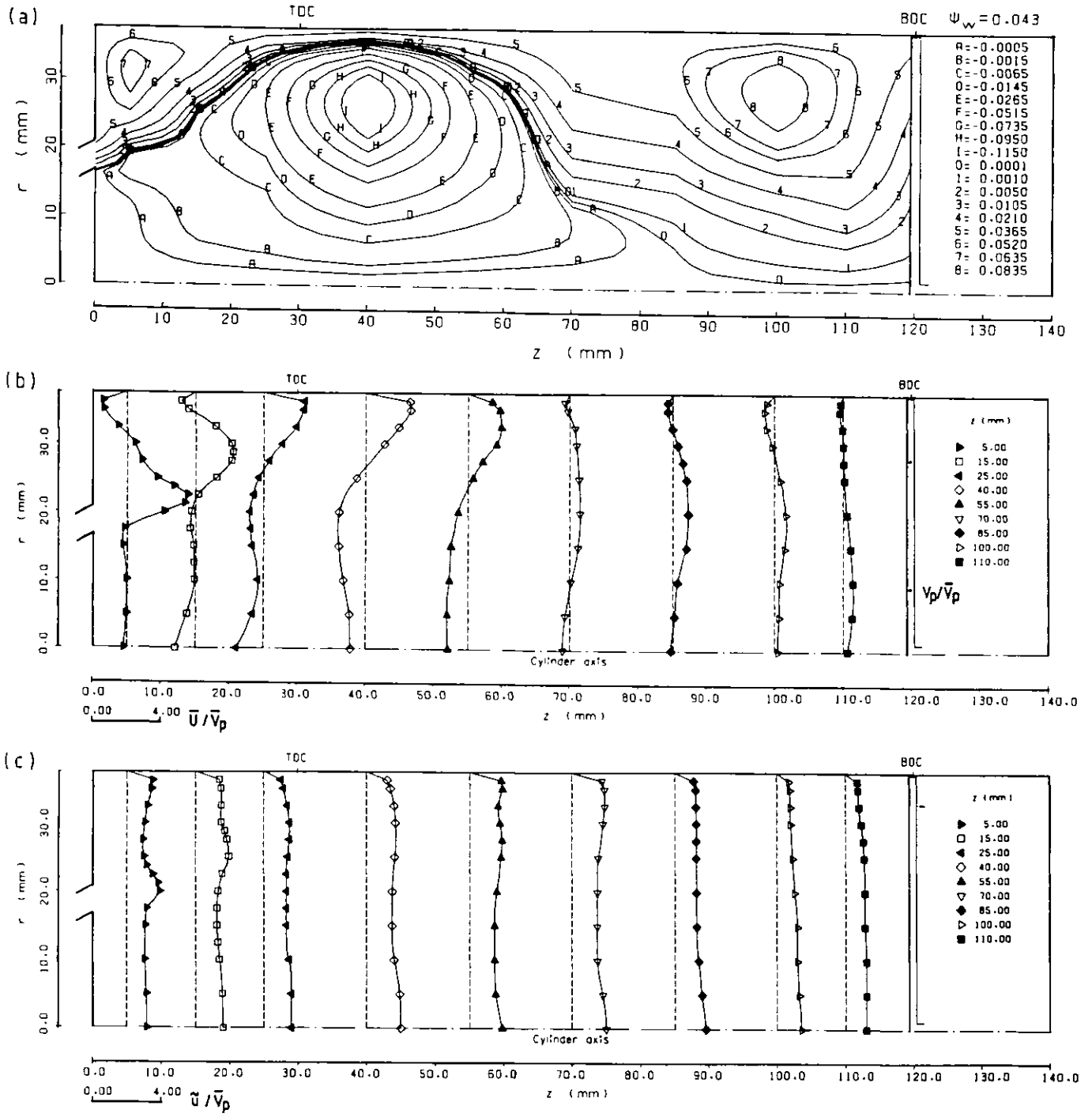

Figure 2.14 Streamline pattern and axial velocity profiles at Θ = 170 degrees; S = 90 mm, c = 30 mm.
(a) Streamline pattern (b) Mean velocity
(c) Rms velocity

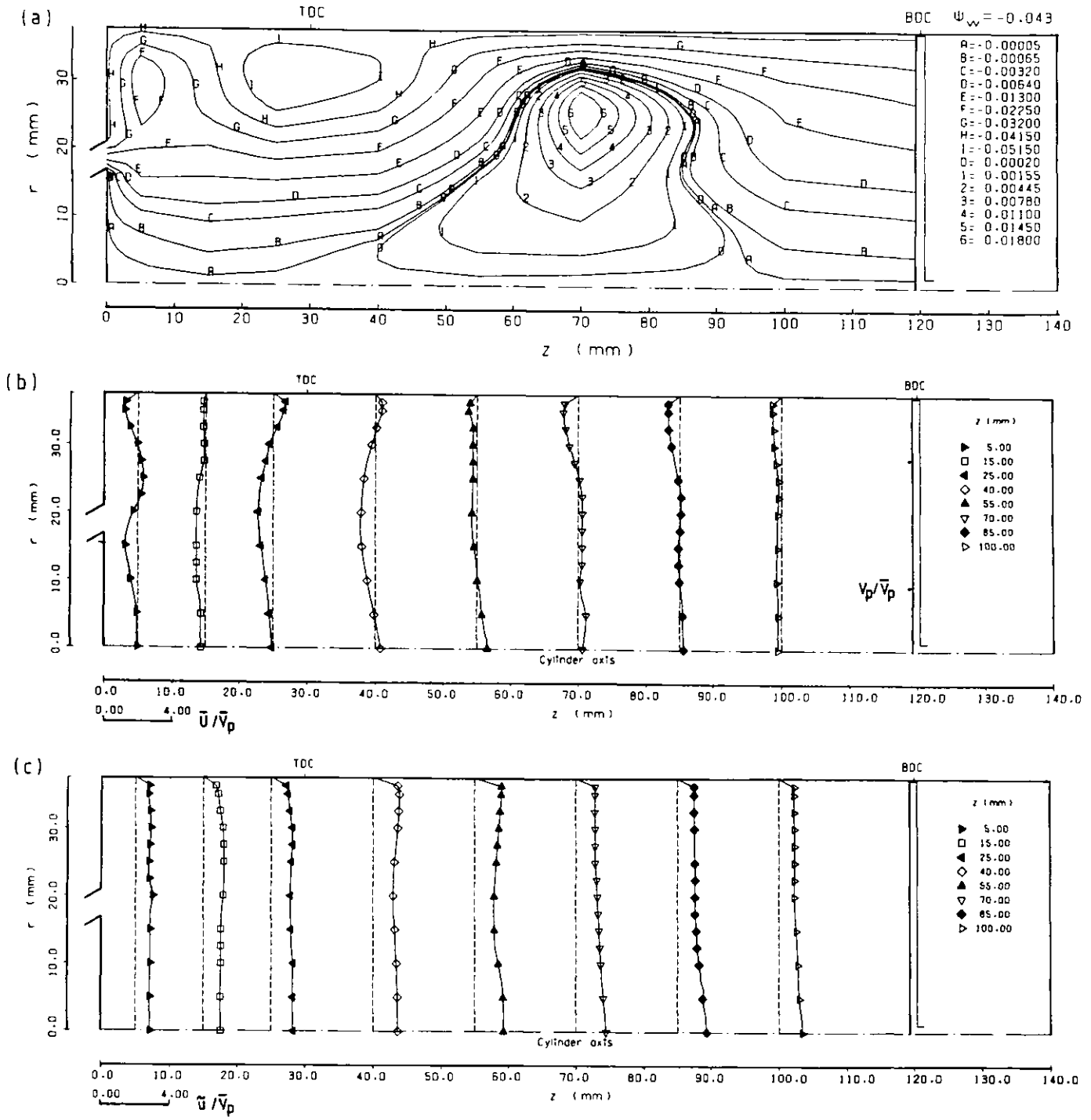

Figure 2.15 Streamline pattern and axial velocity profiles at θ = 190 degrees; S = 90 mm, c = 30 mm.
(a) Streamline pattern (b) Mean velocity
(c) Rms velocity

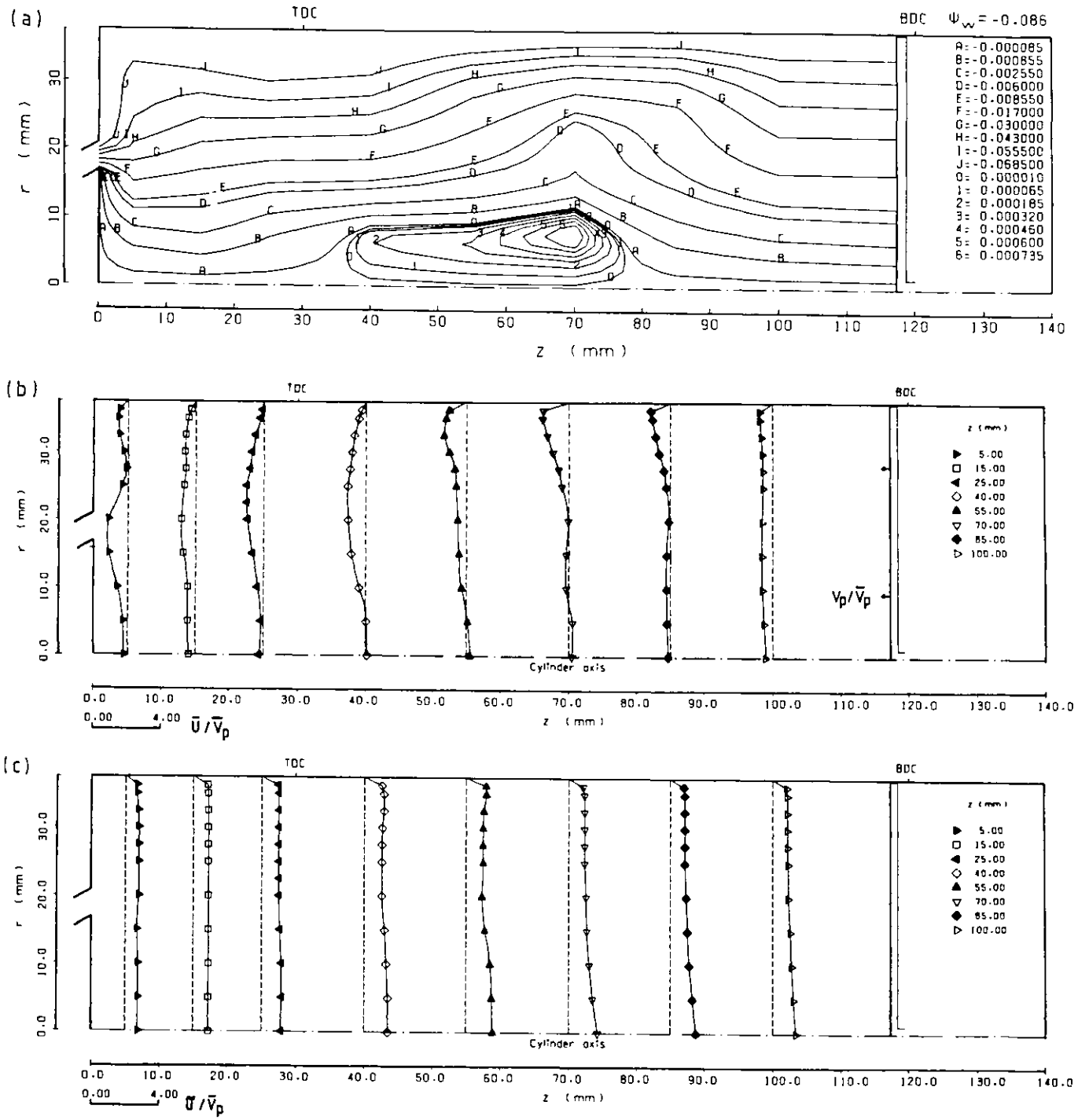

Figure 2.16 Streamline pattern and axial velocity profiles at θ = 200 degrees; S = 90 mm, c = 30 mm.
(a) Streamline pattern (b) Mean velocity
(c) Rms velocity

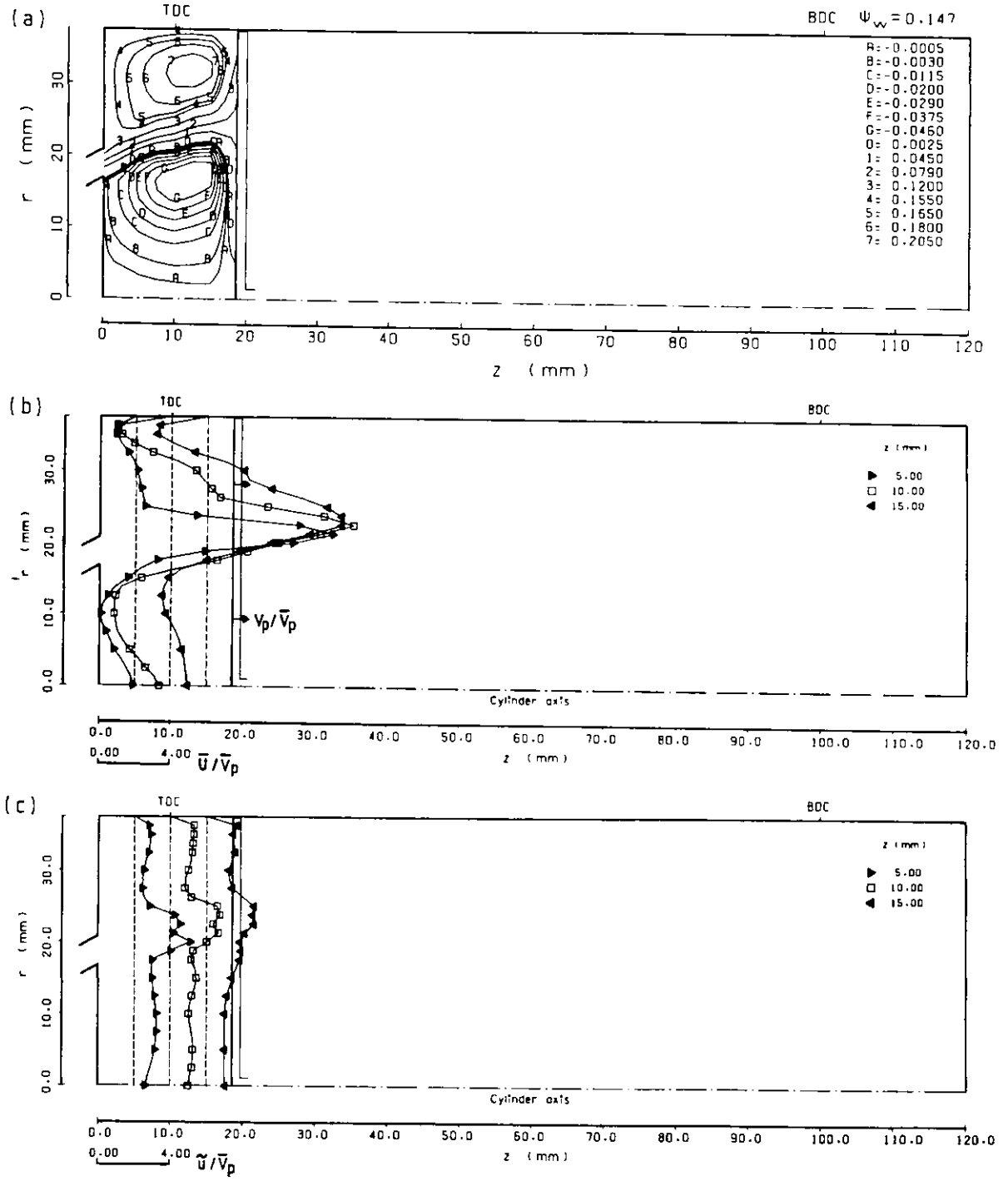

Figure 2.17 Streamline pattern and axial velocity profiles at Θ = 36 degrees; S = 90 mm, c = 10 mm.
(a) Streamline pattern (b) Mean velocity
(c) Rms velocity

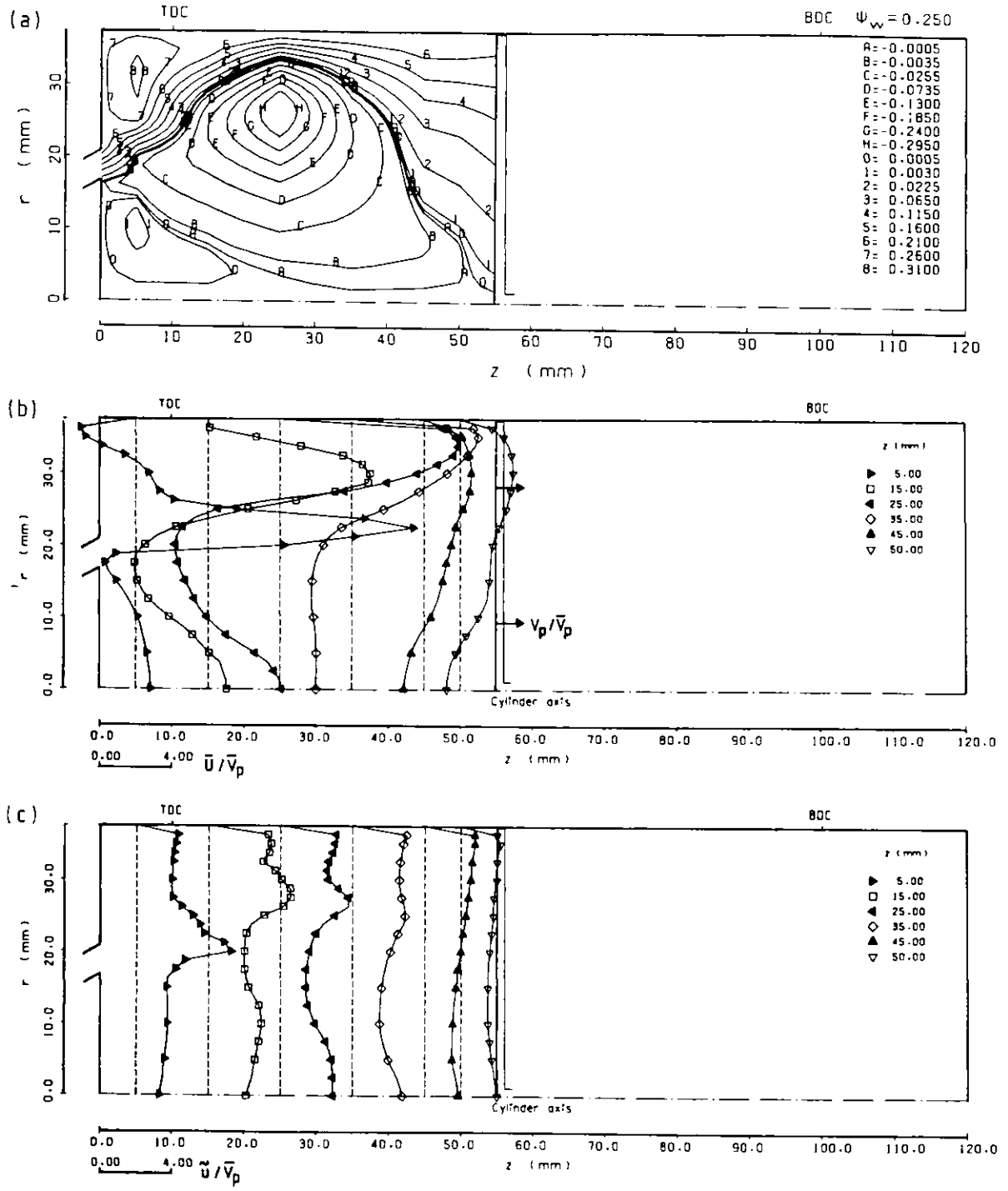

Figure 2.18 Streamline pattern and axial velocity profiles at Θ = 90 degrees; S = 90 mm, c = 10 mm.
(a) Streamline pattern (b) Mean velocity
(c) Rms velocity

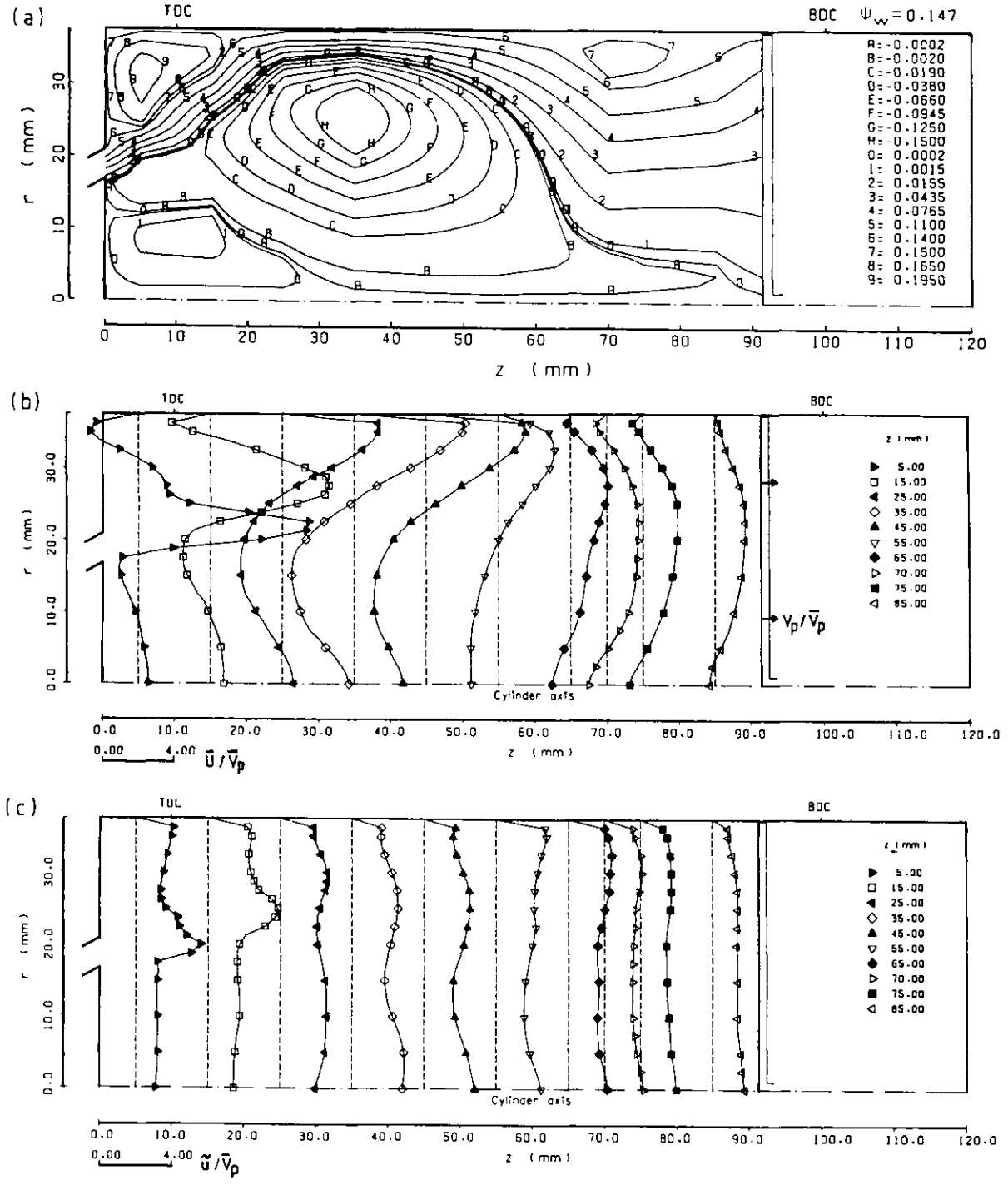

Figure 2.19 Streamline pattern and axial velocity profiles at Θ = 144 degrees; S = 90 mm, c = 10 mm.
(a) Streamline pattern (b) Mean velocity
(c) Rms velocity

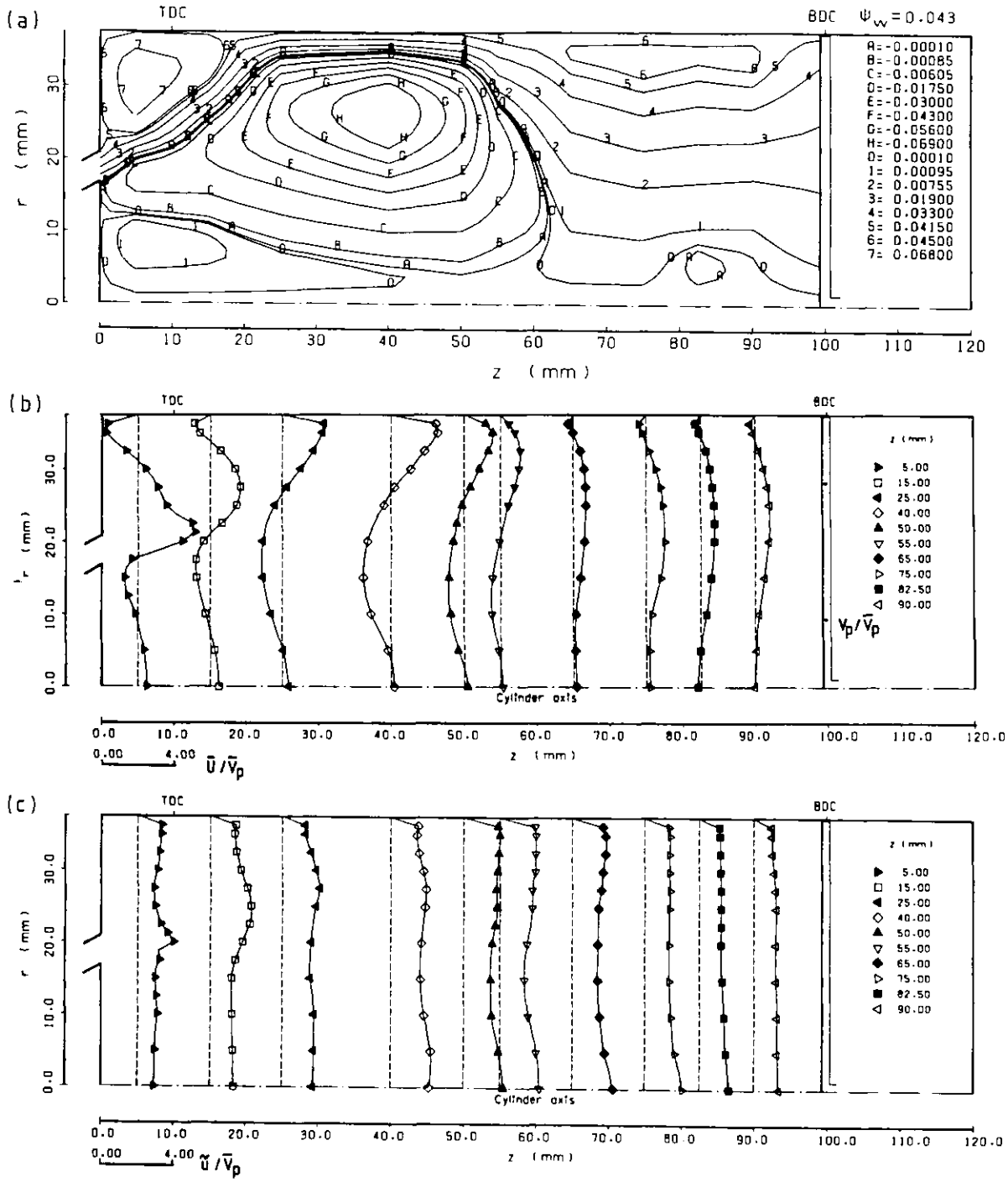

Figure 2.20 Streamline pattern and axial velocity profiles at Θ = 170 degrees; S = 90 mm, c = 10 mm.
(a) Streamline pattern (b) Mean velocity
(c) Rms velocity

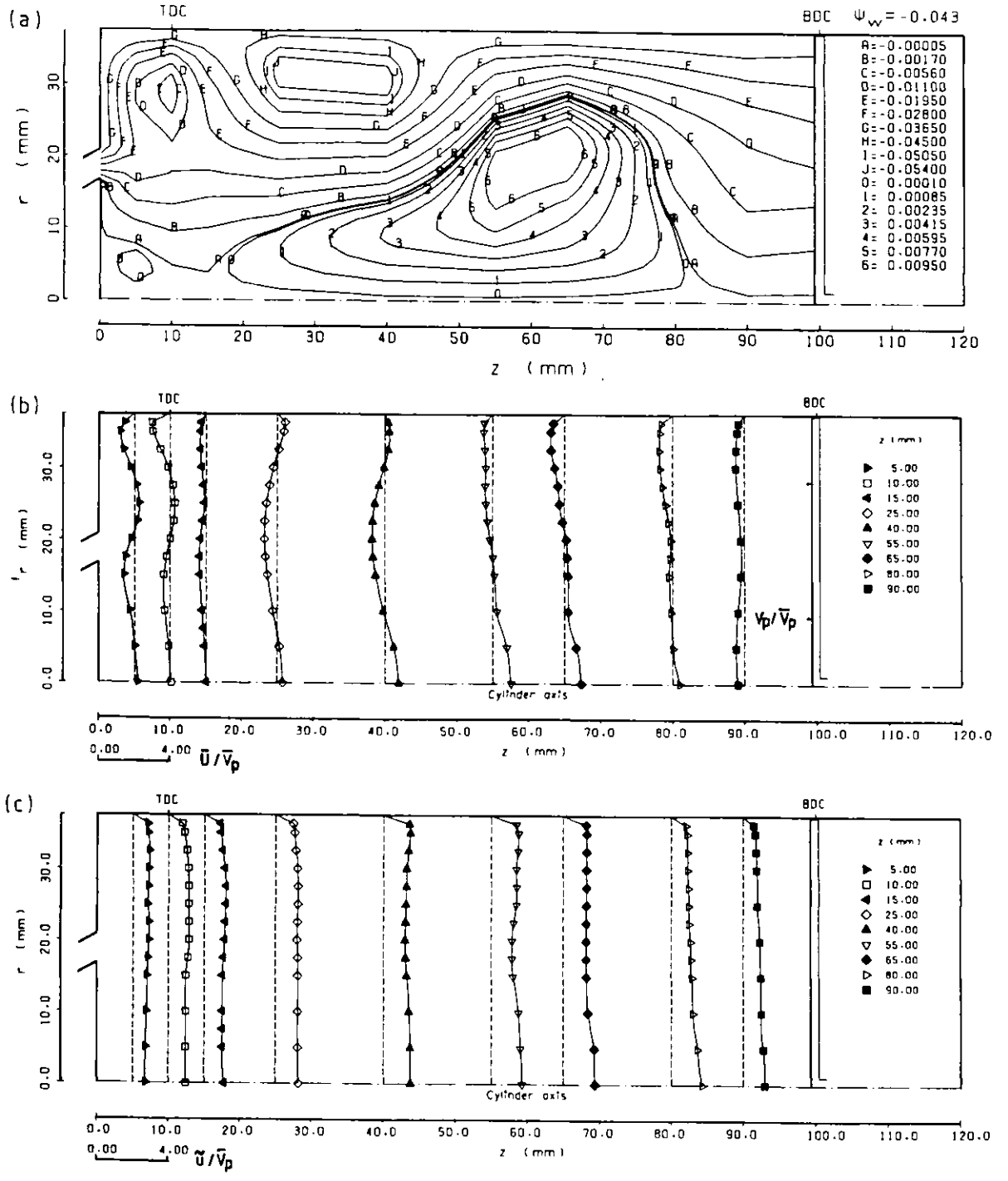

Figure 2.21 Streamline pattern and axial velocity profiles at Θ = 190 degrees; S = 90 mm, c = 10 mm.
(a) Streamline pattern (b) Mean velocity
(c) Rms velocity

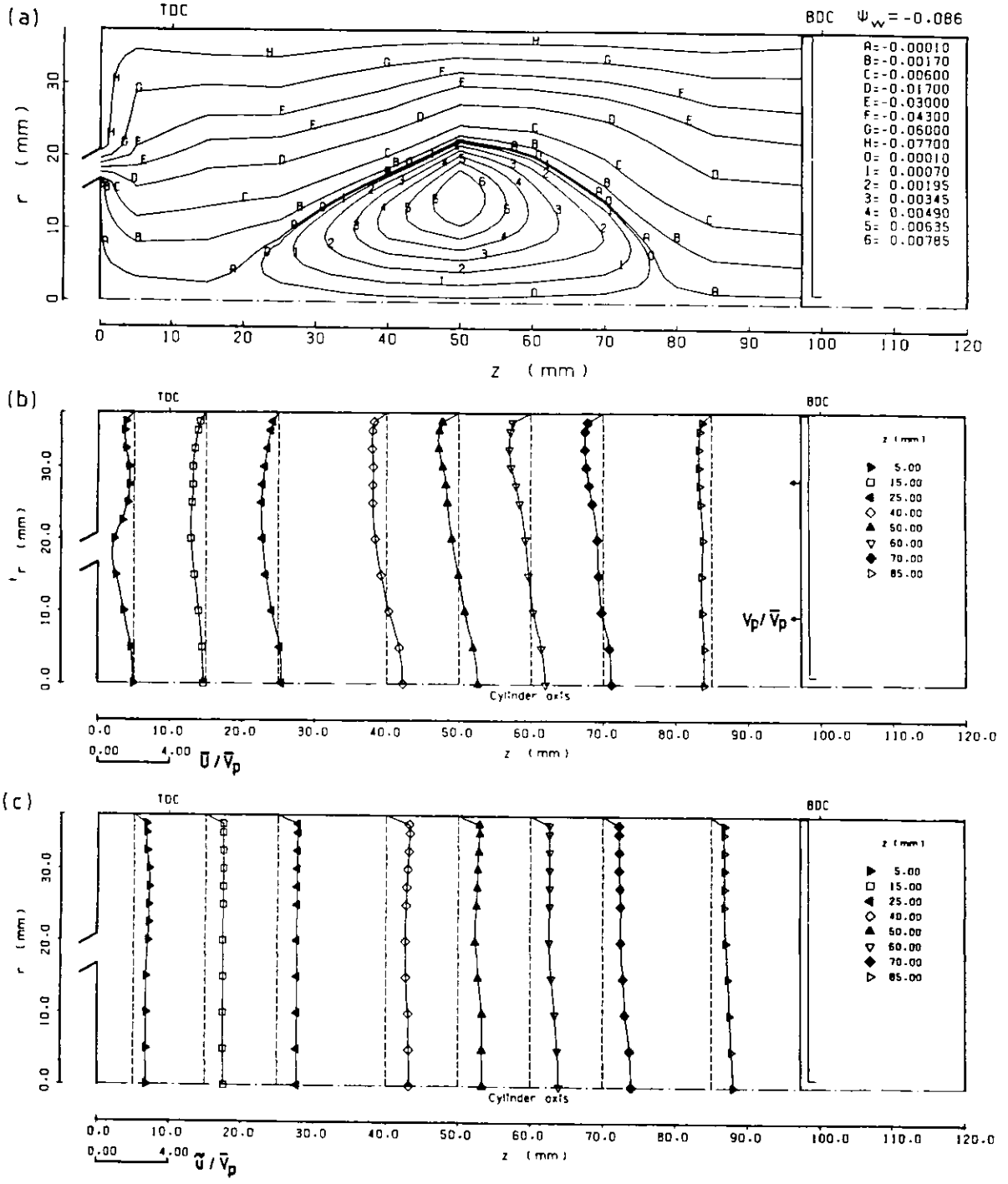

Figure 2.22 Streamline pattern and axial velocity profiles at Θ = 200 degrees; S = 90 mm, c = 10 mm.
(a) Streamline pattern (b) Mean velocity
(c) Rms velocity

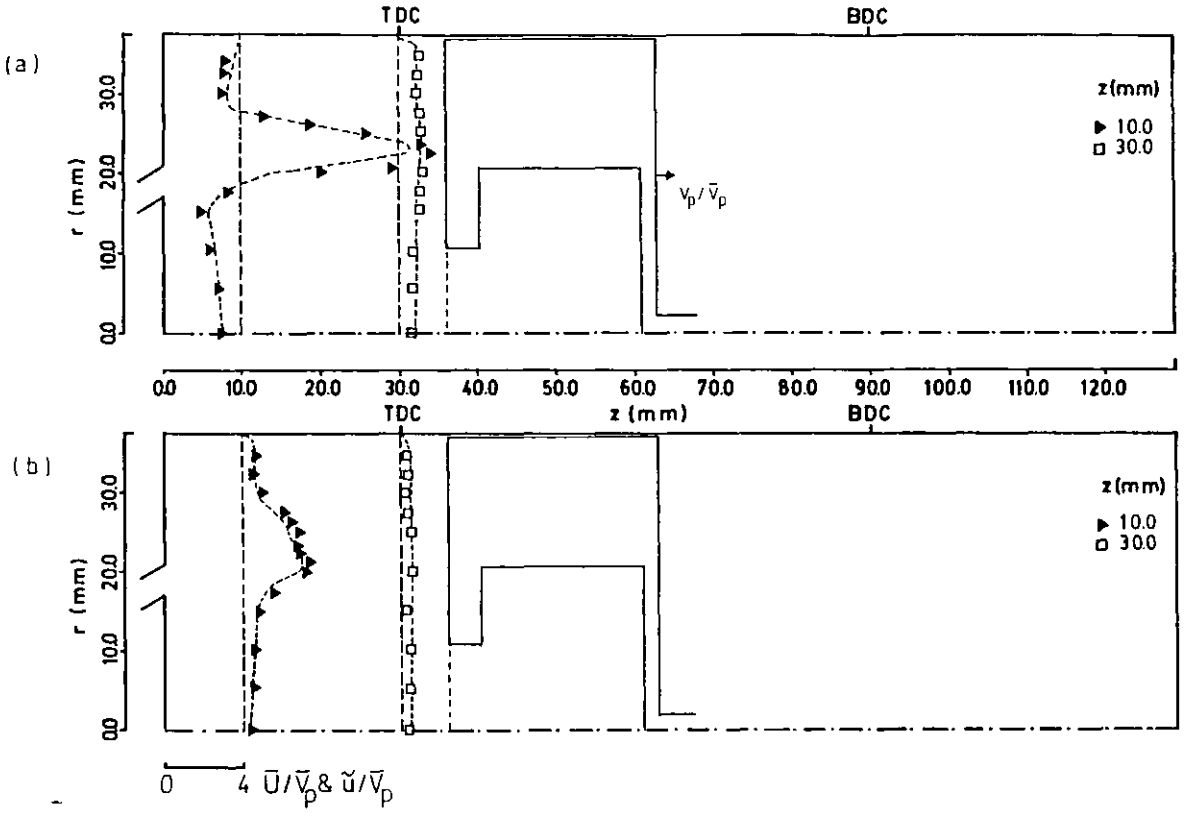

Figure 2.23 Axial velocity profiles at Θ = 36 degrees;
(▶ □) re-entrant type bowl & (-------) flat piston.
(a) Mean velocity (b) Rms velocity

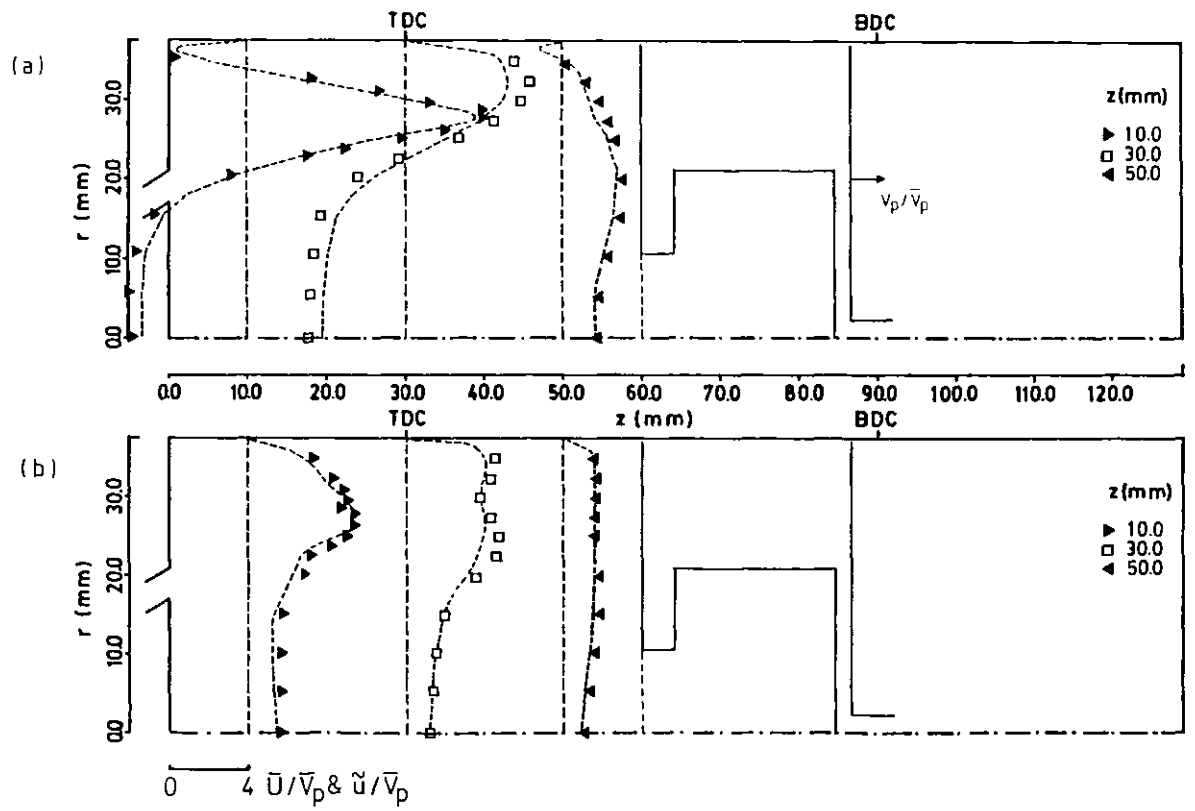

Figure 2.24 Axial velocity profiles at Θ = 90 degrees;
(▶ □ ◀) re-entrant type bowl & (-------) flat piston.
(a) Mean velocity (b) Rms velocity

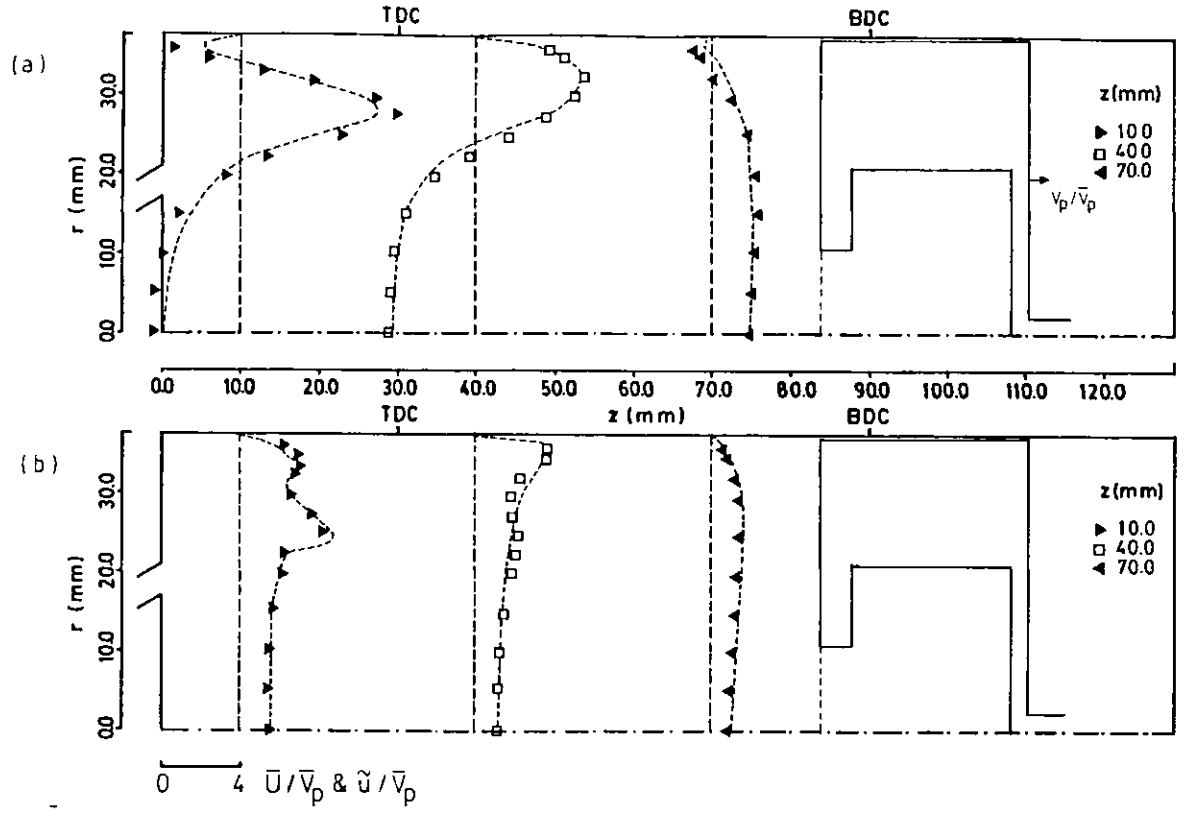

Figure 2.25 Axial velocity profiles at Θ = 144 degrees;
(▸ □ ◂) re-entrant type bowl & (-------) flat piston.
(a) Mean velocity (b) Rms velocity

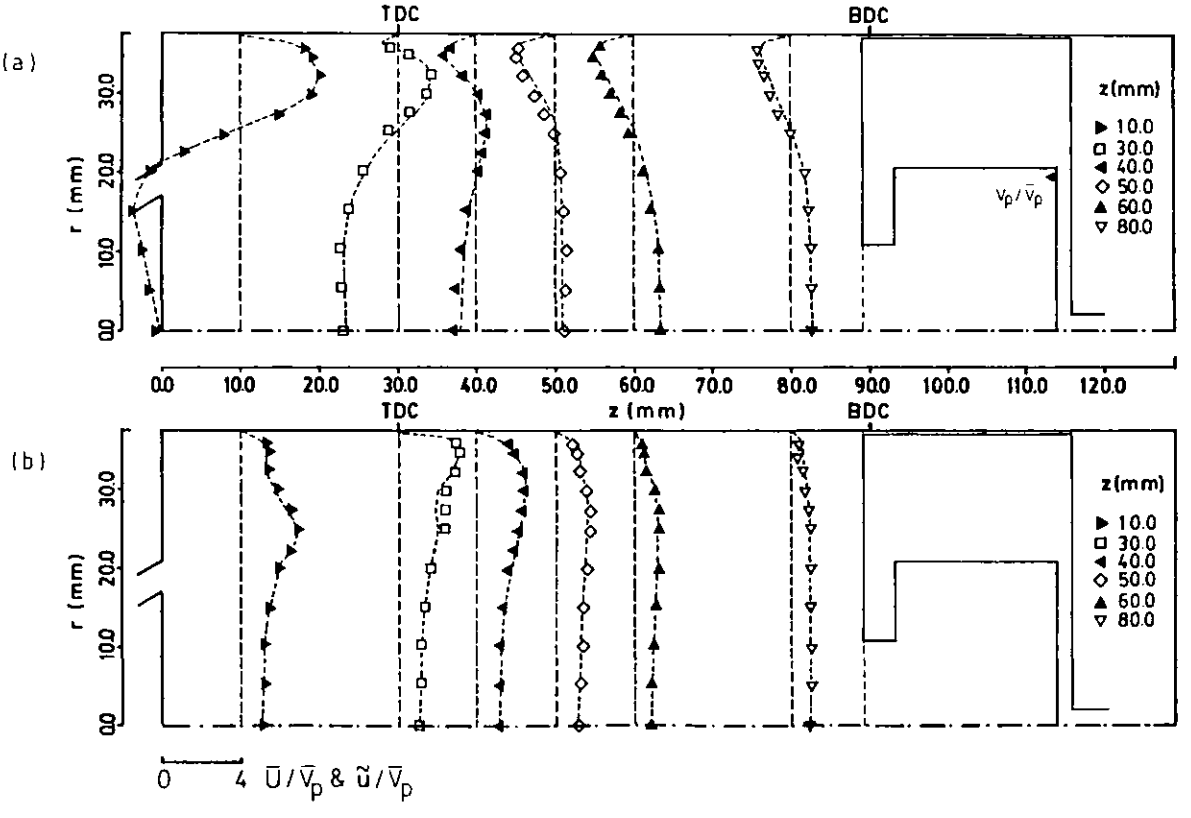

Figure 2.26 Axial velocity profiles at Θ =190 degrees;
(▸□◂◇▲▽) re-entrant type bowl & (------) flat piston.
(a) Mean velocity (b) Rms velocity

CHAPTER 3

IN-CYLINDER FLOW IN A FOUR-STROKE MODEL ENGINE

3.1 Introduction

This Chapter describes the experimental investigation of in-cylinder flow processes in a four-stroke motored model engine in the absence of both mixing and combustion processes. The work emphasises the compression and early expansion phases since they are of particular relevance to fuel-air mixing and subsequent combustion processes. Some of the important flow phenomena around TDC including swirl, which may persist from intake, and/or squish induced in late compression stages by virtue of the combustion chamber geometry, are examined. The effects of compression ratio and piston crown geometry are determined and related to those considered in the previous Chapter with respect to intake flow structures.

The merits of a well-balanced combination of swirl and squish on diesel engine performance has long been recognised, although not as well understood, as it improves the combustion through enhanced mixing of fuel and air. In recent years the designers of spark ignition engines have been encouraged to resort to swirl and/or squish to improve the combustion performance with high compression ratios and lean-burn arrangements (Nagayama et al, 1977). It is this popularity of swirl and/or squish which has motivated the work presented in this Chapter in order to increase further understanding of these late compression flow processes and their interaction with each other.

The description of the model engine is given in the following Section together with that of the measurement techniques for velocity and pressure. The detailed analysis of some relevant uncertainties, such as crank angle broadening, is also included in this Section. The results are presented in Section 3.3 followed by discussion in Section 3.4 which, in addition includes an

assessment of relevant in-cylinder flow calculations. The Chapter concludes by summarising the main findings in Section 3.5.

3.2 Experimental System

3.2.1 Flow Configurations

A schematic diagram of the four-stroke model engine is shown in Figure 3.1. It was built with similar design features as those of the two-stroke model engine reported in Chapter 2. The plexiglass cylinder of 75.8 mm bore had a wall thickness of 12.7 mm which allowed the engine to operate with moderate compression ratios of up to 7. The piston was made from duraluminium with a plexiglass crown which could be removed and interchanged to alter the compression ratio and piston crown geometry. The piston was reciprocated inside the horizontal cylinder in near simple harmonic motion by an electric motor, and crank and connecting rod mechanism. The clearance gap of 0.4 mm between the piston and the cylinder wall was sealed by a pair of rings constructed from graphite-reinforced plastic and by PTFE rings which were also used as guides, bearing most of the wear. The plastic rings were shaped such that their tips were pressed against the wall during compression to minimise leakage. Cooling water coils were wound around the lower region of the cylinder to maintain outside wall temperatures below 40^{o}C. A gravity-fed silicone oil lubricator was installed on the cylinder to minimise, together with water cooling, friction and wear. The motor speed was 1500 rpm but was geared down by means

of a pulley system to result in a constant engine speed of 200 rpm as in the case of the non-compressing engine.

For a crank and connecting rod mechanism the variation of piston speed with crank angle is given by

$$V_p = \frac{S\omega}{2}\left(\sin\theta + \frac{S \sin 2\theta}{2\sqrt{4\, l_c^2 - (S \sin\theta)^2}}\right) \qquad (3.1)$$

where l_c is the connecting rod length. Both the maximum and mean piston speeds (V_{pmax} and $\bar{V}_p$ respectively) were the same as in the case of simple harmonic motion and given by equations 2.2 and 2.3 respectively, as described in sub-section 2.2.1. The variation of the distance between the piston and the head, z_p, with crank angle is given by

$$z_p = c + \frac{S}{2}(1 - \cos\theta) + l_c\left(1 - \sqrt{1 - \left(\frac{S}{2l_c}\sin\theta\right)^2}\right) \qquad (3.2)$$

An axisymmetric single valve with 60 degree seat angle was used to intake and exhaust air seeded with silicone oil. A half-speed shaft drove two cams which operated the valve as shown in Figure 3.1. Both cams had identical profiles and were set with respect to crank angle such that the valve opened for intake at 6 degrees BTDC* and closed at 44 degrees ABDC and then re-opened for exhaust at 44 degrees BBDC and closed at 6 degrees ATDC* (see Figure 3.2). The main characteristics of the model engine are summarised in Table 3.1.

---

* These angles are extrapolated from intake and exhaust lift diagrams since the single valve used did not close at intake/exhaust TDC.

Table 3.1

Main characteristics of four-stroke model engine

Engine speed, rpm	200
Cylinder bore, mm	75.8
Stroke, mm	94
Compression ratios	3.5, 6.7
Connecting rod length , mm	363.5
Valve diameter, mm	34
Valve seat angle, degrees	60
Valve opening for intake, degrees	6 BTDC
Valve closing for intake, degrees	44 ABDC
Valve opening for exhaust, degrees	44 BBDC
Valve closing for exhaust, degrees	6 ATDC
Maximum valve lifts, mm	7.3, 8.0
Dimensionless valve lifts	0.21, 0.24

Two compression ratios (CR) of 3.5 and 6.7 were employed in conjunction with various axisymmetric piston configurations which include a flat piston as a disc chamber and a number of cylindrical bowls with and without a rectangular-sectioned lip as shown in Figures 3.3 and 3.4. The two piston bowl configurations were selected as idealised representations of the open and re-entrant combustion chambers widely used in diesel engines. Two similar cam profiles were used with the two compression ratios. Although it was intended to have identical profiles, the one used with the higher compression ratio resulted in a maximum valve lift of 8.0 mm (a dimensionless lift of 0.24) as opposed to the 7.3 mm (a dimensionless lift of 0.21) achieved with the cam used in the

lower compression ratio case, as shown in Figure 3.2. The valve timing, however, was identical in both cam profiles. The geometric details of the piston crown configurations used with the two compression ratios are given in Table 3.2.

Table 3.2

Geometric details of piston crown configurations

	CR = 3.5	CR = 6.7
Flat piston:		
Diameter, mm	75	75
Clearance, mm	37	16.5
Cylindrical bowls:		
Diameter, mm	43	47
Depth, mm	15, 23	41
Bumping clearance, mm	32.5, 30	0.6
Re-entrant bowls:		
Diameter, mm	43	47
Depth, mm	23	40
Entry diameter, mm	16.5	23
Bumping clearance, mm	29.5	0.6

Swirl was induced, when required, in the same way as in the two-stroke engine (sub-section 2.2.1) by means of 30 degree vanes incorporated into the inlet port as shown in Figure 3.1. Swirl ratio S_r was used as a measure of in-cylinder swirl instead of swirl number S_n which is defined by equation 2.5 and varies during intake as a consequence of the operating valve; for the definition of swirl ratio see Appendix 3.1.

3.2.2 Pressure Measurements

The compression ratios of 3.5 and 6.7 corresponded to effective compression ratios of 3.2 and 5.5 respectively due to the reductions in compressed volume of air associated with the closure of the intake valve at 44 degrees ABDC and with the clearance gap between the piston and cylinder wall. The pressure inside the cylinder was monitored by a piezoelectric pressure transducer (Kistler 6121A) and a charge amplifier (Kistler 5007). The transducer was calibrated on a dead weight calibrating machine, yielding 1.0 Volt per bar, before its installation flush with the cylinder's inner wall surface. The pressure traces were monitored continuously on an oscilloscope as a check on the satisfactory sealing of the pressure rings and indicated a maximum value within 10% of that calculated assuming isentropic compression of air and using the effective compression ratio in question. The difference between the theoretical and measured values can be attributed to friction and heat losses through the walls.
Figure 3.2 shows the variation of the in-cylinder pressure with crank angle for the two compression ratios together with the valve lift and engine speed diagrams. The pressure diagrams were obtained by using a pulse from an optical shaft encoder to trigger the output from the charge amplifier; the triggered output was displayed on an oscilloscope to provide the pressure information.

3.2.3 Laser Doppler Anemometer

The laser Doppler anemometer comrpised a similar optical arrangement and an identical signal processing system to those described in the previous Chapter (sub-section 2.2.2). The data processing system was

also identical to that used for the measurements in the two-stroke cycle model engine and is described in detail in sub-section 2.2.4. The optical system was modified by reducing the probe volume dimensions, in particular its length l_p, to minimise the effect of velocity gradient broadening. This was achieved by employing a shorter focal length, f_1, for the focussing lens L_1 (see equations 2.6 and 2.8). The principal characteristics of the laser Doppler anemometer are summarised in Table 3.3.

Table 3.3

Principal characteristics of laser Doppler anemometer

Half angle of beam intersection, degrees	6.4
Fringe spacing, μm	2.84
Length of probe volume at e^{-2} intensity level, mm	0.52
Diameter of probe volume at e^{-2} intensity level, μm	58
Number of fringes within e^{-2} intensity level	21
Frequency shift, MHz	1.83

3.2.4 Measurement Procedure and System Performance

The optical system was mounted on a horizontal traversing table and could be traversed across horizontal and vertical diameters and parallel to the axis of the engine cylinder. For the axial velocity component, the measurements were obtained on a horizontal diameter with

the beams in the horizontal plane, and in the vertical plane to provide the tangential (swirl) component of the velocity. The radial velocity measurements, on the other hand, were obtained on a vertical diameter with the beams in the vertical plane. Due to changes in the optical path of the laser beams and the half angle of intersection from refractions at the curved optical boundaries of the piston bowl configurations and the cylinder, appropriate corrections were made to the measurement locations and velocity values according to the procedure described in Appendix 3.2.

The signal-to-noise ratios were generally lower, particularly inside the piston bowls, than those encountered in the two-stroke model engine (sub-section 2.2.5) mainly due to the difference in wall thickness. An increase in the scattered-light intensity was observed in the expansion stroke due to water-vapour condensation associated with the humidity of the intake air. The Doppler signals produced by the artificially-induced silicone oil particles were swamped, for a short crank angle increment in the expansion stroke, by those from the water droplets. However, the signals from the condensate were processable by the counter, although the size and thus dynamic behaviour of the droplets was both time-varying and unknown; the implications for mean and rms values were, however, negligible.

A crank angle window of 10 degrees was used and corresponded to 14 pulses of the shaft encoder which was geared down to 2 to 1 to distinguish between the four strokes of the engine cycle. For each measurement within this crank angle window, sample sizes in the range of 400-1500 were obtained depending on the location in the cycle and inside the piston bowl and cylinder to provide

ensemble-averaged mean and rms velocities. The data acquisition rate was twice as low as that in the two-stroke case due to the operation of the encoder on the half-speed shaft.

3.2.5 Measurement Uncertainties

The major sources of error incurred in the measurements are discussed in the previous Chapter (see sub-section 2.2.6). It was concluded that the uncertainties arise mainly from broadening effects due to velocity gradients in both space and time. The effect of the crank angle broadening is further discussed here and quantified for various window sizes (5, 10 and 20 degrees) by comparing the results obtained with each window to those with the 1.5 degrees , which are considered to be error free.

The temporal profiles of the axial rms velocity obtained with various windows are presented in Figure 3.5. The mean velocity profiles are not shown because, as expected, there were no discernible differences during most of the cycle. The maximum error associated with the rms velocities obtained with $\Delta\theta$ = 20 degrees and compared to those with $\Delta\theta$ = 1.5 degrees is shown to be very large (factor of 5) at the crank angle location of 10 degrees reducing to less than 10% in the rest of the stroke with an increase to about 20% near BDC. During compression all window sizes give identical rms values. The mean velocities measured with larger than 1.5 degree windows are also in error during the first 30 degrees of intake by, for example with $\Delta\theta$ = 20 degrees, a factor of 2 at θ = 10 degrees reducing to almost insignificant levels in the rest of the cycle.

The validity of the theoretical analysis of Morse (1977), equations 2.25 and 2.26, has been verified by comparing the measured error to that determined from the analysis based on the measured temporal profiles of both the mean velocity and sample rate with $\Delta\theta$ = 1.5 degrees. The results showed, within experimental accuracy, a reasonable

agreement between the measured and theoretical values. The magnitude of the errors involved in the rms velocities indicates that during the first and last 30 degrees of the intake stroke a crank angle window of 10 degrees is not acceptable and a smaller window is required. Use of a 5 degree window, as suggested by Rask (1981), is an overall better choice but does not alleviate the problem early in intake where, for example at θ = 10 degrees, it still results to an overestimation of the rms values by about 20%.

Figure 3.6 shows the variation of sample rate with crank angle for $\Delta\theta$ = 1,5, 5, 10 and 20 degrees. The profile obtained with $\Delta\theta$ = 1.5 degrees has been used in the theoretical analysis together with the corresponding mean velocity profile to provide the mean velocity and sample rate gradients on which corrections are based. Minimum data acquisition rates have been observed near TDC and BDC of intake with magnitudes of 1 sample/10 sec.. However, during the compression stroke sample rate approaches asymtotically its maximum value due to the increase of the number of particles per unit volume. Although the variation of sample rate with window size should be taken into account, the decision on the optimum crank angle window in an engine application should be based on the maximum experimental uncertainty that can be tolerated and on the expected magnitudes of the temporal velocity graidents. For the present engine configurations, however, the crank angle window of 10 degrees was found to be a good optimum between accuracy and data acquisition rate.

In the light of the above discussion the overall errors in the measurements in the four-stroke engine is expected to reduce from those stated in the previous Chapter, mainly due to the smaller velocity gradients encountered in the compression and expansion strokes as

well as to the reduction made in the probe volume dimensions. The uncertainties in the mean and rms velocity values were estimated to be 3% and 7% respectively in most regions of the flow and, therefore, are not expected to influence the discussion and conclusions reached later in this Chapter.

3.3 Results

3.3.1 Introduction

The results are presented in the form of radial, axial and temporal profiles throughout the four strokes of the engine cycle with more detail of the flow given in the compression stroke, particularly during late-compression. All mean velocities ($\bar{U}$, $\bar{V}$, $\bar{W}$) and their corresponding rms values ($\tilde{u}$, $\tilde{v}$, $\tilde{w}$) are normalised by the mean piston speed, $\bar{V}_p = 0.63\ ms^{-1}$. In most of the figures, radial or axial profiles of the velocity are presented with an outline of the cylinder and piston configuration, the piston position and the normalised instantaneous piston speed ($V_p/\bar{V}_p$) corresponding to the crank angle under consideration. The Reynolds number based on the maximum piston speed, cylinder bore and atmospheric density was calculated to be 5.2×10^3.

3.3.2 Compression Ratio of 3.5

Flat Piston

The temporal profiles of the mean and rms of the axial and swirl velocity components obtained at a location near

the cylinder head and wall (z = 15 mm, r = 25 mm) and throughout the four-stroke cycle, are shown in Figures 3.7 and 3.8, respectively. During the intake stroke maximum mean velocity values of about 12 $\bar{V}_p$ and 3 $\bar{V}_p$ were measured for the axial and swirl velocity components respectively as shown in Figure 3.7. Axial mean velocities decay rapidly and attain very small values during the compression stroke. Swirl velocities, on the other hand, do not decay as fast and persist through to TDC of compression. In the expansion stroke the decay of the mean motion in the axial plane and the persistence of the swirl field are both interrupted by the valve opening at about Θ = 500 degrees, which causes a rapid surge of the fluid in the port into the cylinder. The turbulence follows similar trends to those of the mean motions indicating the close correspondence between the inlet jet flow and turbulence. During the compression stroke, both rms values are almost identical with levels of about 0.5 $\bar{V}_p$. The increased magnitudes of turbulent velocities observed later on in expansion are associated with the production of turbulence due to the fluid surge at exhaust valve opening (EVΘ). These magnitudes decay steadily during the rest of the stroke and result in a small carry over of turbulent fluctuations to the following cycle.

The radial profiles of the axial mean velocity obtained at the crank angle locations of 90, 216, 270, 324, 380, 450 and 630 degrees are shown in Figure 3.9 and those of the corresponding rms velocity in Figure 3.10.

The mean velocity profiles obtained at mid-intake and presented in Figure 3.9a show similar trends to those observed in the previous Chapter, with an open valve and in the absence of compression (see sub-section 2.3.3). A high velocity jet is drawn in by the piston and

generates turbulence near the valve opening, Figure 3.10a, due to the shearing action between the jet and the slower moving fluid inside the cylinder. The velocity peaks in the mean and rms profiles, however, have moved towards the axis in the present case due to the variation of the lift, associated with the operating valve, and consequently of the jet trajectory. The results of Gany et al (1980) also suggest that there is no significant difference in the mean velocity profiles during intake for the cases of an operating valve with a compression ratio of 7 and a valve with constant lift at 31 rpm.

During the early part of the compression stroke and just before IVC, the similarity between the velocity profiles for the compressing (Figures 3.9b and 3.10b) and non-compressing cases is maintained with a small reduction in the mean values due to the initiation of compression. At mid-stroke with the intake valve already closed, Figure 3.9c, the mean flow decays and a vortex is present near the head which may have persisted from intake. Figure 3.10c shows that the intake-generated turbulence has decayed considerably and become near-homogeneous with levels of about 0.5 $\bar{V}_p$. Close to TDC, at θ = 324 degrees, the mean velocity profiles have been further reduced in magnitude and tend to become uniform with higher velocities of the order of 1.0 $\bar{V}_p$ observed close to the piston and lower ones of about 0.3 $\bar{V}_p$ near the head. As a consequence of further compression, the vortex observed behind the valve at mid-stroke has disappeared. The rms levels remain uniform and of the same magnitude as at mid-compression with no further decay of turbulence. The results obtained are in qualitative agreement with other investigations, such as Lancaster (1976) and Rask (1979), in that the intake-generated mean motion and turbulence decay gradually and the near-homogeneous turbulence

remains constant during most of the compression stroke.

At the beginning of the expansion stroke, Figure 3.9e, as the piston reverses its direction a counter-rotating vortex is formed and occupies most of the flow space. The mean velocities have decreased in magnitude but changed in direction near the wall relative to those at θ = 324 degrees. The rms velocities, as Figure 3.10e shows, have also decreased considerably to about 0.3 $\bar{V}_p$. At mid - expansion, the fluid has accelerated following the piston motion with considerably higher velocities of the order of 1.5 $\bar{V}_p$ close to the piston. However, the turbulence continues to decay to a level of about 0.2 $\bar{V}_p$, according to Figure 3.10f.

The axial flow structure in the exhaust stroke of the non-compressing arrangement was investigated in Chapter 2, and it was shown that flow structures created during intake are destroyed before the next intake stroke. The same trends are observed here as indicated in Figure 3.9g. In the exhaust stroke the fluid shows a tendency to move directly from the piston face towards the open valve. As Figure 3.10g shows, the turbulent velocity values have increased in comparison to those at mid-expansion due to the generation of turbulence associated with the sudden-incoming flow at EVO.

The swirling motion prevailing in the normal plane is presented in Figure 3.11 which shows both the swirl mean and rms velocity profiles obtained close to the head at various crank angle locations during the four strokes of the engine cycle. The mean profiles at θ = 36 and 90 degrees, shown in Figure 3.11a and b respectively, are characterised by a region of high velocity near the wall, corresponding to the spiralling inlet jet motion,

and a region of low velocity away from the wall, corresponding to the wake formed behind the valve. The spiralling motion of the jet does not exhibit characteristics associated with either a solid body rotation or free vortex. During the compression stroke, contrary to the supression of the mean flow in the axial plane, the swirling flow is conserved and has organised into near solid body rotation as shown in Figures 3.11c - e. The swirl ratio was calculated according to the procedure described in Appendix 3.1 by integrating the swirl profile at θ = 360 degrees and was found to be 1.9 ($\pm$ 5%). The correspondence of this swirl ratio to that deduced from the measurements of Renshaw and Wigley (1979) shows that the 30 degree swirl vanes produce swirl levels which are similar to those obtained with directed ports in production diesel engines. The near solid body rotation persists through the expansion stroke as indicated in Figures 3.11 f and g. During the exhaust stroke the mean profile exhibits a peak near the wall as the fluid moves out of the cylinder and through the open valve. The velocity peak which is observed near the wall during intake and shown in Figures 3.11a and b is, therefore, most likely to be associated with the residual swirl effect from the previous cycle. The swirl rms velocities have similar profiles to those of the axial ones and tend to become homogeneous and isotropic during the compression stroke.

Cylindrical and Re-entrant Bowls

The axial mean and rms velocity profiles obtained at 270 and 324 degrees during compression and at 380 and 450 degrees in the expansion stroke are shown in Figures 3.12 and 3.13 for the deep cylindrical bowl of 23 mm depth and in Figures 3.14 and 3.15 for the shallow

cylindrical bowl of 15 mm depth. Figures 3.16 and 3.17 present the axial mean and rms velocity profiles, respectively, obtained at the same crank angle locations with the re-entrant type piston bowl.

As pointed out in the previous Chapter, the piston crown configuration does not have a significant effect on the flow patterns and turbulence levels in the absence of compression. Therefore, detailed investigation of the intake stroke was not carried out here and the conclusions of Chapter 2 are considered to remain valid due to the similarities of the operating and geometric boundary conditions.

During the compression stroke at θ = 270 degrees, the mean velocity values, Figure 3.12a, are generally lower than those obtained with the flat piston and presented in Figure 3.9c; the rms velocity values, however, remain almost the same. Later on in the stroke, at θ = 324 degrees and as shown in Figure 3.12b, the mean values are still lower although only in the region close to the cylinder axis. The corresponding rms velocity profiles, Figure 3.13b, show similar trends and magnitudes to those with the flat piston. Results obtained with the shallow cylindrical bowl show almost identical mean and rms profiles at θ = 270 and 324 degrees to those in the case of the deeper bowl. The addition of a lip to the deep bowl causes small differences in the mean flow at mid-compression, Figure 3.16a, but significant ones at the second half of the stroke especially in the region close to the cylinder axis, due to inward bulk motion of the air towards the piston bowl, Figure 3.16b. The rms velocities observed outside the bowl, however, are not affected by the re-entrant bowl geometry. Preliminary results which are not presented here and obtained with

a larger entry diameter showed small quantitative differences only in the mean velocities in the vicinity of the bowl entry plane.

In the expansion stroke the influence of the bowl configuration on the in-cylinder flow outside the bowl becomes even more important. Comparison between the results obtained with the deep cylindrical bowl and flat piston shows small differences in both the mean flow and turbulence. The results obtained with the shallow cylindrical bowl confirm the observation made previously about the insignificant effect of the bowl depth. The re-entrant bowl, however, results in reverse squish effect. As Figures 3.16c and d and 3.17 c and d show, the fluid which was forced inside the bowl during the compression stroke expands to form a jet with consequent increase in velocities near the axis and in the associated turbulence levels. At Θ = 380 degrees the maximum mean velocity of about 1.0 $\bar{V}_p$ was measured near the piston and increases to about 3 $\bar{V}_p$ by mid-expansion. The rms values follow the trend of the mean velocities reaching a peak of about 1.3 $\bar{V}_p$ at Θ = 450 degrees in the region close to the bowl entry. Comparison with the results of the flat piston shows that the re-entrant bowl configuration increases the turbulence levels by a factor of 3 in the region close to the axis. Preliminary results with a larger entry indicated that the effect of entry diameter is only quantitative with decreased velocities without altering the main trends of the flow.

During the exhaust stroke, with the valve open, the flow is not expected to be influenced by the bowl configuration according to the findings of the previous Chapter. Therefore, the results obtained with the flat piston, Figures 3.9g and 3.10g, also apply in the cases of the cylindrical and re-entrant type piston bowls.

3.3.3 Compression Ratio of 6.7

Flat Piston

Temporal profiles of the mean and rms values of the three velocity components obtained at a location near the cylinder head are presented in Figures 3.18 and 3.19, respectively. The axial and radial mean velocities measured during intake steadily decay to insignificant levels during the compression stroke, as indicated in Figure 3.18. In agreement with the lower compression ratio case presented above, the only mean motion which persists during compression is the swirl in the normal plane. A gradual decay of the swirl velocity near TDC, which was not observed with the lower compression ratio, can be attributed to the increase in area-to-volume ratio. The three turbulence levels are similar in magnitude in intake and almost identical during compression (about 0.5 $\bar{V}_p$) confirming the previous finding about the isotropy of turbulence during most of the compression stroke.

Figure 3.20 shows the radial profiles of both the axial mean and rms velocities obtained at 36 degrees in the intake and 324 degrees in the compression stroke. The results during intake show close similarities to those obtained in the non-compressing engine and presented in sub-section 2.3.3; the turbulence which is non-homogeneous is enhanced by the impingement of the inlet jet on the piston face. During the compression stroke the mean velocities, as already observed from the temporal profiles, are very small in comparison to those of the intake and the same is true for the rms velocities, which supports the assumption that the TDC turbulence is homogeneous as well as isotropic. The

velocity peak in the mean profile near the axis may be attributed to the low pressure region on the axis, which results from the radial pressure gradient induced by the swirling flow.

Figure 3.21 exemplifies the swirl field prevailing in the normal plane during the compression stroke and shows that the swirl motion resembles solid body rotation with homogeneous turbulence. The integration of the mean profile at θ = 360 degrees (Figure 3.21a) yields, according to Appendix 3.1, a swirl ratio of 1.7 ($\pm$ 5%) which represents the angular speed of in-cylinder air at TDC as the swirl is distributed uniformly along the axial direction, apart from the region of thin wall boundary layers on both the cylinder head and piston face, as shown in Figure 3.21b.

Cylindrical Bowl with and without Swirl

The results obtained in the absence of induction swirl are shown in Figures 3.22 and 3.23. Early in the intake stroke at θ = 36 degrees, Figure 3.22a, a vortical flow structure exists inside the piston bowl as a consequence of the combined effect of the jet trajectory and bowl geometry. Maximum axial mean velocities of the order of 9 $\bar{V}_p$ were measured close to the bowl periphery with associated turbulence levels of 3 to 4 $\bar{V}_p$. The vortex is no longer apparent at θ = 324 degrees according to Figure 3.22b, which is consistent with the results presented in the previous sub-section. There is, however, some indication of compression-induced squish initiation near the bowl entry plane. By TDC of compression, a squish-induced toroidal vortex is observed to occupy the

whole bowl space, as shown in Figure 3.23 and depicted in schematic form in Figure 3.31a. The schematic descriptions of air motion presented in Figure 3.31 were derived from the corresponding axial and radial mean velocity profiles. Intake-generated turbulence has decayed to levels comparable to those obtained with the flat piston and become near-homogeneous and isotropic, indicating the insignificant effect of squish on overall turbulence in the case of the cylindrical bowl.

Figures 3.24 and 3.25 show the mean and rms profiles of the axial, radial and swirl velocity components obtained in the presence of swirl at Θ = 324 and 360 degrees. The effect of swirl was investigated by Arcoumanis et al (1982c) in the case of a flat piston and was found to affect the overall mean motion but to modify the flow structure in the axial plane only slightly. Late in the compression stroke, however, the interaction of swirl with squish has a significant effect on the axial flow pattern prevailing inside the bowl at TDC and results in a counter-rotating vortex (Figures 3.24 and 3.31c) in contrast to the no swirl case. The mechanism responsible for this is based on the counteracting fields of centrifugal forces, associated with swirl and squish. The balance between the two determines the extent of the inward penetrating jet which, in this case, is confined to the bowl periphery with consequent formation of the counter-rotating vortex. Different levels of intake swirl may, therefore, be expected to result in different flow patterns as indicated by the calculations of Gosman and Johns (1978). The presence of swirl, on the other hand, does not have a strong influence on the bowl turbulence. The increased swirl turbulence levels observed near the axis is probably due to random movements of the swirl centre about the cylinder axis. The swirl

motion at the end of the compression stroke, Figure 3.25b, resembles a solid body rotation particularly near the axis and corresponds to a higher swirl ratio, of about 3.8, than that obtained with the flat piston (1.7) due to the decrease in moment of inertia associated with the piston bowl.

Re-Entrant Bowl with and without Swirl

Figure 3.26a shows that at Θ = 36 degrees, and in the absence of induction swirl, the fluid inside the bowl follows the piston motion and is isolated from the activities taking place outside the bowl contrary to the cylindrical bowl case where a vortex structure was observed due to jet penetration into the bowl. The low levels of homogeneous turbulence detected inside the bowl are likely to stem from the previous cycle. Towards the end of the compression stroke, however, compression-induced velocity gradients inside the bowl cause increased turbulence levels of similar magnitude to those measured early in the intake stroke with both flat and cylindrical bowl pistons. At TDC, according to Figures 3.27 and 3.31b, a flow structure similar to that in the cylindrical bowl is evident but with a stronger toroidal vortex occupying the whole bowl space due to the enhanced squish effect.

As Figures 3.28 and 3.31d indicate, the swirl-squish interaction generates at TDC a system of two counter-rotating vortices in the axial plane of the bowl. The flow moves towards the lower corners of the bowl and then splits either upwards over the sides or inwards over the base. The presence of swirl results in more homogeneous turbulence with generally lower magnitude than that of the no swirl case. Although the swirling motion near the

base of the bowl at TDC approximates solid body rotation, it exhibits deviations of a spiralling nature at the bowl entry plane evolving from sink type flow at θ = 324 degrees as suggested by Figure 3.29a. Calculations of the swirl ratio, based on the two mean profiles of Figure 3.29b, yields a higher swirl ratio near the bowl entry and an average swirl ratio of about 4.8 which is higher than in both previous cases of flat piston and cylindrical bowl. Figure 3.30 shows the evolution of the swirling motion near TDC at four crank angle locations for the four strokes of the engine cycle. With the fluid being forced into the bowl during compression, the mean profile at θ = 324 degrees reflects the spiralling nature of the flow near the bowl entry, which in expansion relaxes into solid body type rotation as shown in Figure 3.30c. Later in the expansion stroke it is expected, as discussed in the previous Chapter, that the fluid inside the bowl moves together with the piston without any significant momentum transfer taking place in and out of the bowl. Under such circumstances the swirling flow prevailing inside the bowl decays due to wall friction (Figure 3.30d) resulting in some residual swirl motion which persists to the next cycle as Figure 3.30a indicates.

3.4 Discussion

3.4.1 Mean Motion and Turbulence in Disc Chamber

The in-cylinder flow structure prevailing in the axial plane during the intake stroke has been investigated and was discussed in great detail in the previous Chapter for the case of an open valve, ie. in the absence of

compression. The present results obtained with an operating valve show a close parallel, with a predominant jet-like flow inducing a system of similar vortices in the axial plane. The results of Gany et al (1980) also show insignificant differences in the axial flow structure during intake under compressing and non-compressing conditions at 31 rpm. The same is true for the mean flow in the normal plane, namely the swirl motion. According to Morse and Whitelaw (1981) the swirl mean velocity values measured during intake show only a small dependence on whether compression is applied. The swirling flow is characterised by a region of high velocity corresponding to the spiralling inlet jet motion, which is obviously a function of the intake valve geometry as indicated by Arcoumanis et al (1982c). The vortex motion is complex and does not exhibit characteristics associated with either forced (solid body) or free vortex. In the present engine, it is the axial flow which dominates during intake and imparts the swirl motion through interaction with vanes incorporated into the inlet port. The intake turbulence is non-homogeneous with high levels of turbulence produced in the shear layers at the edge of the inlet jet. Shortly before the end of induction, however, the turbulence field decays and tends towards homogeneity and isotropy as the inlet velocity falls off and removes the major source of turbulence production.

During the compression stroke the vortex motion in the axial plane is suppressed before IVC as expected according to the results of the previous Chapter. After IVC, the axial mean flow continues to decay under the combined action of the turbulence stresses and pressure changes brought about by the piston as it reverses direction. Swirl motions prevailing in the normal plane, however, are less directly subject to the piston-induced pressure forces and are able to persist through compression,

progressively conforming by virtue of the cylindrical geometry to an organised structure of solid body type rotation since this minimises internal shear. They are, therefore, more likely to influence the fuel injection and combustion processes at late compression and early expansion stages than are the other motions. The present measurements of swirl velocity are in good qualitative agreement with the results of similar in-cylinder investigations outlined in Chapter 1. The organisation of the flow into solid body rotation in the compression stroke with progressive relaxation from the effects of the intake process is also evident in the measurements of Johnston et al (1979), Witze (1980), Morse and Whitelaw (1981) and Cole and Swords (1978) which indicate that relaxation continues into the early part of the expansion stroke under motoring conditions. The present swirl ratios obtained by integrating the measured swirl profiles at TDC were of the order of 2 and show a close correspondence to that obtained by Renshaw and Wigley (1979) and based on the solid body assumption, indicating that the 30 degree vanes result in TDC swirl levels which are similar to those imparted by directed ports in medium swirl, production diesel engines. The results of Arcoumanis et al (1982c) obtained with a 30 degree seat angle and various dimensionless lifts within the practical range (0.12 to 0.27) show a strong dependence of the swirl ratio on valve lift, with a lower swirl ratio and greater tendency towards solid body rotation resulting in the case of the small lift; the similarity of the TDC flow characteristics in the axial plane indicates the short flow "memory" of the inlet boundary conditions contrary to that of the swirl flow which is much longer. The model calculations of Grasso and Bracco (1981) agree with the finding of Arcoumanis et al in that the flow structure at the end of compression, in particular TDC turbulence,

is insensitive to the details of the intake process. The present results show that the axis of the mean swirling motion is coincident with that of the cylinder during almost every part of the cycle. Out of phase movements of the instantaneous swirl centre, however, were observed as also indicated by Witze (1980b) and is evident in the measured high turbulence levels near the axis. More recent measurements of Vafidis (1983) show large increases in this pseudo turbulence near the swirl centre with increased swirl levels, which are attributed to this random precession of the swirl centre across the higher velocity gradients there. According to the measurements of Rask (1979) in an L-head engine, the precession of swirl centre about the cylinder axis in phase with the crank angle from cycle to cycle is also possible during compression, although he does not provide details of the flow around TDC.

As the swirl motion organises into solid body rotation during compression, the turbulence initially decays with the axial mean motion which is mainly responsible for its production; the compression turbulence is, contrary to intake process, homogeneous and also isotropic. Later, however, although the axial mean motion continues to decay, the turbulence is sustained at levels of about $0.5\ \bar{V}_p$ during most of the compression stroke. One possible explanation for such behaviour of compression turbulence can be thought, at first sight, to be that the extra turbulence is produced due to the persisting swirl mean motion. It can, however, be argued that the low levels of shear prevailing in near solid body swirl structures (Bradshaw, 1973) contribute little to turbulence production, apart from near wall regions. Hoult and Wong (1978) propose that under rapid compression and with dissipation neglected, the turbulent eddies are reduced in scale by the piston-induced compressive stresses and

spin up to conserve their angular momentum, thus, resulting in an increase in turbulent kinetic energy. This interpretation is, however, incomplete since it does not explain the observation that different engines with different induction systems produce roughly comparable TDC turbulence levels providing, as in the case of Arcoumanis et al (1982c), evidence of insensitivity to the induction history. On the other hand all the early hot wire measurements, apart from those of Lancaster (1976), show an increase in turbulent kinetic energy near TDC in agreement with the reasoning of Hoult and Wong. The difficulties associated with the interpretation of hot wire signals during compression, however, cast doubts on the reliability of those measurements near TDC; more recent LDA measurements, for example Rask (1979), show as in the present case no such trends. Probably the most plausible explanation for such behaviour of turbulence is that related to the piston-induced motions. As the piston decelerates in the second half of the compression phase, favourable gradients for turbulence production by normal stresses are generated consequently sustaining the levels during most of the stroke. Observation of rapid decrease in turbulence levels soon after TDC substantiates this argument as the source for production (deceleration) is removed and, on the contrary, a stabilising effect due to acceleration is imposed on the turbulence field during the expansion phase.

The measurements obtained with and without induction swirl show differences in turbulence level during the compression stroke, as also indicated by Arcoumanis et al (1982c). The levels are generally lower with swirl, by about 20%, than those without. This observation can be attributed to the stabilising effect of a state close to solid body rotation. With the square of the angular momentum increasing with radius, as in the case of solid

body rotation, the interchange of position between fluid at different radii will require energy which may be extracted from the energy of turbulent motion (Townsend, 1980). Thus, the streamline curvature associated with the swirl motion, of near solid body, in the normal plane exerts a stabilising effect on turbulence resulting in decrease in overall turbulent kinetic energy. The stabilising effect can, therefore, be expected to increase with increasing angular momentum gradient. The measurements of Witze (1980), for example, show that as the TDC swirl level is varied by changing the shroud orientation on the intake valve of an L-head engine, the turbulence intensity changes dramatically increasing, although not in a monotonic manner, with decreasing swirl rate.

Under motoring conditions the expansion and exhaust phases are not directly relevant, apart from early expansion, to real engine situations due to the absence of mixing (if any) and combustion processes. The swirl motion persists through TDC with the axial motion still of secondary importance. This trend is, however, interrupted at EVO with increased velocities near the head due to sudden inflow of fluid through the valve. New turbulence is, therefore, generated which subsequently diffuses and increases overall in-cylinder turbulence levels, but progressively decays to insignificant levels before the beginning of the next engine cycle. The persistence of swirl motions continues through to the next cycle and is thus expected to contribute to the angular momentum content of the following cycle. This residual motion explains some of the reasons why steady flow rigs which are used to evaluate the swirl producing ability of the inlet system of an engine, results in lower angular velocities as observed by Tanabe et al (1978) and Brandl et al (1979). The increase in both the

measured and turbulence levels due to exhaust valve opening is also evident in the measurements of Lancaster (1976), Rask (1979) and Ramos et al (1981). The results of Ramos et al, however, do not show the detail of the flow at and after EVO and they attribute the increase in turbulence levels observed later on in exhaust to the mean velocity gradients induced by the fluid moving towards the exhaust valve.

3.4.2 Influence of Compression Ratio

The influence of compression ratio may be quantified by comparison between the two compression ratio cases of 3.5 and 6.7. The effect on the intake flow structure inside a cylindrical chamber with a flat piston shows a close parallel to that of the clearance volume investigated in the absence of compression and discussed in sub-section 2.4.3 of the previous Chapter.

The effect of compression ratio subsequently becomes less pronounced during the compression stroke as the fluid motions decays, particularly the one in the axial plane, resulting in insignificant axial mean velocities in both compression ratio cases but in identical turbulence levels of about 0.5 $\bar{V}_p$ during most of the stroke. This observation of the TDC flow insensitivity to compression ratio shows a close correspondence to that of Arcoumanis et al (1982c) which indicates, as mentioned earlier on, the short "memory" of the axial flow to the induction history. A similar conclusion was also drawn by Lancaster (1976) for higher compression ratios ranging between 6.8 and 10.5 in a similar flow configuration and at engine speeds of 1000 - 2000 rpm.

The swirl at TDC is near solid body rotation in both cases with comparable swirl ratios S_r of the order of 2. The corresponding angular momenta per unit mass h_o (see Appendix 3.1 for its definition and evaluation) are almost identical, although the total angular momentum at TDC, H_o, is higher with the compression ratio of 3.5 due to the larger mass of fluid taken in during the induction process. It is reasonable to expect that the losses due to wall friction will be larger in the high compression ratio case due to the relative increase in area-to-volume ratio. The observation of the identical angular momenta per unit mass, however, is contradictory to this expected trend, unless a higher angular momentum was imparted during intake with the higher compression ratio,which in this case balances the extra loss. The measurements of Huebner and McDonald (1972) clearly indicate such effect of the compression ratio, within the similar range of 4.01 to 6.20, on the swirl field of induction process in that the angular momentum generated decreases with decreasing compression ratio. This decrease is attributed mainly to the larger amount of mass to be accelerated with decreasing compression ratio and partly to the reduced interaction of the piston crown with the incoming flow, which otherwise suppresses the axial motion and causes more of the incoming linear momentum to be converted to angular momentum.

Overall, it can be concluded that the effect of compression ratio is likely to remain more important to the thermodynamic behaviour of an internal combustion engine with a disc shape chamber, as it determines its thermal efficiency, rather than to its in-cylinder flow structure near TDC. The compression ratio may, on the other hand, influence the flow structure inside the bowl type combustion chambers by virtue of the changes in geometry

near TDC generating new, compression-induced mean motions and turbulence as will be discussed in the following sub-section.

3.4.3 Squish and Swirl-Squish Interaction

The above findings with regard to disc shape combustion chambers explain some of the motivations for practices in engine design of deliberately inducing swirl during induction and squish during compression. As discussed earlier on, the low levels of shear prevailing in near solid body swirl structures, however, contribute little to turbulent mixing and turbulence production during compression, apart from near the walls. Thus, squish is induced by virtue of both the compression process and combustion bowl geometry to disturb this swirl structure as well as to regenerate motions in the axial planes with consequent turbulence enhancement.

The results obtained in cylindrical and re-entrant type piston bowls in the absence of induction swirl clearly indicate that the squish-induced motions in the axial plane are much stronger, particularly in the re-entrant bowl case, than any which would be expected to persist from the induction process. In both piston bowl configurations a single toroidal vortex is observed to prevail inside the bowl at TDC. The mean motion inside the cylindrical bowl, however, is weak and as a consequence no significant turbulence production is observed and the TDC turbulence thus remains homogeneous and isotropic with levels of about 0.5 $\bar{V}_p$ as in the disc shape combustion chamber. The steep mean velocity gradients induced during compression inside the re-entrant bowl, on the other hand, result in increased TDC turbulence

levels comparable to those generated in intake with both flat and cylindrical bowl pistons. This turbulence enhancement together with the stronger mean motion induced by squish inside re-entrant type combustion bowls can, therefore, be expected to augment the fuel-air mixing in diesel engines through both increased convection and turbulent diffusion. The re-entrant piston bowl also results in a reverse squish effect during expansion with a consequent increase in mean and turbulent velocities outside the bowl near the cylinder axis. The measurements of Brandl et al (1979) in a toroidal type piston bowl (close to the present cylindrical bowl geometry) show a similar trend of the TDC turbulence to that in the cylindrical bowl, indicating that the squish or squish-induced motions have little effects on overall turbulence prevailing in open type combustion chambers. The model calculations of Ahmadi-Befrui et al (1982) for a similar bowl configuration also reveal the behaviour of turbulence in that the overall bowl turbulence is little affected and remains nearly homogeneous apart from a local high-intensity region near the bowl edge caused by the strong shear stresses there.

The interaction of swirl, generated during induction, with squish causes profound changes in the axial motion persisting in both type piston bowls near TDC. This interaction between squish, whose inward-penetrating jet drives the vortex described above, and swirl, which limits the extent of this penetration through centrifugal forces and thus confines the main activity to the outer part of the bowl, results in the formation of a counter-rotating vortex in the cylindrical bowl case and a system of two vortices (a ring and a toroidal type) inside the re-entrant piston bowl. Similar conclusions

are also drawn by Williams and Tindal (1980) especially with regard to the flow structure in re-entrant type piston bowls. Their measurements inside a toroidal piston bowl, however, show differences which may be attributed to a different degree of induction swirl. The velocities measured near the bowl periphery indicate evidence of opposite-rotating vortex which may either be a single vortex as observed with the present cylindrical bowl in the absence of swirl or a part of a vortex system, which is probably the more plausible case as indicated by the calculations of Gosman and Johns (1978). Different degrees of intake swirl and/or squish can, therefore, be expected to result in different flow structures at TDC.

The swirl motions prevailing inside piston bowls near TDC are much more complex than that envisaged, for example, by Fitzgeorge and Allison (1962) since the interaction with the swirl field of vortices induced by squish and swirl mechanism, produces distributions of tangential velocities which are far from the idealised structure of solidy body rotation, as also noted by Williams and Tindal (1980). This is particularly true in the case of the re-entrant type piston bowl where deviations from solid body rotation of a spiralling nature are observed near the bowl entry. Although the swirl motion closely resembles solid body rotation near the axis, it approximates free vortex in the regions close to the entry and away from the cylinder axis. Swirl velocities are generally increased inside the piston bowls, although not in line with the principle of angular momentum conservation, in comparison to those in the disc shape chamber due to the decrease in moment of inertia associated with both piston bowl geometries. The integration of the swirl profiles at TDC yields swirl ratios of the order of 4 and 5 corresponding to

the cylindrical and re-entrant type piston bowls, respectively, compared to about 2 in the case of the flat piston. Williams and Tindal have made similar observations in that the re-entrant bowl causes higher maximum swirl rates than in the toroidal bowl, which are naturally attributed to the relative shapes and dimensions of the two chambers. The recent measurements of Vafidis (1982) in a similar engine configuration with flat piston indicate that the angular momentum loss during compression is of the order of 30% for various degrees of swirl induced during intake. If it is assumed that the total angular momentum is the same for all cases at IVC, which is a reasonable assumption since the same inlet port and swirl vanes are used in all three piston configurations, and that the residual effects are ignored, the angular momenta at TDC of compression should provide an indication of the effect of piston geometry on the swirl motion. Comparison of the angular momenta at TDC shows that both piston bowls result in 40% higher losses than in the flat piston case. This relative increase in angular momentum loss is in agreement with that observed by Brandl et al (1979) and is mainly attributed to the increase in the surface area over which the wall shear stress acts. Vafidis (1982) also reports similar losses with increased swirl levels, although they are generally higher by about 10% due to the increased friction associated with the higher velocities encountered in this case. The angular momenta in the two piston bowl configurations are almost equal, within the experimental and integration procedure accuracy, contrary to the swirl ratios which are not, as previously mentioned above. This points out the relatively greater effect of piston bowl geometry on the distribution of swirl velocity at TDC, rather than on the total angular momentum which is more closely associated with the inlet geometry and thus with the degree of induction swirl.

3.4.4 Assessment of Relevant Flow Calculations

The measurements obtained in the absence of induction swirl with a flat piston and a compression ratio of 3.5 are presented in Appendix 3.3 together with the relevant flow calculations of Ahmadi-Befrui et al (1982). These measurements, and the rest presented in this thesis, serve not only to provide new understanding of the effects of influential parameters such as geometry and flow boundary conditions but also provide a testing ground for calculations. Although the latter can produce results more quickly and over a wider range of conditions than experiments, they embody approximations which can give rise to appreciable errors, and hence they need experimental verifications.

The particular multi-dimensional calculation method to be evaluated and used by Ahmadi-Befrui et al, which is code-named RPM, solves by a finite-difference procedure the governing equations in a flexible curvilinear coordinate frame with turbulence effects represented by a two-equation ($k - \varepsilon$) turbulence model. This method has been assessed for the accuracy of its fluid dynamic calculations at a number of stages in its development. Early comparisons with experimental data relating to laminar and turbulent flows in a non-compressing engine are reported by Gosman et al (1978b) followed by further comparisons for turbulent flows by Gosman et al (1978a), Gosman and Whitelaw (1980) and Johns (1980). The present comparison is based on measurements and calculations relating to a compressing four-stroke motored engine.

The computer model used is a version of the finite-difference procedure originally developed by Gosman and Watkins (1976) (see also Watkins, 1977) and subsequently extended by Gosman and Johns (1978 and 1980). It

employed a flexible curvilinear computational grid (45 x 45) which can expand and contract with the piston and valve motions. The equations solved are given by Ahmadi-Befrui et al (1981) and represent conservation of mass, axial and radial momentum, energy, and the turbulence energy k and its dissipation rate ε. The treatment of the boundary conditions has been outlined by Ahmadi-Befrui et al (1982) and given in more detail by Gosman et al (1978a). In particular, for the prescription of induction and exhaust boundary conditions in the plane of the valve orifice it was assumed that the flow enters at the valve seat angle with plug distributions of velocities; it should be noted that the results of the following Chapter suggest that this is inappropriate. The velocities were deduced from the calculated mass flow, based on a conventional orifice relation, with varying discharge coefficient as prescribed by Kastner et al (1963).

Figure 1 of Appendix 3.3 displays some global features of the flow which includes the variations with crank angle of cylinder pressure, inlet velocity and mass flow rate through the valve orifice. Measurements are only available for the first-mentioned quantity and lie some 10% above the predictions, due either to underprediction of the intake mass or overestimation of the heat losses which is thought to be the more likely explanation. The point measurements and calculations of Figure 2 indicate a qualitative agreement with respect to the mean velocity. Quantitatively, however, the calculations tend to underpredict the strength of the jet and recirculation velocities in some areas and this is consistent with the earlier indication that the inlet flow is underestimated. The trend of the measured and calculated turbulence levels during intake correlates with that of

the mean velocity in respect of both the temporal and spatial behaviour, confirming that the jet flow is the origin of the turbulence. The calculations underestimate the turbulence levels which are expected on the basis of the lower mean flow predictions, but there may be other contributing factors. The quantitative agreement between the measurements and calculations progressively improves during compression exhibiting two noteworth features, namely tendency to level off to a constant level of about 0.6 $\bar{V}_p$ during most of the compression stroke, Figure 2, and to become nearly homogeneous as indicated in Figure 3c. The agreement with respect to both the mean motion and turbulence encouragingly continues to improve throughout the late compression and early expansion phases and is acceptable at and on either side of TDC.

The overall picture emerging from the above evaluation work indicates that the calculated mean flow information is usually in reasonable quantitative agreement with the measurements. Significant discrepancies have, however, been observed, which are most evident during the intake stroke and particularly in respect of turbulence quantities. Their causes are difficult to isolate. Numerical, turbulence and initial or boundary condition assumptions may each or all be at fault to some extent. The elimination of numerical errors, or reduction of them to tolerable levels, by refining grid intervals and time steps in the calculations requires computing resources which are not always adequate. The merits and limitations of turbulence models are known, to a considerable extent, from investigations of steady flows but have not been thoroughly appraised for engine configurations. Probing of the inlet region in experiments, as reported in the next Chapter, should provide the correct boundary conditions reducing the overall uncertainty and thus allowing proper assessment and improvement of the remain-

ing source of uncertainty, namely the turbulence model, with particular interest in the effects of compression (Ahmadi-Befrui et al, 1981), swirl (Gosman and Jahanbakhsh, 1981) and streamline curvature (McGuirk et al, 1981).

3.5 Conclusions

The main findings of this Chapter can be listed as follows:

(1) In disc shape chambers the intake-generated mean motions in the axial plane decay to insignificant levels while the turbulence initially decays becoming isotropic and later attains near homogeneous levels of 0.5 - 0.6 $\bar{V}_p$. The intake-induced swirl has a complex structure during the induction process and develops into near solid body rotation augmenting the mean motions during compression, but with little effect on overall TDC turbulence.

(2) Compression ratio has a very small effect on the compression mean motions and turbulence in the case of a disc shape combustion chamber.

(3) For the case of the cylindrical piston bowl and in the absence of induction swirl, a squish-induced toroidal vortex occupies the whole bowl space at TDC. Interaction of swirl with compression-induced squish, however, results in the formation of a counter-rotating vortex in the axial plane in addition to the swirl motion in the normal plane, whose distribution varies along the depth of the piston bowl. The squish, in the presence

or absence of swirl, does not alter the overall turbulence levels which remain comparable to those obtained in the disc shape chamber.

(4) In the re-entrant bowl configuration and without swirl, the squish induces a similar axial flow structure to that in the cylindrical bowl but of a stronger nature. The addition of swirl, however, results in the formation of a vortex structure which comprises a ring and a toroidal vortex rotating in opposite directions. The swirl motions exhibit characteristics of a spiralling nature near the bowl entry but of solid body rotation close to the base of the bowl. The turbulence inside the bowl is considerably enhanced, independent of swirl, to levels typical of the intake-generated turbulence.

(5) The distribution of swirl velocities at TDC depends more on the piston bowl geometry rather than on the intake swirl field which is better reflected in the final angular momentum of the bowl content.

(6) Squish and swirl have been shown to be important contributors to the mean motion rather than to the overall turbulence prior to combustion, with the exception of the re-entrant bowl configuration which has also caused significant turbulence production.

(7) In the expansion stroke, the re-entrant bowl configuration results in a strong reverse squish effect with consequent increase in both mean motion and turbulence near the bowl exit. Later in the stroke, the sudden inflow through the valve at EVO produces new turbulence which thereafter decays rapidly.

(8) During exhaust, the piston configuration is not important. The fluid moves towards the open valve with further decay of the lately generated turbulence and with some residual swirl motions persisting to the next engine cycle.

(9) Parallel measurements and calculations of the present model engine flow are in moderate overall agreement, with some discrepancies which are most evident during the induction stroke, arising mainly from numerical errors, turbulence modelling inadequacies and inlet condition uncertainties.

APPENDIX 3.1

CALCULATION OF

SWIRL RATIO AND ANGULAR MOMENTUM

Swirl Ratio S_r

Swirl ratio is a measure of in-cylinder swirl at TDC of compression and is defined as the ratio of the average angular velocity of fluid at TDC ($\bar{\omega}_f$) to that of the engine crankshaft (ω). It is evaluated by integrating a number (N) of swirl profiles at various axial locations and is given by

$$S_r = \frac{\bar{\omega}_f}{\omega} = \frac{\frac{1}{N}\sum_{i=1}^{N}\left(\frac{1}{R}\int_0^R \frac{\bar{W}}{r}\,dr\right)_i}{\omega} \qquad (1)$$

$$= \frac{30}{R\ \pi\ rpm}\ \frac{1}{N}\sum_{i=1}^{N}\left(\int_0^R \frac{\bar{W}}{r}\,dr\right)_i$$

If it is assumed that the fluid rotates like a solid body at TDC (ie. $\bar{\omega}_f = \bar{W}/r$), the equation above reduces to

$$S_r = \frac{30\ \bar{W}}{r\ \pi\ rpm} \qquad (2)$$

which has been used almost exclusively by other investigators due to the difficulty of obtaining detailed swirl velocity profiles.

Angular Momentum per Unit Mass h_o

Angular momentum of a fluid particle is defined as the moment of its linear momentum about the cylinder axis and is evaluated as follows:

Let us assume that at a given crank angle θ, the fluid density $\rho(\theta)$ is uniform in space and the angular velocity ω_f varies only with r. Then consider an infinitesimal fluid element at radius r with thickness dr and length $z_p(\theta)$ corresponding to the crank angle under consideration.

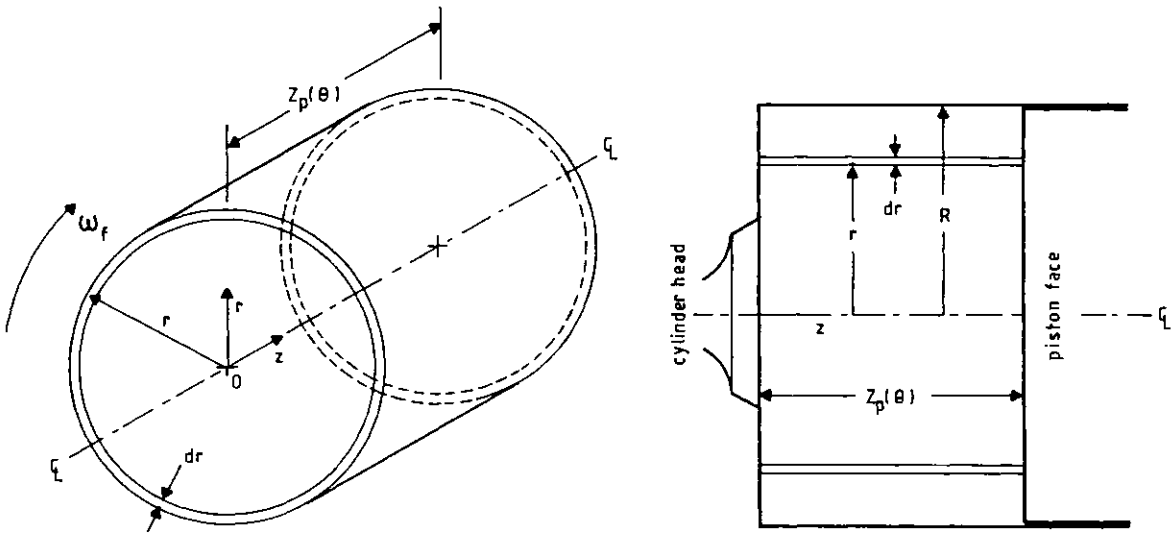

Figure 1 Infinitesimal fluid element at a given crank angle θ

The angular momentum of the element , dH_o, is thus given by

$$dH_o = dm\ \omega_f\ r^2 = dm\ \bar{W}\ r \qquad (3)$$

where the mass of the fluid element, dm, is

$$dm = 2\ \pi\ r\ dr\ z_p\ (\theta)\ \rho(\theta) \qquad (4)$$

Integrating equation (3) over the cylinder radius R yields the angular momentum of the fluid, H_o, at crank angle θ:

$$H_o = 2 \pi z_p(\theta) \rho(\theta) \int_o^R \bar{W} r^2 dr \qquad (5)$$

and the corresponding fluid mass, obtained by integrating equation (4), is

$$m = \pi R^2 z_p(\theta) \rho(\theta) \qquad (6)$$

- Angular momentum per unit mass, h_o (= H_o/m), is therefore given by

$$h_o = \frac{2}{R^2} \int_o^R \bar{W} r^2 dr \qquad (7)$$

Here it is calculated at a certain crank angle by averaging the angular momenta per unit mass obtained, using equation (7), from a number (N) of swirl profiles at various axial locations:

$$h_o = \frac{1}{N} \sum_{i=1}^{N} (h_o)_i \qquad (8)$$

The integration of swirl profiles to deduce both the swirl ratio S_r and the angular momentum per unit mass h_o, is performed by using a piecewise quadratic approximation as described by Taylor et al (1982).

APPENDIX 3.2

REFRACTION CORRECTION FOR LDA MEASUREMENTS IN FLOWS WITH CURVED OPTICAL BOUNDARIES

(Published in TSI Quarterly, V.8,
No. 2, 1982 - see Bicen, 1982)

NOMENCLATURE

C_f	correction factor for fluid velocity
d_e	effective displacement in axial plane
f	Doppler frequency
n_a	refraction index of outer medium
n_f	refraction index of inner medium (working fluid)
n_w	refraction index of cylinder wall
R_o	outer radius of cylinder wall
R_i	inner radius of cylinder wall
r_a	radius of virtual position of beam intersection without refraction
r_f	true radius of position of beam intersection with refraction
t	thickness of cylinder wall, $R_o - R_i$
t_e	effective wall thickness
V	fluid velocity
V_{za}, $V_{\phi a}$, V_{ra}	components of fluid velocity calculated from equation (1) using half angle of unrefracted beams and wavelength in outer medium
V_{zf}, $V_{\phi f}$, V_{rf}	corrected components of fluid velocity
z, ϕ, r	cylindrical coordinates
α_a	an angle given by equation (4c)
α_w	an angle given by equation (4d)
α'_w	an angle given by equation (4e)
α_f	an angle given by equation (4f)
β	an angle given by equation (4g)
θ	half angle of laser beams
θ_a	half angle of unrefracted laser beams
θ_f	half angle of refracted laser beams
λ	wavelength of laser light
ϕ_f	angle between r_a and r_f

1. INTRODUCTION

In laser-Doppler anemometry, the equation connecting the fluid velocity to the measured frequency of light-scattering by particles in the fluid as they cross a fringe zone formed by the intersection of two laser beams is given by, from reference 1,

$$V = \frac{\lambda}{2 \sin \theta} f \qquad (1)$$

The wavelength and the paths of the laser beams, therefore the half angle of the beams and their point of intersection, will change if the beams should travel through different optical media due to the differences in refraction index. In addition, if the interfaces between the optical media are curved, as in the cases of cylinders, and curved ducts and tubes, the half angle and point of intersection may undergo further changes due to the geometry. Therefore, the correction of position of intersection point and fluid velocity is necessary for LDA measurements in fluids within curved boundaries. Although the foregoing analysis is given for flows in cylinders, the results will equally apply to other flows with curved boundaries. These results are summarized in Section 3 for the benefit of other investigators who wish to make LDA measurements in such flows. Similar, but incomplete, analysis is also given in references 1 and 2.

2. VELOCITY MEASUREMENTS

Figs. 1-4 show the beam orientations for measurements of different velocity components in cylindrical coordinates, axial, tangential and radial respectively. In all those figures half angle of beams is exaggerated for clarity; in practice it is usually a smaller angle not exceeding 15 degrees.

The correction factor for fluid velocity and the relationship between the real refracted position of beam intersection and the virtual position without refraction are derived using the law of refraction (Snell's Law) and the related geometries in Figs.1-4.

2.1 Axial Velocity Measurements

For measurements of axial velocity, the optical system should be oriented such that the plane containing the beams passes through the cylinder axis with the bisector between the beams at right angles to it. Two possible movements of the point of intersection exist:

Case (a) - The intersection point is moved along a diameter on which the bisector lies. In this case the refraction is only in the axial plane since the refracting surfaces are perpendicular to the bisector as shown in Fig.1. The point of intersection will be moved according to the equation below.

$$r_f = \frac{n_f}{n_a} r_a + (1 - \frac{n_f}{n_w})t - (1 - \frac{n_f}{n_a})R_o \qquad (2)$$

The equation above is based on the assumption that sine and tangent of half angles, since they are usually very small, are approximately equal, and it is linear in terms of r_a for a given experimental set up.

The fluid velocity will be given by the equation below with a correction factor of unity (ie. no correction is needed).

$$V_{zf} = C_f V_{za} \qquad \text{where} \quad C_f = 1 \qquad (3)$$

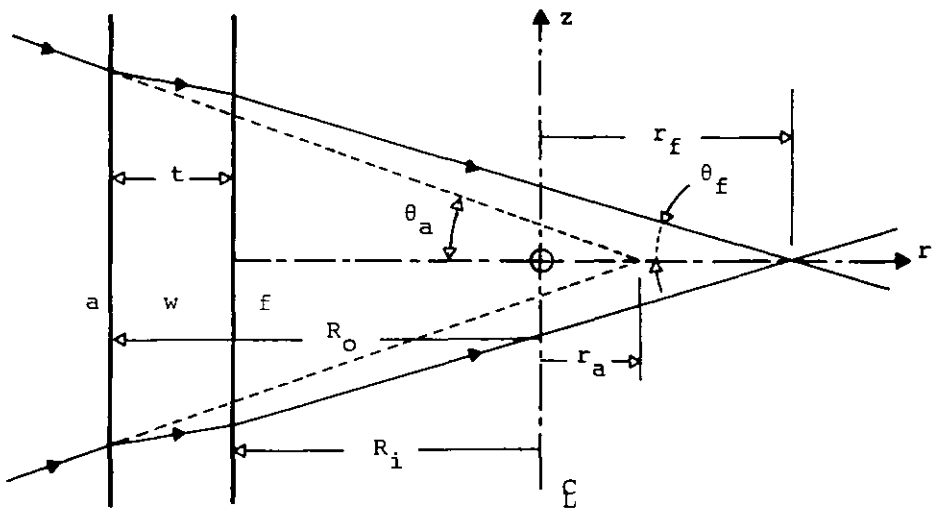

Fig.1 Refraction of laser beams during axial velocity measurements;Case(a).

Case (b) - Alternatively, the intersection point is moved along the orthogonal diameter. In this case, in addition to the refraction of beams in the axial plane, the whole plane containing the beams will refract radially as shown in Fig.2. Equation (3) above will still apply for the fluid velocity. However, the intersection point will wander off the orthogonal diameter due to the changes in the effective wall thickness as the beams traverse different portions of the cylinder wall. Assuming as before that for small angles the sine and tangent are equal, the coordinates of the true intersection point, r_f and ϕ_f, are given by

$$r_f = R_i \sin\beta - (R_i \cos\beta + d_e) \tan(\beta - \alpha_f) \qquad (4)$$

where

$$d_e = \left(1 - \frac{n_f}{n_w}\right)(t_e - t) + \left(1 - \frac{n_f}{n_a}\right)(1 - \cos\alpha_a)R_o \qquad (4a)$$

$$t_e = R_i \cos(\alpha_a - \alpha_w)(\cot\alpha_w \sin\alpha'_w - \cos\alpha'_w)$$

for $R_i \geq r_a > 0$

$$t_e = t \quad \text{for} \quad r_a = 0 \qquad (4b)$$

$$\alpha_a = \sin^{-1} \left(\frac{r_a}{R_o} \right) \tag{4c}$$

$$\alpha_w = \sin^{-1} \left(\frac{n_a r_a}{n_w R_o} \right) \tag{4d}$$

$$\alpha_w' = \sin^{-1} \left(\frac{n_a r_a}{n_w R_i} \right) \tag{4e}$$

$$\alpha_f = \sin^{-1} \left(\frac{n_a r_a}{n_f R_i} \right) \tag{4f}$$

$$\beta = \alpha_a + \alpha_w' - \alpha_w \tag{4g}$$

and the angle ϕ_f by

$$\phi_f = \sin^{-1} \left(\frac{d_e}{r_f} \right) \tag{5}$$

The angles α_a, α_w, α_w', β , α_f and ϕ_f are also shown in Fig.2. Note the sign convention that r_a is positive for positions above the cylinder axis when the laser source is considered to be on the LHS, and the angle ϕ_f is clockwise when its value is positive; Fig.2 however, shows a negative angle.

It should also be mentioned that in most practical cases with reasonable wall thicknesses (up to 0.5 R_i) and same fluid on either side of the cylinder, the variation in the position of intersection point can be ignored; the changes in r_f, even close to the wall region, will be less than 3% with corresponding ϕ_f being no more than 4 degrees.

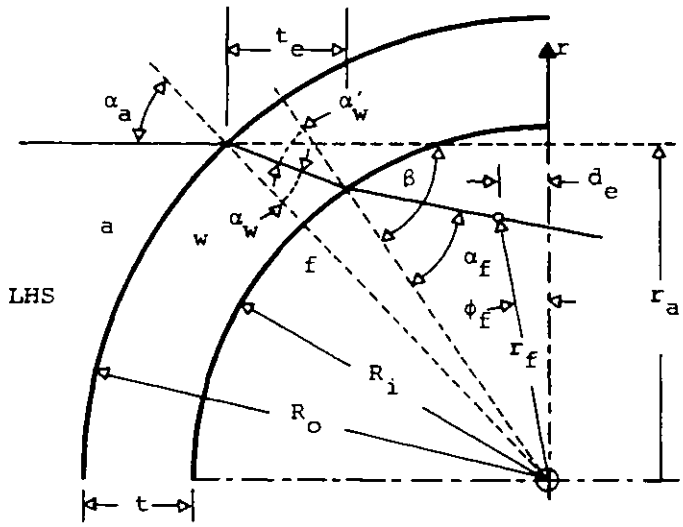

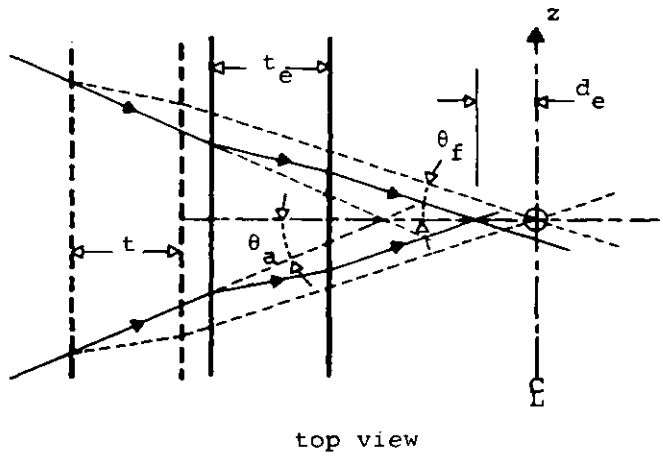

Fig.2 Refraction of laser beams during axial velocity measurements;Case(b).

2.2 Tangential Velocity Measurements

For measurements of tangential velocity, the optical system should be oriented such that the plane containing the beams is perpendicular to the cylinder axis with the bisector passing through it. The point of intersection is moved along the diameter on which the bisector lies, as shown in Fig.3.

Assuming that the sine of a small angle, which is an algebraic sum of some other small angles, is equal to the

sum of individual sines of those angles, a simplified correction factor, of which reciprocal is linear in terms of r_a for a given experimental set up, is derived and given by the equation below.

$$C_f = \frac{n_a}{n_f}\left[1 + n_a \frac{r_a}{R_o}\left[\left(\frac{R_o}{R_i}\right)\left(\frac{1}{n_w} - \frac{1}{n_f}\right) + \left(\frac{1}{n_a} - \frac{1}{n_w}\right)\right]\right]^{-1} \quad (6)$$

Note that r_a is positive for positions beyond the cylinder axis with respect to the laser source.

The true radius of beam intersection and correct fluid velocity are therefore given by equations (7) and (8) below, respectively.

$$r_f = C_f r_a \quad (7)$$

$$V_{\phi f} = C_f V_{\phi a} \quad (8)$$

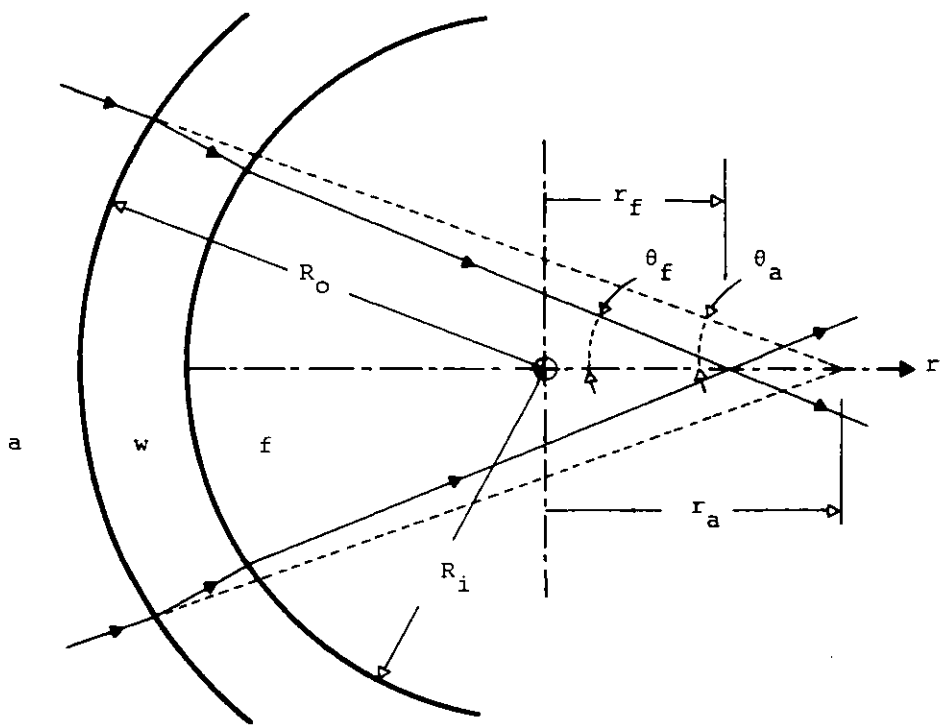

Fig.3 Refraction of laser beams during tangential velocity measurements.

2.3 Radial Velocity Measurements

For measurements of radial velocity, the optical system should be oriented as for tangential velocity measurements, but the point of intersection is now moved, as shown in Fig.4, along the orthogonal diameter which is at right angles to the unrefracted beam bisector.

Although the geometry, in this case, will lead to more tedious trigonometric equations without any simplifying assumptions due to the larger angles encountered, the final results for the correct fluid velocity and the true radius of the intersection point are simply those given by equations (9) and (10) below respectively. However, the true point of intersection will not lie on the orthogonal diameter but on one inclined to it by an angle ϕ_f, given by equation (11) below, to which the bisector of refracted beams are at right angles.

$$V_{rf} = C_f V_{ra}, \quad \text{where } C_f = \frac{n_a}{n_f} \tag{9}$$

$$r_f = C_f r_a \tag{10}$$

$$\phi_f = \sin^{-1}\left(\frac{n_a r_a}{n_w R_i}\cos\theta_a\right) - \sin^{-1}\left(\frac{n_a r_a}{n_w R_o}\cos\theta_a\right) - \sin^{-1}\left(\frac{n_a r_a}{n_f R_i}\cos\theta_a\right) + \sin^{-1}\left(\frac{r_a}{R_o}\cos\theta_a\right) \tag{11}$$

Note that r_a is positive for positions above the cylinder axis when the incident beams are on the LHS and also that ϕ_f is clockwise for a positive angle as shown in Fig.4.

It is pertinent to point out that the optical path difference between the two beams may result in the formation

of a fringe volume at a region away from the beam waists. The volume is then distorted with unequally spaced fringes due to interference of spherical, rather than plane, wave fronts outside the waist region; the phenomenon and its consequences on Doppler signals are outside the scope of this note and given elsewhere, for example in references 3 and 4.

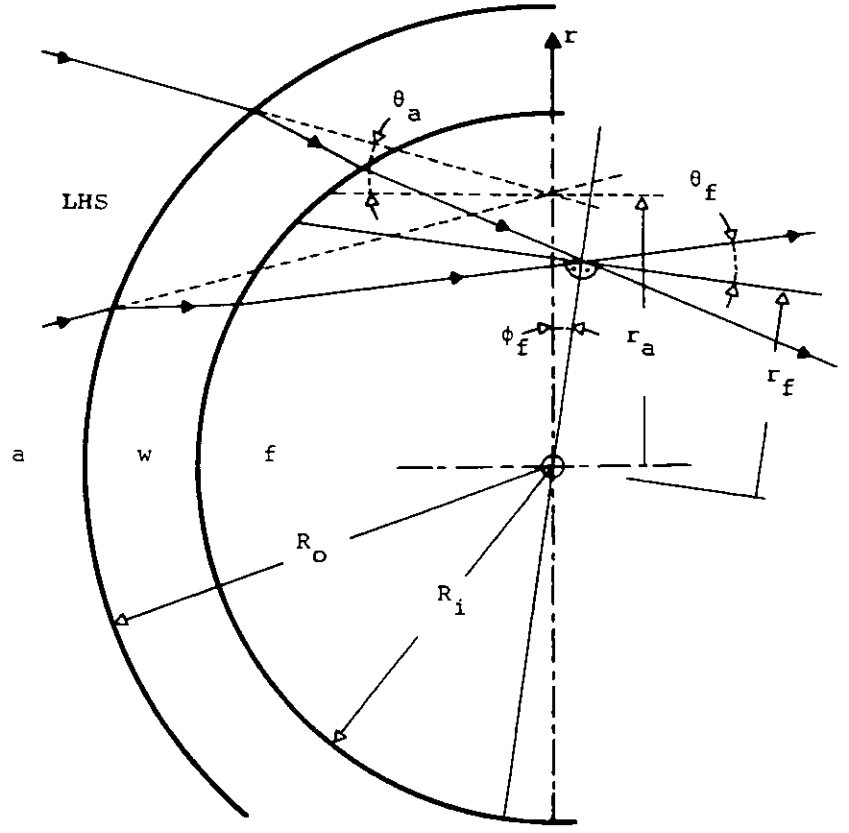

Fig.4 Refraction of laser beams during radial velocity measurements.

3. SUMMARY

Due to the refraction of laser beams at curved interfaces during the LDA measurements in flows with curved boundaries, the position of beam intersection and the half

angle may undergo non-linear changes, in addition to the linear changes in wavelength, with respect to the ones without refraction. Therefore, the corrections may be necessary for the measurements of three velocity components.

The true position of the intersection point, r_f and ϕ_f, and velocity correction factor, C_f, for all three velocity components of flow in cylinders are summarized in the table below. These corrections may also apply for other flows with curved boundaries, such as curved ducts and tubes.

Velocity Component	r_f	ϕ_f	C_f
Axial, Case (a)	eqn.(2)	0	1
Axial, Case (b)	eqn.(4)	eqn.(5)	1
Tangential	$C_f r_a$	0	eqn.(6)
Radial	$C_f r_a$	eqn.(11)	n_a/n_f

Note for axial velocity measurements, Case (a) should be preferred to Case (b) wherever possible, due to the extra refractions and subsequent calculations in the latter case.

REFERENCES

1. F. Durst, A. Melling and J.H. Whitelaw "Principles and Practice of Laser-Doppler Anemometry" Academic Press, 1976.

2. J.D. Boadway and E. Karahan "Correction of Laser Doppler Anemometer Readings for Refraction at Cylindrical Interfaces" DISA Information, No.26, 1981.

3. S. Hanson "Coherent Detection in Laser Doppler Velocimeters" Opto-electronics 6, 263, 1974.

4. H. Kogelnik and T. Li "Laser Beams and Resonators" Appl. Optics 5, 1550, 1966.

APPENDIX 3.3

COMPARISON BETWEEN MEASUREMENTS AND RELEVANT FLOW CALCULATIONS

(This work is published in Proc. Symposium on Three Dimensional Turbulent Shear Flows, ASME Spring Meeing, St. Louis, 1982 - see Ahmadi-Befrui et al, 1982)

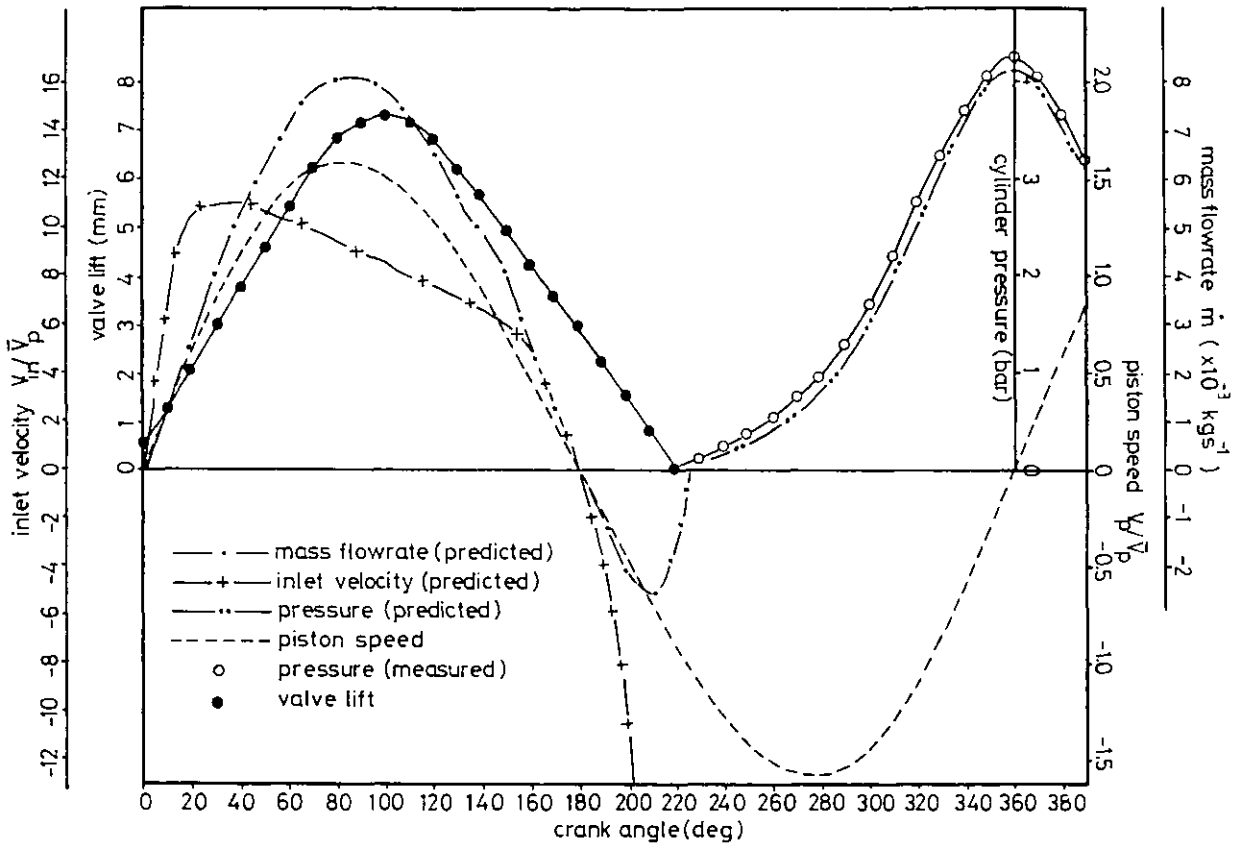

Figure 1 Variation of mass flow rate, inlet velocity, cylinder pressure, piston speed and valve lift with crank angle; flat piston, no swirl, CR = 3.5.

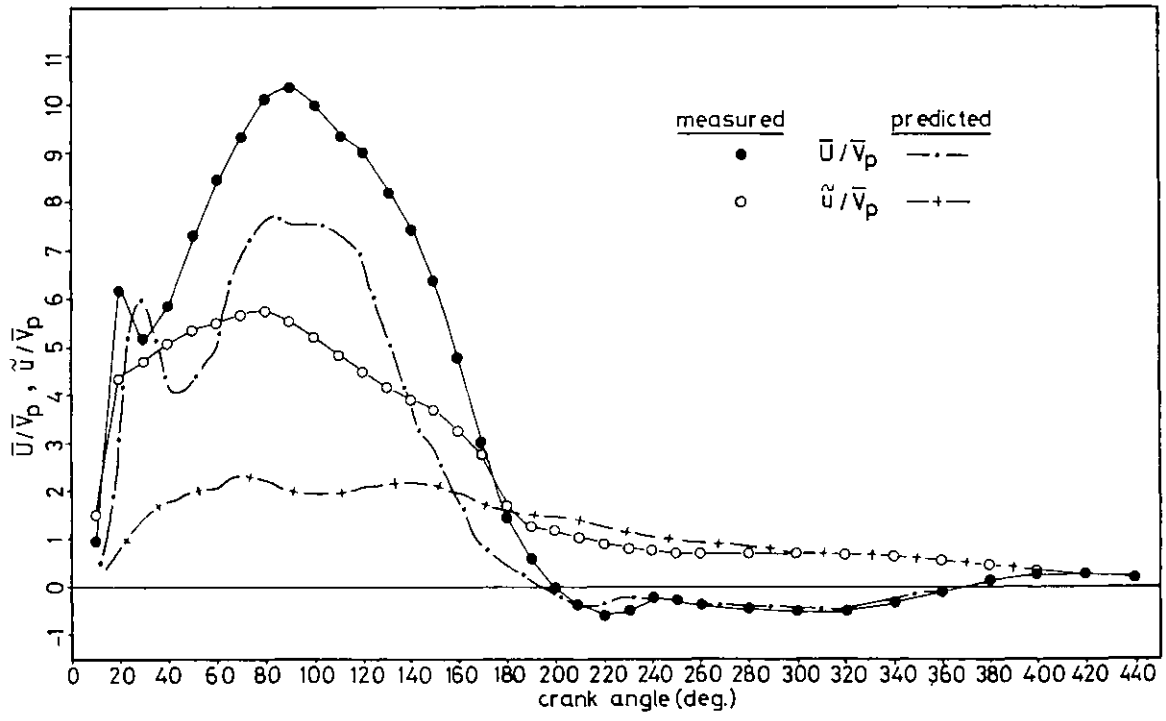

Figure 2 Temporal profiles of axial mean and rms velocities at z = 15 mm, r = 25 mm; flat piston, no swirl, CR = 3.5.

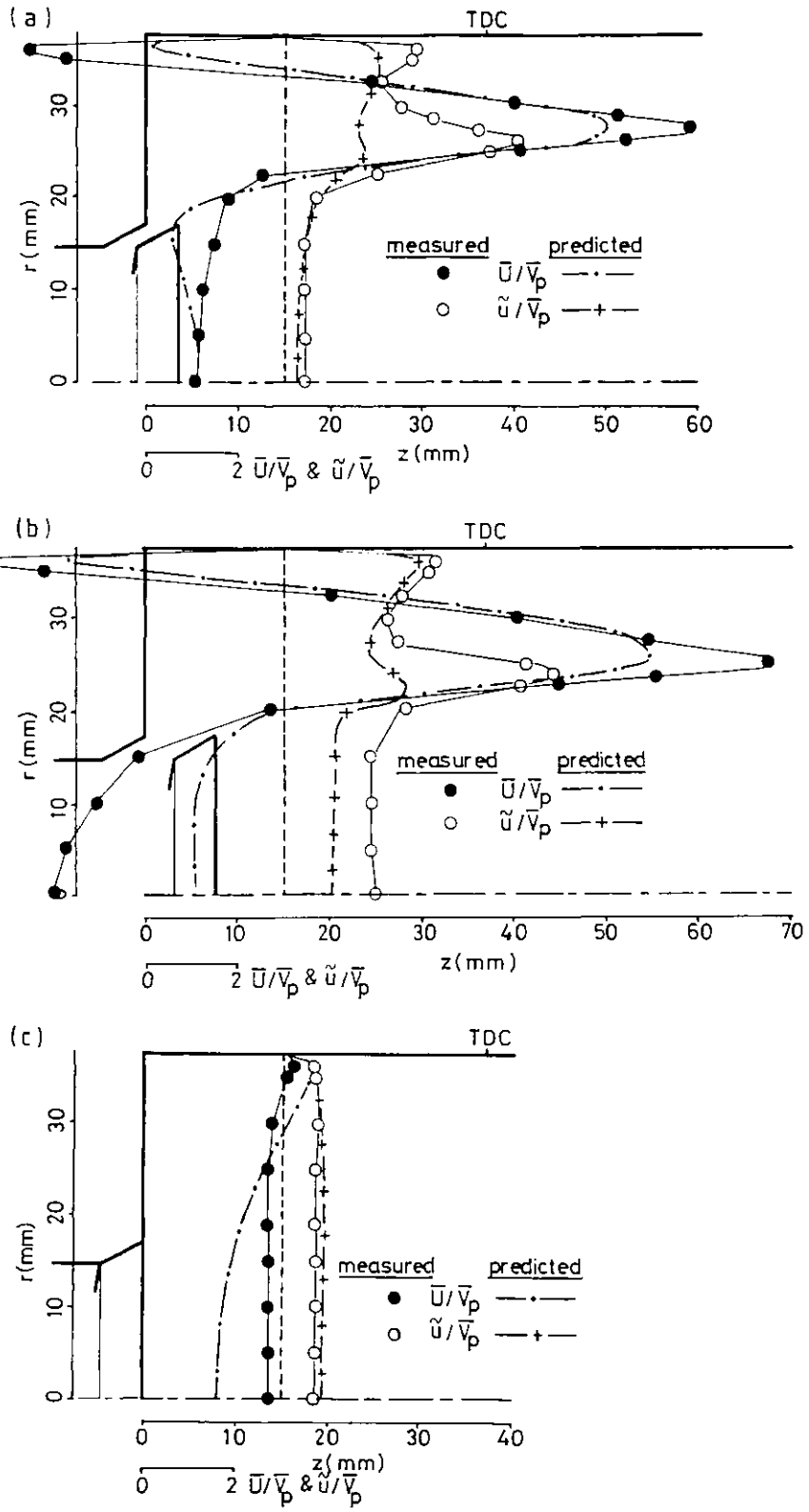

Figure 3 Axial mean and rms velocity profiles at z = 15 mm; flat piston, no swirl, CR = 3.5. (a) θ = 36 degrees (b) θ = 90 degrees (c) θ = 270 degrees

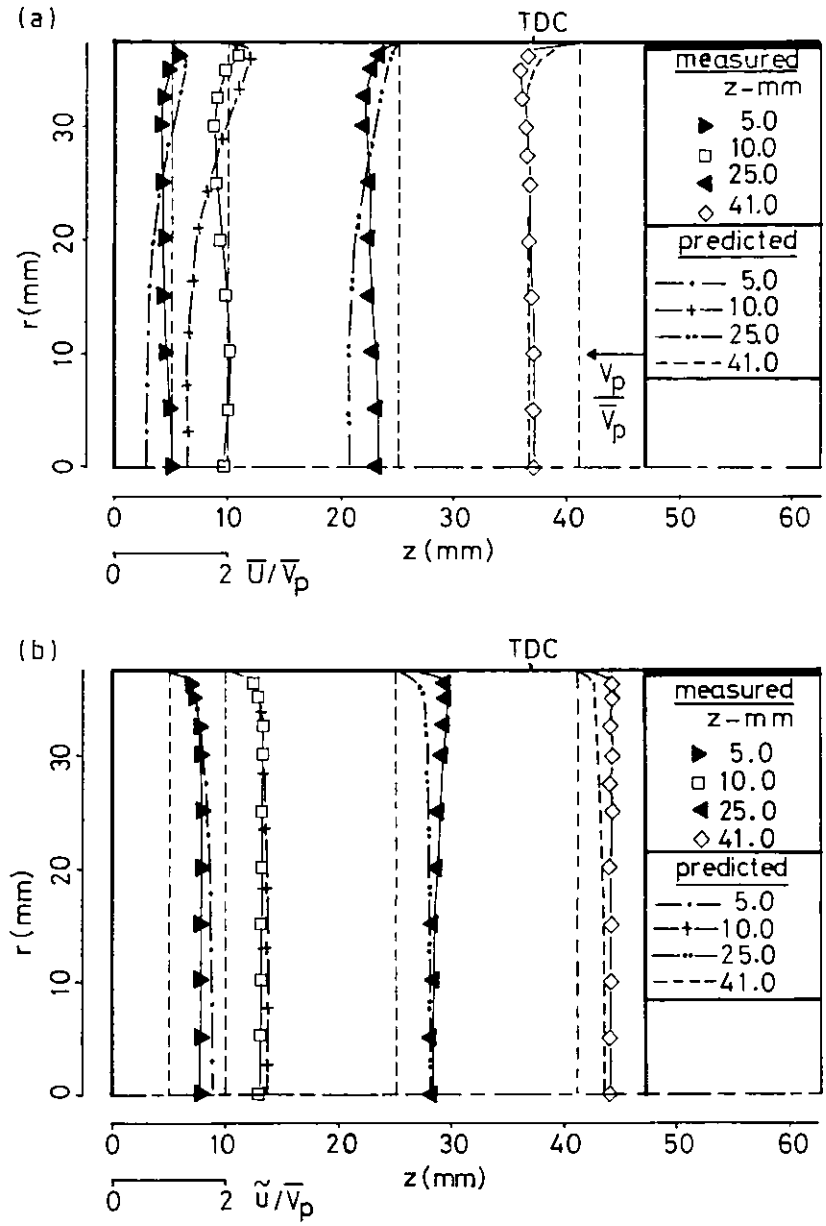

Figure 4 Axial velocity profiles at θ = 324 degrees; flat piston, no swirl, CR = 3.5.
(a) Mean velocity
(b) Rms velocity

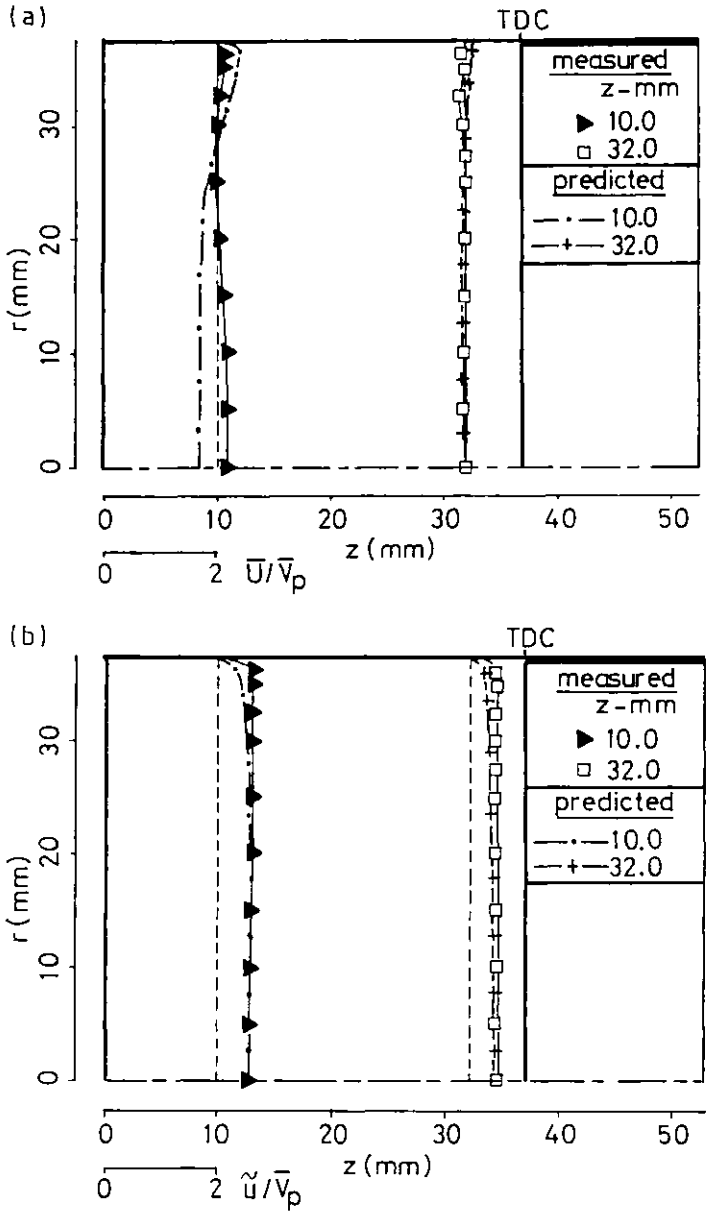

Figure 5 Axial velocity profiles at θ = 360 degrees; flat piston, no swirl, CR = 3.5.

(a) Mean velocity

(b) Rms velocity

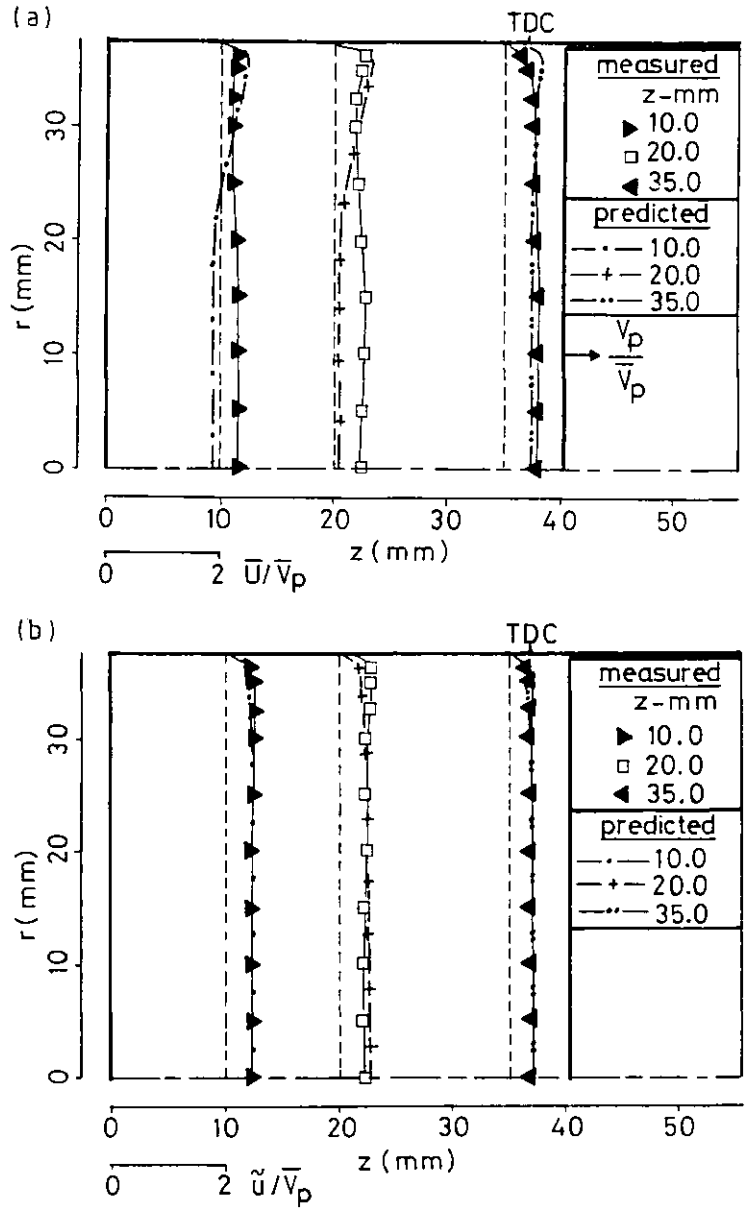

Figure 6 Axial velocity profiles at θ = 380 degrees; flat piston, no swirl, CR = 3.5.
(a) Mean velocity
(b) Rms velocity

FIGURES

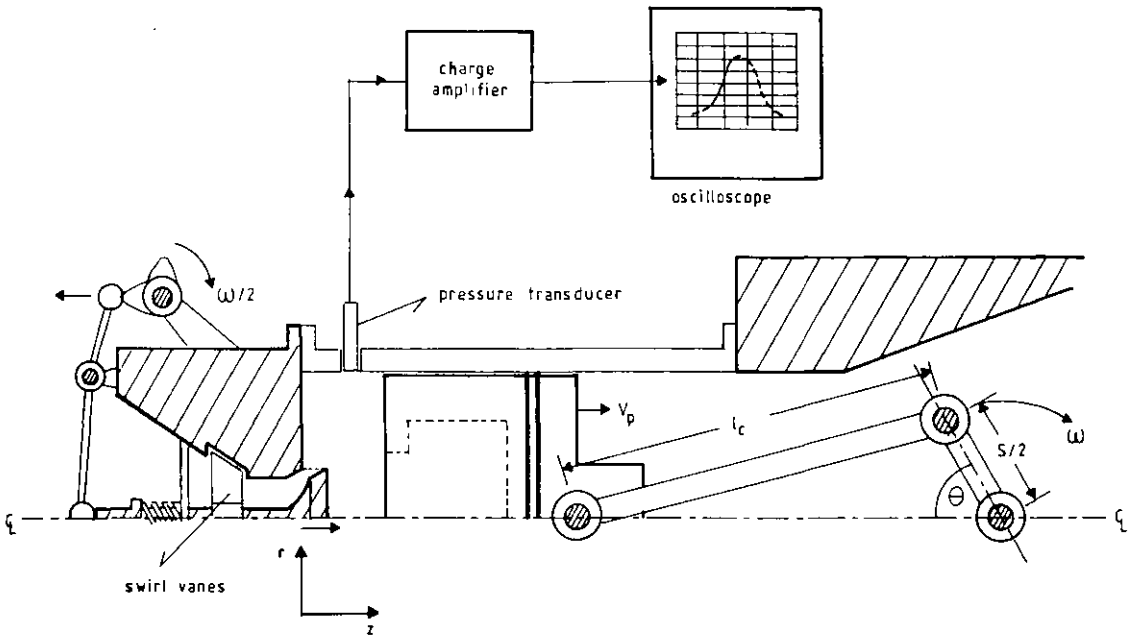

Figure 3.1 Schematic of four-stroke model engine and pressure measurement system.

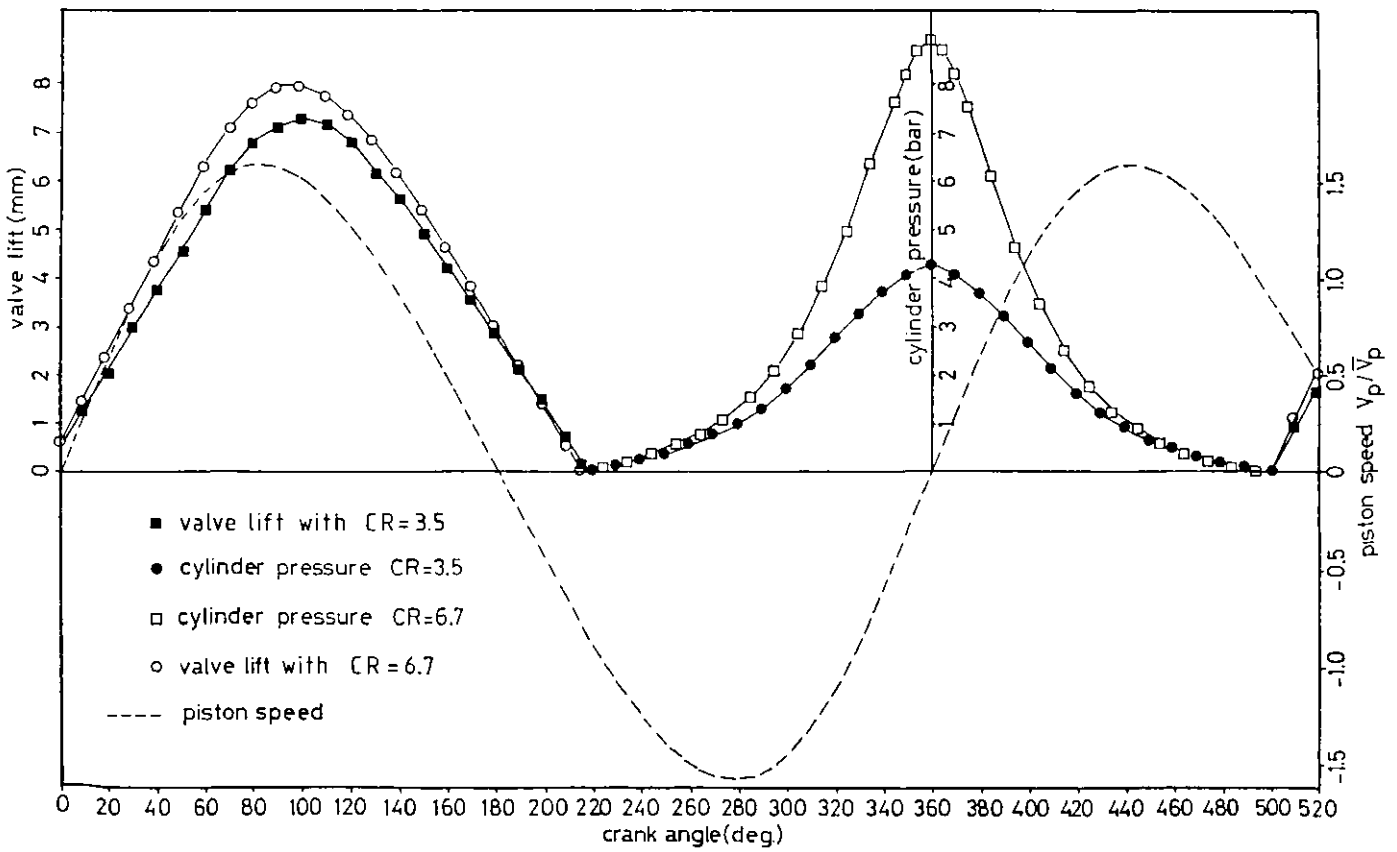

Figure 3.2 Variation of cylinder pressure, valve lift and piston speed with crank angle.

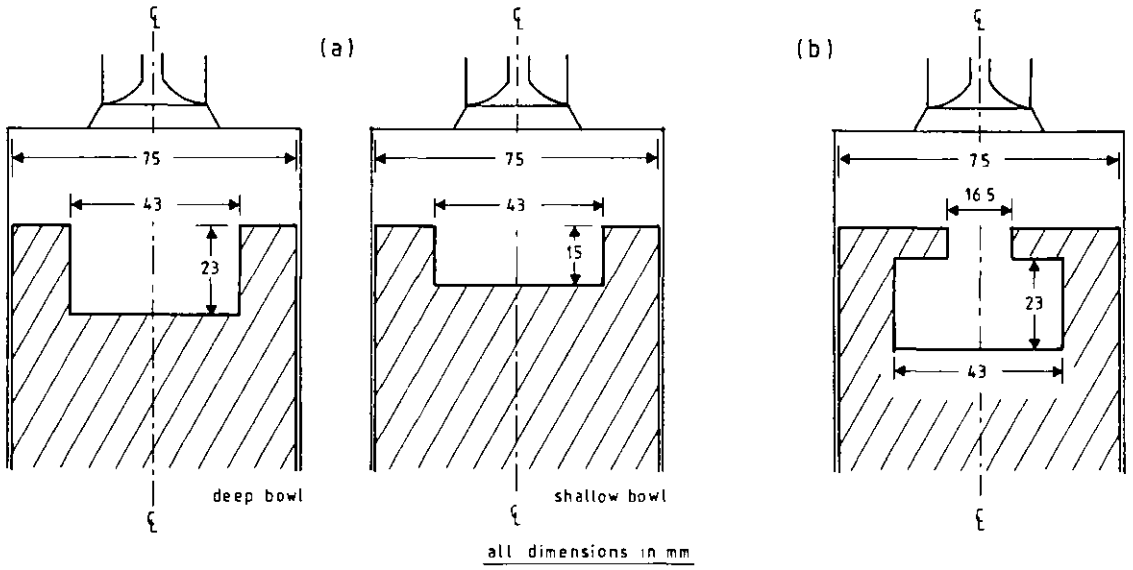

Figure 3.3 Piston bowl configurations used with CR = 3.5.
(a) Cylindrical bowls
(b) Re-entrant type bowl

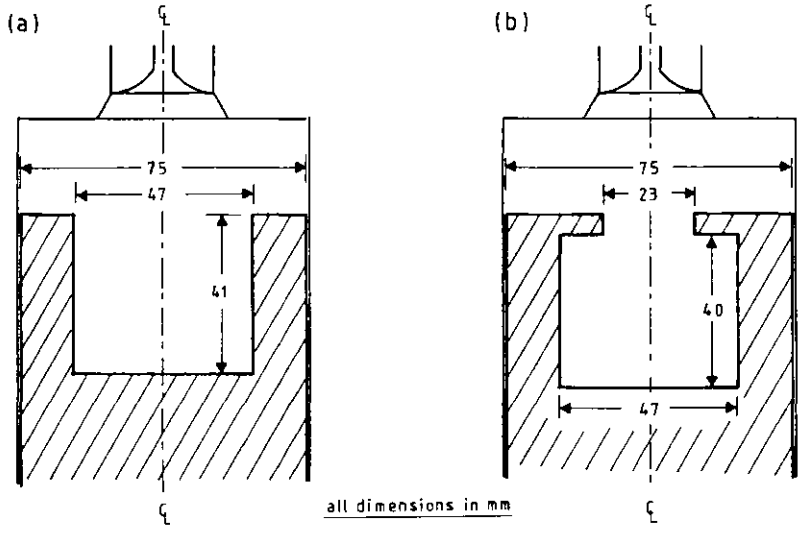

Figure 3.4 Piston bowl configurations used with CR = 6.7.
(a) Cylindrical bowl
(b) Re-entrant type bowl

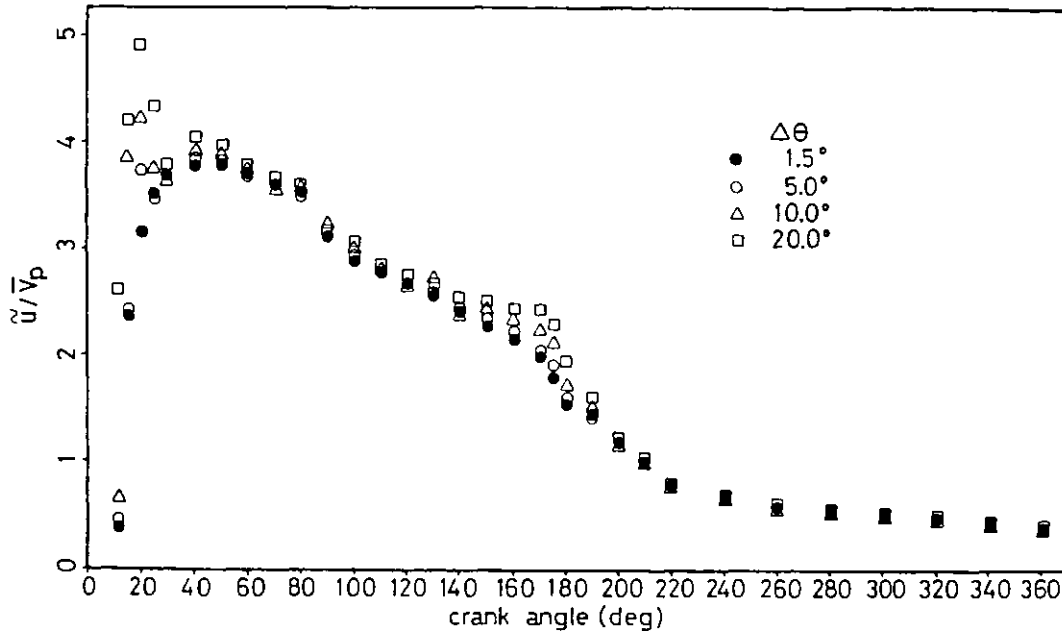

Figure 3.5 Variation of axial rms velocity with crank angle for various crank angle windows at z = 15 mm, r = 25 mm; flat piston, CR = 3.5.

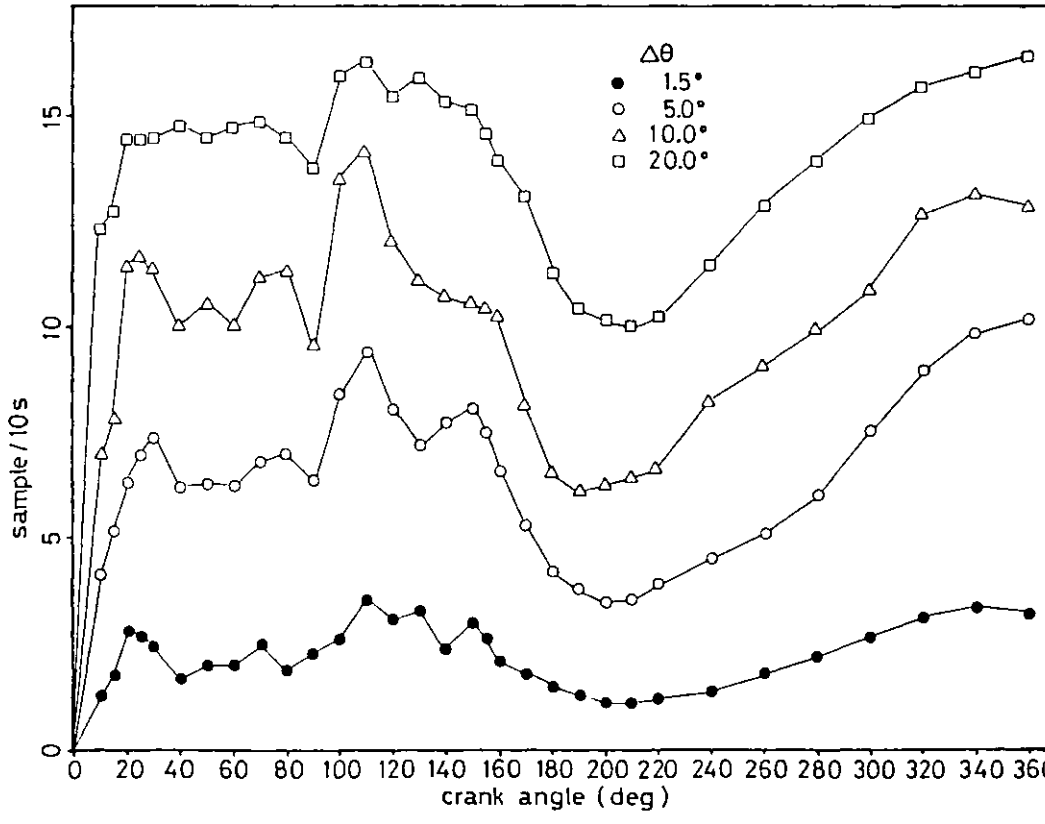

Figure 3.6 Variation of sample rate with crank angle for various crank angle windows at z = 15 mm, r = 25 mm; flat piston, CR = 3.5.

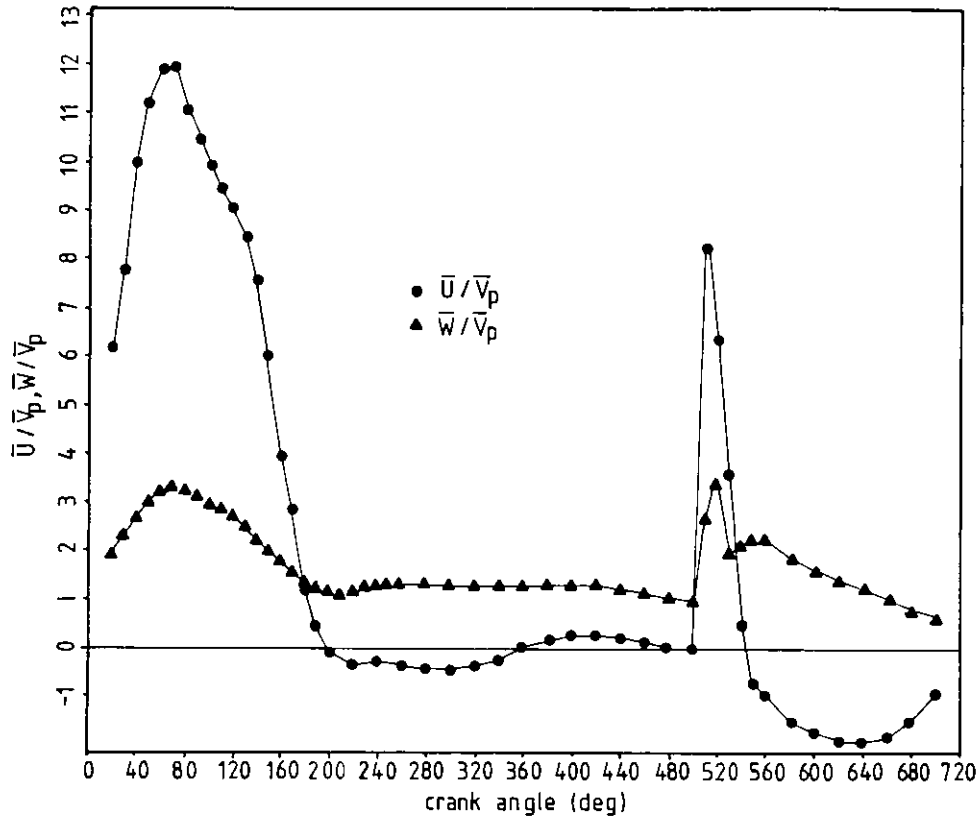

Figure 3.7 Temporal profiles of axial and swirl mean velocity components at z = 15 mm, r = 25 mm; flat piston, CR = 3.5.

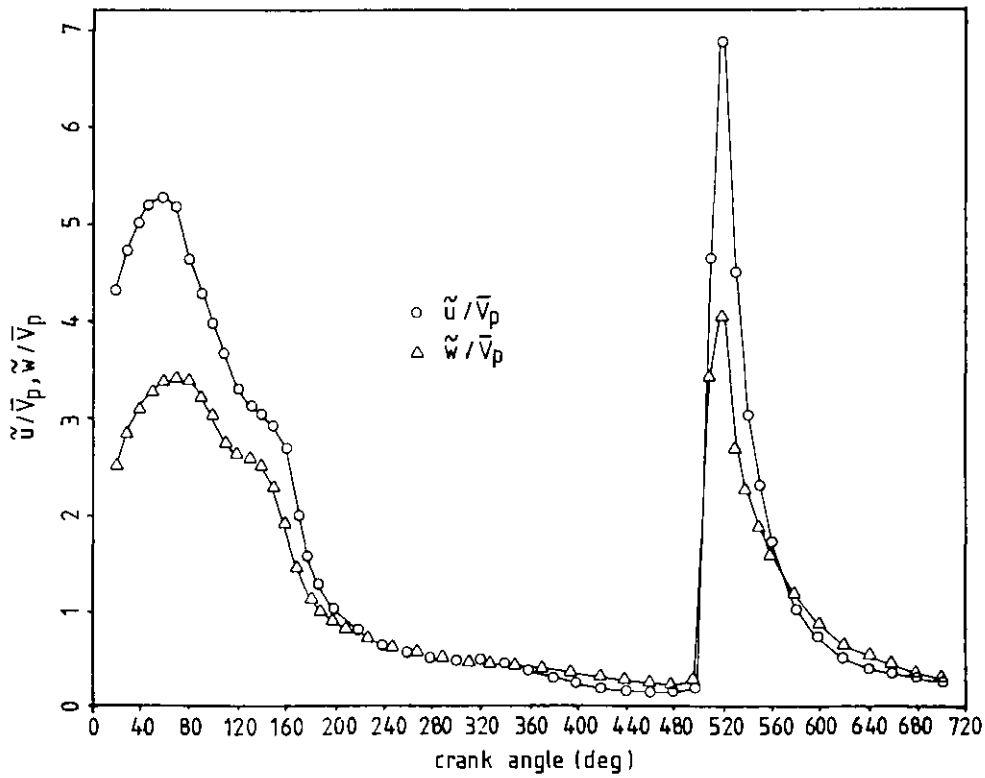

Figure 3.8 Temporal profiles of axial and swirl rms velocity components at z = 15 mm, r = 25 mm; flat piston, CR = 3.5.

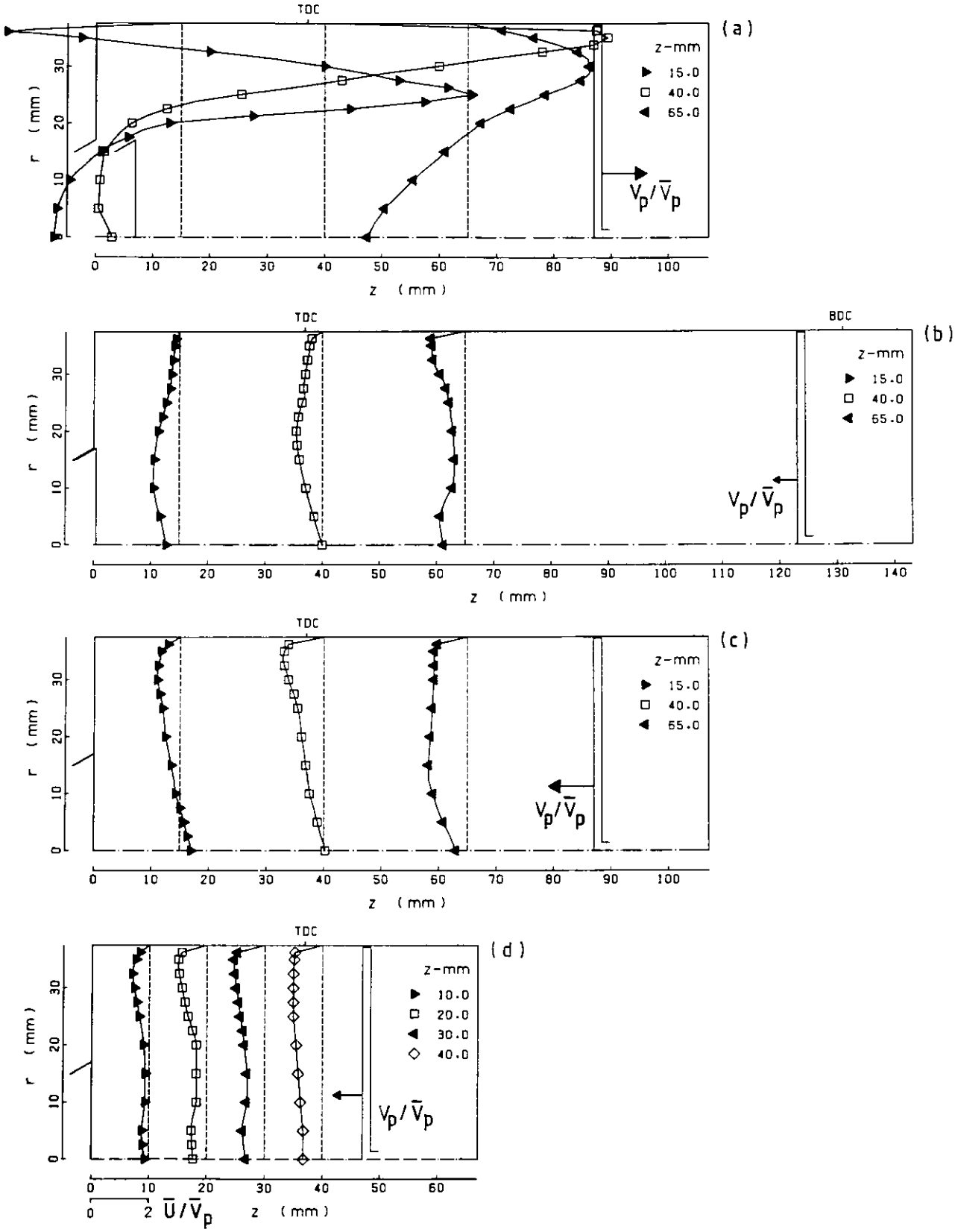

Figure 3.9 cont'd...

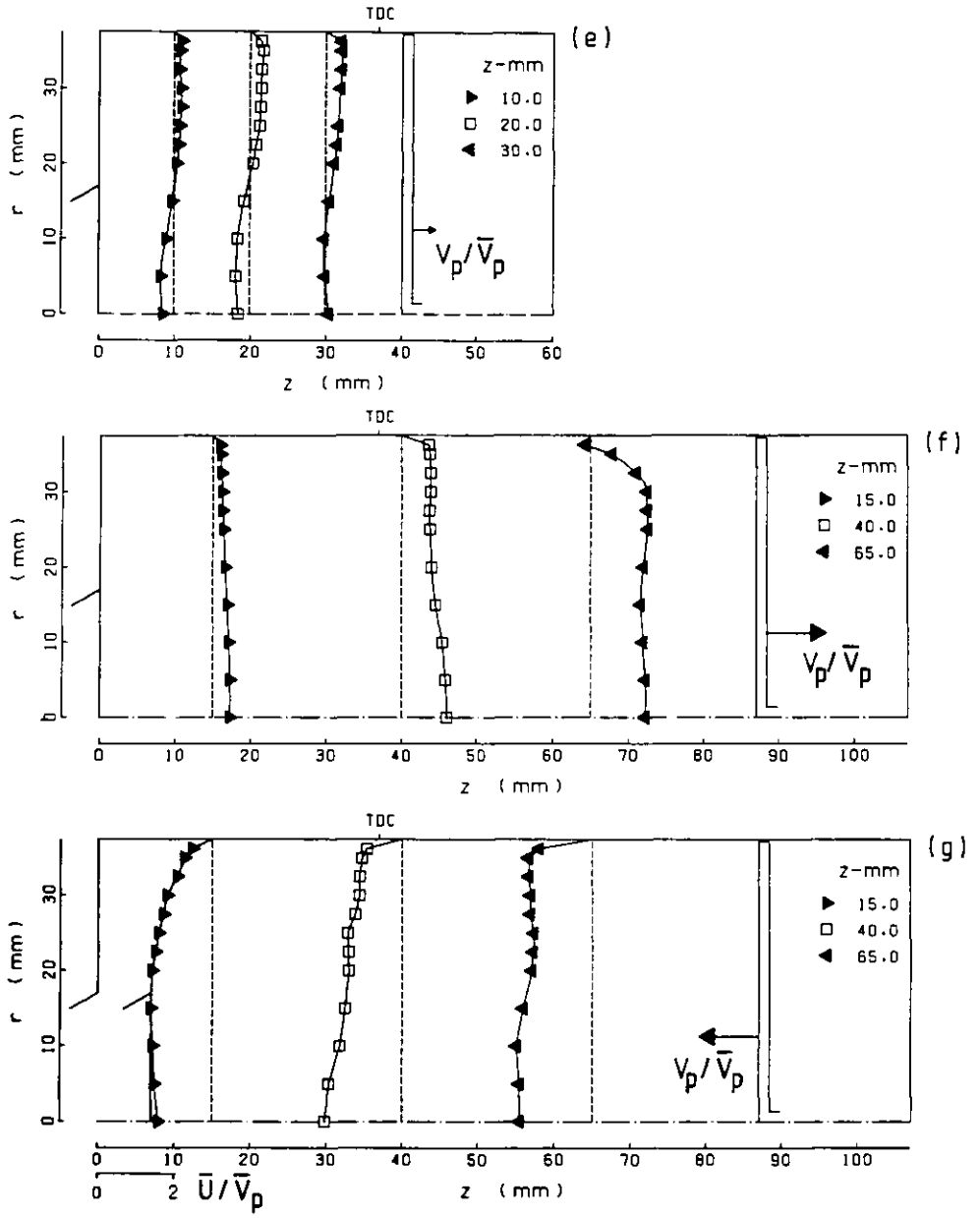

Figure 3.9 Axial mean velocity profiles;flat piston, CR = 3.5. (a) θ = 90 degrees (b) θ = 216 degrees (c) θ = 270 degrees (d) θ = 324 degrees (e) θ = 380 degrees (f) θ = 450 degrees (g) θ = 630 degrees

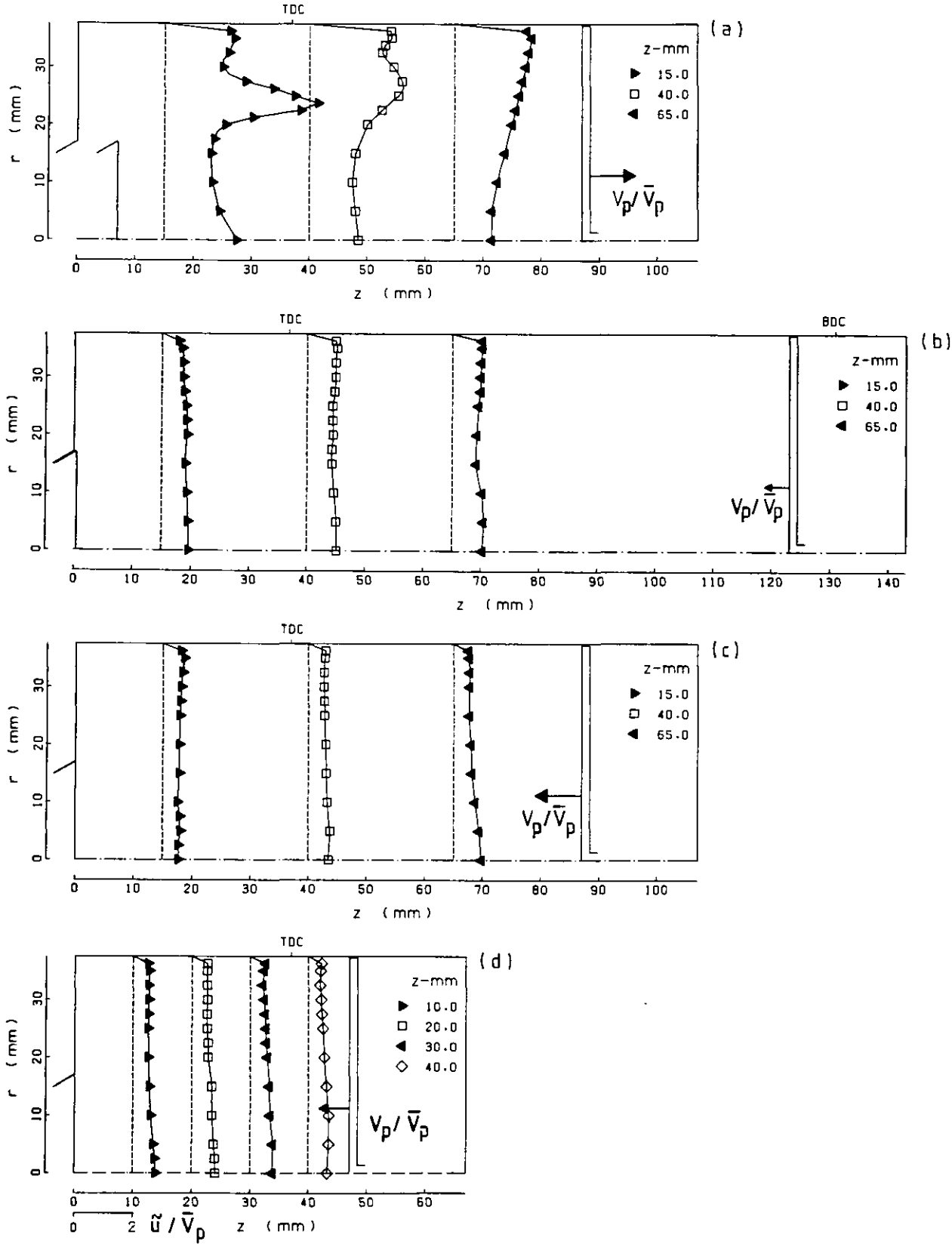

Figure 3.10 cont'd...

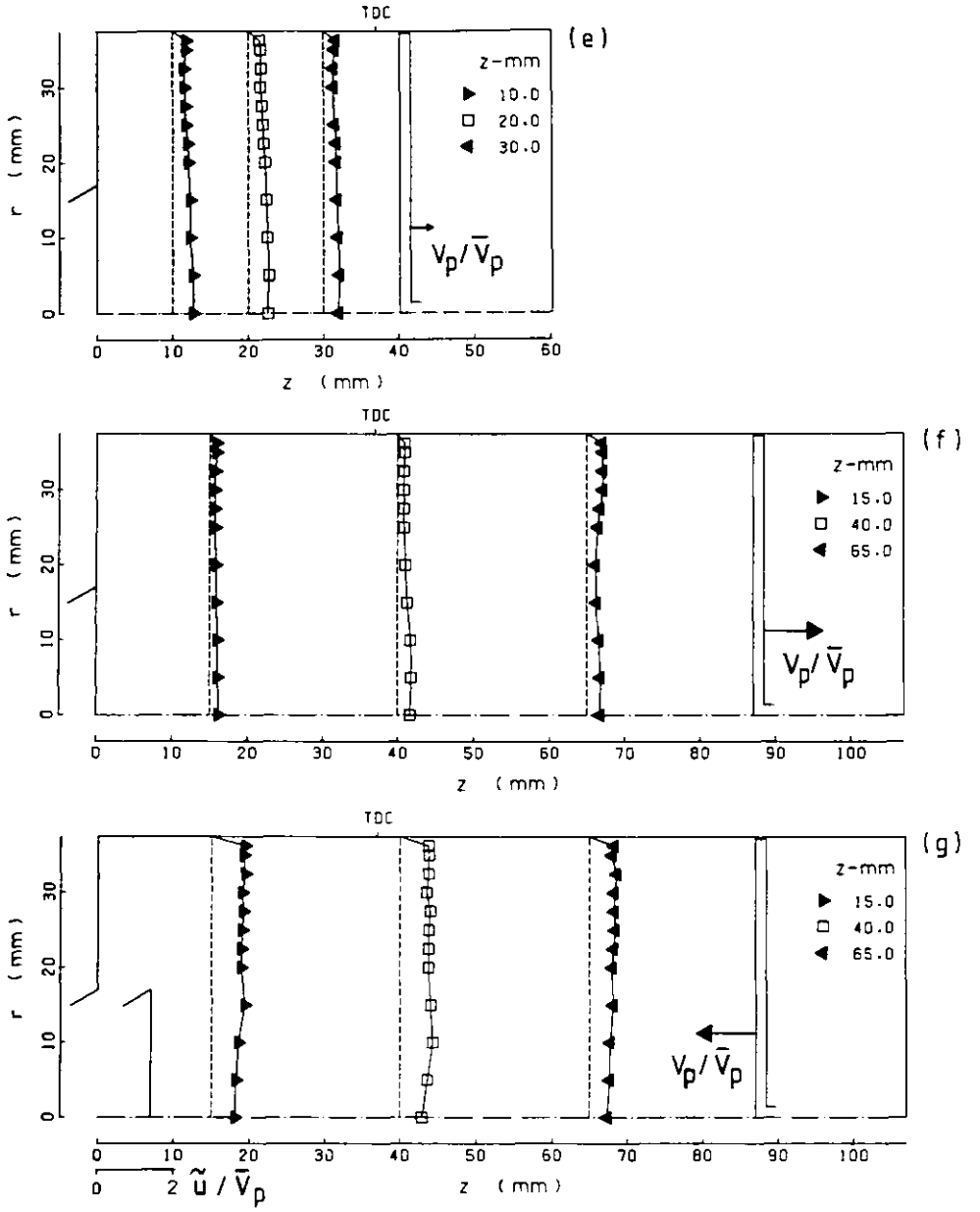

Figure 3.10 Axial rms velocity profiles; flat piston, CR = 3.5. (a) θ = 90 degrees (b) θ = 216 degrees (c) θ = 270 degrees (d) θ = 324 degrees (e) θ = 380 degrees (f) θ = 450 degrees (g) θ = 630 degrees

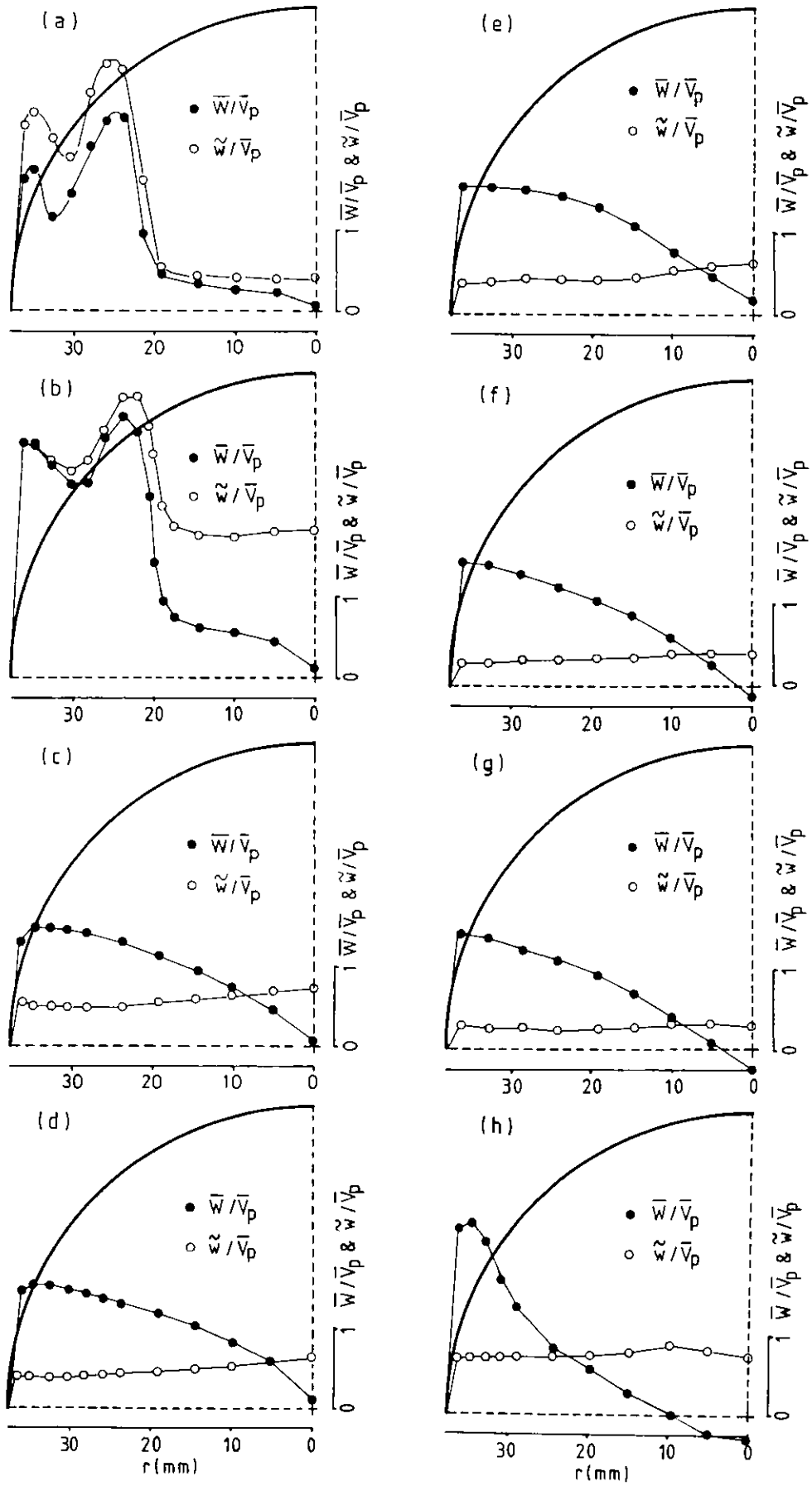

Figure 3.11 Swirl mean & rms velocity profiles at z = 15 mm; flat piston, CR = 3.5. (a) Θ = 36 degrees (b) Θ = 90 degrees (c) Θ = 270 degrees (d) Θ = 324 degrees (e) Θ = 360 degrees (f) Θ = 396 degrees (g) Θ = 450 degrees (h) Θ = 684 degrees

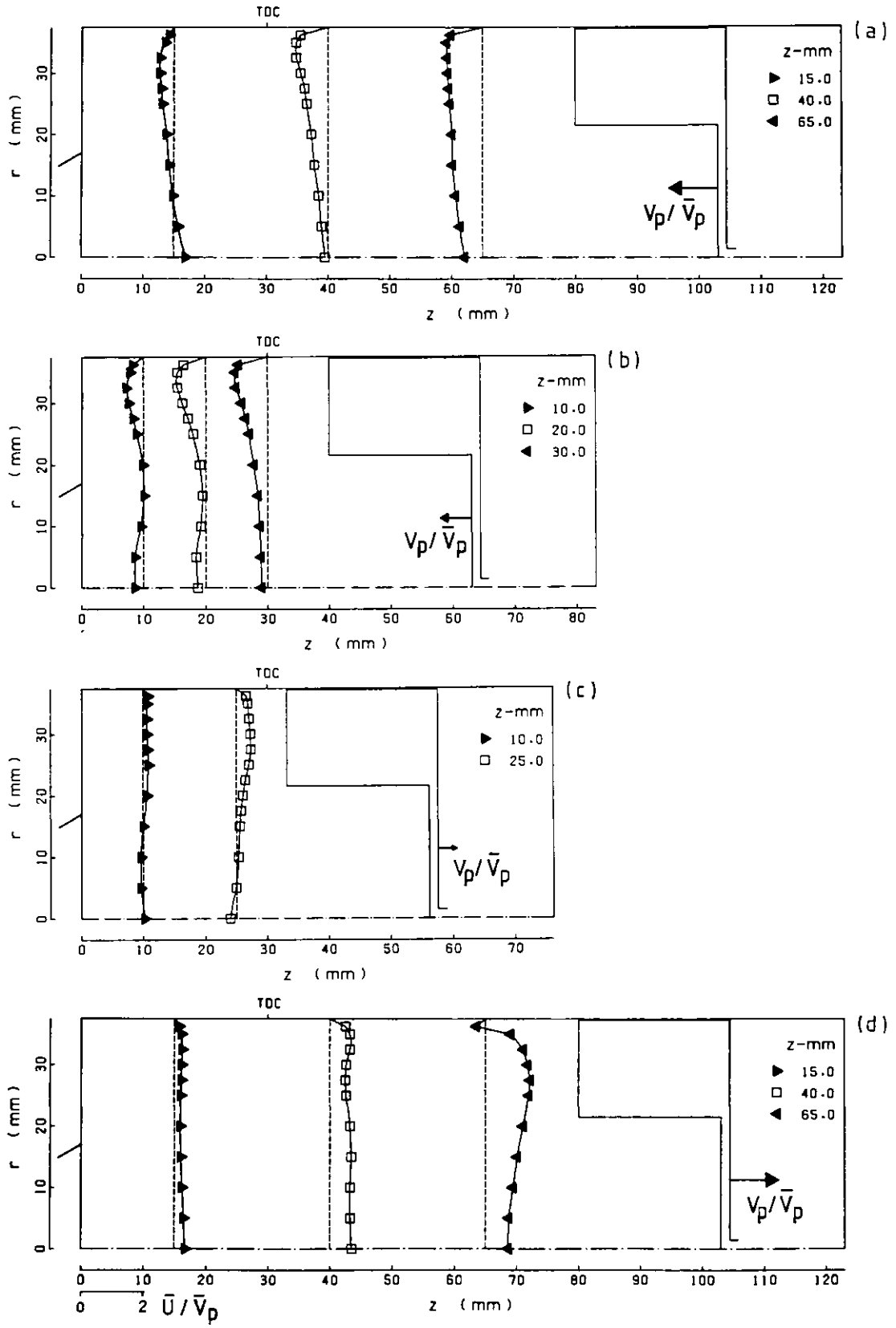

Figure 3.12 Axial mean velocity profiles; deep cylindrical bowl, CR = 3.5. (a) θ = 270 degrees (b) θ = 324 degrees (c) θ = 380 degrees (d) θ = 450 degrees

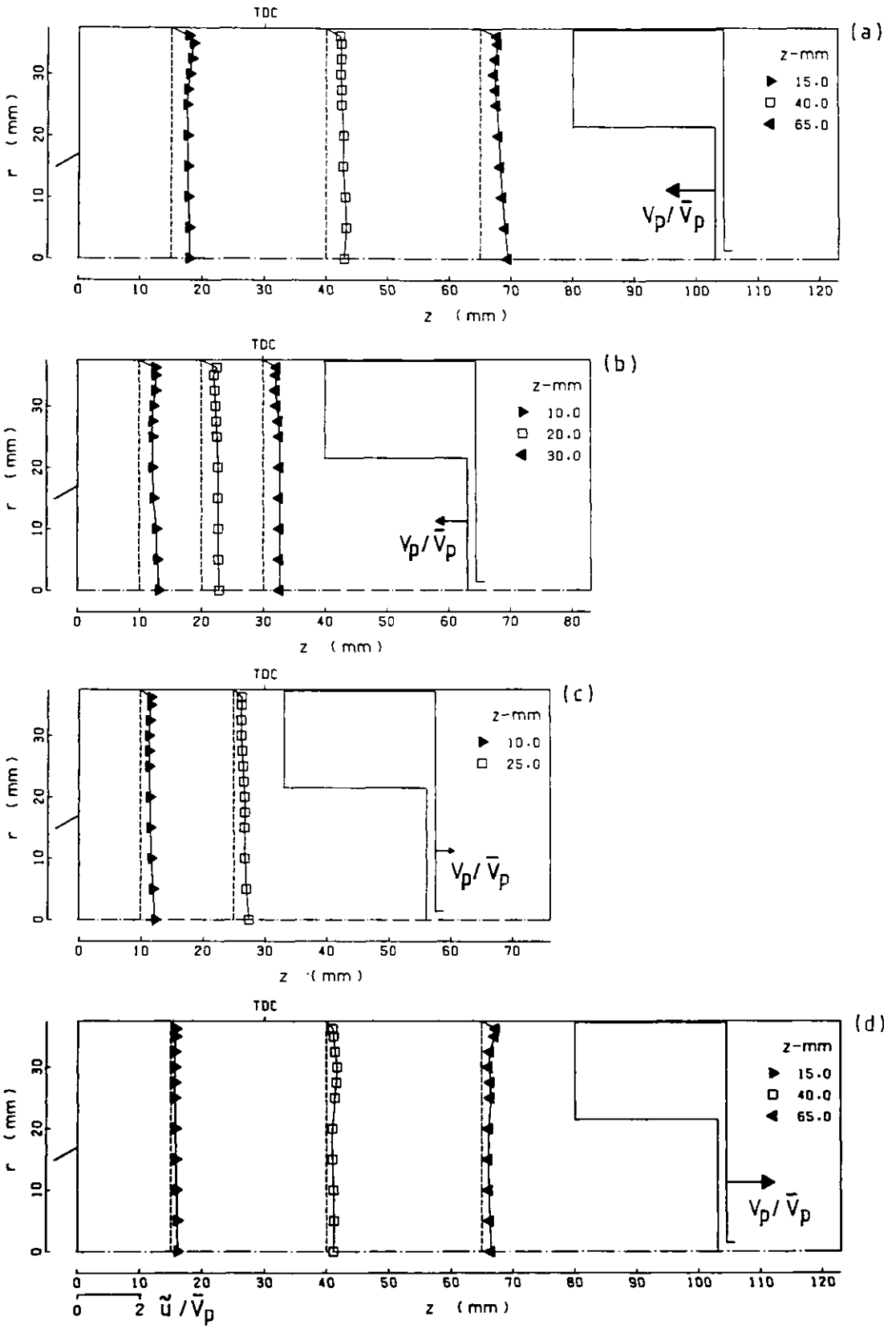

Figure 3.13 Axial rms velocity profiles; deep cylindrical bowl, CR = 3.5. (a) θ =270 degrees (b) θ = 324 degrees (c) θ = 380 degrees (d) θ = 450 degrees

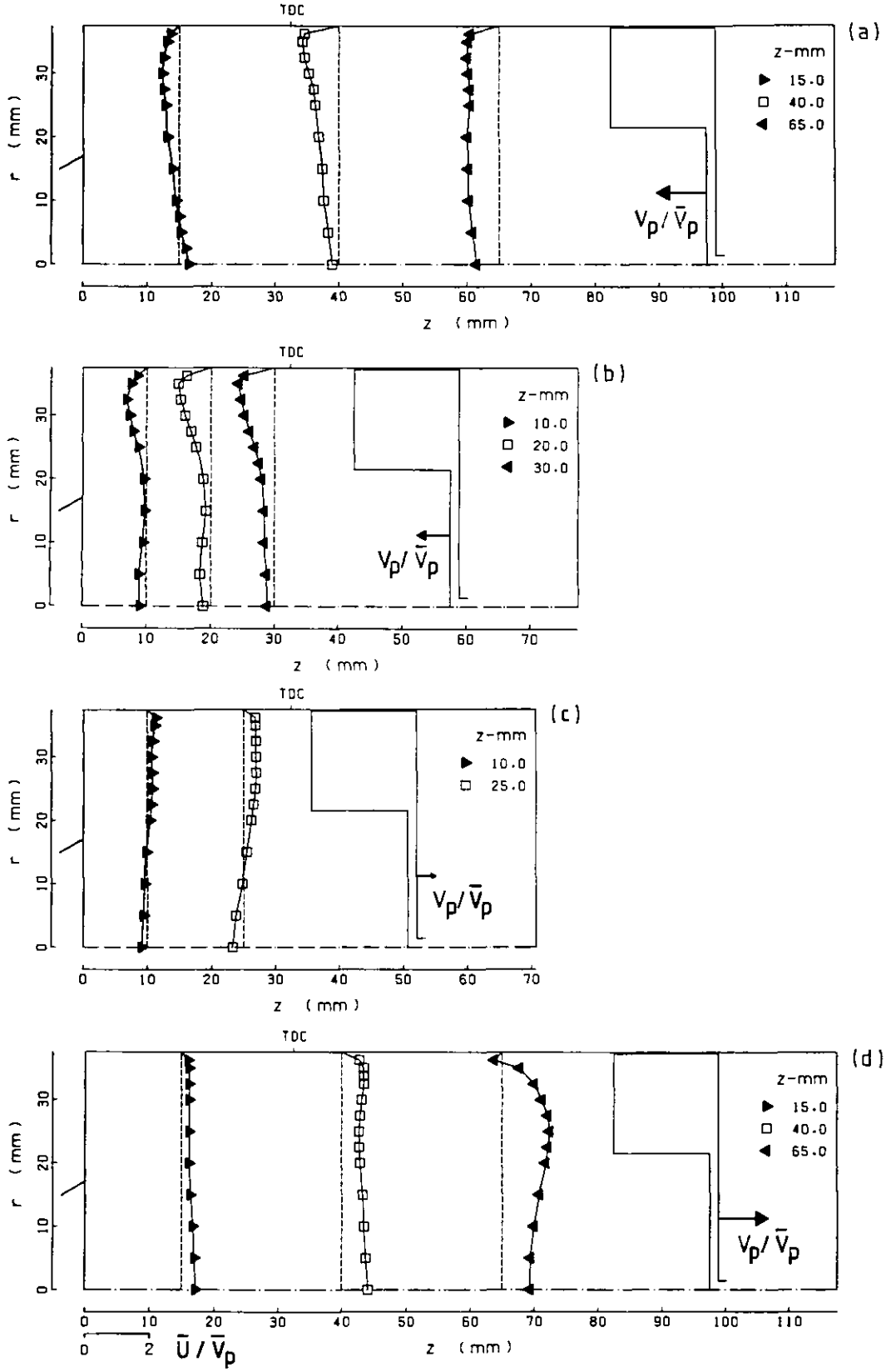

Figure 3.14 Axial mean velocity profiles; shallow cylindrical bowl, CR = 3.5. (a) θ = 270 degrees (b) θ = 324 degrees (c) θ = 380 degrees (d) θ = 450 degrees

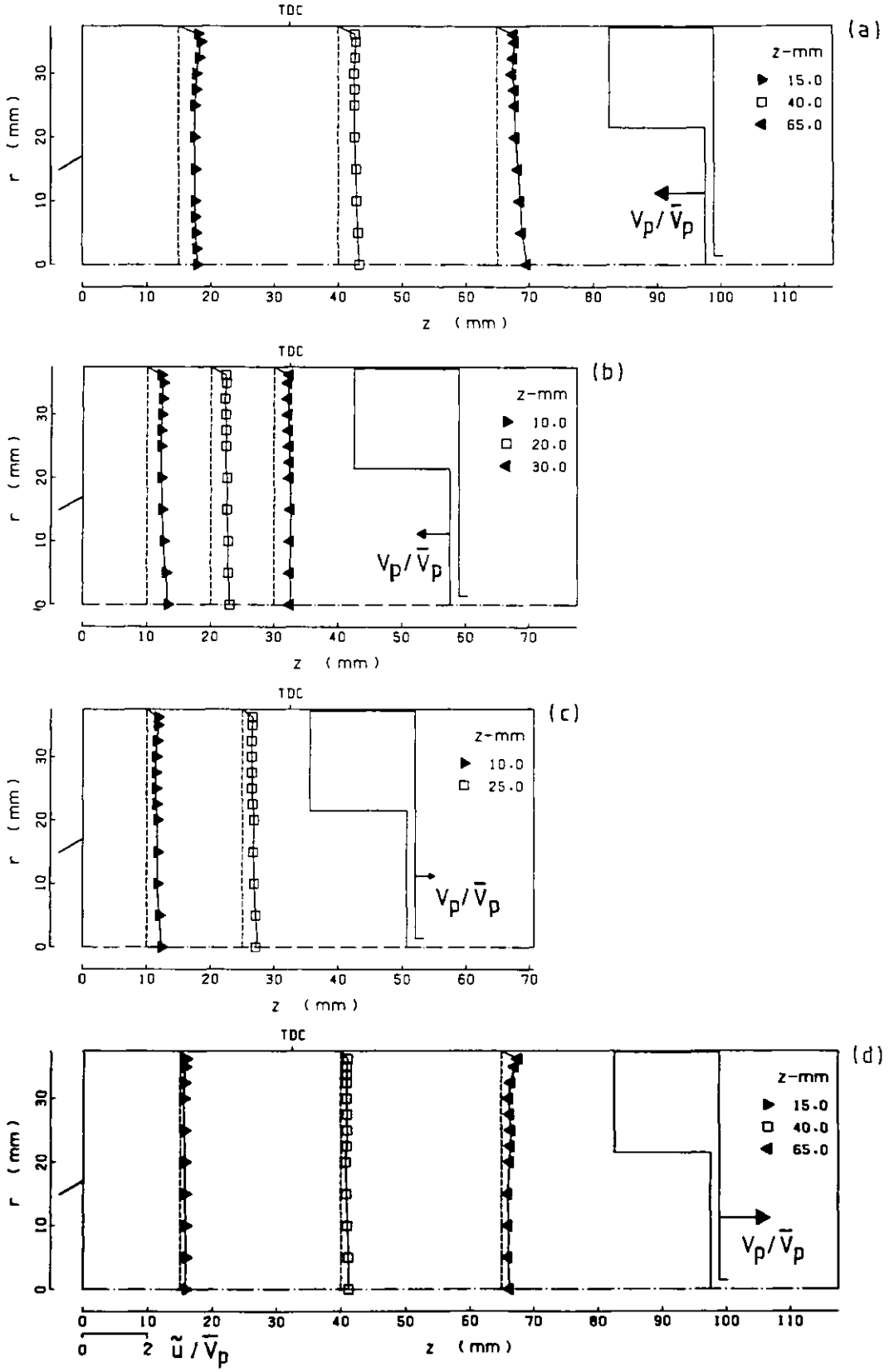

Figure 3.15 Axial rms velocity profiles; shallow cylindrical bowl, CR = 3.5. (a) θ = 270 degrees (b) θ = 324 degrees (c) θ = 380 degrees (d) θ = 450 degrees

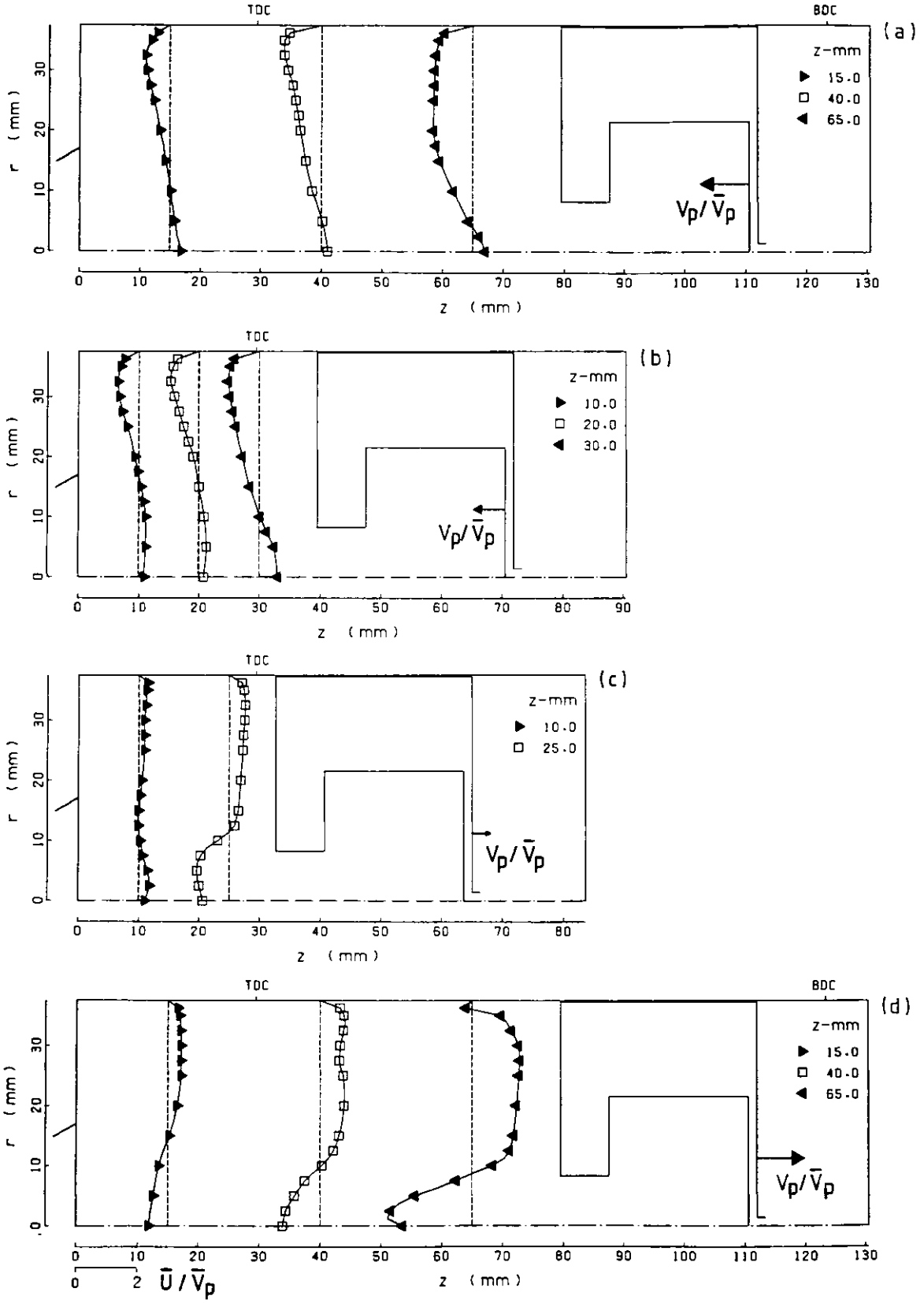

Figure 3.16 Axial mean velocity profiles; re-entrant type bowl, CR = 3.5. (a) Θ = 270 degrees (b) Θ = 324 degrees (c) Θ = 380 degrees (d) Θ = 450 degrees

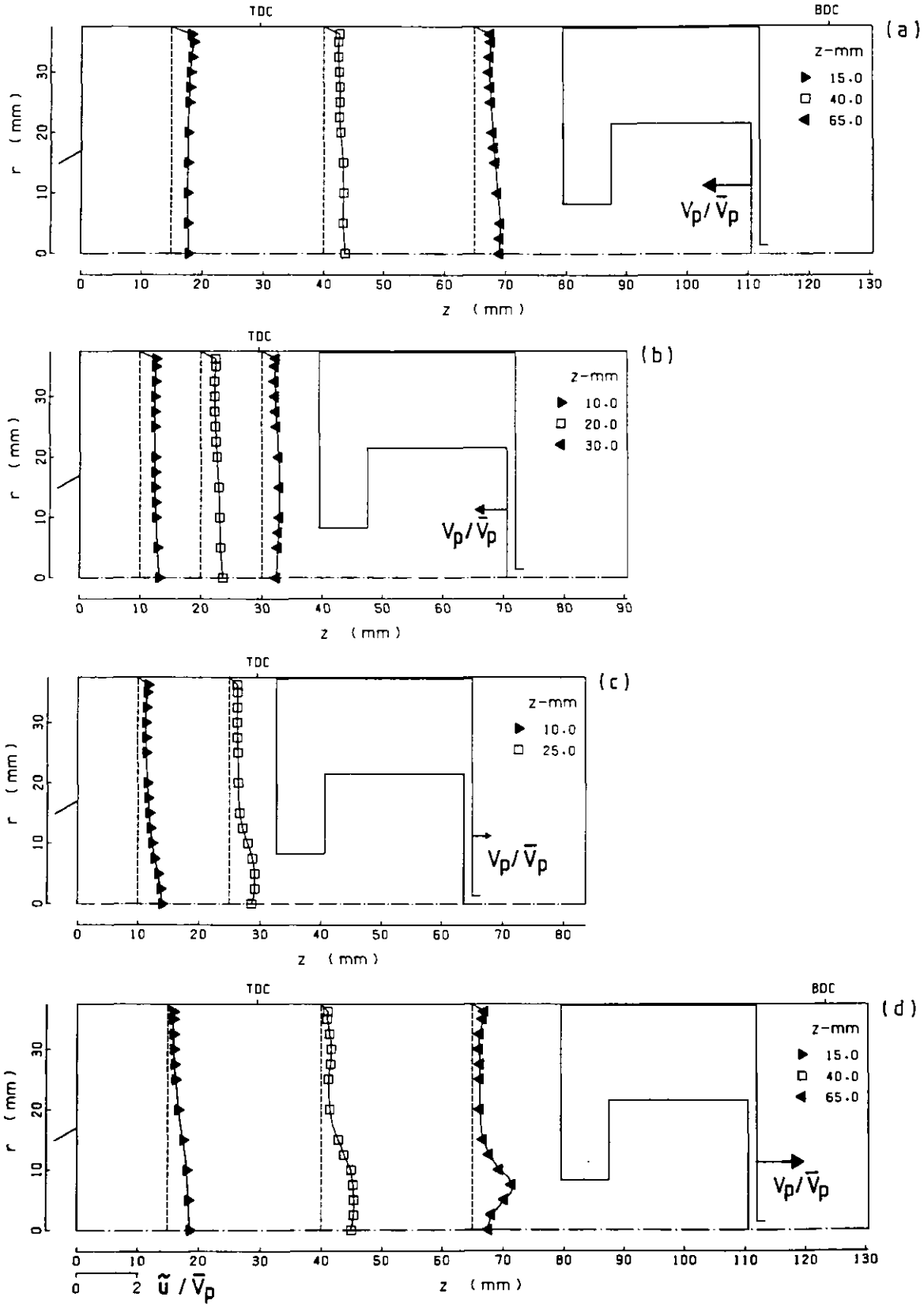

Figures 3.17 Axial rms velocity profiles; re-entrant type bowl, CR = 3.5. (a) Θ = 270 degrees (b) Θ = 324 degrees (c) Θ = 380 degrees (d) Θ = 450 degrees

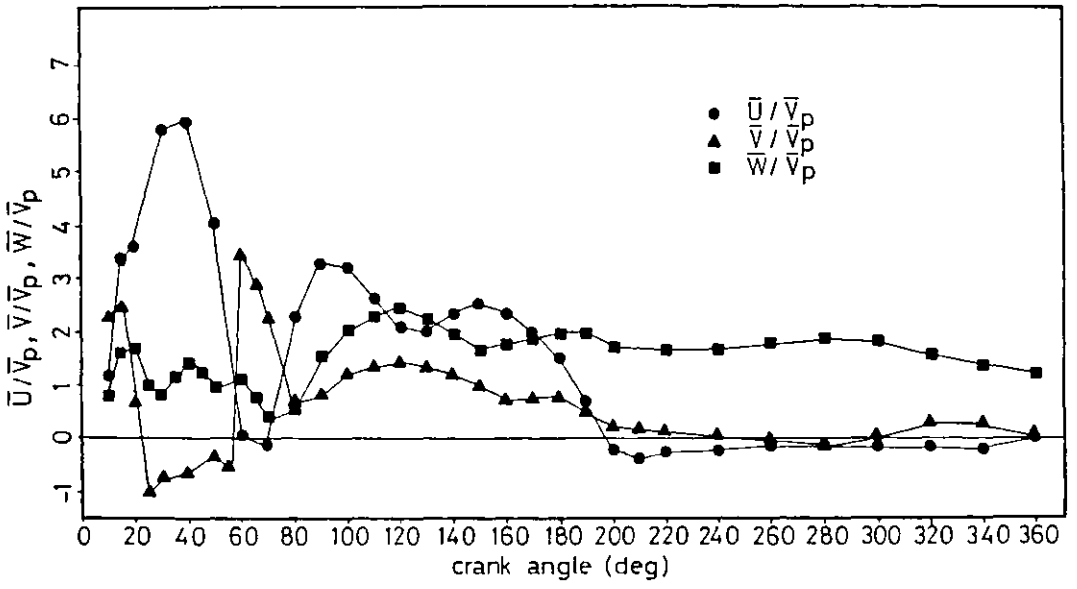

Figure 3.18 Temporal profiles of axial,radial and swirl mean velocity components at z = 10 mm, r = 25 mm; flat piston, CR = 6.7.

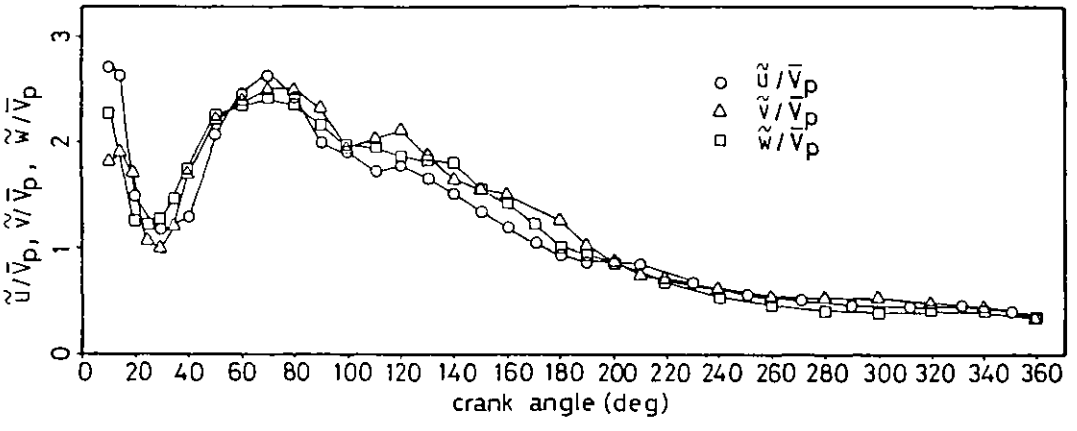

Figure 3.19 Temporal profiles of axial,radial and swirl rms velocity components at z = 10 mm, r = 25 mm; flat piston, CR = 6.7.

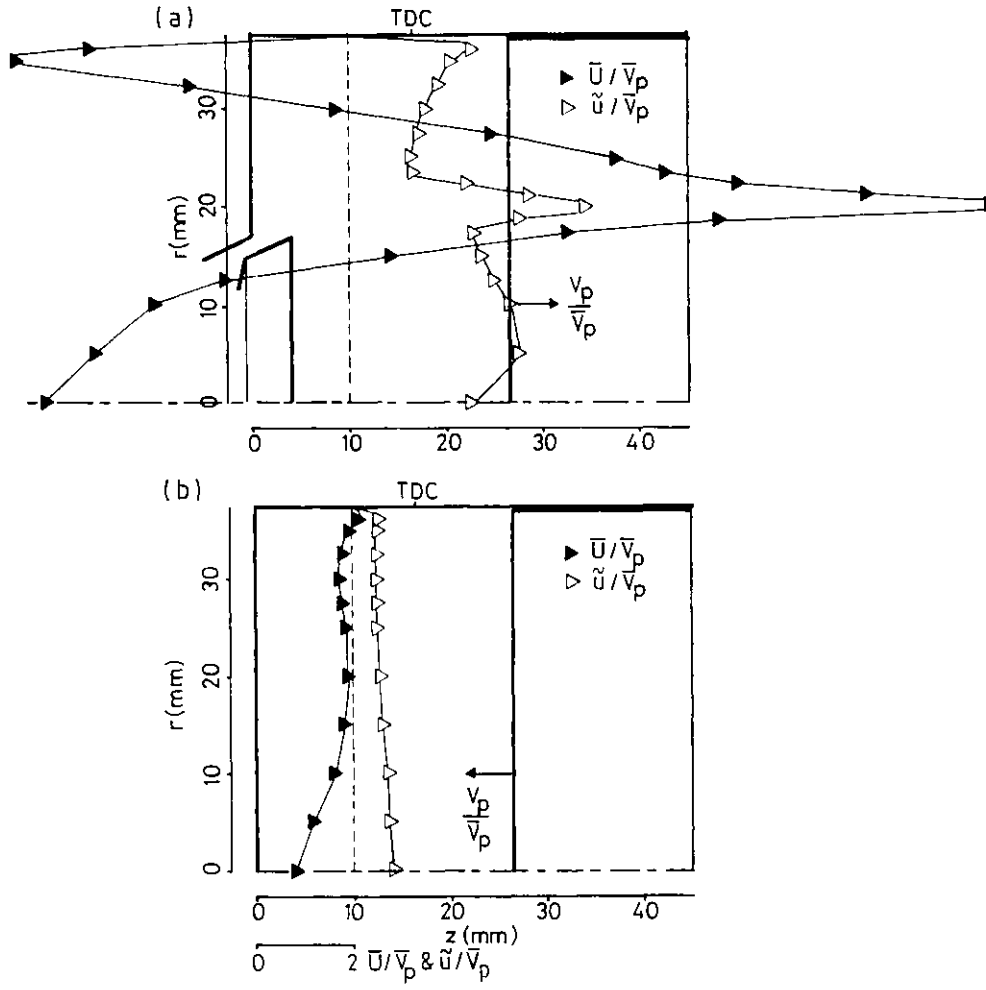

Figure 3.20 Axial mean and rms velocity profiles at z = 10 mm; flat piston, CR = 6.7. (a) Θ = 36 degrees (b) Θ = 324 degrees

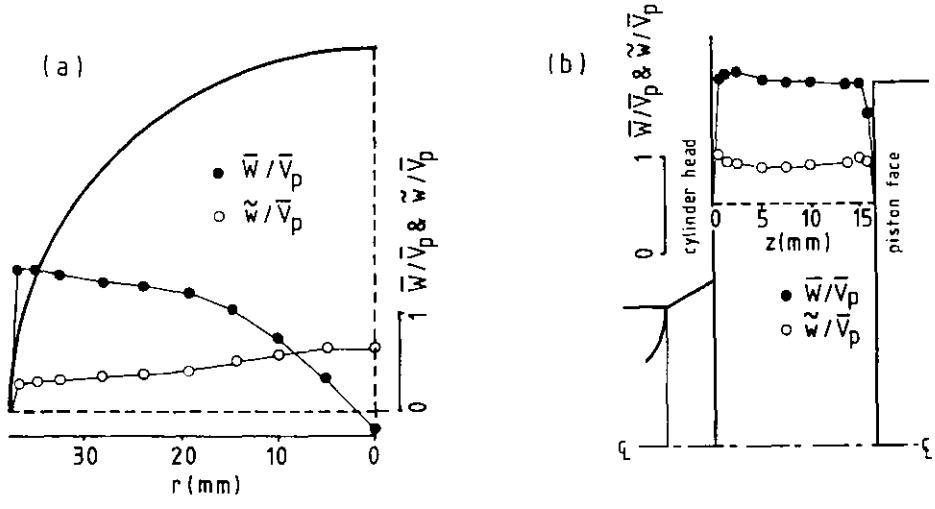

Figure 3.21 Swirl mean and rms velocity profiles; flat piston, CR = 6.7. (a) Radial profiles at Θ = 360 degrees, z = 10 mm (b) Axial profiles at Θ = 360 degrees, r = 25 mm

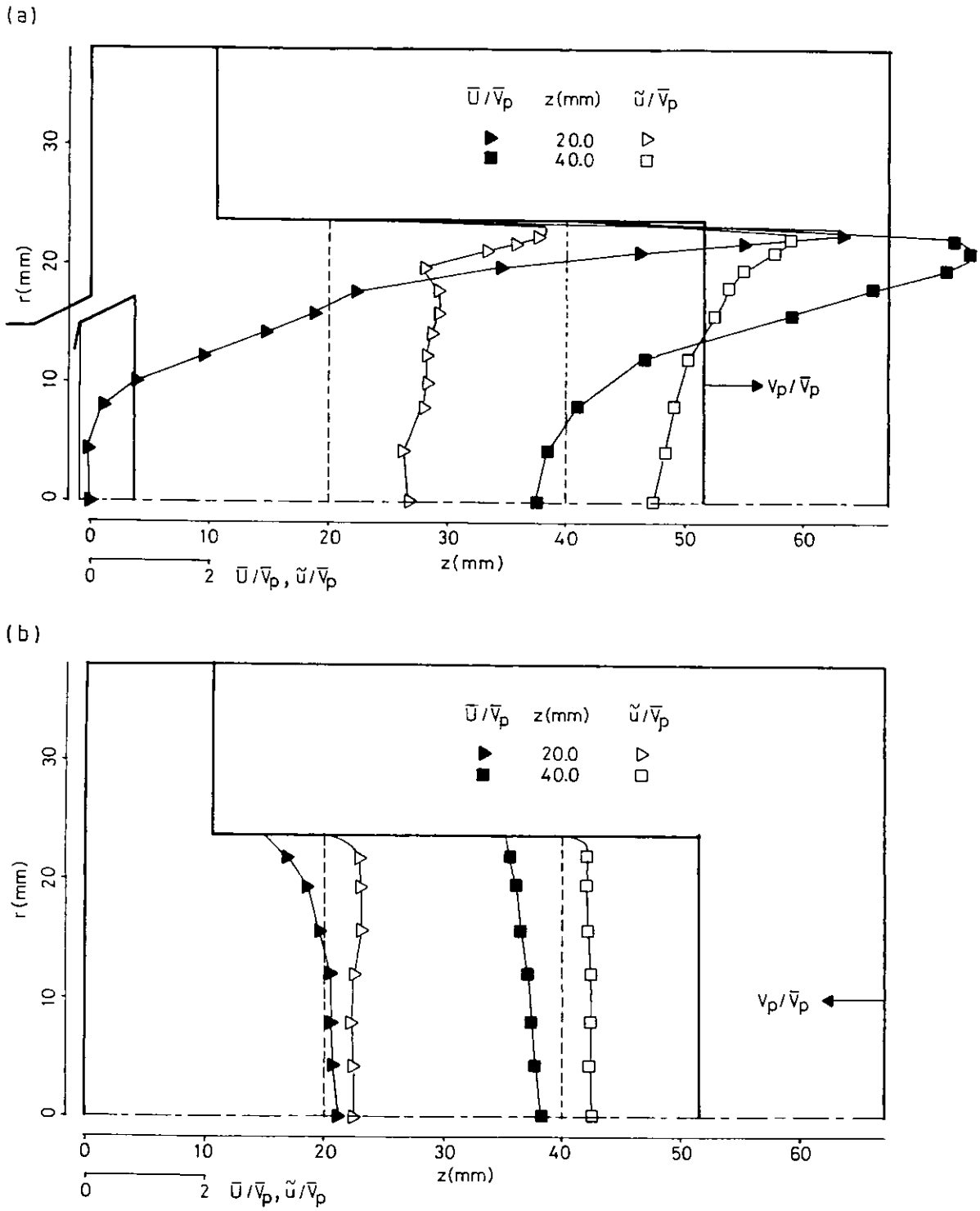

Figure 3.22 Axial mean and rms velocity profiles; cylindrical bowl, no swirl, CR = 6.7.
(a) θ = 36 degrees
(b) θ = 324 degrees

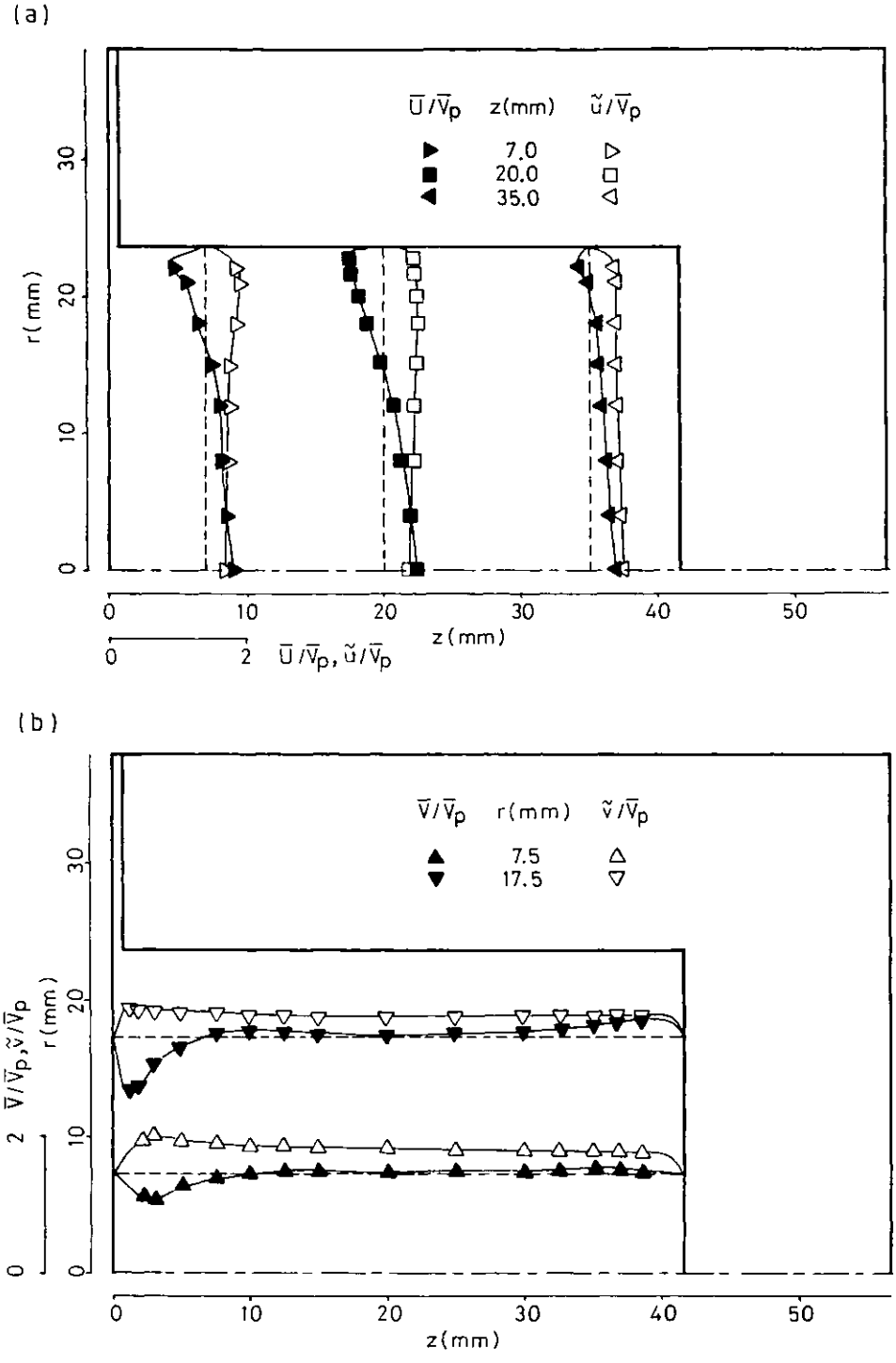

Figure 3.23 Mean and rms velocity profiles at θ = 360 degrees; cylindrical bowl, no swirl, CR = 6.7.
(a) Axial velocity
(b) Radial velocity

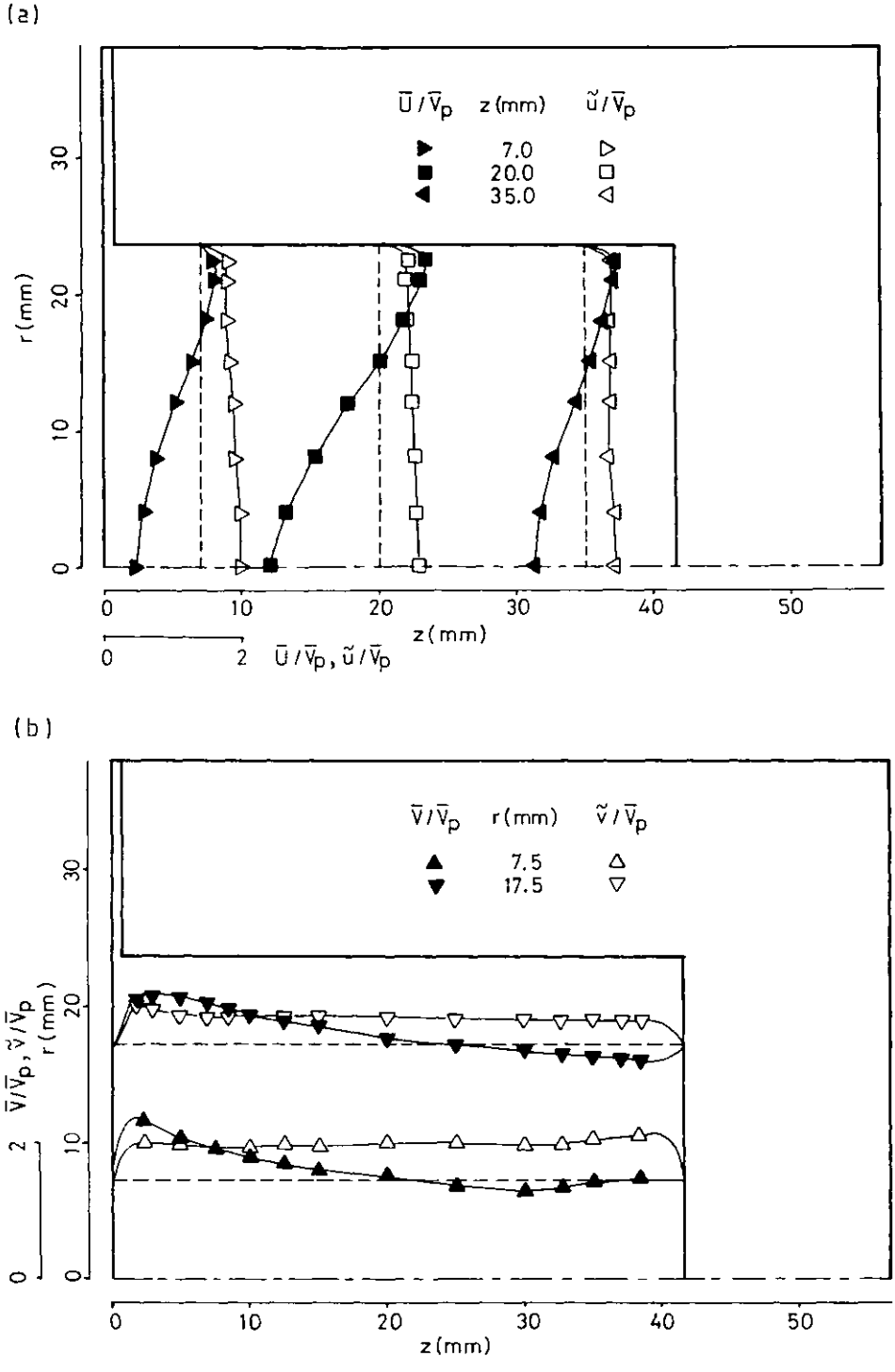

Figure 3.24 Mean and rms velocity profiles at Θ = 360 degrees; cylindrical bowl,with swirl,CR=6.7.
(a) Axial velocity
(b) Radial velocity

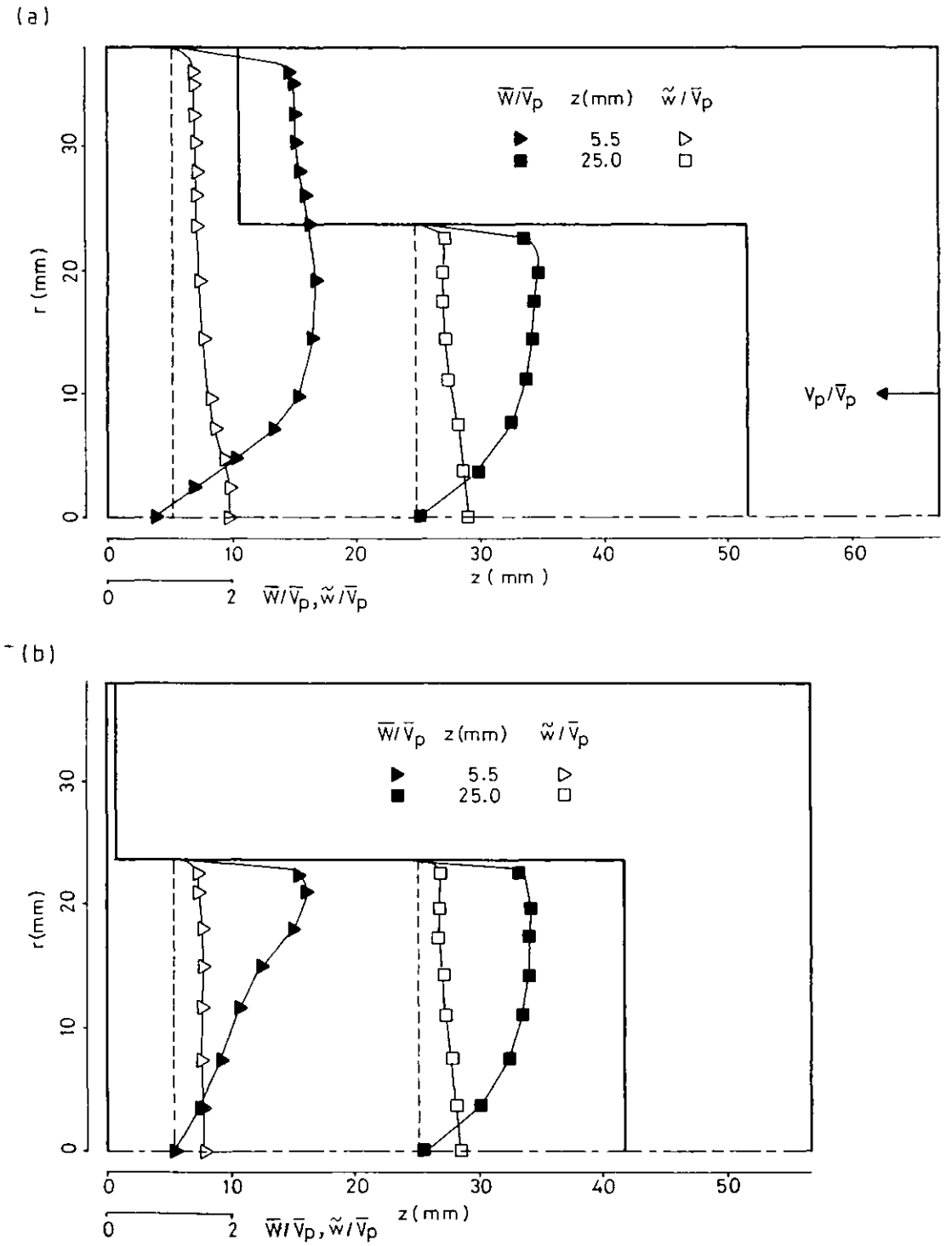

Figure 3.25 Swirl mean and rms velocity profiles; cylindrical bowl, CR = 6.7.
(a) θ = 324 degrees
(b) θ = 360 degrees

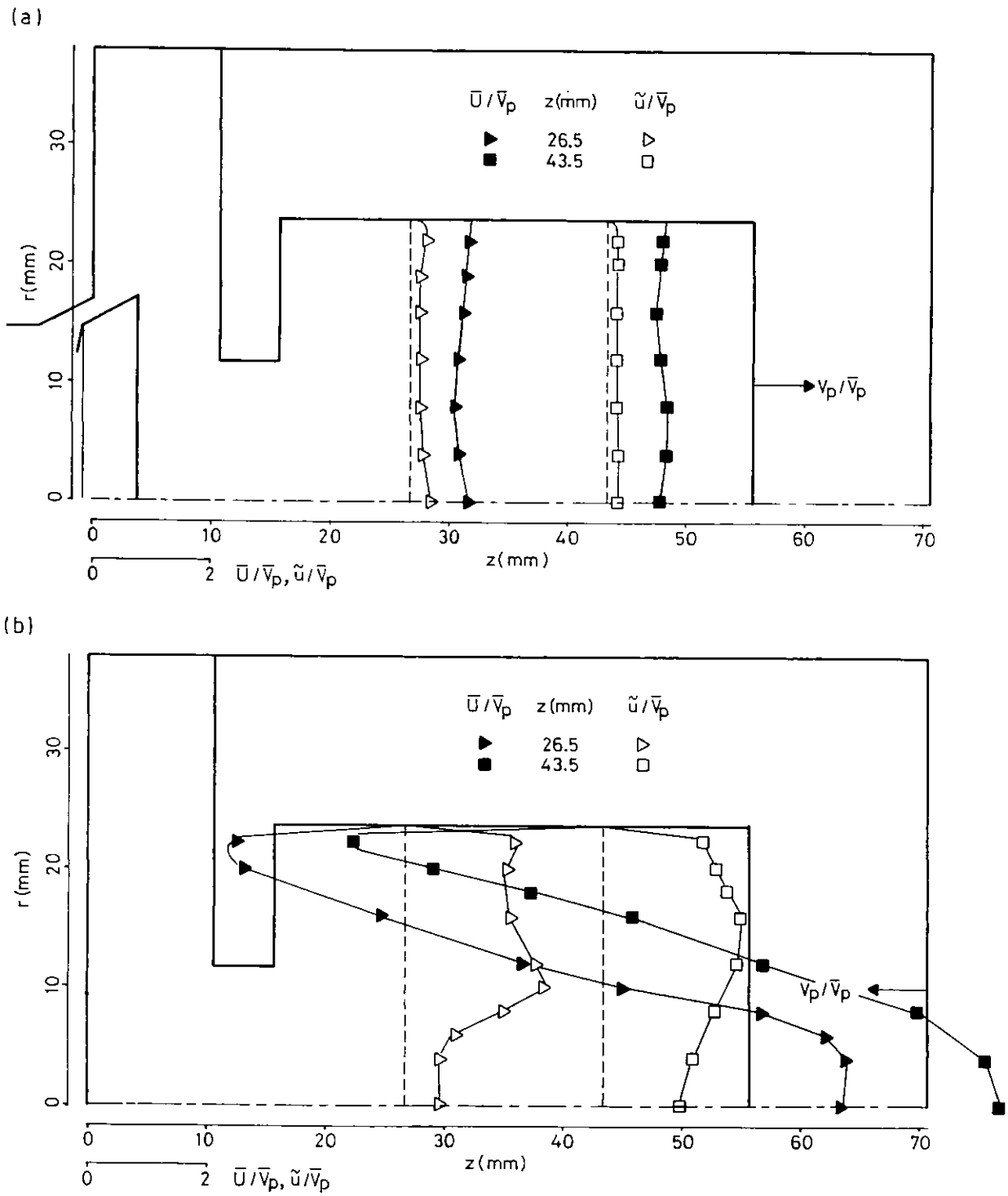

Figure 3.26 Axial mean and rms velocity profiles; re-entrant bowl, no swirl, CR = 6.7.
(a) Θ = 36 degrees
(b) Θ = 324 degrees

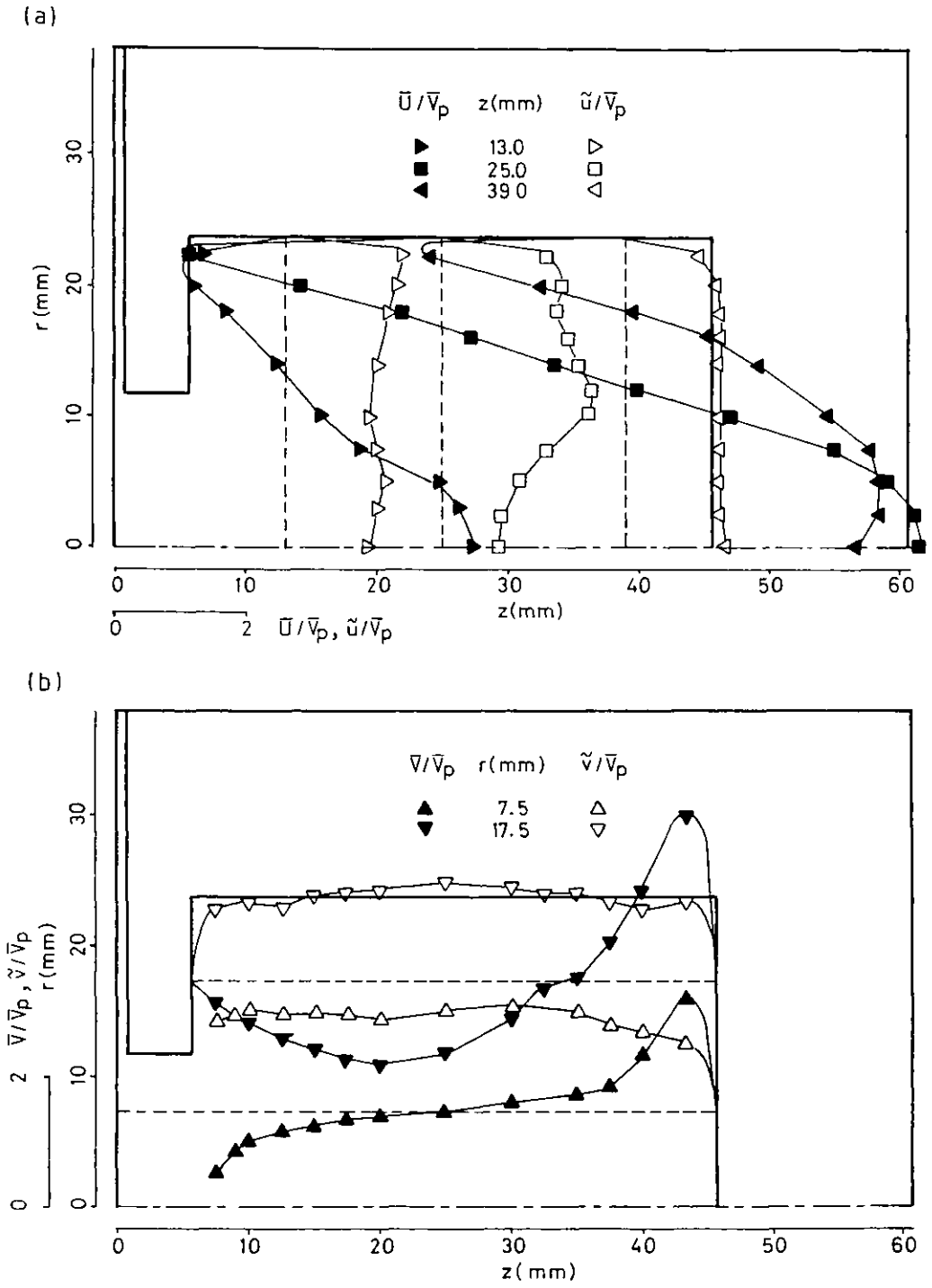

Figure 3.27 Mean and rms velocity profiles at Θ = 360 degrees; re-entrant bowl,no swirl, CR = 6.7.
(a) Axial velocity
(b) Radial velocity

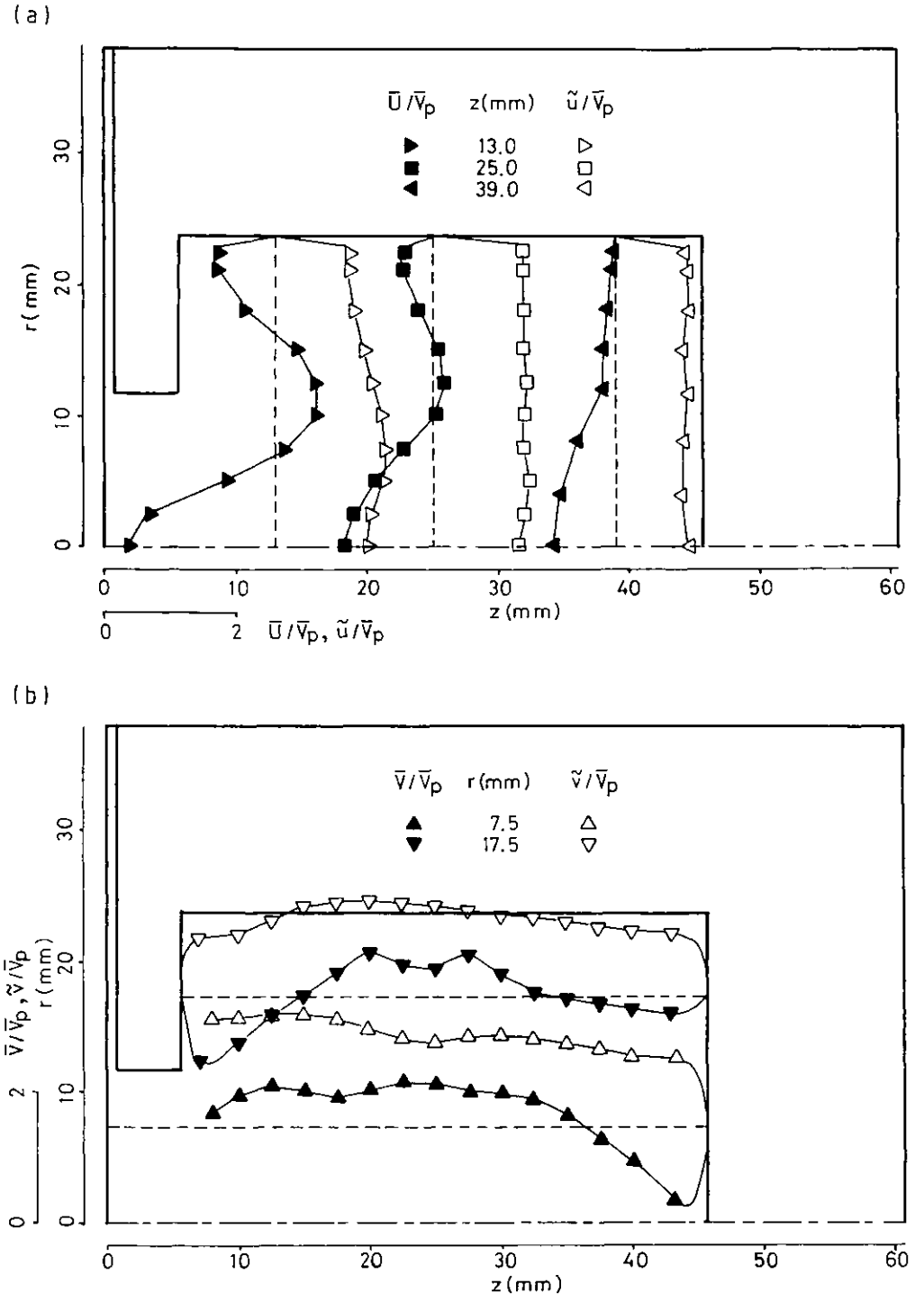

Figure 3.28 Mean and rms velocity profiles at θ = 360 degrees; re-entrant bowl, with swirl, CR= 6.7.
(a) Axial velocity
(b) Radial velocity

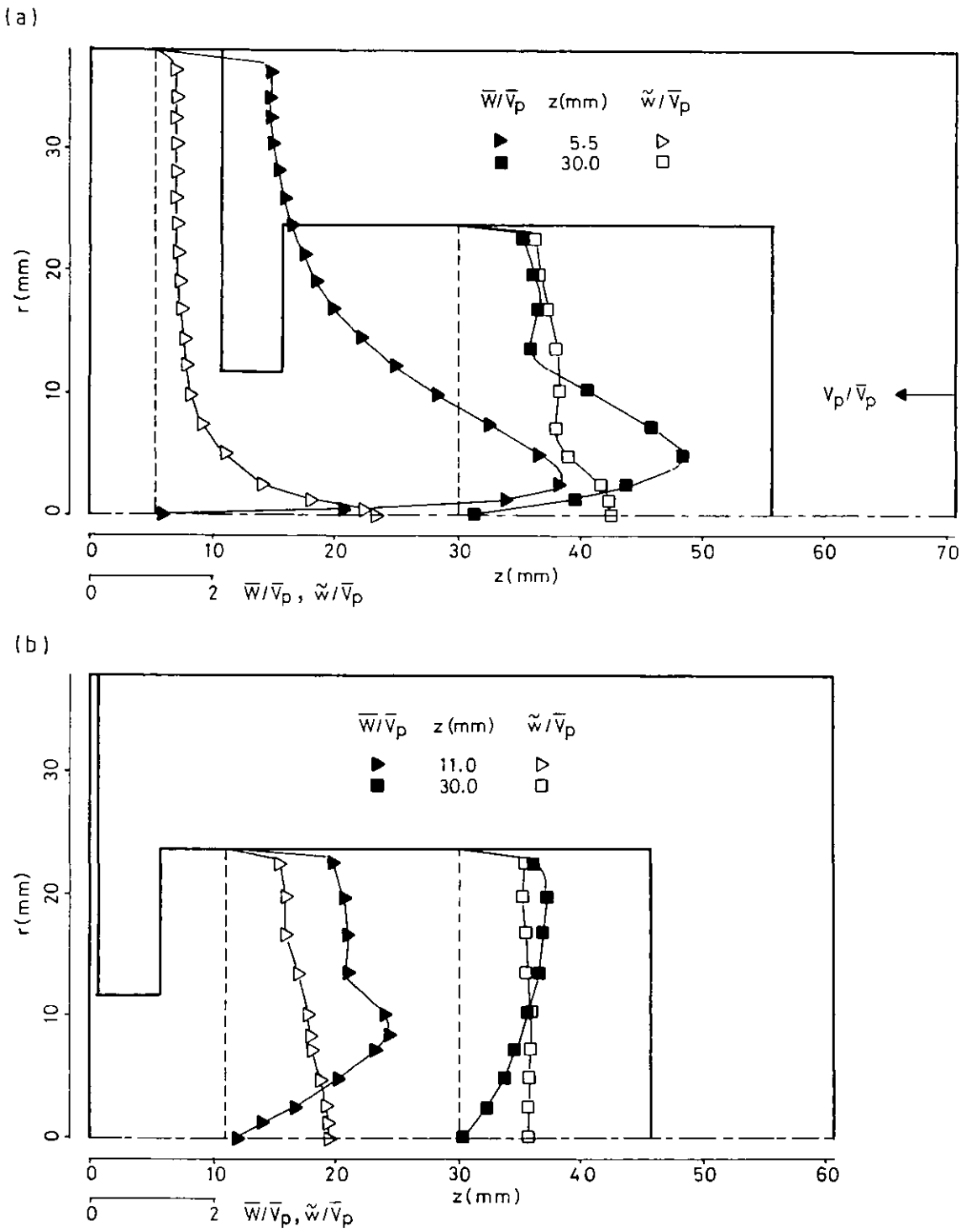

Figure 3.29 Swirl mean and rms velocity profiles; re-entrant bowl, CR = 6.7.
(a) θ = 324 degrees
(b) θ = 360 degrees

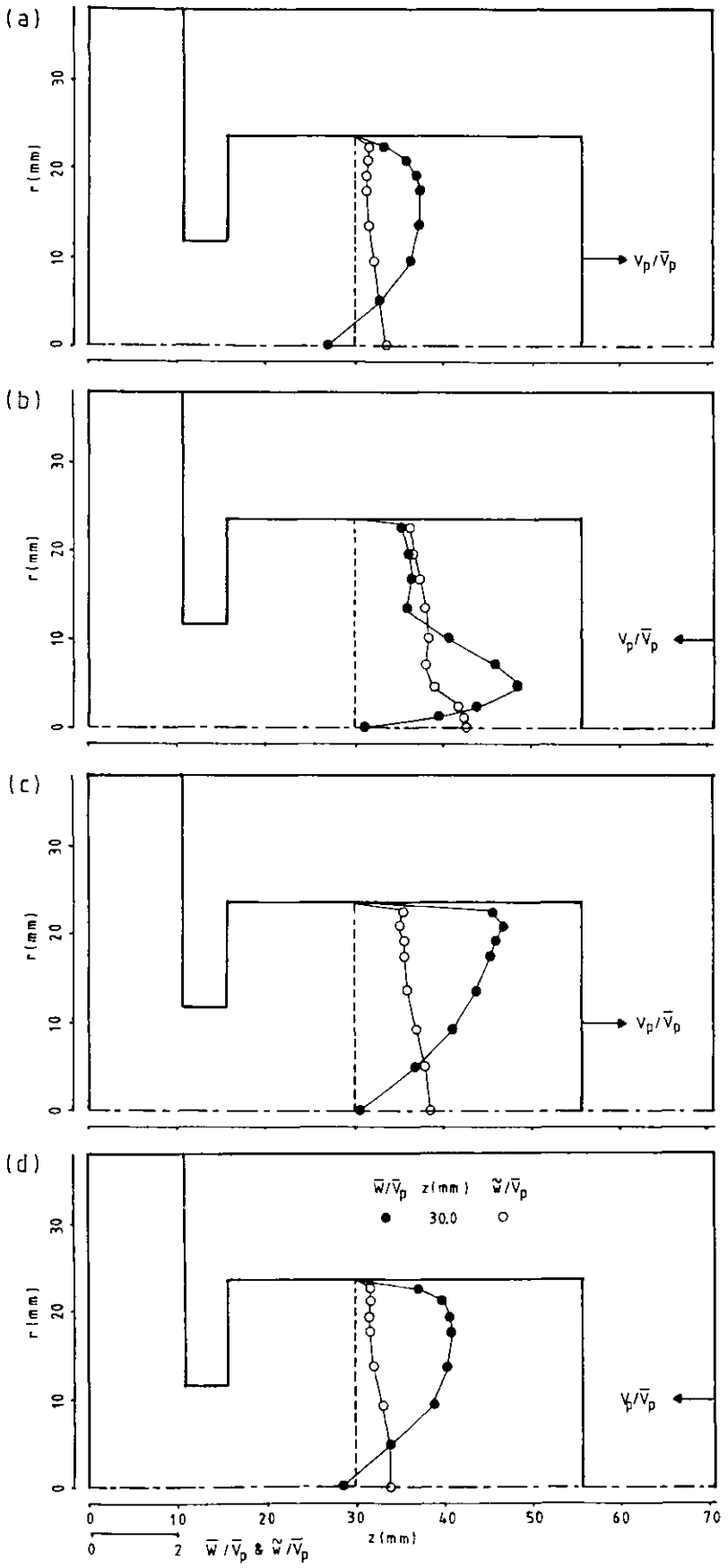

Figure 3.30 Swirl mean and rms velocity profiles at z = 30 mm; re-entrant bowl, CR = 6.7. (a) θ = 36 degrees (b) θ = 324 degrees (c) θ = 396 degrees (d) θ = 684 degrees

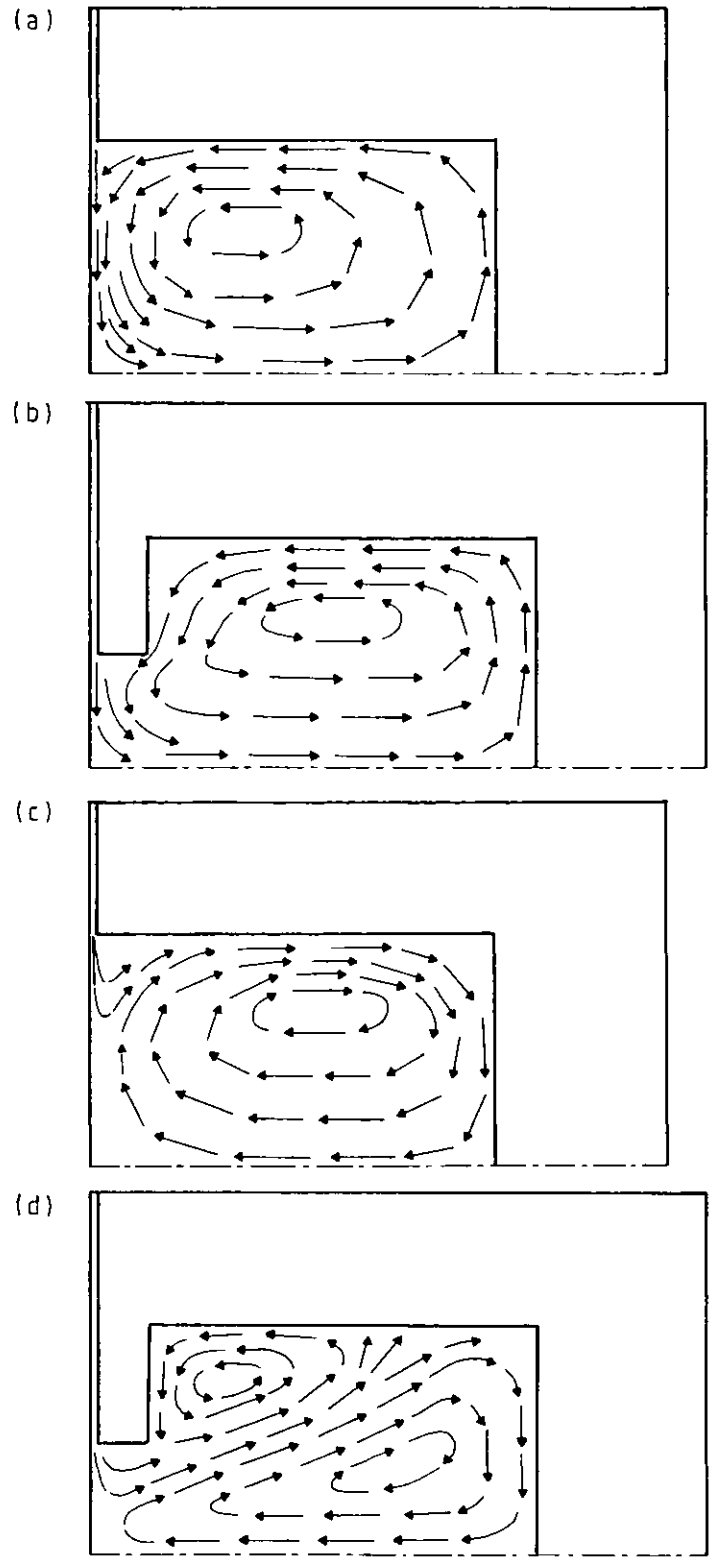

Figure 3.31 Schematic diagrams of air motion in piston bowls at TDC; CR =6.7.
(a) & (b) No swirl
(c) & (d) With swirl

CHAPTER 4

STEADY AND UNSTEADY FLOW THROUGH AN INTAKE VALVE

4.1 Introduction

The importance of an inlet port and, in particular, of an intake valve is well recognised as it determines the breathing capacity of a reciprocating internal-combustion engine. The flow behaviour through the intake valve is expected to play an important role in the performance of an engine as it can, by careful design, improve its volumetric efficiency. Quantitative knowledge of the velocity field at the valve exit plane is equally important, since calculation methods require correct boundary conditions as inputs in order to predict correctly the in-cylinder flow behaviour of an engine. If the flow at the valve is considered to be quasi-steady, then steady flow experiments can be conducted to determine the boundary conditions and to test a number of inlet port and valve designs with convenience and economy compared to engine tests with arduous in-cylinder measurements. The significance of the validity of quasi-steady assumption is, therefore, apparent and the present work is initiated to study the validity of this assumption by experimentally investigating the air flow through an intake valve in the subsonic range and under both steady and unsteady state conditions.

The flow configurations and experimental techniques employed are described in the following section together with the uncertainties incurred in the experiments. The measurements of the velocity field by laser Doppler anemometry, obtained under both steady and unsteady conditions at a number of fixed valve lift positions, are presented together with the measurements of discharge coefficient conducted under steady state in Section 4.3. The results are discussed in Section 4.4, which is followed by a summary of the more important findings of this Chapter in Section 4.5.

4.2 Experimental System

4.2.1 Flow Configurations

The flow configurations comprised the steady flow rig shown in Figure 4.1 and an engine rig identical to that described in Chapter 3, where unsteady flow experiments were conducted. As the detailed description of the engine rig is presented in the previous Chapter, only the modifications made on the engine are described here.

The air required for the steady flow tests was supplied by an air compressor delivering into a straight pipe of 75 mm diameter and about 170 cm length. An orifice type flow meter was connected in the flow line upstream of the straight pipe together with a valve to control the air flow rate. A pressure regulator was installed at the compressor outlet to compensate short term pressure fluctuations which could occur in the supply air; the long term fluctuations were compensated by adjusting the control valve setting. The cylinder head tested under both steady and unsteady flow conditions is that used with the four-stroke engine of Chapter 3 and comprised an axisymmetric valve with a 60 degree seat angle. The geometric details of the valve and port arrangement are presented in Figure 4.2. For both steady and unsteady flow experiments, the valve was held open for a series of constant lifts by locking the valve stem at a spider arrangement situated in the port. A plexiglass cylinder of 75 mm diameter, identical to that previously employed in the two-stroke engine, was used to confine the flow space downstream of the valve and at the same time to provide the optical access for the velocity measurements by laser Doppler anemometry at and near the valve exit.

The unsteady flow experiments for the same valve and port arrangement were conducted in the four-stroke model engine described in sub-section 3.2.1. Since the valve was to remain at a constant lift throughout the engine cycle, the cam mechanism was disconnected, and the engine was operated in a two-stroke cycle (intake and exhaust strokes only), in the absence of compression. The engine, as in the previous cases, was motored at a constant speed of 200 rpm.

4.2.2 Flow Metering and Pressure Drop Measurements

The flow characteristics of the valve configuration were examined under steady flow conditions by obtaining its discharge coefficient for a number of fixed valve lifts. This required the measurement of the flow through the valve and the pressure drop across it for each lift tested.

An orifice type flow meter with D and D/2 pressure tappings was used to meter the air flow and was manufactured according to the standards set by BS1042. The orifice meter was 12.7 mm in diameter and had an orifice-to-pipe diameter ratio of 0.5 Metering a compressible fluid flow such as air meant that the flow through the orifice meter was limited, for unambiguous metering (see BS1042), due to the compressibility effect. The maximum air flow that could be metered safely was about 50 m^3hr^{-1} corresponding to about 75 $kghr^{-1}$. The pressure drop across the orifice and the upstream pressure were measured by either water or mercury manometers, depending on the ranges encountered. With these pressure values, and assuming ambient temperature for the working air, the flow rate for each test was calculated according to the procedure outlined in BS1042. Experimental checks carried

out using a gas meter indicated a maximum deviation of no more than 2% from the calculated value. The pressure upstream of the valve was measured at a tapping by means of a water manometer and taken to be the upstream stagnation pressure P_{uo}; the calculation of the velocity head based on the maximum flow rate achievable and with the assumption of uniform flow at the location where pressure was measured, showed a negligible contribution (less than 0.02%) to the total pressure and hence confirmed this assumption. The downstream pressure P_d was assumed to be atmospheric and equal to that at the valve throat. The pressure drop across the valve, ΔP, was then taken as $P_{uo} - P_d$.

4.2.3 Velocity Measurements

Laser Doppler anemometry was used to measure the velocity fields at and downstream of the valve. The optical arrangement and signal/data processing systems used previously in Chapter 3 were also employed here. In the unsteady flow experiments silicone oil droplets were introduced to the flow as seeding particles in a similar way to that for the engine configurations by filling with seeded air a plenum located upstream of the port (see sub-section 2.2.2). For steady flow measurements the seeding air was introduced, less than 2% of the total mass flow, far upstream of the port in the straight pipe section as illustrated in Figure 4.1. A honeycomb was installed downstream of the seeding location to minimise flow disturbance and result in a uniform flow at the port entry. Ensemble averages were used to obtain the mean and rms velocity values and are defined in sub-section 2.2.3. For each measurement obtained under unsteady conditions, sample sizes of between 1000 - 2000 were collected within a crank angle window of 10 degrees

to provide the ensemble-averaged mean and rms velocity values. In the steady flow measurements, the sample sizes used were generally above 2000.

4.2.4 Measurement Uncertainties

A full error analysis associated with measured velocity values is given in sub-sections 2.2.6 and 3.2.5 and expected to equally apply for the present unsteady flow experiments. In the steady flow measurements, however, the experimental uncertainty is considered to be much less, mainly due to the absence of crank angle broadening, and was estimated to be of the order of 2% and 5% for the axial mean and rms velocity values, respectively. A considerable reduction in velocity gradient broadening associated with radial velocity measurements is also expected to reduce the corresponding uncertainties to better than those stated above and previously.

The pressure drop across the valve could be measured on the manometer within $\pm$ 0.5 mm of water and this, together with the uncertainty encountered in the measured flow rate, implies a maximum error of about $\pm$ 1% in the values of the discharge coefficient. These error magnitudes do not influence the conclusions reached on the basis of the results and discussion of the following sections.

4.3 Results

4.3.1 Introduction

In the steady flow tests, the flow through the valve $\dot{m}$ and the pressure drop across it, Δp, were measured for a number of fixed lifts, and the "theoretical flow" for each lift was calculated assuming isentropic expansion through the valve for the same lift and pressure drop ΔP. The ratio of the measured to theoretical flow is defined as the discharge coefficient. In the calculations of the theoretical flow, two separate valve areas were used for the same conditions resulting in two different values of the discharge coefficient, C_m and C_l. These two areas are the minimum geometric areas A_m and the peripheral lift area A_l which are defined in Appendix 4.1. It was assumed that the pressure downstream of the valve was equal to that at the throat, and it is therefore possible for the discharge coefficient C_m to be greater than unity due to the pressure recovery after the valve passage of a convergent/divergent shape.

The valve was tested up to a dimensionless lift (L/D_v) of 0.294, a range which is commonly used in practice, and up to a pressure drop of about 100 cm of water covering a Reynolds number range from 10^3 to 2.3×10^4 based on the cylinder diameter D. In some tests, however, the maximum pressure drop could not be achieved because the air supply and/or the range of the orifice meter was insufficient.

The mean and rms velocity values of the radial and axial velocity components were measured at and downstream of the valve exit under both steady and unsteady flow conditions and are presented in profile forms and normalised by the cylinder bulk velocity V_c. The velocity measurements for the steady flow conditions were all

obtained with a constant mass flow rate of 3.32×10^{-3} kgs^{-1} corresponding to a Reynolds number of 3.1×10^{3} and a cylinder bulk velocity of 0.63 ms^{-1}. This flow rate was chosen to be equal to the mean flow rate $\bar{m}_p$ of the unsteady flow obtained with the engine speed of 200 rpm. In the unsteady flow experiments, the cylinder bulk velocity was taken to be equal to the instantaneous piston speed V_p and was, therefore, crank angle dependent. The instantaneous value of V_c corresponding to the crank angle, Θ, under consideration was used as the normalising velocity in order to make a direct comparison between the steady and unsteady flow cases. The instantaneous values of V_c correspond to 0.64, 0.98 and 0.52 ms^{-1} for the crank angle locations of 36, 90, and 144 and 216 degrees respectively. These locations were chosen to describe the flow during intake and exhaust.

4.3.2 Steady Flow

The variations of the discharge coefficients C_m and C_l with the pressure drop ΔP and the mass flow rate $\dot{m}$ are shown, with L/D_v as a parameter, in Figures 4.3 and 4.4 respectively. Both discharge coefficients show, for almost all lift cases, a decrease with reducing values of ΔP and $\dot{m}$ (ie. at low Reynolds numbers). This is attributed to a higher friction loss associated with pronounced viscous effects at low Reynolds numbers. As the Reynolds number increases with increasing ΔP or $\dot{m}$, viscous effects become less and less important and the discharge coefficient progressively improves tending to become constant at large values of ΔP and $\dot{m}$. The observed spread in the values of C_m for the lift range considered is wider than that in the values of C_l and can be explained by the smaller rate of change of the minimum geometric area A_m with valve lift L, compared to that of the peripheral area A_l; compare, for example,

the first derivatives with respect to L of equations 6 and 8 of Appendix 4.1.

A typical variation of the discharge coefficient with valve lift at a constant mass flow rate of 12 x 10^{-3}kgs^{-1} as well as at a constant pressure drop of 15 cm H_2O is shown in Figure 4.5. At the small values of valve lift the discharge coefficient is generally high and exhibits a peak at about L/D_v = 0.06, suggesting that the flow boundaries remain close to the walls of the valve passage and any separation occurring in the passage is very small. Both values of the discharge coefficient, in particular the value of C_m, fall sharply to a minimum at about L/D_v = 0.11. This abrupt fall is associated with the flow separation near the tip of the valve head as the curvature on the underside of the valve diverts the flow outwards. The discharge coefficient progressively recovers at higher lifts and reaches to a second peak at about L/D_v = 0.20. Above this lift another rapid fall, this time only in the value of C_m, is observed reaching to its minimum value at about L/D_v = 0.30.

The radial mean and rms velocity profiles obtained at the valve exit plane for the 3, 6, 9 and 12 mm valve lifts are shown in Figure 4.6, together with the corresponding axial mean and rms velocity profiles measured at a location 15 mm away from the cylinder head. At L = 3 mm (L/D_v = 0.088), the flow at the valve exit plane has a uniform mean velocity profile, and this confirms the above argument justifying the high discharge coefficient at the low range of the valve lift. The corresponding turbulence levels are generally very low with intensities of about 3%. The flow near and downstream of the valve closely resembles those observed in two and four-stroke engines with the jet-like flow driving two vortices, one in the corner between the wall and the head, and the

other near the cylinder axis, as indicated in Figure 4.6a. As the valve lift increases to L = 6 mm (L/D_v = 0.176), the flow separates at some location in the valve passage due to the outward trajectory of the flow associated with the curvature on the underside of the valve, thus resulting in the observed fall in the value of the discharge coefficient. The separation bubble and the shear layer near the tip of the valve head result in increased turbulence with a maximum level of about 2.7 V_c. The corresponding axial velocity profiles downstream of the valve show similar trends to those at L = 3 mm but with reduction in magnitude as shown in Figure 4.6b. The peak in the mean velocity value has, however, moved nearer to the cylinder wall in parallel with the outward diversion of the flow at the exit plane. The flow at L = 9 mm (L/D_v = 0.265) again reveals similar trends with reduced velocity values at the downstream location as well as at the valve exit plane, see Figure 4.6c. The size of the separation bubble at the exit plane is almost the same as that at L = 6 mm, and this explains the progressive improvement in the discharge coefficient in the range above L/D_v = 0.11. At L = 12 mm (L/D_v = 0.353) another mode of the flow is observed at the valve exit plane, since the flow is separated not only at the valve but also at the valve seat, with increased turbulence levels there as shown in Figure 4.6d. As a consequence, the flow is diverted inwards and away from the cylinder head. This change in the flow direction is also reflected in the axial velocity profile downstream of the valve where the position of the peak in the mean velocity has moved towards the cylinder axis. Although discharge coefficients were not obtained for L/D_v greater than 0.3, it can be anticipated that this change in the flow mode will cause a reduction in the value of discharge coefficient, as it further restricts the flow passage; such observations are reported, for example, by Tanaka (1929) and Kastner et al (1963).

A complete picture of the in-cylinder flow structure downstream of the valve is presented in Figure 4.7, which shows the axial mean and rms velocity profiles at various downstream locations. The profiles obtained across a full diameter at z = 15 and 65 mm indicate excellent symmetry of the flow throughout the cylindrical confinement. The mean velocity profiles suggest that the vortex near the cylinder axis extends to about 80 mm away from the cylinder head with the velocity peak gradually moving towards the wall and reducing in magnitude at downstream locations. The profile at z = 95 mm is near uniform, with a magnitude of about V_c.

4.3.3 Unsteady Flow

Both the axial and the radial mean and rms velocity profiles obtained at and near the valve exit plane with a fixed valve lift of 6 mm are shown in Figure 4.8 and correspond to a crank angle location of 36 degrees. Although the flow at the exit shows a similar trend to that of the steady flow at the same lift, the mean velocity profile suggests that the size of the separation bubble is smaller due to the inward movement of the inlet jet. The turbulence levels under unsteady flow conditions are generally higher, almost twice as much, indicating a turbulence intensity of, for example, 6% at a position 2 mm away from the valve seat as opposed to 3% at the same location under steady flow conditions. These differences are mainly attributed to residual turbulence carried over to the next cycle, as will be shown later, and to a small extent (no more than 5%) to the crank angle broadening discussed in sub-section 3.2.5 of the previous Chapter. In line with the observed difference at the valve exit, the axial

velocity profiles downstream of the valve exhibit peaks closer to the cylinder axis confirming the more acute angle of the flow at the exit plane. The turbulence levels close to the cylinder axis are lower, as indicated in Figure 4.8, than those in the steady flow (see also Figure 4.6b).

The flow behaviour at the valve exit with 9 mm lift during the engine cycle is indicated in Figure 4.9 which presents the radial mean and rms velocity profiles obtained at 36, 90 and 144 degrees in intake and 216 degrees in the exhaust stroke. As the mean velocity profiles suggest, the flow throughout the intake process remains unchanged and almost identical to that obtained under steady flow conditions, see Figure 4.6c. Although the turbulence has generally higher absolute levels at mid-intake than those earlier in the stroke, they are lower in relative terms, indicating that the increase in turbulence is not in line with that in the mean flow. The levels at 144 degrees, both in absolute and relative terms, are generally higher than those at 36 degrees, probably due to the enhanced mixing taken place between the beginning and the end of the intake process. During the exhaust stroke at 216 degrees, as indicated in Figure 4.9d, the flow moves out through the opening with higher velocities encountered away from the tip of the valve head. No flow separation is observed. The rms velocity profile is almost uniform and suggests a possible carry-over of some turbulence residue to the next engine cycle.

A similar set of measurements to that in Figure 4.9 was obtained for a valve lift of 12 mm at crank angle locations of 36, 90 and 216 degrees, and is presented in Figure 4.10. The mean velocity profiles during intake show, both qualitatively and quantitatively, a close resemblance to each other as well as to that obtained with the same lift under the steady flow conditions

(Figure 4.6d). The corresponding turbulence levels, however, are much higher under unsteady conditions, as discussed above. The flow behaviour during exhaust also shows some differences from those at lower lifts. A flow separation is observed near the valve tip and limits the flow passage resulting, therefore, in similar mean velocity values to those obtained with the lower lift of 9 mm.

Figure 4.11 shows the axial mean and rms velocity profiles obtained throughout the cylinder and at a crank angle location of 90 degrees. The same valve lift as that used for the steady flow measurements presented in Figure 4.7 was employed in order to allow direct comparison of the two in-cylinder flow structures. Apart from the abovementioned differences near the valve exit, the two flow structures show a reasonable parallel to each other in the rest of the cylinder, with some differences being observed generally more in the detail of the flow.

4.4 Discussion

The measurements of the velocity field at the valve exit and the corresponding discharge coefficient obtained at a wide range of valve lift under steady flow conditions clearly indicate the four modes of the flow which were first noted by the flow visualisation tests of Tanaka (1929) and later confirmed, again qualitatively, by Kastner et al (1963). At very low lifts, the flow remains attached to the valve boundaries and fills the entire exit plane resulting in high values of discharge coefficient. In the second mode, the flow boundary breaks away from the seat face on the valve as the curvature on

the underside of the valve diverts the flow outwards, towards the cylinder head; an abrupt fall observed in the discharge coefficient is associated with the occurrence of this mode. At higher values of intermediate lift, a gradual improvement in the discharge coefficient is evident and corresponds to the third mode of the flow. Although the flow is still separated only at the valve face, the size of the separation bubble remains virtually constant thus resulting in a gradual increase in effective flow area and, therefore, the discharge coefficient at increasing values of valve lift. In the last and the fourth mode of the flow, a second flow separation, this time from the seat face on the head, is also observed at the same time and expected to further influence the discharge coefficient of the valve.

Similar observations on the discharge coefficient of a valve with a 45 degree seat angle were reported by Kastner et al (1963). The gradual decrease in the intermediate-to-high lift range reported by Kastner et al is also evident in the present measurements of the discharge coefficient C_m, based on the minimum geometric area A_m, but occurs at a slightly higher value of L/D_v, which is probably due to the larger seat angle used with the present valve. Kastner et al attribute this decrease in C_m to the changes in the flow similar to that described above in the fourth mode of the flow. The present measurements of the velocity field at the valve exit plane show no such trends in the corresponding lift range of decreasing C_m. It can, however, be argued that the observed decrease in C_m in the present case and, to some extent, by Kastner et al is misleading and rather attributed to the change in the definition of the minimum geometric area (see Appendix 4.1) at the beginning of this range. The rate of increase of the minimum area with lift increases sharply above that critical lift and subsequently results in a deceiving decrease in the

discharge coefficient. The absence of such decrease in the values of the discharge coefficient C_l based on the peripheral lift area A_l confirms the above argument and substantiates the reasoning of Annand (1969) with respect to the use of the peripheral area in the definition of discharge coefficient rather than the minimum geometric area A_m.

The separation bubble observed near the valve face and almost in the entire range of the valve lift encountered in practice remains nearly constant in size and independent of valve lift, and it is thought to be a function of the seat angle and the underside geometry of the valve. It is, therefore, possible to improve the breathing performance of an inlet port by a careful design of the valve configuration. The decrease in the valve seat angle can be expected, at first sight, to reduce the size of the separation bubble and therefore to improve the discharge coefficient, but may also have disadvantages such as to encourage an earlier flow separation at the valve seat face and a weaker mechanical structure due to the decreased valve thickness. More definite improvements, however, can be achieved by rounding off the sharp edges in the valve passage to minimise the possibility of flow separation. Marked improvements in the values of discharge coefficient by such methods have already been reported by, for example, Wood et al (1942), Kastner et al (1963), Wallace (1967) and Annand (1969).

The measurements of the velocity field at the valve exit plane obtained under unsteady flow conditions and for a number of fixed valve lifts show a close correspondence to those obtained under steady conditions, indicating that the data available in steady state testing can be used with confidence in determining the performance characteristics of inlet ports and valves, rather than undertaking more complicated, expensive and time-consuming tests in actual engines. Similar conclusions

are also drawn by Fukutani and Watanabe (1982) from their tests for so called "static" and "dynamic" flow coefficients. The probing of the valve flow under steady conditions with relatively less effort can also provide the correct boundary conditions, particularly with respect to the mean flow, for prediction methods calculating time-varying in-cylinder flows. The mean velocity profiles obtained at the valve exit plane show large deviations from a plug type flow which was assumed for the boundary conditions in the calculations presented and assessed in sub-section 3.4.4. Underestimation of the inlet momentum with a plug flow is a possible reason for the underprediction of both the in-cylinder mean flow and turbulence. The turbulence levels obtained under steady conditions, however, are not a good representation but, on the other hand, are thought to be of secondary importance, as the similar levels of turbulence result in both flows downstream of the valve. The higher levels of turbulence observed in the unsteady flow and during early intake are considered to be due to residual effects carried over from the previous cycle.

The steady mean flow structure in the axial plane downstream of the valve shows only a qualitative correspondence to that during early intake of the unsteady flow. However, this was expected, as a transition phase for vortex growth takes place under unsteady conditions and particularly during early intake, as already indicated by the results in Chapter 2. However, later in the stroke and after this transition, a closer correspondence between the two in-cylinder flows is achieved with some quantitative differences observed more in the detail of the flow near the cylinder head. The lower levels of turbulence measured near the axis with the unsteady flow, particularly at the early part

of the engine cycle, are considered to be due to the small time scale for turbulence diffusion and its convection by the mean flow. Later in the cycle, however, the turbulence is increased as it finds time to diffuse and be convected, reaching to levels comparable to those obtained under the steady state condition.

4.5 Conclusions

The most important findings of this Chapter are as follows:

(1) The quantitative investigation of the velocity field at the valve exit indicates four different modes of the flow which explain some of the trends observed in the variation of discharge coefficient with valve lift.

(2) The measurements under both steady and unsteady state conditions confirm, to a reasonable extent, the validity of the quasi-steady assumption for the valve flow. Steady flow testing may, therefore, be used to obtain the correct boundary conditions for calculation methods, particularly with regard to the mean flow, and to determine the performance characteristics of various inlet ports and valves of production engines.

(3) The mean velocity field at the valve exit plane shows, apart from those in the small lift range, large deviations from a plug type flow usually assumed in most calculation methods.

(4) The unsteady axial flow downstream of the valve, and during early intake, shows only a qualitative agreement with that under the steady state condition. A closer correspondence both in qualitative and quantitative terms, however, is observed later in the intake stroke.

APPENDIX 4.1

DEFINITION OF DISCHARGE COEFFICIENT AND CALCULATIONS OF EFFECTIVE AND GEOMETRIC VALVE AREAS

Discharge Coefficient C_m or C_l

Discharge coefficient is defined as the ratio of effective flow area* (A_e), which is considered to be the throat area of an imaginary, frictionless, parallel-exit nozzle and through which the measured flow passes, to some geometric area representative of the valve configuration. The choice of the geometric area is arbitrary and various reasonable choices exist. Most widely used areas are minimum valve area A_m (Kastner et al, 1963) and peripheral lift area A_l (Annand, 1969) which are both functions of valve lift and are given below in more detail. The others include some fixed areas such as that of the valve head, as used for example by Woods and Khan (1965).

$$C_m = A_e/A_m \tag{1}$$

$$C_l = A_e/A_l \tag{2}$$

Effective Area A_e

The effective area may be calculated, see for example Streeter and Wylie (1975), using the steady flow energy and the continuity equations together with the assumption of isentropic expansion through the valve and is given by

$$A_e = \dot{m}\,(2\,P_{uo}\,\rho_{uo}\,K)^{-\frac{1}{2}} \tag{3}$$

where:

(i) for subsonic flow

$$K = \frac{\gamma}{\gamma-1}\left(\frac{P_d}{P_{uo}}\right)^{\frac{2}{\gamma}}\left[1 - \left(\frac{P_d}{P_{uo}}\right)^{\frac{\gamma-1}{\gamma}}\right] \tag{4}$$

---

* Effective area is also referred to as theoretical or isentropic flow area.

(ii) for sonic flow

$$K = \frac{\gamma}{2}\left(\frac{2}{\gamma+1}\right)^{\frac{\gamma+1}{\gamma-1}} \qquad (5)$$

Geometric Areas A_l and A_m

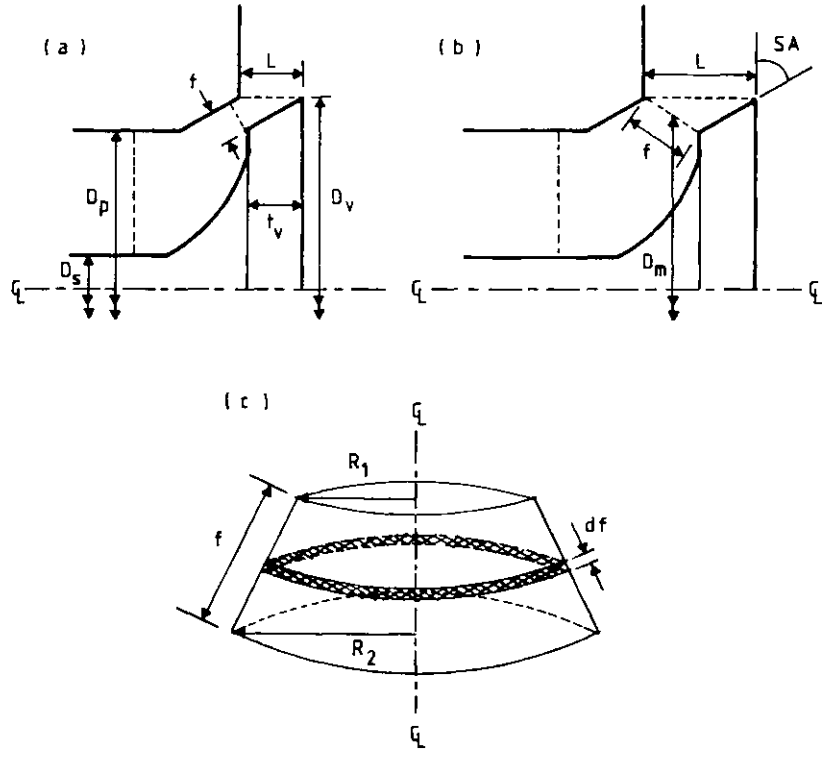

Figure 1 Diagrams for calculating the geometric areas of a valve configuration.

For the calculation of discharge coefficient corresponding to a lift of given value, two different geometric areas were used; the peripheral lift area A_l and the minimum area A_m. The area A_l is calculated by

$$A_l = \pi D_v L \qquad (6)$$

In calculating the minimum area A_m of a valve as shown in Figure 1, three cases may be encountered depending on the valve lift.

Case 1: $t_v/\sin^2(SA) \geq L > 0$

This case is indicated in Figure 1a. The minimum area corresponds to a frustum of a cone as shown in Figure 1c with slant height f perpendicular to the valve seat faces. The minimum area can be calculated as follows:

$$A_m = \int_0^f 2\pi r \, df$$

$$= \frac{2\pi}{\sin(SA)} \int_{R_1}^{R_2} r \, dr$$

$$= \pi f \, (D_v - 2t_v \cot(SA) + f \sin(SA))$$

Since $f = L \cos(SA)$

$$A_m = \pi L \cos(SA) \, (D_v - 2t_v \cot(SA) + \frac{L}{2} \sin 2(SA)) \qquad (7)$$

For the present valve configuration this lift range corresponds, in terms of dimensionless lift L/D_v, to $0.192 \geq L/D_v > 0$ and the minimum area is give by

$$A_m = 1.32 \, D_v L + 0.68 \, L^2 \qquad (8)$$

Case 2:

$$\left[\left(\frac{D_p^2 - D_s^2}{4D_m}\right)^2 - \left(t_v\cot(SA)\right)^2\right]^{\frac{1}{2}} + t_v \geq L \geq t_v/\sin^2(SA)$$

This case is illustrated in Figure 1b. Here the slant height f of the frustum is no longer perpendicular to the valve seat faces and the corresponding minimum area can be calculated by

$$A_m = \pi D_m\left[(L - t_v)^2 + (t_v\cot(SA))^2\right]^{\frac{1}{2}} \quad (9)$$

where $$D_m = D_v - t_v\cot(SA) \quad (10)$$

For the present valve configuration, this case corresponds to a lift range of $0.307 \geq L/D_v \geq 0.192$ with the minimum area in this range given by

$$A_m = (3.14\ D_v - 8.89)\ (L^2 - 9.80\ L + 32.01)^{\frac{1}{2}} \quad (11)$$

Case 3:

$$L \geq \left[\left(\frac{D_p^2 - D_s^2}{4D_m}\right)^2 - \left(t_v\cot(SA)\right)^2\right]^{\frac{1}{2}} + t_v$$

In this case the minimum area becomes a constant and hence is no longer a function of valve lift. It corresponds to the port area minus the area of the valve stem and is therefore given by

$$A_m = \frac{\pi}{4} (D_p^2 - D_s^2) \qquad (12)$$

For the present valve, this minimum area is 611 mm^2 and corresponds to the dimensionless lift range above 0.307.

FIGURES

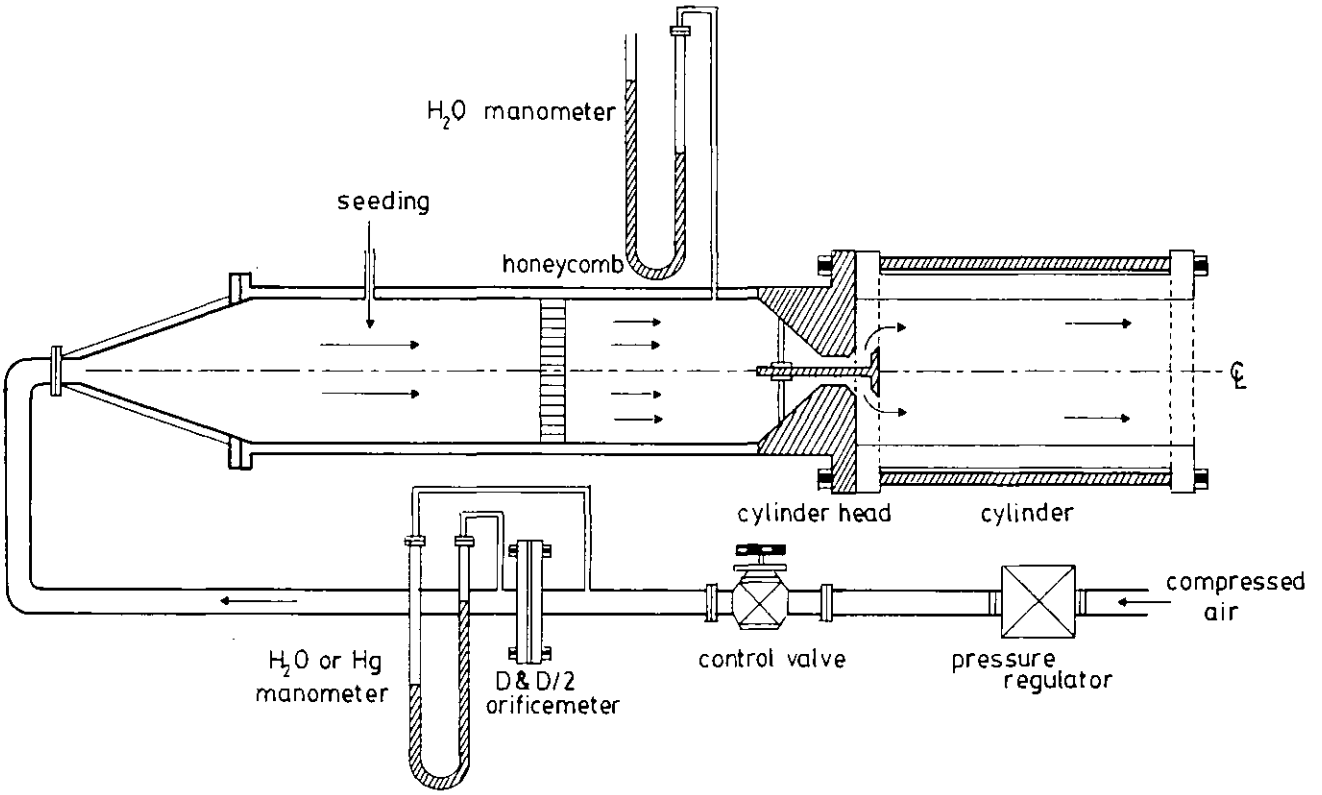

Figure 4.1 Schematic of steady flow test rig.

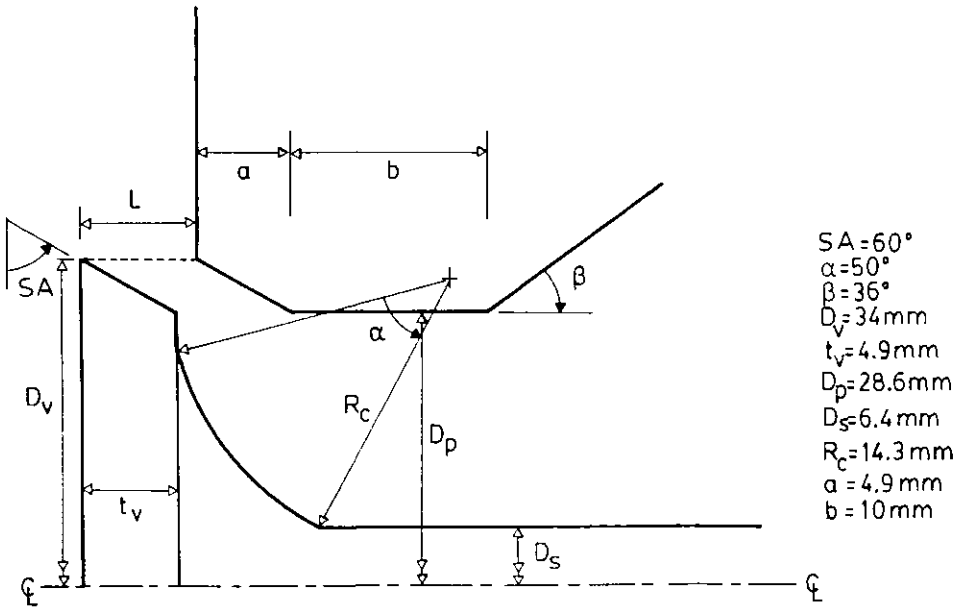

Figure 4.2 Geometric details of port and valve arrangement.

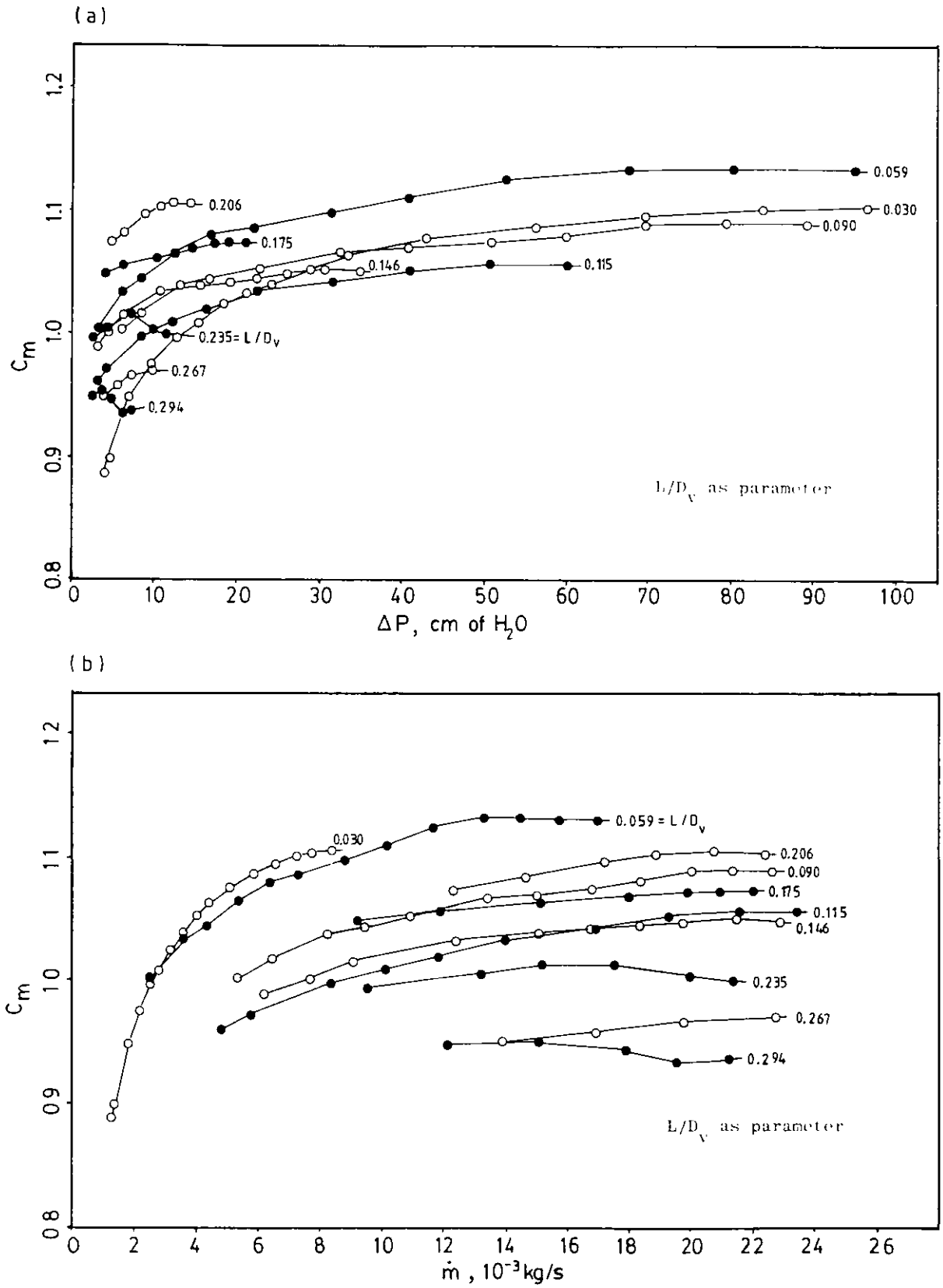

Figure 4.3 Variations of discharge coefficient C_m with (a) Pressure drop (b) Mass flow rate

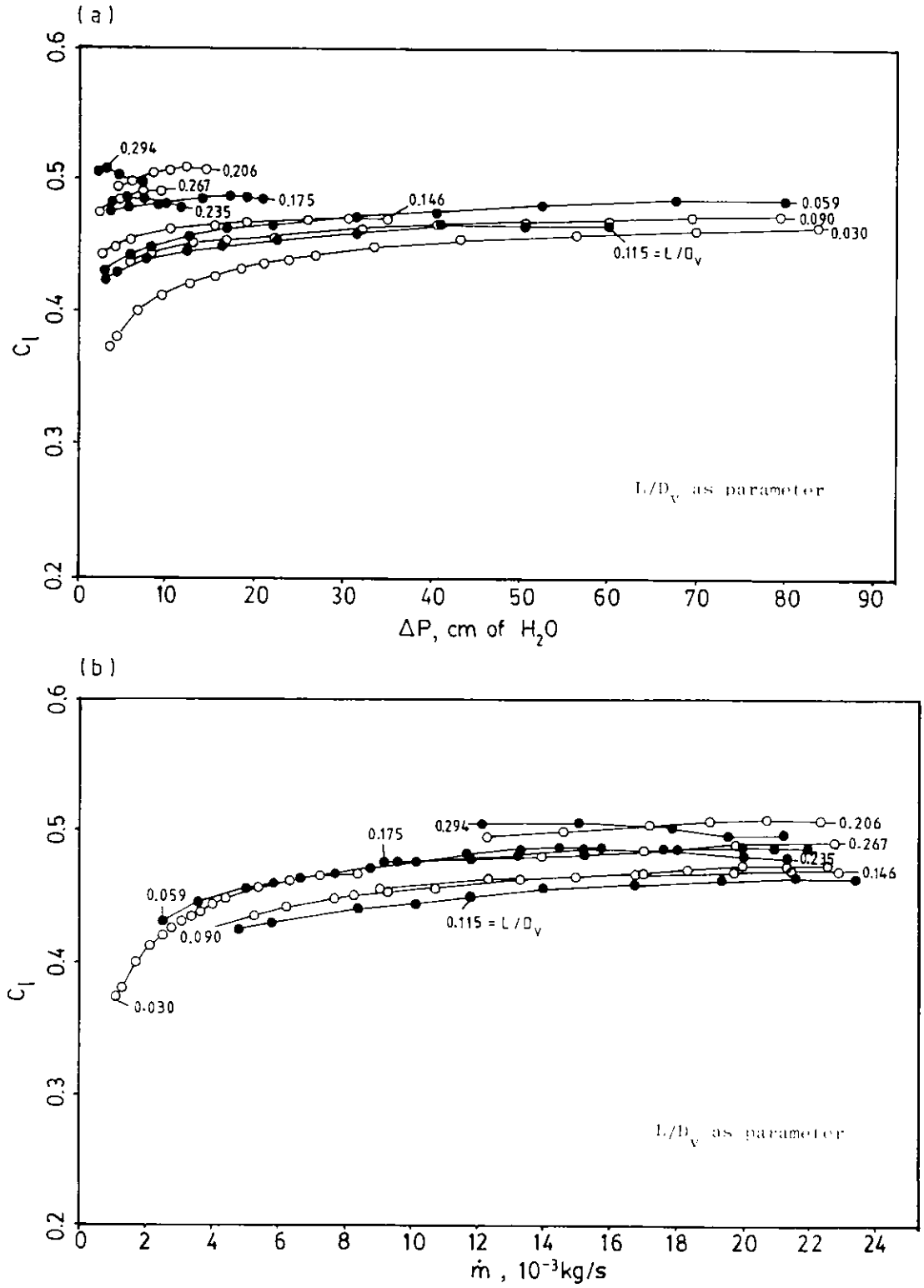

Figure 4.4 Variations of discharge coefficient C_1 with (a) Pressure drop (b) Mass flow rate

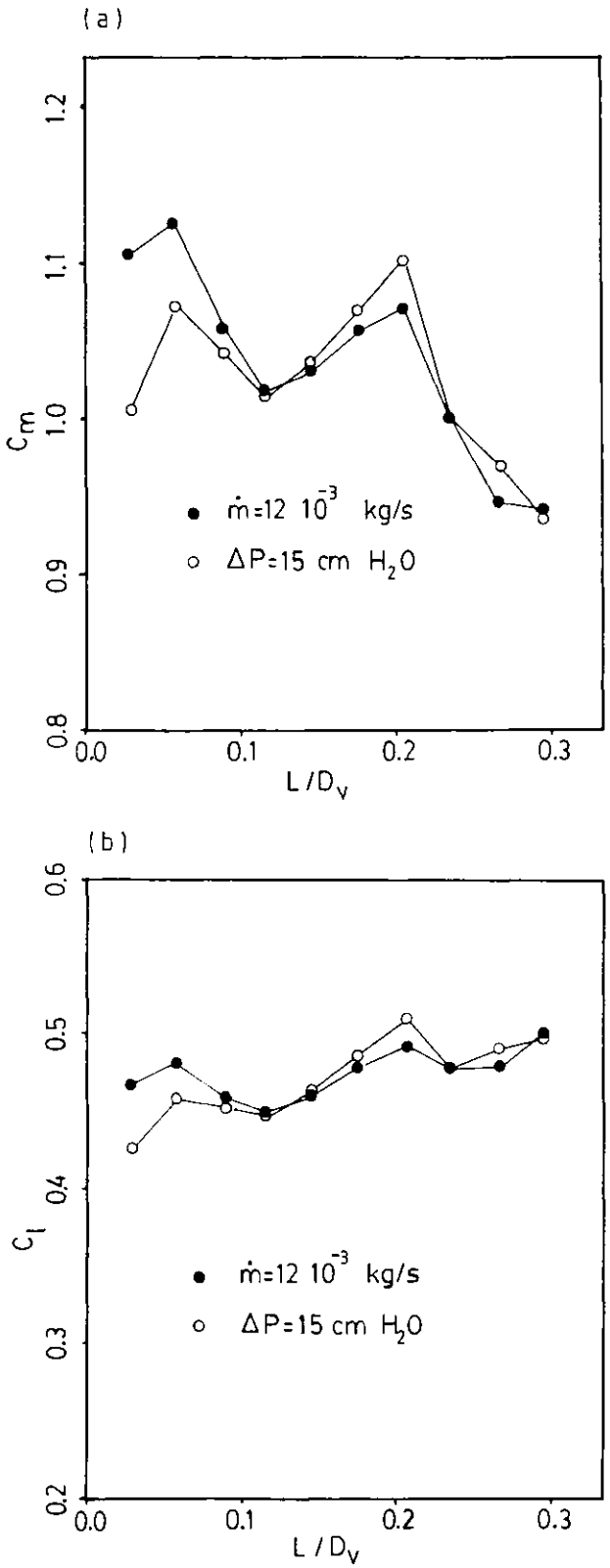

Figure 4.5 Variations of discharge coefficients with valve lift.(a) C_m, based on minimum geometric area (b) C_l, based on peripheral lift area

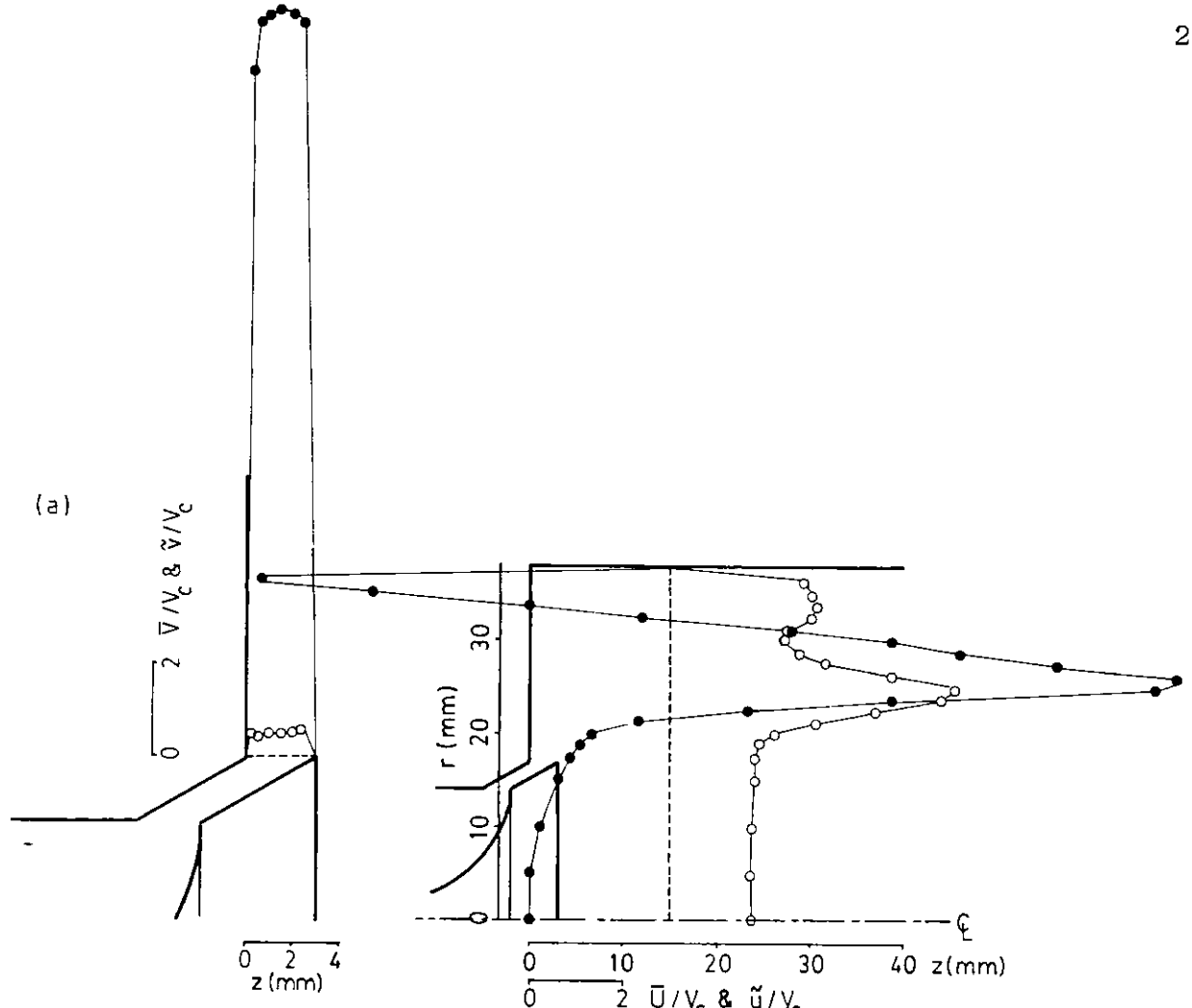

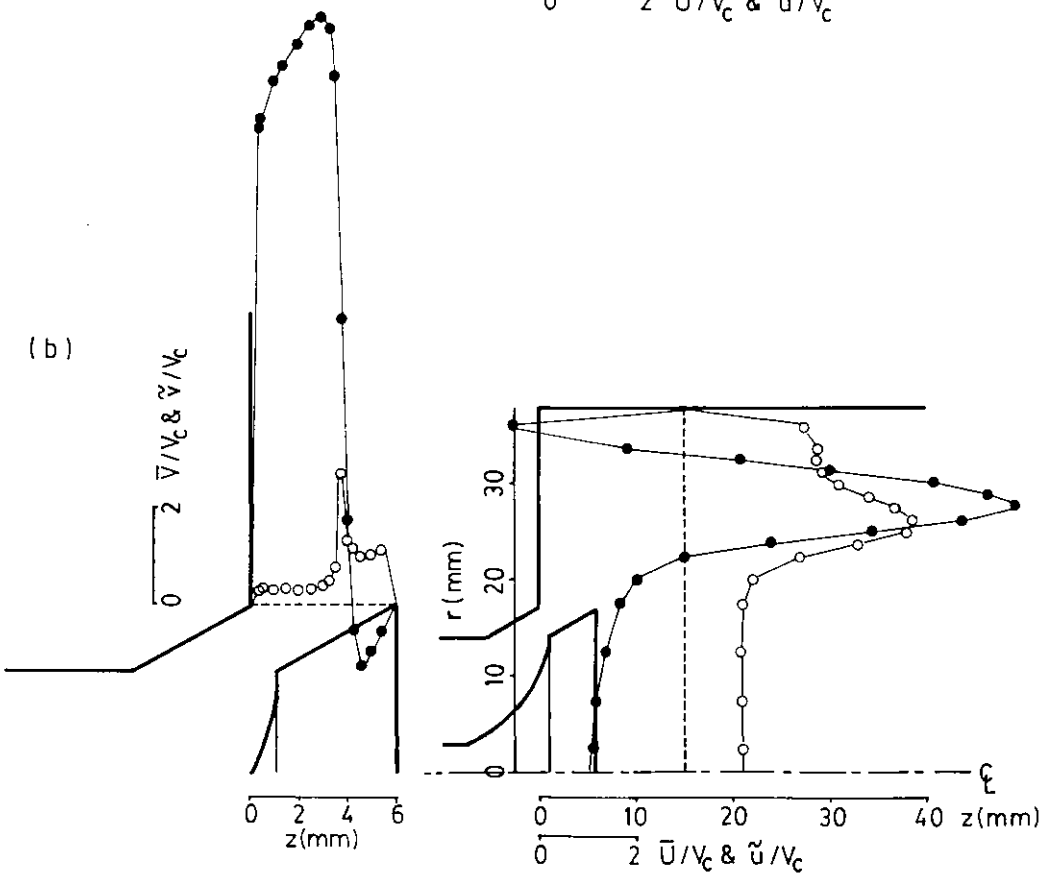

Figure 4.6 cont'd...

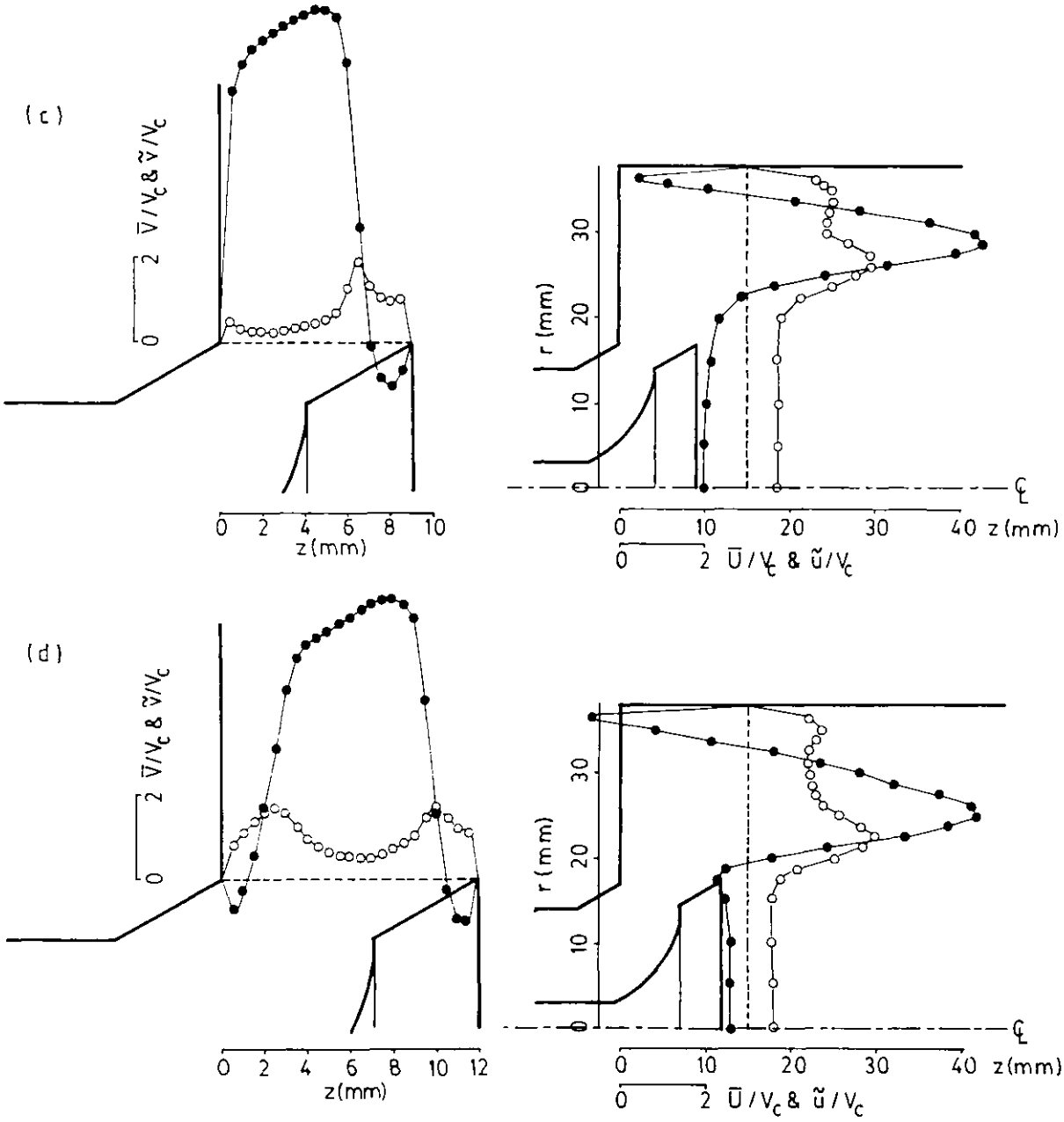

Figure 4.6 Axial mean and rms velocity profiles at z = 15 mm and radial mean and rms velocity profiles at valve exit plane; steady flow, (●) mean, (o) rms.
(a) L = 3 mm (b) L = 6 mm (c) L = 9 mm (d) L = 12 mm

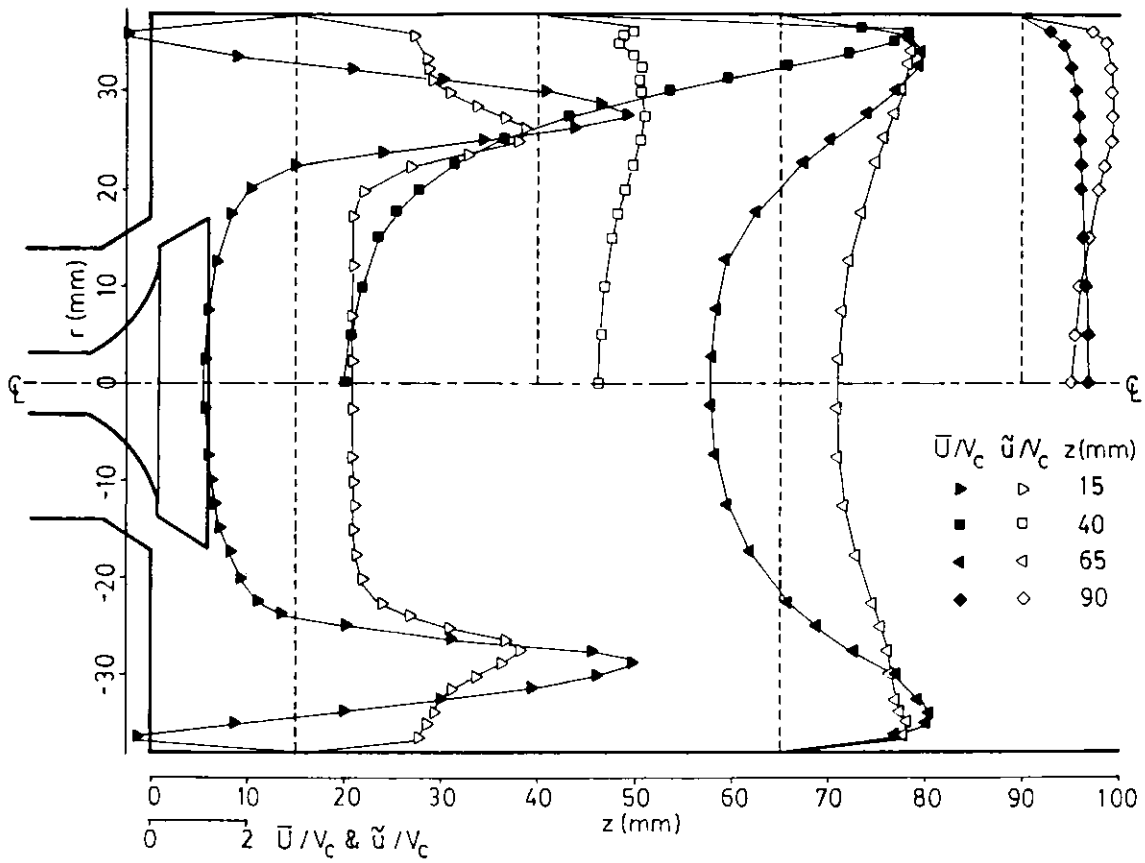

Figure 4.7 Axial mean and rms velocity profiles; steady flow, L = 6 mm.

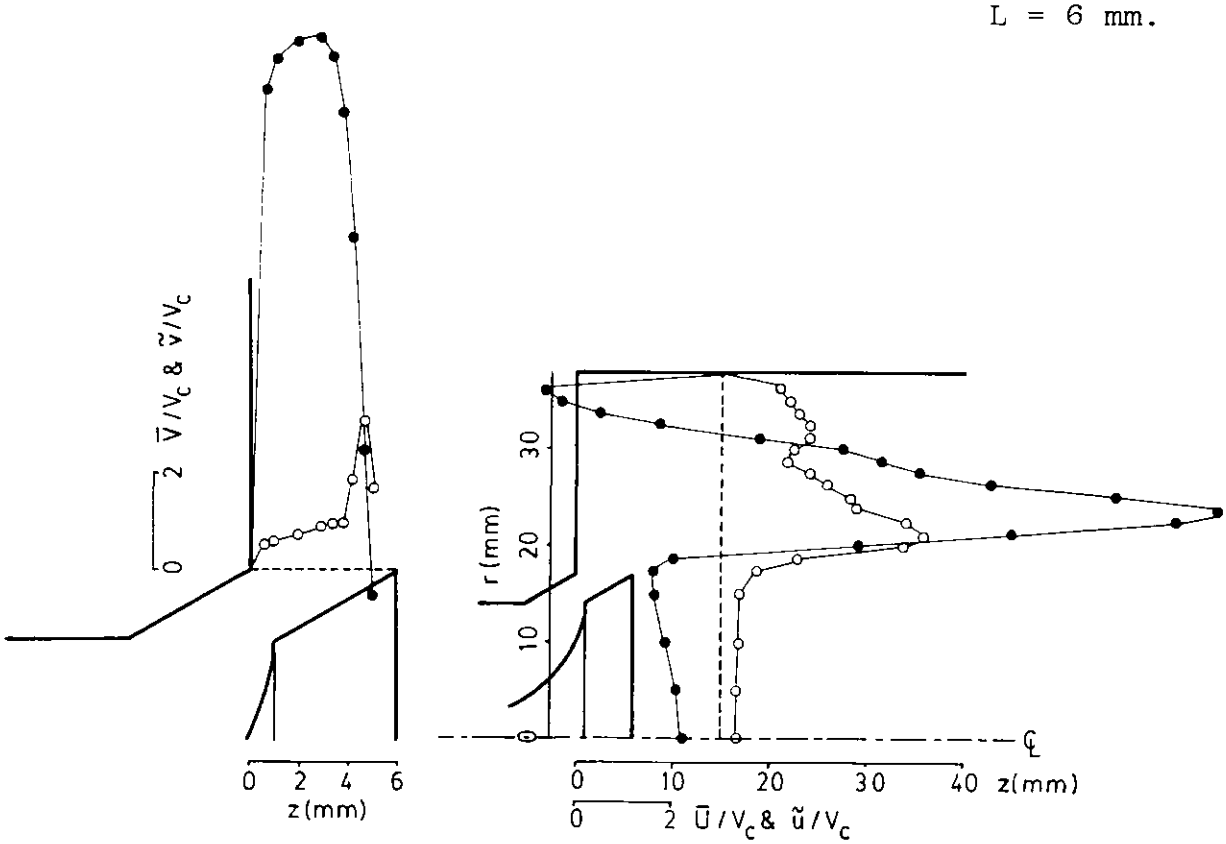

Figure 4.8 Axial mean and rms velocity profiles at z = 15 mm and radial mean and rms velocity profiles at valve exit plane; unsteady flow, Θ = 36 degrees, L = 6 mm, (•) mean, (o) rms.

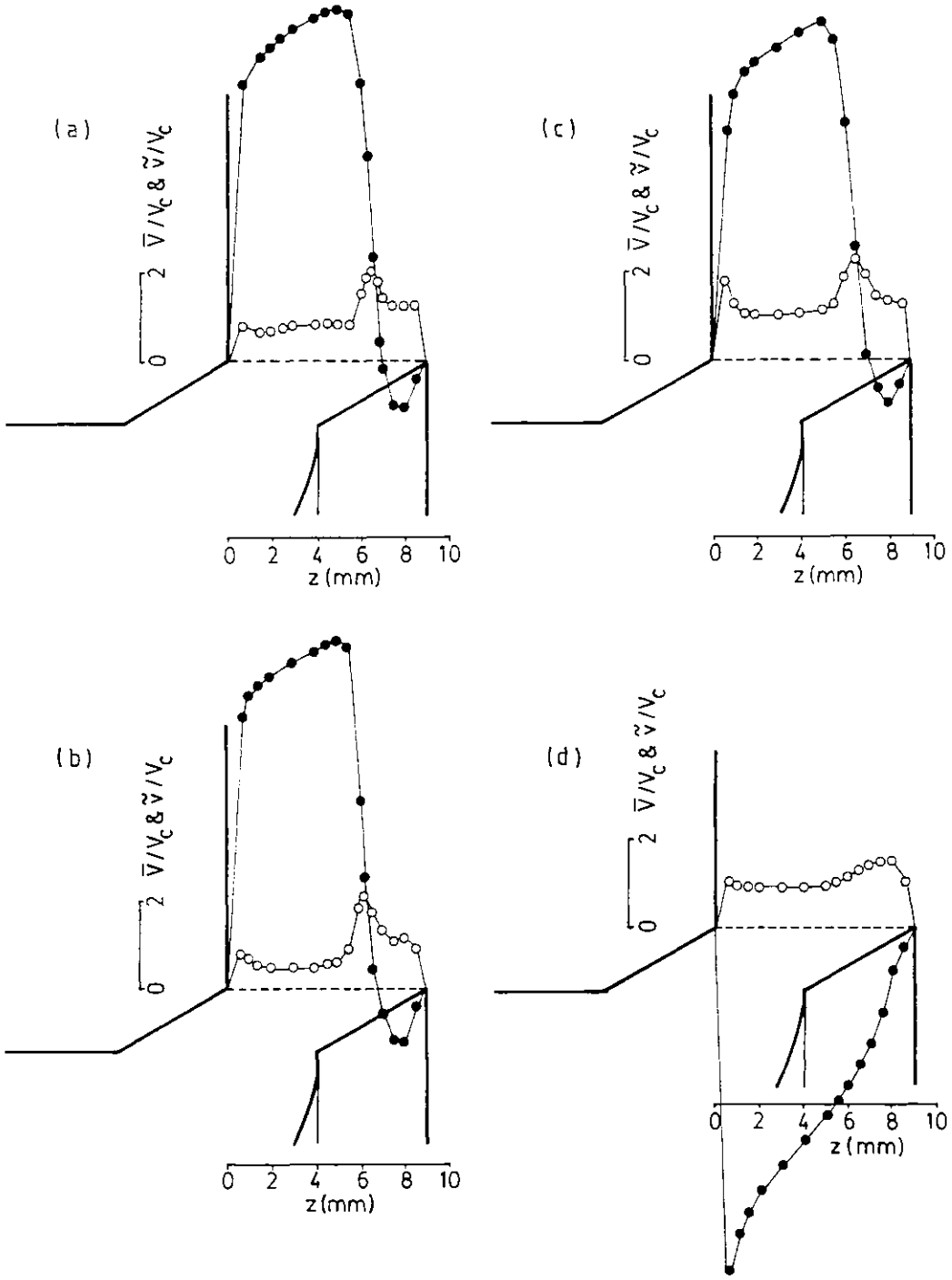

Figure 4.9 Radial mean and rms velocity profiles at valve exit plane; unsteady flow, L = 9 mm,(●) mean, (○) rms. (a) Θ = 36 degrees (b) Θ = 90 degrees (c) Θ = 144 degrees (d) Θ = 216 degrees

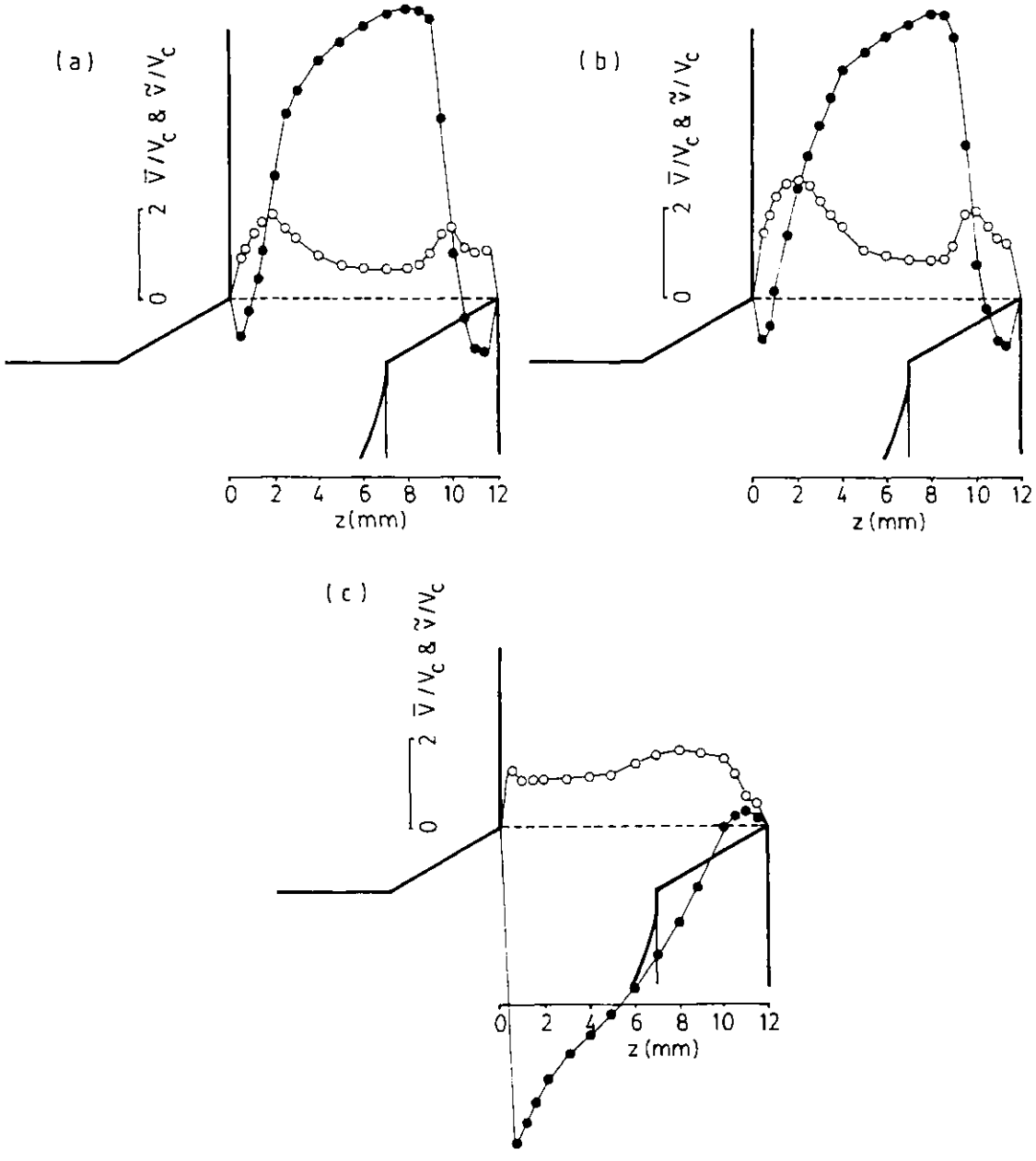

Figure 4.10 Radial mean and rms velocity profiles at valve exit plane; unsteady flow, L = 12 mm, (•) mean, (o) rms. (a) θ = 36 degrees (b) θ = 90 degrees (c) θ = 216 degrees

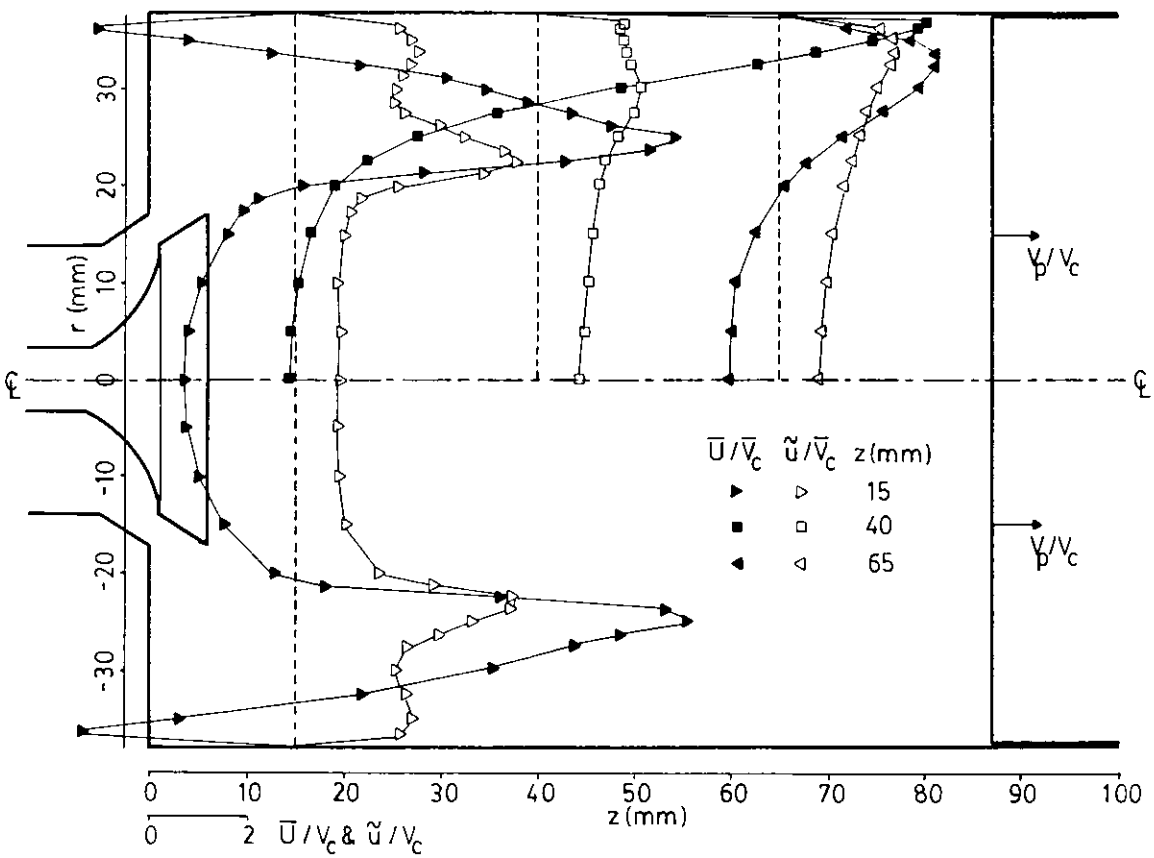

Figure 4.11 Axial mean and rms velocity profiles;unsteady flow, Θ = 90 degrees, L = 6 mm.

CHAPTER 5

CONCLUDING REMARKS

This Chapter outlines those findings which are considered to be the main contributions of this thesis to the current knowledge of internal aerodynamics in reciprocating internal-combustion engines. The detailed information has been summarised at the end of each Chapter and is not repeated here. On the basis of the present and previous studies, areas in which further research is needed are identified and recommendations are made for the way in which future work should proceed.

The measurement of velocity characteristics were obtained by laser Doppler anemometry in axisymmetric model engines motored with and without compression and a steady flow simulation of an inlet port. The results reflect some of the most important flow phenomena related to the intake and compression phases of four-stroke engines, which include intake valve and in-cylinder flow structures, swirl and squish.

A detailed investigation of the intake flow pattern was conducted in the non-compressing arrangement and included the effects of operating parameters, such as stroke, clearance volume and piston crown geometry. In all configurations the vortical flow pattern prevailing in the axial plane, and induced by a jet-like flow during the intake, collapsed before the piston has moved 10% of its travel in the return stroke. The effect of piston stroke and clearance volume was more of a quantitative nature and the vortices elongated or contracted to accommodate the changes in geometry. The piston crown geometry did not have any significant effect on the in-cylinder flow structure during intake and in the return stroke as there was no compression.

Compression related flow processes including squish and its interaction with swirl field were investigated in the four-stroke model engine and the effect of piston bowl geometry on TDC flow structure quantified. In disc shape combustion chambers the only mean motion existing during compression and carried over from intake was the swirl motion in the normal plane as it was least affected by the piston-induced compressive stresses. Compression turbulence was homogeneous and isotropic and remained virtually constant after IVC at levels of around 0.5 times the mean piston speed. Squish and swirl have been shown to be major contributors to the mean motion rather than to overall turbulence prior to combustion, with the exception of the re-entrant type piston bowl which has also resulted in significant turbulence production. The interaction of squish with swirl caused marked changes in the TDC flow structure, which are determined by the mechanism of counteracting fields of pressure forces associated with squish and centrifugal forces due to swirl.

The suitability of the present data as a testing ground for calculation methods has been demonstrated. The comparison of the experimental data with the related calculations showed a reasonable qualitative agreement with discrepancies stemming mainly from uncertainties in boundary conditions and numerical errors. The errors associated with specific turbulence models are difficult to isolate unless other sources of uncertainty such as initial and boundary conditions are rendered insignificant.

For this purpose, the measurements of the velocity characteristics were obtained at and near the exit plane of an intake valve. The extent to which the valve flow

can be considered quasi-steady was also demonstrated by obtaining velocity information under both steady and unsteady state conditions at fixed valve lifts. The quantitative description of the flow at the valve exit plane showed, in most parts of the lift range, large deviations from the plug type flow widely assumed in most calculation methods, which explains some of the reasons for the underprediction of in-cylinder mean flow and turbulence. Good agreement between the steady and unsteady valve flows was observed and suggests that the valve performance of an engine can be determined in steady test rigs with less effort and more economy than in engines.

The close correspondence between results obtained in motored production engines and the present results, together with others obtained in similar model engines and referred to in Chapter 1, indicates the importance of model engines to engine research. The results are readily available with increased detail, economy and accuracy and can be extrapolated to real engines. At the same time the requirements for calculation methods, which are restricted to simple-than-practice geometries, are better satisfied. The model engines are, on the other hand, limited to low engine speeds and compression ratios. The present and previous results cited in the literature indicate, however, only a small dependence on engine speed and compression ratio and justify, despite the constraints, the use of model engines in engine research. On the basis of this, it is recommended that model engines should go on to be used in future works to improve and understand the processes concerned.

The focus of this thesis has been the internal aerodynamics of piston engines which, however, involve other processes including fuel-air mixing and subsequent combustion. Future work should be directed to address the process next in line, ie. fuel-air mixing, by injecting a passive scalar into the cylinder in the form of a tracer gas and of diesel type sprays, and measuring the scalar/air mixture density fluctuations with a non-intrusive technique such as Rayleigh scattering. Laser Doppler anemometry may also be used in parallel to determine spray characteristics and their effect on mean motion and turbulence especially near TDC.

The present work on the intake valve flow should be extended to include velocity measurements under unsteady flow conditions with an operating valve and constant pressure drop across it, simulating more closely the real valve situation. Further extension of the work can then be made to incorporate measurements under normal operating conditions, hence quantifying further the extent to which the valve performance of an engine can be determined away from the engine environment.

REFERENCES

AHMADI-BEFRUI B., GOSMAN A.D., LOCKWOOD F.C. & WATKINS A.P. (1981)
"Multidimensional Calculation of Combustion in an Idealised Homogeneous Charge Engine: a Progress Report", SAE Paper 810151.

AHMADI-BEFRUI B., ARCOUMANIS C., BICEN A.F., GOSMAN A.D., JAHANBAKHSH A. & WHITELAW J.H. (1982)
"Calculations and Measurements of the Flow in a Motored Model Engine and Implications to Open-Chamber Direct-Injection Engines", Proc. Symp. on Three Dimensional Turbulent Shear Flows, St. Louis.

ALCOCK J.F. (1934)
"Air Swirl in Oil Engines", Proc. I. Mech. E., 128.

ALCOCK J.F. & SCOTT W.M. (1962)
"Some More Light on Diesel Combustion", Proc. I. Mech. E., (AD), No.5.

ANNAND W.J.D. (1969)
"Engine Breathing-Aerodynamics of Low Speed Flow Through Inlet Valves and Ports for Reciprocating Engines", Automobile Engineer, 59.

ARCOUMANIS C. & VLACHOS N.S. (1980)
"The Influence of Valve Seat Angle on the Flow Patterns in a Motored Piston-Cylinder Assembly", Imperial College, Mech. Eng. Dept., Report FS/80/25.

ARCOUMANIS C., BICEN A.F. & WHITELAW J.H. (1981)
"Turbulent Flow Field in a Motored Four-Stroke Engine with an Off-Centre Valve", Imperial College, Mech. Eng. Dept, Report FS/81/33.

ARCOUMANIS C., BICEN A.F., VLACHOS N.S. & WHITELAW J.H. (1982a)
"Effects of Flow and Geometry Boundary Conditions on Fluid Motion in a Motored I.C. Model Engine", Proc. I. Mech. E., 196, 4.

ARCOUMANIS C., BICEN A.F. & WHITELAW J.H. (1982b)
"Application of LDA to Four-Stroke Motored Model Engines", Proc. International Conference on LDA Applications in Fluid Mechanics, Lisbon.

ARCOUMANIS C., BICEN A.F. & WHITELAW J.H. (1982c)
"Effects of Inlet Parameters on the Flow Characteristics in a Four-Stroke Model Engine", SAE Paper 820750.

ARCOUMANIS C., BICEN A.F. & WHITELAW J.H. (1982d)
"Measurements in a Motored Four-Stroke Reciprocating Model Engine", J. Fluids Engng., 104, 235.

ARCOUMANIS C., BICEN A.F. & WHITELAW J.H. (1983)
"Squish and Swirl-Squish Interaction in Motored Engines", J. Fluids Engng., 105, 105.

ARNOLD M.J., TINDAL M.J. & WILLIAMS T.J. (1972)
"Measurement of Induction Gas Velocities in a Reciprocating Engine Cylinder", SAE Paper 720115.

ASANUMA T. & OBOKATA T. (1979)
"Gas Velocity Measurements of a Motored and Firing Engine by Laser Anemometry", SAE Paper 790096.

BICEN A.F. (1980)
"Effect of a Lipped Cylindrical Piston Bowl on the Flow Characteristics of a Motored Piston-Cylinder Assembly", Imperial College, Mech. Eng. Dept., Report FS/80/33.

BICEN A.F. & VLACHOS N.S. (1980)
"The Influence of Stroke and Clearance on the Flow Patterns in Motored Piston-Cylinder Assemblies", Imperial College, Mech. Eng. Dept., Report FS/80/28.

BICEN A.F., VLACHOS N.S. & WHITELAW J.H. (1980)
"The Creation and Destruction of Vortices in Unsteady Flows", Letters in Heat and Mass Transfer, 7, 77.

BICEN A.F., LAKER J. & VLACHOS N.S. (1981)
"A Microprocessor Controlled Data Acquisition and Processing System for LDA Signals", Imperial College, Mech. Eng. Dept. Report.

BICEN A.F. (1982)
"Refraction Correction for LDA Measurements in Flows with Curved Optical Boundaries", TSI Quarterly, 8, No.2.

BICEN A.F. & WHITELAW J.H. (1983)
"Steady and Unsteady Flow Through an Intake Valve", Imperial College, Mech. Eng. Dept., Report FS/83/11.

BLUMBERG P.N., LAVOIE G.A. & TABACZYNSKI R.J. (1979)
"Phenomenological Models for Reciprocating Internal Combustion Engines", Prog. Energy Combust. Sci., 5, 123.

BOADWAY J.D. & KARAHAN E. (1981)
"Correction of Laser Doppler Anemometer Readings for Refraction at Cylindrical Interfaces", DISA Information, No.26.

BORGNAKKE C., DAVIS G.C. & TABACZYNSKI R.J. (1981)
"Predictions of In-Cylinder Swirl Velocity and Turbulence Intensity for an Open Chamber Cup in Piston Engine", SAE Paper 810224.

BRADSHAW P. (1973)
"Effects of Streamline Curvature on Turbulent Flow", AGARDograph 169.

BRANDL F., REVERENCIC I., CARTELLIERI W. & DENT J.C. (1979)
"Turbulent Air Flow in the Combustion Bowl of a D.I. Diesel Engine and its Effect on Engine Performance", SAE Paper 790040.

BRITISH STANDARD INSTITUTION (1964)
"Methods for Measurements of Fluid Flow in Pipes" BS1042, Part 1.

BUCHHAVE P. (1975)
"Biassing Errors in Individual Particle Measurments with the LDA Counter Signal Processor", Proc. of the LDA-Symposium Copenhagen 1975, 258.

CATANIA A.E. (1982)
"3-D Swirling Flows in an Open-Chamber Automotive Diesel Engine with Different Induction Systems", Proc. Symp. on Flows in Internal Combustion Engines, Arizona.

COLE J.B. & SWORDS M.D. (1978)
"Optical Studies of Turbulence in an Internal Combustion Engine", Proc. of Seventeenth International Combustion Symp., 1295.

COLE J.B. & SWORDS M.D. (1980)
"An Investigation of the Ignition Process in a Lean-Burning Engine Using Conditionally Sampled Laser-Doppler Anemometry", SAE Paper 800043.

COGHE A., FERRARI G., AGOSTONI G., BRIOSCHI C., BRUNELLO G., CALDERINI F., GUARNERI C. & VOLPI A. (1980)
"Velocity Measurements on the Motored Single Cylinder Fiat Engine", CNPM Report NT-8053.

DAVIS G.C. & KENT J.C. (1979)
"Comparison of Model Calculations and Experimental Measurements of the Bulk Cylinder Flow Processes in a Motored PROCO Engine", SAE Paper 790290.

DENT J.C. & DERHAM J.A. (1974)
"Air Motion in a Four-Stroke Direct-Injection Diesel Engine", Proc. I. Mech. E., 188, 269.

DENT J.C. & SALAMA N.S. (1975a)
"Turbulence and Structure in the Spark Ignition Engine", I. Mech. E. Paper C83/75.

DENT J.C. & SALAMA N.S. (1975b)
"The Measurement of the Turbulence Characteristics in an Internal Combustion Engine Cylinder", SAE Paper 750886.

DERHAM J.A. (1972)
"Air Motion in a Four-Stroke Direct-Injection Diesel Engine", Ph.D. Thesis, Loughborough University of Technology.

DICKSEE C.B. (1940)
"The High Speed Compression Ignition Engine", Blackie & Son.

DIMOTAKIS P. (1976)
"Single Scattering Particle Laser Doppler Measurements of Turbulence", Paper 10, AGARD Conference No.193, Applications of Non-Intrusive Instrumentation in Fluid Flow Research.

DRAIN L.E. (1980)
"The Laser Doppler Technique", John Wiley, Chichester.

DURAO D.F.G. & WHITELAW J.H. (1975)
"The Influence of Sampling Procedures on Velocity Bias in Turbulent Flows", Proc. of the LDA-Symposium Copenhagen 1975, 138.

DURAO D.F.G. (1976)
"The Application of Laser Anemometry to Free Jets and Flames with and without Recirculation", Ph.D. Thesis, University of London.

DURAO D.F.G. & WHITELAW J.H. (1978)
"Relationship Between Velocity and Signal Quality in Laser Doppler Anemometry", J. Phys. E.: Sci. Instrum., 12, 47.

DURAO D.F.G., LAKER J. & WHITELAW J.H. (1980)
"Bias Effects in Laser Doppler Anemometry", J. Phys. E.: Sci. Instrum., 13, 442.

DURST F. & ZARE M. (1974)
"Removal of Pedestals and Directional Ambiguity of Optical Anemometer Signals", Appl. Optics, 13, 2562.

DURST F., MELLING A. & WHITELAW J.H. (1981)
"Principles and Practice of Laser-Doppler Anemometry", Second Edition, Academic Press, London.

EDWARDS R.V. (1981)
"A New Look at Particle Statistics in Laser-Anemometry Measurement", J. Fluid Mech., 105, 317.

EKCHIAN A. & HOULT D.P. (1979)
"Flow Visualisation Study of the Intake Process of an Internal Combustion Engine", SAE Paper 790095.

EL-KHAFAJI A.H.A., TINDAL M.J. & WILLIAMS T.J. (1971)
"Engine Cylinder Gas Flow Measurements by Hot-Wire Anemometry", Proc. Symp. on Flow - Its Measurement and Control in Science and Industry, Pittsburgh.

EL-TAHRY S.H. (1982)
"A Numerical Study on the Effects of Fluid Motion at Inlet-Valve Closure on Subsequent Fluid Motion in a Motored Engine", SAE Paper 820035.

FITZEGEORGE D. & ALLISON J.L. (1962)
"Air Swirl in a Road Vehicle Diesel Engine", Proc. I. Mech. E., (AD), No.4.

FUKUTANI I. & WATANABE E. (1982)
"Air Flow Through Poppet Inlet Valves - Analysis of Static and Dynamic Flow Coefficients", SAE Paper 820154.

GANY A., LARREA J.J. & SIRIGNANO W.A. (1980)
"Laser Doppler Velocimetry Measurements in a Motored I.C. Engine Simulator", AIAA Paper 80-0079.

GOSMAN A.D. & WATKINS A.P. (1976)
"Simulation of Flow and Heat Transfer During a Four-Stroke Motored Engine Cycle", Imperial College, Mech. Eng. Dept. Report.

GOSMAN A.D., MELLING A., WATKINS A.P. & WHITELAW J.H. (1977)
"Axisymmetric Laminar Flow in a Motored Reciprocating Engine", Imperial College, Mech. Eng. Dept., Report CHT/77/3.

GOSMAN A.D. & JOHNS R.J.R. (1978)
"Development of a Predictive Tool for In-Cylinder Gas Motion in Engines", SAE Paper 780315.

GOSMAN A.D., JOHNS R.J.R. & WATKINS A.P. (1978a)
"Assessment of a Predictive Method for In-Cylinder Processes in Reciprocating Engines", Proc. Symp. on Combustion Modelling in Reciprocating Engines, General Motors Res. Labs., Detroit.

GOSMAN A.D., MELLING A., WHITELAW J.H. & WATKINS A.P. (1978b)
"Axisymmetric Flow in a Motored Reciprocating Engine", Proc. I. Mech. E., 192, 11.

GOSMAN A.D. & JOHNS R.J.R. (1980)
"Computer Analysis of Fuel-Air Mixing in Direct-Injection Engines", SAE Paper 800091.

GOSMAN A.D. & WHITELAW J.H. (1980)
"Calculation and Measurement of Flow and Heat-Transfer Properties of Reciprocating Piston-Cylinder Arrangements", Proc. of SRC/UnICEG Symposium, 131.

GOSMAN A.D. & JAHANBAKHSH A. (1981)
"Comparisons Between Measurements and Predictions of Swirl in a Reciprocating Engine", Contribution to "Comparisons Between Measurement and Analysis of Fluid Motion in Internal Combustion Engines", Ed. Witze P.O., Sandia National Labs., Report SAND81-8242.

GOSMAN A.D. & HARVEY P.S. (1982)
"Computer Analysis of Fuel-Air Mixing and Combustion in an Axisymmetric D.I. Diesel", SAE Paper 820036.

GRASSO F. & BRACCO F.V. (1981)
"Computed and Measured Turbulence in Axisymmetric I.C. Engines", Princeton University, Mech. and Aerospace Eng. Dept. Report, also submitted to AIAA Journal.

HANSON S. (1974)
"Coherent Detection in Laser Doppler Velocimeters", Opto-Electronics 6, 263.

HARVEY P.S. & GOSMAN A.D. (1982)
"An Analysis of the Influence of Swirl on Combustion in D.I. Diesel Engines by Computer Simulation", Imperial College, Mech. Eng. Dept., Report FS/82/16.

HEYWOOD J.B. (1980)
"Engine Combustion Modelling - An Overview", Combustion Modelling in Reciprocating Engines, Eds. Mattavi J.N. and Amann C.A., Plenum Press, New York, 1.

HIROTOMI T., NAGAYAMA I., KOBAYASHI S. & YAMAMASU M. (1981)
"Study of Induction Swirl in a Spark Ignition Engine", SAE Paper 810496.

HOESEL H. & RODI W. (1977)
"New Biasing Elimination Method for Laser Doppler Velocimeter Counter Processing", Rev. Sci. Instrum., 48, 910.

HORVATIN M. & HUSSMANN A.W. (1969)
"Measurement of Air Movement in Internal Combustion Engine Cylinders", DISA Information, No.8.

HOULT D.P. & WONG V.W. (1978)
"The Generation of Turbulence in an Internal Combustion Engine", Proc. Symp. on Combustion Modelling in Reciprocating Engines, General Motors Res. Labs., Detroit.

HUEBNER K.H. & McDONALD A.T. (1972)
"Experimental Determination of Airflow Patterns in Piston Engines with Induction Swirl", SAE Paper 720026.

ISHIKAWA N. & DAILY J.W. (1978)
"Observations of Flow Characteristics in a Model I.C. Engine Cylinder", SAE Paper 780230.

JAMES E.H. (1972)
"Investigations of Turbulent Flow in the Combustion Chamber of a Spark Ignition Engine", Ph.D. Thesis, Loughborough University of Technology.

JAMES E.H. & LUCAS G.G. (1975)
"Turbulent Flow in Spark Ignition Engine Combustion Chambers", SAE Paper 750886.

JOHNS R.J.R. (1980)
"Prediction of Flow in Diesel Engine Cylinders", Ph.D. Thesis, University of London.

JOHNSTON S.C., ROBINSON C.W., RORKE W.S., SMITH J.R. & WITZE P.O. (1979)
"Application of Laser Diagnostics to an Injected Engine", SAE Paper 790092.

JONES W.P. & LAUNDER B.E. (1972)
"The Prediction of Laminarisation with a Two-Equation Model of Turbulence", Int. J. Heat Mass Transfer, 15, 301.

KASTNER L.S., WILLIAMS T.J. & WHITE J.B. (1963)
"Poppet Inlet Valve Characteristics and Their Influence on the Induction Process", Proc. I. Mech. E., 178, 955.

KOGELNIK H. & LI T. (1966)
"Laser Beams and Resonators", Appl. Optics, 5, 1550.

LANCASTER D.R. (1976)
"Effects of Engine Variables on Turbulence in a Spark Ignition Engine", SAE Paper 760159.

LEE D.W. (1939)
"A Study of Air Flow in an Engine Cylinder", NASA Report 653.

LIOU T.M. & SANTAVICCA D.A. (1982)
"Cycle Resolved LDV Measurements in a Motored I.C. Engine", Proc. International Conference on LDA Applications in Fluid Mechanics, Lisbon.

LUCAS G.G. & ANTON R. (1979)
"The Effect of Squish on Charge Turbulence and Flame Propogation in an S.I. Engine", I. Mech. E. Paper C87/79.

McGUIRK J.J., TAYLOR A.M.K.P. & WHITELAW J.H. (1981)
"The Assessment of Numerical Diffusion in Upwind-Difference Calculations of Turbulent Recirculating Flows", Imperial College, Mech. Eng. Dept., Report FS/81/30.

McLAUGHLIN D.K. & TIEDERMAN W.G. (1973)
"Biasing Correction for Individual Realisation of Laser Anemometer Measurements in Turbulent Flows", Phys. Fluids, 16, 2082.

MELLING A. (1971)
"Scattering Particles for Laser Anemometry in Air: Selection Criteria and Their Realisation", Imperial College, Mech. Eng. Dept., Report ET/TN/B/7.

MELLING A. & WHITELAW J.H. (1973)
"Seeding of Gas Flows for Laser Anemometry", DISA Information, No.15.

MELLING A. & WHITELAW J.H. (1976)
"Design of Laser Doppler Anemometers for Reciprocating Engines", Imperial College, Mech. Eng. Dept., Report CHT/76/6.

MELLING A. (1977)
"Axisymmetric Turbulent Flow in a Motored Reciprocating Engine", Imperial College, Mech. Eng. Dept., Report CHT/77/4.

MOLCHANOV L.K. (1953)
"On the Problem of Gas Motion and Combustion in a Light Fuel Engine", Trudy Makowkogo Automil' No-Dorozhnogo Instituta, Autatransizdat, Moscow.

MONAGHAN M.L. & PETTIFER H.F. (1981)
"Air Motion and its Effect on Diesel Performance and Emissions", SAE Paper 810255.

MOREL T. & MANSOUR N.N. (1982)
"Modelling of Turbulence in Internal Combustion Engines", SAE Paper 820040.

MORSE A.P. (1977)
"The Effect of Crank-Angle Broadening on Laser Doppler Measurements in Reciprocating Engines", Imperial College, Mech. Eng. Dept., Report FS/77/8.

MORSE A.P., WHITELAW J.H. & YIANNESKIS M. (1979a)
"Turbulent Flow Measurements by Laser Doppler Anemometry in Motored Piston-Cylinder Assemblies", J. Fluids Engng., 101, 208.

MORSE A.P., WHITELAW J.H. & YIANNESKIS M. (1979b)
"The Effect of Engine Speed on the Flow Patterns in Reciprocating Engines", Imperial College, Mech. Eng. Dept., Report FS/79/12.

MORSE A.P., WHITELAW J.H. & YIANNESKIS M. (1980a)
"The Influence of Swirl on the Flow Characteristics of a Reciprocating Piston-Cylinder Assembly", J. Fluids Engng., 102, 478.

MORSE A.P., WHITELAW J.H. & YIANNESKIS M. (1980b)
"The Flow Characteristics of a Piston-Cylinder Assembly with an Off-Centre Open Port", Proc. I. Mech. E., 194, 31.

MORSE A.P. & WHITELAW J.H. (1981)
"Measurements of the In-Cylinder Flow of a Motored Four-Stroke Reciprocating Engine", Proc. R. Soc. Lond., A377, 309.

NAGAYAMA I., ARAKI Y. & LIOKA Y. (1977)
"Effects of Swirl and Squish on S.I. Engine Combustion and Emission", SAE Paper 770217.

NAMAZIAN M., HANSEN S., LYFORD-PIKE E., SANCHEZ-BARSSE J., HEYWOOD J. & RIFE J. (1980)
"Schlieren Visualisation of the Flow and Density Fields in the Cylinder of a Spark-Ignition Engine", SAE Paper 800044.

NAMAZIAN M. & HEYWOOD J.B. (1982)
"Flow in the Piston-Cylinder-Ring Crevices of a Spark-Ignition Engine: Effects of Hydrocarbon Emissions, Efficiency and Power", SAE Paper 820088.

OHIGASHI S., HAMAMOTO Y. & TANABE S. (1972)
"Swirl - Its Measurement and Effect on Combustion in a Diesel Engine", Proc. I. Mech. E., C134, 129.

OLDENGARM J., VAN KRIEKEN A.H. & RATERNIK H.J. (1976)
"Development of a Rotating Grating and its Use in Laser Velocimetry", Proc. of the ISL/AGARD Workshop on Laser Anemometry, St. Louis, France.

RAMOS, J.I., HUMPHREY J.A.C. & SIRIGNANO W.A. (1979)
"Numerical Prediction of Axisymmetric Laminar and Turbulent Flows in Motored Reciprocating Internal Combustion Engines", SAE Paper 790356.

RAMOS J.I. & SIRIGNANO W.A. (1980)
"Axisymmetric Flow Model with and without Swirl in a Piston-Cylinder Arrangement with Idealised Valve Operation", SAE Paper 800284.

RAMOS J.I. & SIRIGNANO W.A. (1981)
"Turbulent Flow Field in Homogeneous-Charge Spark-Ignition Engines", Proc. of Eighteenth International Combustion Symp., 1825.

RAMOS J.I., GANY A. & SIRIGNANO W.A. (1981)
"Study of Turbulence in a Motored Four-Stroke Internal Combustion Engine", AIAA Journal, 19, No.5, 595.

RASK R.B. (1978)
"Velocity Measurements Inside the Cylinder of a Motored Internal Combustion Engine", Third International Workshop on Laser Velocimetry, Purdue University.

RASK R.B. (1979)
"Laser Doppler Anemometer Measurements in an Internal Combustion Engine", SAE Paper 790094.

RASK R.B. (1981)
"Comparison of Window, Smoothed-Ensemble and Cycle-to-Cycle Data Reduction Techniques for Laser Doppler Anemometer Measurements of In-Cylinder Velocity", Proc. Symp. on Fluid Mechanics of Combustion Systems, Colorado.

RENSHAW J. & WIGLEY G. (1979)
"In-Cylinder Swirl Measurements by Laser Anemometer in a Production Diesel Engine", AERE, Harwell, Report R9646.

REYNOLDS W.C. (1978)
"Modelling of Fluid Motions in Engines - an Introductory Overview", Proc. Symp. on Combustion Modelling in Reciprocating Engines, General Motors Res. Labs., Detroit.

RUDD M.J. (1969)
"A New Theoretical Model for the Laser Dopplermeter", J. Phys. E.:Sci. Instrum., 2, 55.

SEMENOV E.S. (1958)
"Studies of Turbulent Gas Flow in Piston Engines", NASA Tech. Transl., F97, 1963.

SHIMAMOTO Y. & AKIYAMA K. (1970)
"A Studay of Squish in Open Combustion Chambers of a Diesel Engine", Bulletin of the JSME, 13, No.63, 1096.

STREETER V.L. & WYLIE E.B. (1975)
"Fluid Mechanics", Sixth Edition, McGraw-Hill, New York.

TABACZYNSKI R.J., HOULT D.P. & KECK J.C. (1970)
"High Reynolds Number Flow in a Moving Corner", J. Fluid Mech., 42, 249.

TANABE S., HAMAMOTO Y. & OHIGASHI S. (1978)
"Swirl in a Four-Stroke Cycle Engine Cylinder", Bulletin of the JSME, 21, No.152, 287.

TANAKA K. (1929)
"Air Flow Through Suction Valve of Conical Seat", Aeronautical Research Institute Report, Tokyo Imperial University, Part I, 260; Part 2, 361.

TAYLOR C.F. (1978)
"The Internal Combustion Engine in Theory and Practice, Vol.1; Thermodynamics, Fluid Flow, Performance, Vol.2", John Wiley and Technology Press, M.I.T..

TAYLOR A.M.K.P. (1981)
"Confined Isothermal and Combusting Flows Behind Axisymmetric Baffles", Ph.D. Thesis, University of London.

TAYLOR A.M.K.P., WHITELAW J.H. & YIANNESKIS M. (1982)
"Report on the Calculation of Mass Flow Rate from Velocity Profiles Measured in Square Ducts", Imperial College, Mech. Eng. Dept., Report FS/82/13.

TINDAL M.J., WILLIAMS T.J. & EL-KHAFAJI A.H.A. (1974)
"Gas Flow Measurements in Engine Cylinders", SAE Paper 740719.

TINDAL M.J., WILLIAMS T.J. & ALDOORY M. (1982)
"The Effect of Inlet Port Design on Cylinder Gas Motion in Direct Injection Diesel Engines", Proc. Symp. on Flows in Internal Combustion Engines, Arizona.

TOWNSEND A.A. (1980)
"The Structure of Turbulent Shear Flow", First Paperback Edition, Cambridge University Press, Cambridge.

VAFIDIS C. (1982)
"Influence of Induction Swirl and Piston Configuration on Air Flow in a Four-Stroke Model Engine", Imperial College, Mech. Eng. Dept., Report FS/82/22.

VAFIDIS C. (1983)
"More on the Influence of Piston Configuration on In-Cylinder Swirling Flows", Imperial College, Mech. Eng. Dept., Report FS/83/10.

VLACHOS N.S. (1977)
"Blood Flow in Small Diameter Duct; Particularly in Venules", Ph.D. Thesis, University of London.

WAKISAKA T., HAMAMOTO Y. & SHIMAMOTO Y. (1982)
"Turbulence Structure of Air Swirl in Reciprocating Engine Cylinders", Proc. Symp. on Flows in Internal Combustion Engines, Arizona.

WALLACE W.B. (1967)
"High-Output Medium-Speed Diesel Engine Air and Exhaust System Flow Losses", Proc. I. Mech. E., 182, 134.

WATKINS A.P. (1973)
"Calculation of Flow and Heat Transfer in the Combustion Chamber of a Reciprocating Engine", M.Sc. Thesis, University of London.

WATKINS A.P. (1977)
"Flow and Heat Transfer in Piston/Cylinder Assemblies", Ph.D. Thesis, University of London.

WIGLEY G. & HAWKINS M.G. (1978)
"Three-Dimensional Velocity Measurements by Laser Anemometry in a Diesel Engine Under Steady State Inlet Flow Conditions", SAE Paper 780060.

WIGLEY G., PATTERSON A.C. & RENSHAW J. (1981)
"Swirl Velocity Measurements in a Firing Production Diesel Engine by Laser Anemometry", Proc. Symp. on Fluid Mechanics of Combustion Systems, Colorado.

WILLIAMS T.J. & TINDAL M.J. (1980)
"Gas Flow Studies in Direct Injection Diesel Engines with Re-entrant Combustion Chambers", SAE Paper 800027.

WILLIS D.A., MEYER W.E. & BIRNIE C. Jnr (1966)
"Mapping of Airflow Patterns in Engines with Induction Swirl", SAE Paper 660093.

WILSON N.M. (1978)
"Digital Signal-Processing Techniques for Laser Doppler Velocimetry", J. Phys. E.: Sci. Instrum., 11, 555.

WITZE P.O. (1976a)
"Hot-Wire Measurements of the Turbulence Structure in a Motored Spark-Ignition Engine", AIAA Paper 76-37.

WITZE P.O. (1976b)
"Preliminary Hot-Wire Measurements in a Motored Engine with an Axisymmetric Cylinder Geometry", Sandia National Laboratories Report.

WITZE P.O. (1977)
"Measurements of the Spatial Distribution and Engine Speed Dependence of Turbulent Air Motion in an I.C. Engine", SAE Paper 770220.

WITZE P.O. (1978)
"Application of Laser Velocimetry to a Motored Internal Combustion Engine", Third International Workshop on Laser Velocimetry, Purdue University.

WITZE P.O. (1980a)
"A Critical Comparison of Hot-Wire Anemometry and Laser Doppler Velocimetry for I.C. Engine Applications", Sandia National Laboratories, Report SAND79-8685.

WITZE P.O. (1980b)
"Influence of Air Motion Variation on the Performance of a Direct-Injection Stratified-Charge Engine", I. Mech. E. Paper C394/80.

WITZE P.O. (1981)
"Comparisons Between Measurement and Analysis of Fluid Motion in Internal Combustion Engines", Sandia National Laboratories, Report SAND81-8242.

WITZE P.O. (1982)
"The Effect of Spark Location on Combustion in a Variable-Swirl Engine", SAE Paper 820044.

WOOD G.B., HUNTER D.U., TAYLOR E.S. & TAYLOR C.F. (1942)
"Air Flow Through Intake Valves", Transaction of SAE, 50, 212.

WOODS W.A. & KHAN S.R. (1965)
"An Experimental Study of Flow Through Poppet Valves", Proc. I. Mech. E., 180, 32.

WOODS W.A. & GHIRLANDO R. (1975)
"Radial Flow in an Engine Cylinder Near the End of Compression", I. Mech. E. Paper C82/75.

YANTA W.J. (1973)
"Turbulence Measurements with a Laser Doppler Velocimeter", Naval Ordinance Labs., White Oak, Silver Spring, Report NOLTR 73-94.

YIANNESKIS M. (1982)
"Flow in Reciprocating Engine Cylinders and Curved Ducts", Ph.D. Thesis, University of London.